Flutter Vulnerability Assessment of Flexible Bridges

Dissertation

submitted to, and approved by,

the Department of Architecture, Civil Engineering and Environmental Sciences
of the Technische Universität
Carolo-Wilhelmina
zu Braunschweig
and
the Faculty of Engineering
Department of Civil Engineering
of the University of Florence

in candidacy for the degree of a
Doktor-Ingenieur (Dr.-Ing.)/
Dottore di Ricerca in Risk Management on the Built Environment*)

by
Claudio Mannini
from Florence, Italy

Submitted on	31 March 2006
Oral examination on	19 May 2006
Professoral advisor	Prof. Udo Peil
	Prof. Gianni Bartoli

2006

*) Either the German or the Italian form of the title may be used.

The dissertation is published in an electronic form by the Braunschweig university library at the address

http://www.biblio.tu-bs.de/ediss/data/

Tutors

Prof. Dr.-Ing. Gianni Bartoli	*University of Florence*
Prof. Dr.-Ing. Udo Peil	*Technical University of Braunschweig*

Doctoral course coordinators

Prof. Dr.-Ing. Claudio Borri	*University of Florence*
Prof. Dr.-Ing. Udo Peil	*Technical University of Braunschweig*

Examining Committee

Prof. Dr.-Ing. Gianni Bartoli	*University of Florence*
Prof. Dr.-Ing. Reinhard Leithner	*Technical University of Braunschweig*
Prof. Dr. Giorgia Giovannetti	*University of Florence*
Prof. Dr.-Ing. Herald Budelmann	*Technical University of Braunschweig*
Prof. Dr.-Ing. Claudio Borri	*University of Florence*
Prof. Dr.-Ing. Hocine Oumeraci	*Technical University of Braunschweig*
Prof. Dr.-Ing. Enrica Caporali	*University of Florence*
Prof. Dr.-Ing. Udo Peil	*Technical University of Braunschweig*
Prof. Dr.-Ing. Marcello Ciampoli	*University of Rome "La Sapienza"*
Prof. Dr. rer. nat. Heinz Antes	*Technical University of Braunschweig*
Prof. Dr.-Ing. Andrea Vignoli	*University of Florence*
Prof. Dr.-Ing. Jörn Pachl	*Technical University of Braunschweig*
Prof. Dr.-Ing. Renzo Ciuffi	*University of Florence*
Prof. Dr.-Ing. Joachim Stahlmann	*Technical University of Braunschweig*

This thesis is dedicated to my family

Abstract

Risk management is a modern concept concerning the way to cope with natural and man-induced catastrophic events. Definitions of risk are reported and discussed and the particular relevance of Aeolian risk for a built environment is highlighted. Due to their strategic and neuralgic role, the importance of bridge structures as "elements at risk" is clear. It is also well known that fluid-structure interaction (aeroelasticity) can give rise to phenomena of major concern for the design of flexible bridges. In particular flutter can induce diverging oscillations and consequently bring to the collapse of the structure. This doctoral work focuses on the vulnerability assessment of flexible bridges with respect to flutter and two main contributions can be remarked.

First, the Performance-Based Design approach is applied to the collapse limit state due to flutter, following the Pacific Earthquake Engineering Research Center (PEER) formulation. This risk-consistent design philosophy has been developed in the seismic engineering field and only recently some attempts have been made to adapt it to wind engineering applications but never taking into account aeroelastic phenomena. For the first time flutter derivatives are considered as random variables and the flutter problem is approached in a probabilistic way via Monte-Carlo simulations. A single-box girder deck is experimentally studied in the CRIACIV wind tunnel in order to make available data for this particular analysis. Interesting results are obtained both for this section model and for two rectangular cylinders.

The second main contribution of this work is a sort of "pre-normative" study concerning flutter assessment, which could be useful to enhance the codes, as a measure of risk mitigation. The final goal is the set-up of a simplified method to estimate the flutter critical wind speed without performing wind-tunnel tests. Such a tool could be very useful for bridge engineers, especially concerning medium-span flexible bridges and/or pre-design stages. As a matter of fact, deep wind-tunnel investigations are expensive and time-consuming and, albeit absolutely necessary over all the design steps for long-span suspension bridges, they could be sometimes avoided or limited to the final validation stage for less important structures, for which aeroelastic phenomena are less concerning, even though they cannot be excluded a priori. In this context, the relationship between multimodal and bimodal approach to flutter is carefully analyzed and discussed, also with the support of two case studies, and then approximate formulas retaining only three aeroelastic functions are derived. This strong simplification is validated on the basis of a wide range of structural and aerodynamic data, showing its extensive applicability. Finally, a relatively large number of flutter derivative sets are compared according to the definition of a few classes of deck cross-sectional geometry. These data include the trapezoidal single-box deck section with lateral cantilevers, whose experimental tests in the CRIACIV wind tunnel are described in details. The previously mentioned simplified formulas, reducing to three the flutter derivatives to be accounted for, make possible an attempt of generalization. Although this is only a first step towards this ambitious goal, it shows all the difficulties which have to be overcome but also highlights some interesting and promising results.

Acknowledgements

First of all I would like to thank my tutors, Prof. Gianni Bartoli and Prof. Udo Peil, for their support and advice. I feel particularly grateful to Prof. Gianni Bartoli for the enthusiasm for scientific research that he has always transmitted to me, as well as for the continuous supervision of the progress of my work. A special thanks to Prof. Claudio Borri for the strong support and encouragement he has given me during the entire period of study and to Prof. Francesco Ricciardelli, who extensively reviewed this dissertation, for his useful remarks and suggestions. All my gratitude to Lorenzo Procino for his constant and indispensable help during the long wind-tunnel test campaign and to Serena Cartei who has friendly supported me in all the bureaucratic issues. I sincerely also have to thank all the colleagues of the International Doctoral Course for the help I have often received during these three years and for their friendly companionship. Then a special thanks to Carlotta Costa, Stefano Pastò and Luca Salvatori for the extremely fruitful scientific discussions and exchange of ideas.

A grateful acknowledgement to CSTB-Nantes, and in particular to Olivier Flamand and Gérard Grillaud, for the large quantity of data they made available for this research work. It is also impossible to forget the warm welcome I received at DLR-Göttingen and the precious scientific enrichment I got meeting Dr. Günter Schewe, Dr. Ralph Voß and Ante Soda. Finally I would like to thank Prof. Masaru Matsumoto and Prof. Partha Sarkar for the data they kindly sent me.

Contents

List of Figures

List of Tables

Chapter 1

The risk management framework

1.1 What is risk management?

Risk management is a quite modern concept and it refers to the ensemble of "coordinated activities to direct and control an organization with respect to risk" (Shortreed *et al.*, 2003). This definition obviously implies the presence of elements at risk, that is of a *built environment*, where a given catastrophic event can produce human or economic losses.

Risk management can be considered both as an operational process (*operational risk management*) concerning an existing protection system, and a process of design and implementation (*risk mitigation*) of a new protection system (Plate, 2000). Operational risk management includes concepts such as maintenance, preparedness and disaster response (Fig. 1.1).

It is obvious that an existing protection system has to be continuously maintained in order to function as planned and improved to respond to the changes in the concept of protection. *Risk analysis* is the instrument that allows this dynamic update of the system. Nevertheless it must be clear that the presence of a *residual risk* is unavoidable, that is the probability that the protection system fails or a rare event exceeding the design one occurs, is never zero. For this reason preparedness to catastrophic events is a fundamental ring in the chain of risk management. Early warning systems are nowadays a more and more powerful tool relying on fairly sophisticated forecasting techniques and technologies. The final step of operational risk management is disaster response and relief and it includes all the actions that must be taken when disasters occur, such as humanitarian aid to the victims and reconstructions of lifelines and damaged or destroyed buildings.

As it has already been claimed, the dual concept of operational risk management is risk mitigation, which is related to the planning of a new protection system (Fig. 1.2). When the existing protection system, if any, does no longer meet the demands of the present society, in other words when the residual risk is larger than the *acceptable risk*, a new system has to be planned and implemented. It is worth noting that acceptable risk is determined by society perception and attitude toward risk, whereas residual risk depends on human activities and natural changes (such as climate changes) which modify the boundary conditions of the problem. The definition of the acceptable risk level is by itself a very challenging problem since it concerns the allocation of the limited resources of a nation, that means it should be a

Figure 1.1: Operational risk management according to Plate (1998, 2000) and Eikenberg (1998)

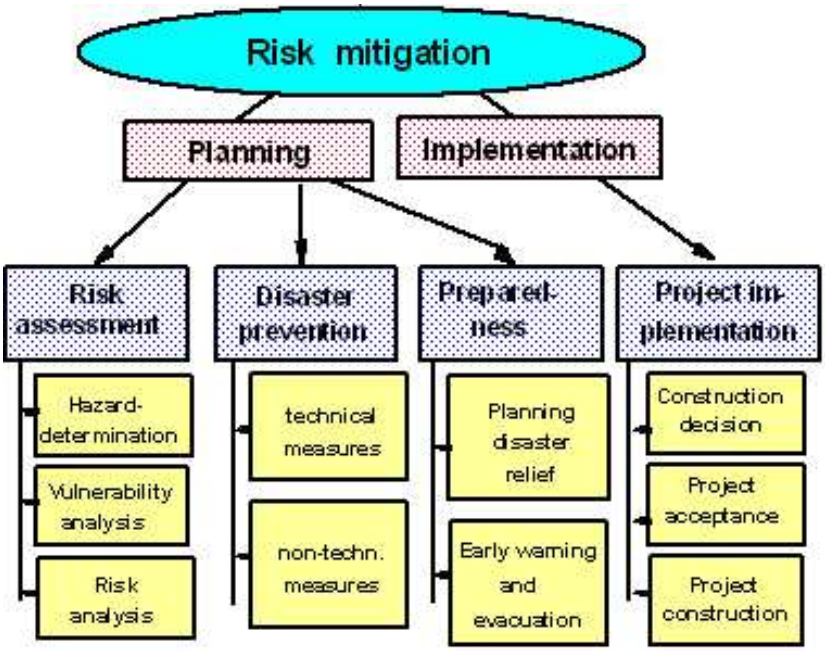

Figure 1.2: Risk mitigation diagram according to Plate (1997, 2003a,b)

reasonable compromise between several exigencies. In order to answer to the capital question "how safe is safe enough and how much are we willing to spend for safety?", Rackwitz defined an optimization problem based on the Life-Quality Index (Rackwitz, 2003).

The basis of risk mitigation planning is *risk assessment*, which includes collection of data, construction of mathematical models, definition of possible scenarios and risk quantification through calculations. This fundamental step is the main task for engineers, at least in a narrow sense, whereas the whole project requires the contribution and collaboration of many different professional subjects. As a matter of fact risk mitigation planning also consists of disaster prevention and preparedness. From the structural engineering point of view (but not only), project implementation is very important since it concerns normative codes, which indirectly allow to design structures and infrastructures with the desired level of risk.

The concept of risk so far has been employed several times only relying on its common idea, which does not perfectly coincide with the technical definition. According to ISO/IEC guide 73 (Shortreed *et al.*, 2003), *risk* is the "combination of the probability of an event and its consequences":

$$Risk = Probability \times Consequences \tag{1.1}$$

The concept of probability in Eq. (1.1) can be detailed in a few components, so that the following definition of risk is obtained:

$$Risk = Hazard \times Exposure \times Vulnerability \times Consequences \tag{1.2}$$

The products of Eqs. (1.1)-1.2 have to be extended over all probabilities of the event, i.e. over all hazard levels, therefore they actually are convolution integrals. Given a natural or man-induced event that can produce life or economic losses (earthquake, flood, wind storm, fire, terrorist attack and so on), the probability of occurrence of this event is the *hazard*. Indeed the event can be characterized by different levels of magnitude, so that in practice the hazard can be expressed by one or more curves that associate the exceeding probability to one significant parameter (peak ground acceleration, mean wind speed, etc.) that sum up the intensity of the event. In order to be practically employed in a risk analysis, the chosen parameter has to satisfy the requirements of *sufficiency*, *computability* and *efficiency* (Cornell and Luco, 2001).

The *exposure* is defined as the probability that the hazardous event meets something to destroy or damage, that is urbanized areas, lifelines, structures, power plants or vulnerable facilities in general. Historical or archaeological sites must definitely be included in this list. Nevertheless, the concept of exposure is still ambiguous in literature, since it can be sometimes included in the hazard. For instance, if a particular structure is concerned, such as an important bridge, and the risk with respect to wind has to be assessed, then the hazard is determined through in-situ wind measurements at different heights. Therefore, in this case, the exposure is already considered in the hazard or, in other words, the probability that the considered hazardous event (with its probability of occurrence) strikes the structure is equal to unity. Nevertheless, if the seismic risk assessment of an urban area is considered, the hazard can be defined as the probability of occurrence of an earthquake in the area with a specified magnitude, while the exposure gives, for each single element at risk, the probability, given that

earthquake, to have a particular peak ground acceleration (for instance), taking into account the distance from the epicenter, soil characteristics, etc.. It is also worth noting that sometimes the same meaning of consequences is given to the concept of exposure.

The *vulnerability* is the sensitivity of the facilities to the event in terms of damage (Augusti *et al.*, 2001). It is the "structural" term in the risk equation since it can express the probability to have a certain structural damage once an hazardous event, characterized by a given energy, has occurred.

Finally the *consequences* represent the "economic" term in the product and it refers to the losses produced by the event. It is also called *cost of damage* (Augusti *et al.*, 2001). Consequences can be economic losses, casualties or cultural-social losses. The last two cannot be monetarily interpreted and hence they are defined as *intangible* (Augusti *et al.*, 2001). Conversely the first kind of losses can be treated in monetary terms and they can be *direct*, if caused immediately by the event, or *indirect*, if they are long-term secondary effects of the event (loss of value of facilities, alteration of economic or social equilibriums, etc). In addition among the direct costs the lack of profit must be considered as well and in some cases this can be the most important loss (it often happens when industrial facilities are struck). Obviously the indirect costs must be discounted considering an appropriate interest rate in order to be added to the direct losses. It is also important to point out that the consequences are the risk component which can often be strongly reduced thanks to early warning systems or emergency plans.

It is worth noting that the definition of risk of Eq. (1.2) is not unique but probably the one which better applies in the field of structural engineering. As a matter of fact, concerning for instance flood protection engineering, another definition is preferred because more appropriate (Plate, 2003a,b; Alexander, 2003):

$$Risk = Hazard \times Vulnerability \tag{1.3}$$

Practically, with respect to the expression of Eq. (1.2), exposure and consequences are already included in the concepts of hazard and vulnerability respectively.

Eq. (1.1) makes clear the unit dimension of risk, that is $losses/year$. As a matter of fact, $year^{-1}$ is the unit dimension of probability and consequences can be measured in terms of money, if they are tangible, whereas they are more difficult to handle if they are intangible. Some attempts have been done to homogenize the two types of losses [e.g. Rackwitz (2003)].

The given definitions of risk apply to single structures or facilities, as well as to systems or communities. Nevertheless, as it will be clear in the third section of this chapter, the convolution in Eq. (1.2) is very useful for explicative purposes but it must be substituted by a convolution integral in practical applications.

1.2 Aeolian risk and aeroelastic phenomena

The relevance of Aeolian risk is evident to everybody after the devastations produced by the passage of the hurricane Katrina over the coasts of Louisiana and Mississippi in August 2005, when the richest and most technological country of the world showed its vulnerability and non-preparedness with respect to such an event. However, apart from this particular recent

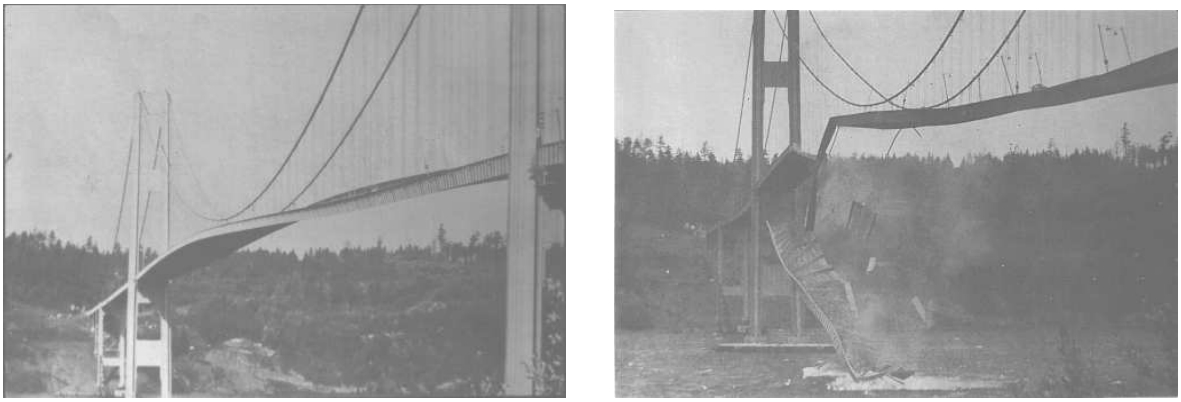

(a) (b)

Figure 1.3: The infamous collapse of the Tacoma Narrows Bridge on November 7^{th} 1940, Washington State, USA

evidence stressed by the mass media, available data about Aeolian risk are already quite eloquent. According to the Munich Reinsurance Group (Augusti *et al.*, 2001), windstorms are the third cause of economic losses due to natural hazards with 28 % of the total amount, following earthquakes (35 %) and floods (30 %). Conversely, concerning insurers' total claims, windstorms are by far the first natural disaster in the list, whereas they are not much behind earthquakes regarding human fatalities (45 % vs. 47 %) and much more concerning than floods (7 %). All these figures confirm the relevance of Aeolian risk and suggest the importance of doing research in wind engineering field, carefully designing the structures taking into account in a correct way wind effects, and improving methods of weather forecasting, early warning systems and evacuation plans.

In addition to all that, in the last years Aeolian risk has been sensibly increasing despite the fact that scientific knowledge of wind effects has been noticeably improved and the provisional codes have been enhanced. The reason for this trend must be searched in the combined increase of three terms in Eq. (1.2): hazard, exposure and vulnerability.

Hazard is increasing because of climate changes which seem to have started at the beginning of last century, probably because of several reasons but there is little doubt that human activities play a crucial role in these phenomena. The planet is globally warming, more energy is consequently available in the atmosphere and as a result the frequency and probably the intensity of extreme events like tropical cyclones or windstorms in general have sensibly increased. It is worrying the fact that this trend is expected to continue in the next decades and for instance it will be probably necessary to design structures with different wind loads depending on the year of construction and expected lifetime (Augusti *et al.*, 2001).

Exposure is increasing as well due to the migration of population, goods and facilities into wind-hazardous areas, where many megacities were born in the last decades.

Finally new structures tends to be always lighter and consequently more vulnerable to wind. The diffusion of light and high-resistance materials leads in this direction the construction industry. In addition, always more challenging designs are realized (long-span bridges, high-

rise buildings, large flexible roofs, etc.) and that requires that wind effects are considered as carefully as possible.

It is very important to underline that Aeolian risk concerns a large number of phenomena and it cannot be treated considering extreme events only. As a matter of fact, even if we limit our interest to structural problems, along with the collapse that is concerned by very rare and strong winds, the partial damage or the serviceability of structures must be treated as well and those limit states can be affected by medium-intensity events. Furthermore the damage of non-structural parts can be produced by small storms and the costs of repairing and maintenance can be definitely non-negligible, sensibly affecting the total risk. Particular attention must be paid to fatigue problems which can lead to the collapse of a structure or a part of it: usually frequent and consequently less severe events are determinant in this case, especially if combined with particular aeroelastic phenomena such as lock-in [e.g. Pastò (2005)]. All these considerations show that it is not enough to be given by codes of a design wind speed related to extreme events (usually the 10-min-average speed with a 2 % yearly probability of exceedance) in order to perform thorough analyses. Several design wind speeds are therefore absolutely necessary and the ideal condition would be to dispose of a curve expressing the probability of exceedance as a function of the wind velocity. Nevertheless for more sophisticated approaches the mean wind speed as design parameter is not enough and other data, such as wind direction, turbulence intensity, integral length scales of turbulence, turbulence spectra, etc., are needed. In this case it would be more appropriate to speak about "design storms".

A separate section would be necessary to discuss the very important role of combined actions, such as wind-rain or wind-snow, which can increase the total risk for a structure very much, also introducing new phenomena that the designer must deal with (e.g. water rivulet-induced vibrations for cables).

It must be added that Aeolian risk does not involve structural problems only. Other sources of risk can be identified in pedestrian or vehicles discomfort in urban areas, in stadiums (Borri and Biagini, 2005), over bridges or in vibrating buildings (Paulotto *et al.*, 2004) or in pollution dispersion and accumulation. All these non-structural phenomena are tentatively been grouped under the term *dissatisfaction risk* (Augusti *et al.*, 2001).

After this panoramic view of risk management and Aeolian risk it is important to remind that this research work deals with *aeroelastic phenomena* and in particular with *flutter*, which are only a component, though important, of what has been discussed so far. Aeroelasticity groups all those phenomena which involve the mutual interaction between the fluid flow (in this case the wind) and the structural motion. This discipline was already well known in the aeronautical field in 1940 when it suddenly captured the attention of civil engineers after the infamous collapse of the suspended-span bridge over the Tacoma Narrows (Washington, USA), a very light structure considered at that time a marvellous example of technology (Fig. 1.3). As a matter of fact that bridge had been statically designed for a very high wind speed but collapsed during a non-extraordinary wind storm because of flutter, a phenomenon which had not been absolutely taken into account in the design. Since then aeroelasticity concerning flexible structures and above all bridges has been deeply investigated through theoretical, experimental and numerical methods and many progress have been doing, although several open problems still need to be deeply studied. After 1940 other problems and collapses due

to aeroelastic phenomena have been observed, though not so astonishing as Tacoma failure, but nowadays very challenging designs are conceived accounting for aeroelastic stability as one of the most important requirements. The more eloquent example is surely the proposal of Messina Strait Bridge but many other light modern structures with very low eigenfrequencies of oscillation and damping levels are designed all over the world. These structures tend to be less sensitive to seismic action and geotechnical settlements but much more vulnerable to wind loads and in particular to aeroelastic effects. Therefore the relevance of aeroelastic phenomena for a risk analysis is absolutely evident, also given the economic and strategic importance of the aforementioned types of structures.

A brief critical review of aeroelastic phenomena, with particular attention to bridges, will be detailed in Chapter 2.

1.3 Performance-Based Design

Performance-Based Design (PBD) represents the structural design philosophy consistent with risk management approach, which is aimed directly to the achievement and optimization of well specified performance objectives. This modern approach does not exclude prescriptions and consequently it should not be considered an alternative to provisional codes. In PBD it is not new the idea of fixing some performance objectives but the probabilistic way to achieve them. In fact modern codes, even the most recent such as Eurocode 1 (ENV1991-2-4, 1995; EN1990, 2002), translate these performance objectives in several limit states but the safety partial coefficients they give are not calibrated in a probabilistic way but just on empirical basis.

PDB has been developed mainly in the USA for seismic risk applications and design [e.g. Baker and Cornell (2003)] but it is still at an embryonic stage concerning wind engineering (Paulotto *et al.*, 2004). A very interesting translation of PBD in equation was proposed by the Pacific Earthquake Research Center (PEER) [e.g. Paulotto *et al.* (2004)]:

$$p(DV) = \int\int\int p(DV|DM) \cdot |dp(DM|EDP)| \cdot |dp(EDP|IM)| \cdot dp(IM) \qquad (1.4)$$

where:
IM (Intensity Measure) denotes a measure of the magnitude of the action;
EDP (Engineering Demand Parameter) denotes a parameter which describes the structural response;
DM denotes a measure of the damage (cracking level, spalling, etc.);
DV denotes a decision variable, that is a parameter which determines the design decision (for instance a limit state, the amount of economic or human losses, etc.);
$p(\cdot)$ denotes a probability of exceedance;
$p(\cdot|\cdot)$ denotes a conditional probability of exceedance.
The integrals extend over all the possible Intensity Measures whose probabilities of exceedance are determined through *hazard analysis*. The term $p(EDP|IM)$ represents the probability of exceedance of a certain level of structural response, given a particular measure of the event, whereas the term $p(DM|EDP)$ is the probability of exceedance of a certain structural

damage, once the structural response is given. The former is obtained through the *structural analysis*, the latter by means of the *damage analysis*. Their product can be identified as the vulnerability in Eq. (1.2). Finally the term $p(DV|DM)$ represents a probability measure of the cost of damage, that is of the consequences. It is obtained through the *loss analysis*. Several professional figures are involved in the outlined risk analysis: hazard analysis usually competes to pure scientists (meteorologists, geophysicists, etc.), vulnerability analysis (structural and damage analysis) is the main task of engineers, while in loss analysis economists can give the most important contribution.

One of the most difficult terms to treat in the equation is the one that relates the measure of the damage DM to the structural response EDP. As a matter of fact, to simulate numerically the actual damage of a structure is a very hard task. In addition the available experimental data are too limited, especially concerning the damage of non-structural components and goods present inside the buildings. For this reason, in particular in the wind engineering field, attempts have been made to express the damage through the structural response itself [e.g. Paulotto *et al.* (2004)]. The PEER equation consequently simplifies as follows:

$$p(DV) = \int\int p(DV|DM) \cdot |dp(DM|IM)| \cdot dp(IM) \tag{1.5}$$

Fragility curves are the practical expression of the term $p(DM|IM)$ in the previous equation. They express the probability of exceeding a specific damage state, conditioned on the value of the parameter synthesizing the magnitude of the natural or man-induced event. There are two types of fragility curves: system fragility and component fragility curves. System fragility refers to the damage of the entire structure whereas component fragility curves take into account only a specific part of the structure. The fragility of the entire structure can be approximated assembling the component fragilities. In wind engineering practice the intensity measure is usually the mean wind speed so that the fragility curves express a relation between the probability of exceedance of a damage state and the mean wind speed.

In order to make Eq. (1.5) and all the concepts discussed so far easier to apply in practice, it is possible to fix a certain number of limit states as performance objectives. In particular, distinction can be made between *low performance levels* and *high performance levels*. Hence collapse and damage limit states require low structural performance with respect to the hazardous event, whereas serviceability and comfort limit states are related to limited losses and consequently require high performance behavior. The concept of comfort is very general and refers to pedestrians, vehicles, occupants of buildings or structures and so on. For each limit state a maximum probability of exceedance in a fixed time period has to be specified in order to verify the safety of the design. The way to fix these probabilities, as we have already discussed in the first section of this chapter, is a very complex problem which should involve economic and political considerations through an optimization process [e.g. Rackwitz (2003)].

It is worth noting that fragility curves for high performance levels exist in literature while it is not possible to find examples for low performance levels (Paulotto *et al.*, 2004), thus confirming the still primitive state of PBD in wind engineering.

The complete PBD approach is often difficult to apply, especially in those fields where the state of the art has not reached yet the same level of development as in seismic engineering. A fully probabilistic structural design would often be a significant step forward. This is equivalent

to simplify the PEER equation by taking a *Limit State* as Decision Variable ($SL \equiv DV$) and then relating it directly to a structural response parameter ($DV \equiv DM \equiv EDP$):

$$P_{fail} \equiv p(SL) = \int p(SL|IM) \cdot dp(IM) \tag{1.6}$$

Once a set of relevant limit states have been identified and the acceptable probability of failure has been fixed on the basis of socioeconomic issues, the safety of the structure can be checked by comparing the probability of failure P_{fail} with its acceptable value. This more strictly engineering formulation of the PEER equation allows to apply the Performance-Based Design in common design practice (national and international recommendations) and it is particularly convenient for our purposes.

Aeroelastic phenomena play a key role with respect to all limit states, both for low and high performance levels, when flexible structures, such as cable-stayed or suspension bridges, are concerned. Nevertheless the adaptation of Performance-Based Design to aeroelastic phenomena is a very challenging task at the present state of the art.

1.4 Contribution of the present research work

Concerning the large sphere of risk management this research work focuses on vulnerability, that is mainly on the step of structural analysis in the process of risk assessment or risk analysis. As we have already pointed out, wind engineering as a modern discipline is fairly young and risk-consistent approaches in this field are still not very well codified. Then, if we concentrate on aeroelastic phenomena, to perform risk analyses and to conceive risk mitigation planning is even much more difficult, since this phenomena are already quite difficult to treat in a traditional, deterministic way. The ambitious attempt of this work is to include in risk analysis bridge aeroelasticity and specifically flutter stability. Two contributions in this direction are given: the first one is a sort of pre-normative study, which is related to risk mitigation through code implementation; the second one is a probabilistic approach to flutter problem which should allow to treat this phenomenon coherently with Performance-Based Design philosophy.

The importance to perform careful risk analyses concerning bridges is fairly clear. As a matter of fact, these structures are very expensive to build and to maintain, therefore they have a very high intrinsic value. Moreover they usually play important strategic roles for connections and traffic circulation. Therefore the closure of a bridge because of a windstorm can produce a large amount of economic losses, even though the structure is not at all damaged. Also wind-induced discomfort is very concerning for bridges since it affects traffic safety. Finally in a catastrophic scenario due to a natural or man-induced hazardous event, the collapse or the serviceability failure of important bridges can make extremely difficult the disaster response concerning emergency plans and humanitarian assistance. On the other hand, improvements in material technology and technical knowledge allow nowadays to build superlong-span or very light medium-span bridges. Consequently these structures are always more vulnerable to wind actions and in particular to aeroelastic phenomena, which have to be carefully accounted for in any structural analysis.

Aeroelastic phenomena are usually dealt with through wind-tunnel tests, which at the present state-of-the-art are the only reliable tool to treat aerodynamics and fluid-structure

coupling for bluff-bodies such as bridge decks. Complete extensive experimental investigations can be very expensive and time-consuming but they are absolutely necessary since the really first design stages for large-span bridges, for which aerodynamics and aeroelasticity are usually the key points of the design. Conversely for medium-span bridges and conventional geometries these problems are less concerning even though they cannot be excluded a priori. In addition extensive experimental campaigns are not always possible in these cases, above all for reasons of budget, and often wind-tunnel tests, if any, are performed only at the last design stage as final validation. Therefore for bridge engineers it could be very useful to dispose of an instrument able to highlight or to exclude with a certain degree of reliability the possibility of aeroelastic instabilities or large amplitudes of vibration, without performing wind-tunnel tests, at least at pre-design stages. Unfortunately this instrument is not provided by the national or international provisional codes, which always refer to wind tunnel tests when aeroelasticity is concerned. Indeed, empirical formulas for classical flutter, galloping and vortex shedding were given in the ECCS recommendations (ECCS, 1987), which was, to the knowledge of the writer, the most courageous provisional document at this regard, but they were afterwards not reported in the following documents of Eurocode 1 [e.g. ENV1991-2-4 (1995)]. In the present research work we limited our attention to bridge deck flutter instability and we tried to set up a simplified method of calculation which could be used in order to understand if a given bridge, for a specified level of the hazard, is safe enough (flutter is definitely not a problem) or the design must be definitely modified (the flutter wind speed is definitely too low) or if wind tunnel tests are needed in order to better assess the actual vulnerability of the structure. This tool could be useful to better design medium-span conventional bridges and in this sense we can speak about a pre-normative study, which could help to improve the codes, therefore as a measure of risk mitigation.

The aforementioned simplified approach is based on Scanlan's definition of linearized self-excited forces via flutter derivative functions (see Chapter 2) and it consists of three main steps. In the first one, described in Chapter 5, the possibility to pass from a multimodal with eighteen flutter derivatives to a bimodal approach to flutter with eight aeroelastic functions is checked. Then in Chapter 6 the flutter equations are analyzed in details, manipulate and simplified on the basis of a large database of dynamic and aerodynamic data. The resulting formulas depend on three or even two flutter derivatives only, which are recognized to be the most reliable, the easiest to be identified through wind-tunnel tests and those for which more data are available in literature. Apart from the practical interest of the formulas, in the writer's opinion this result is also scientifically important for the insight it gives in the flutter mechanism. Finally, thanks also to the contribution of the Centre Scientifique et Technique du Bâtiment (CSTB) of Nantes, France, a relatively large number of data are collected for a few classes of bridge deck geometries and in Chapter 7 a first step towards flutter derivative generalization is attempted. A scheme of the explained procedure is shown in Fig. 1.4. It is worth noting that the last step is crucial in order to be able to assess flutter boundaries with a certain degree of reliability without performing wind-tunnel tests and it still needs further research.

In Chapter 3 an extensive wind tunnel test campaign is described. A bridge deck section-model is tested in the DIC-CRIACIV Boundary Layer Wind Tunnel of Prato in order to investigate its static-aerodynamic and in particular its aeroelastic behavior. One of the main

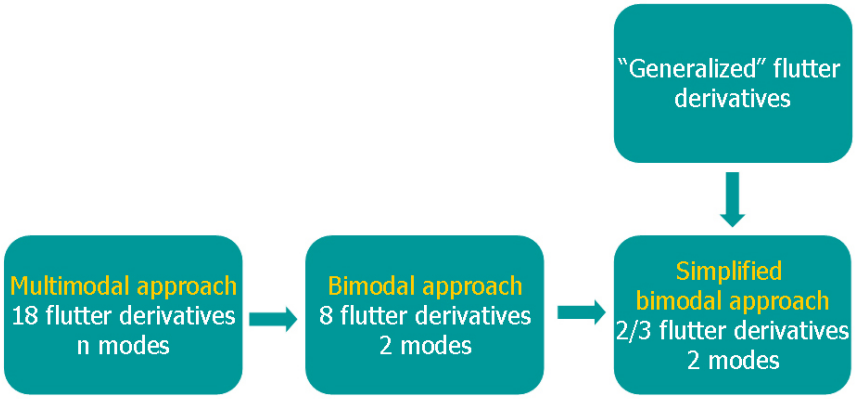

Figure 1.4: Scheme of the simplification procedure for flutter problem

reasons for these tests is the exigency to enlarge and complete the available aeroelastic data (Chapter 7). In fact the trapezoidal single-box deck cross-section with lateral cantilevers we tested is a very common geometry in medium-span cable-stayed bridges. Nevertheless not many data are available in literature.

The second contribution of the present work to vulnerability analysis still concerns bridge flutter stability but it is more oriented towards Performance-Based Design. A stochastic approach to flutter is proposed in order to account for all the uncertainties in the mathematical model and in the measurement and identification procedure. Therefore the result of the analysis is a probability density function for the flutter boundaries instead of the deterministic critical wind speed and frequency. Consequently this approach could be used to determine the term $p(SL|IM)$ in Eq. (1.6), where the ultimate limit state for flutter instability is concerned. Obviously, as flutter stability is concerned, the contribution refers to low performance levels and in particular to collapse limit state. An attempt to apply this procedure has already been done with some interesting results in Bartoli and Mannini (2005) using the experimental data measured by Righi in the DIC-CRIACIV wind tunnel for two different rectangular cylinders (Righi, 2003). In Chapter 4 the same procedure with some improvements is applied to the experimental data for the bridge deck section previously mentioned (Chapter 3), whose tests are conceived with the explicit purpose to fit this particular application.

Finally, as a future development, the two original contributions of this work could be made converge if it was possible to specify in a probabilistic way the "generalized" flutter derivatives for classes of bridge deck cross-sectional geometries. As a matter of fact the stochastic approach to flutter could be applied to the aforementioned simplified formula of flutter assessment, hence allowing the determination of the probability of collapse (due to flutter) given a certain magnitude of the hazard (mean wind speed) without performing wind tunnel tests. In this case the pre-normative tool we described would be perfectly consistent with a risk analysis. Needless to say that the difficulty of this additional effort is mainly the specification of the probability density functions corresponding to flutter derivatives, also due to the lack of experimental data exploitable for this purpose.

Chapter 2

Aeroelastic phenomena

2.1 Fluid-structure interaction

The complex interaction between air flow and solid structures has always been a very important issue. Although not fully understood, it was of great concern for civil engineers already in the XIX century, when several bridges collapsed or were severely damaged because of wind effects. In the first half of the XX century, the fluid-structure interaction phenomena were practically forgotten in civil engineering, whereas they were carefully studied in the aeronautical field, where the theory of aeroelasticity was funded. After the Tacoma Bridge failure in 1940 this discipline has got back to the civil engineering sphere as well and nowadays the effects of the fluid-structure coupling are more and more important due to the increased flexibility of modern constructions.

The basic idea of the fluid-structure interaction is that the flow around a solid structure produces steady and unsteady loads which tend to elastically deform the structure inducing vibration. If this motion is large enough, it is able to influence the flow field around the body and consequently to change the aerodynamic loads. This feedback is the actual core of aeroelasticity. In particular, since bridges and civil structures in general cannot be considered streamlined profiles, we are mainly interested in bluff-body aerodynamics and aeroelasticity, where flow separation plays a key role.

The second section of this chapter gives a brief overview of the most common aeroelastic phenomena in the civil engineering field, referring to the design limit states involved. Then, the following sections give deeper details concerning the fundamental theory and models to describe self-excited forces and calculate flutter instability.

2.2 Aeroelastic phenomena

2.2.1 Torsional divergence

Torsional divergence is a static instability phenomenon produced by the loss of torsional stiffness due to steady aerodynamic moment. Considering a cylinder-type structure, the latter can

be written as follows:

$$M(\alpha) = \frac{1}{2}\rho U^2 B^2 C_M(\alpha) \tag{2.1}$$

where ρ is the air density, U the mean airflow speed, B the cylinder chord length, C_M the aerodynamic moment coefficient around the twist axis (positive clockwise) and α the mean angle of twist (positive clockwise). Considering a single-degree-of-freedom linear structure, the equilibrium position is given by the equation:

$$K_\alpha \alpha = \frac{1}{2}\rho U^2 B^2 C_M(\alpha) \tag{2.2}$$

The aerodynamic moment coefficient can be linearized around the undeformed position (α=0):

$$C_M(\alpha) = C_M(0) + \frac{dC_M}{d\alpha}(0)\alpha \tag{2.3}$$

so that Eq. (2.2) can be written as:

$$K_\alpha \alpha = qB^2[C_M(0) + \frac{dC_M}{d\alpha}(0)\alpha] \tag{2.4}$$

where $q = \frac{1}{2}\rho U^2$ is the kinematic pressure. Reorganizing the terms in the previous equation, static angle of twist can be expressed as follows:

$$\alpha = \frac{qB^2 C_M(0)}{K_\alpha - qB^2 \frac{dC_M}{d\alpha}(0)} \tag{2.5}$$

It is evident from Eq. (2.5) that the mean angle of twist tends to increase indefinitely when $K_\alpha - qB^2 \frac{dC_M}{d\alpha}(0) \to 0$, that is when the total stiffness (structural + aerodynamic) tends to zero. The corresponding mean wind speed U_{div} is called critical divergence wind speed:

$$U_{div} = \sqrt{\frac{2K_\alpha}{\rho B^2 \frac{dC_M}{d\alpha}(0)}} \tag{2.6}$$

In case the aerodynamic moment coefficient is not linear with respect to the angle of attack, the same linearization may be applied around a generic static twist angle $\alpha = \alpha_0$ or the more general nonlinear Eq. (2.2) could have been solved numerically. Furthermore it is evident from Eqs. (2.5)-(2.6) that static divergence can occur only if the moment coefficient is characterized by a positive slope $\frac{dC_M}{d\alpha}(0) > 0$.

It is also worth noting that the previous analysis refers to single-degree-of-freedom structures but it may readily be generalized to three-dimensional structures such as bridge decks [e.g. Simiu and Scanlan (1996)].

Torsional divergence, which refers to the ultimate limit state, is usually not a very concerning problem for real bridges as it tends to appear at sensibly higher wind speed than the dynamic instability called flutter (see section 2.2.4). Nevertheless this cannot be trusted in case of bridges with frequency ratio between torsion and bending critical modes close to one or even lower than unity [e.g. Dyrbye and Hansen (1997)].

2.2.2 Galloping

Galloping is a single-degree-of-freedom instability typical of slender structures characterized by particular cross-sectional geometry, such as rectangular or D-shaped. It can lead to very large-amplitude oscillations in the across-wind direction.

The phenomenon is usually approached with the quasi-steady theory, thus meaning that the influence of fluid memory on the instability mechanism can be neglected. In order to determine the galloping critical wind speed U_g for the condition of incipient instability in two-dimensional cylinders, the aerodynamic lift due to the heaving vibration can be linearized around the mean deformed configuration (see section 2.4.3) and the equation of motion can be written as follows:

$$m[\ddot{h} + 2\zeta_h\omega_h\dot{h} + \omega_h^2 h] = \frac{1}{2}\rho U^2 B[\frac{dC_L}{d\alpha}(\alpha_0) + C_D(\alpha_0)]\frac{\dot{h}}{U} \tag{2.7}$$

where m is the mass per unit length, ζ_h is the damping ratio for the bending mode and ω_h is the bending circular frequency; $C_D(\alpha_0)$ and $\frac{dC_L}{d\alpha}(\alpha_0)$ are the drag coefficient and the first derivative of the lift coefficient evaluated at the mean angle of attack α_0. According to the Glauert-Den Hartog criterion [e.g. Blevins (1990); Simiu and Scanlan (1996); Dyrbye and Hansen (1997)] galloping occurs when the total damping (structural+aerodynamic) vanishes:

$$2m\zeta_h\omega_h - \frac{1}{2}\rho U B[\frac{dC_L}{d\alpha}(\alpha_0) + C_D(\alpha_0)] = 0 \tag{2.8}$$

Therefore one obtains:

$$U_g = -\frac{4m\zeta_h\omega_h}{\rho B[\frac{dC_L}{d\alpha}(\alpha_0) + C_D(\alpha_0)]} \tag{2.9}$$

It is evident from Eq. (2.9) that a structure can gallop in a bending mode only if $[\frac{dC_L}{d\alpha}(\alpha_0) + C_D(\alpha_0)] < 0$. That is why circular cylinders, characterized by $\frac{dC_L}{d\alpha} \equiv 0$ and $C_D > 0$, are not prone to this type of instability. Nevertheless, cables too can undergo galloping oscillations when their circular shape is altered, for instance by ice coating.

In order to calculate the limit-cycle amplitude of oscillation at a certain post-critical wind speed and not merely the critical wind speed, a nonlinear model for the aerodynamic forces is necessary. In one of the most famous models, the vertical force coefficient C_{Fz} is expressed as a polynomial series retaining the terms up to the third or seventh order (Blevins, 1990; Simiu and Scanlan, 1996; Dyrbye and Hansen, 1997; Thompson and Stewart, 2002):

$$C_{Fz} = A_1\frac{\dot{z}}{U} - A_3(\frac{\dot{z}}{U})^3 + A_5(\frac{\dot{z}}{U})^5 - A_7(\frac{\dot{z}}{U})^7 \tag{2.10}$$

Parkinson and Smith (1964) determined the coefficients A_1 to A_7 for a square cylinder applying a polynomial fit to the static experimental values for $C_{Fz}(\alpha)$ and compared with experiments the resulting limit-cycle amplitudes, observing a very good agreement (Fig. 2.1). It is clearly shown in Fig. 2.1 that the seventh order model is able to capture the Hopf bifurcation suggested by the experiments, while this nonlinear dynamic feature cannot be appreciated adopting the third order polynomial fit (Blevins, 1990).

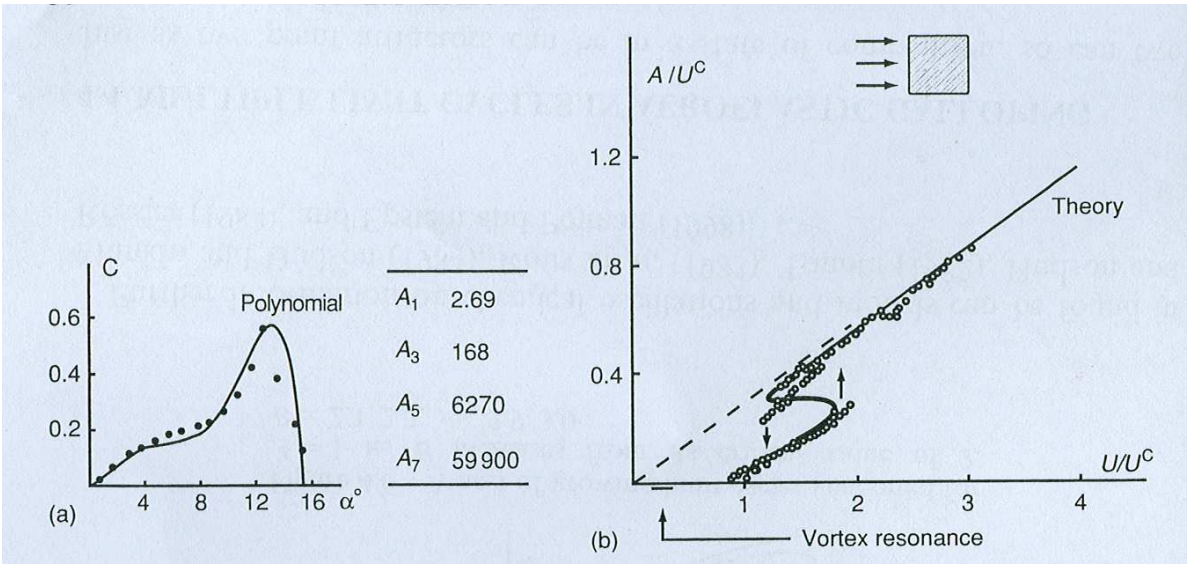

Figure 2.1: Seventh order polynomial fit to the measured vertical force coefficient $C(\alpha)$ for a square cross section (a) and corresponding theoretical and experimental results (Parkinson and Smith, 1964) on a plot of galloping vibration amplitude against wind velocity (b); U^C is the galloping critical wind speed. [From Thompson and Stewart (2002)]

Galloping in the bending mode is usually recognized not to be a problem for bridge decks. Conversely torsional galloping can be a concerning issue but the quasi-steady theory is usually not able to properly describe this phenomenon. This particular instability concerning bridge decks, often called torsional flutter, will be discussed in the next section.

Parkinson and Wawzonek (1981), Obasaju (1983) and Nakamura and Matsukawa (1987) have investigated the coupling of galloping and vortex shedding as well as the limitations of the quasi-steady theory. Simiu and Scanlan (1996) also discuss the phenomenon called wake galloping, in which two cylinders interact and the limit-cycle oscillations of the downstream one are induced by the turbulent wake of the upstream cylinder.

Another very peculiar type of instability, in the in-wind direction but somehow similar to galloping, can concern circular cylinders for Reynolds numbers very close to the critical range where drag crisis occurs. The mechanism of excitation is basically the following: assuming to be in the transition range, if the cylinder starts to move in the in-wind direction the apparent wind speed and therefore the Reynolds number decrease. This can cause the circular cylinder to pass in the subcritical regime with consequent increment of the drag force. Conversely, a decrease of the drag force can be observed when the body moves in the opposite direction. It is easy to understand that this mechanism is able to lead to large amplitude of oscillation. In Moe and Henriksen (1999) and Schewe (2005) the following criterion for instability is proposed and discussed:

$$2C_D + Re\frac{\partial C_D}{\partial Re} < 0 \tag{2.11}$$

where

$$Re = \frac{UB}{\nu} \tag{2.12}$$

is the Reynolds number based on the chord length and ν is the air kinematic viscosity ($\nu = 1.5 \cdot 10^{-5}$ m^{2}s^{-1} for the air at 20°C).

Due to the large-amplitude vibrations, galloping in its basic across-wind quasi-steady nature mainly concerns the ultimate limit state for cables and other linelike structures.

2.2.3 Vortex shedding and lock-in

It is well known that a bluff body in a fluid flow develops a turbulent wake, wherein periodical vortical structures are recognizable. Boundary layers separate and produce unstable shear layers that tend to roll up and generate alternate eddies that are then convected downstream.

At the end of the nineteenth century an experimental study of Strouhal (Strouhal, 1878) showed that there is a linear relation between the frequency of shedding of vortical structures (f_s) and the undisturbed flow velocity (U), which allows the definition of a nondimensional quantity known as Strouhal number:

$$St = \frac{f_s D}{U} \tag{2.13}$$

where D is a characteristic body dimension (usually the cross-section thickness). The Strouhal number is known to be dependent on the body geometry and Reynolds number.

An analytical study concerning the stability of the vortex patterns in the wake of a stationary cylindrical body was carried out in 1911 by von Kármán and Rubach (von Kármán and Rubach, 1912). Assuming irrotational flow except in concentrated vortices and adopting the two-dimensional potential flow theory, they were able to show that the vortex trail is stable only if the eddies are organized in alternate double row pattern (Kármán's vortex street). They also calculated the steady drag induced by this vortex trail. More recent studies tried to find an expression for the fluctuating lift based on the ideal Kármán's vortex street [e.g. Chen (1972); Sallet (1973)].

Flow separation that generates vortex shedding can be geometrically induced, when the separation point is fixed by the presence of sharp edges, or flow induced, when the boundary layer physical properties determine where separation occurs. Common examples for the first case are the square cylinder [e.g. Lyn *et al.* (1995); Schewe (1984, 1990)] and the H-shaped cross-section cylinder, similar to Tacoma Narrows Bridge deck (Schewe, 1984, 1989), whereas for the second case the most studied example is the circular cylinder [e.g. Roshko (1954, 1961); van Nunen (1974); Schewe (1983, 1986); Lourenco and Shih (1993); Ong and Wallace (1996); Zdravkovich (1997); Kravchenko and Moin (2000)]. When separation is induced by geometry the unsteady wake is less sensitive to flow parameters such as Reynolds number, even though some significant effects have been sometimes observed (Okajima, 1982; Schewe, 1984, 2006). Conversely for smooth bodies the shedding process is extremely sensitive to Mach and Reynolds numbers. In the case of the circular cylinder several wake regimes were identified according to Reynolds number [e.g. Roshko (1954) or Pastò (2005) for an extensive critical review] and an abrupt wake transition can be observed around $Re \cong 3 \div 4 \cdot 10^5$, called critical region (Roshko, 1961; Wooton and Scruton, 1970; Schewe, 1983).

Apart from global Reynolds number (and Mach number for compressible flows) other flow parameters can have a strong influence on the vortex formation process. For instance very important is the role played by local Reynolds numbers associable to the degree of sharpness of the corners and to the surface roughness of the body [e.g. Simiu and Scanlan (1996)]. Also the oncoming turbulence can strongly affect the shedding mechanism, usually reducing its overall intensity [e.g. Simiu and Scanlan (1996)].

Moreover the vortex-shedding process is characterized by pronounced three-dimensional features, also for two dimensional body. As a matter of fact the unstable shear layers roll up with a limited coherence and then the forming eddies stretch in the spanwise direction. A comprehensive discussion of the physics standing behind this phenomenon is reported in Buresti (1998) and the three-dimensional structure of the eddies are clearly shown by the experiments performed by Schewe on the airfoil of a Growian wind-power plant (Schewe, 2001).

It is also worth noting that the vortex shedding mechanism is particularly complicate for quasi-streamlined body, such as modern bridge deck cross sections, whose aerodynamics is characterized by separation, reattachment and merging of small eddies structures, so that often several Strouhal numbers corresponding to different shedding processes are detectable [e.g. Bruno and Khris (2003)].

The previous discussion and particularly the Strouhal law [Eq. (2.13)] are valid for stationary two-dimensional bodies but peculiar aeroelastic phenomena appear when the cylinder is let free to vibrate. It is well known that the alternate shedding of eddies produces nearly periodic drag, lift and moment. Consequently, when the the shedding frequency is close to the structural eigenfrequencies, resonance effects are expected. Nevertheless this kind of resonance usually cannot be treated through the classical theory of structural dynamics due to several nonlinear phenomena. As a matter of fact, when the shedding frequency approaches a natural frequency, the Strouhal law is violated since the shedding frequency remains constant and equal to the frequency of vibration for a relatively large range of flow speeds (Fig. 2.2), giving rise to large amplitude harmonic vibrations usually in the across-wind direction or in torsion. This is the reason why this aeroelastic phenomenon is called "lock-in". In addition, the frequency of oscillation does not always precisely coincide with the natural frequency of the structure, due to the effect of the airflow added mass, and the drag is different from its steady-state value [e.g. Pastò (2005)].

In addition, hysteretic behavior is detectable crossing the lock-in regime, since the amplitude and the shape of the resonance curve are significantly different moving from lower or higher wind speeds [e.g. Schewe (1989); Pastò (2005)], as shown in Fig. 2.3.

Another nonlinear phenomenon is the fact that minor but still significant resonances and synchronizations take place when the shedding frequency is a subharmonic or a super-harmonic of the eigenfrequencies (Schewe, 1989), as it can be observed in Fig. 2.4.

It is also well known that for elastic structures the coherence of the vortex-shedding process strongly increases with the vibration amplitude [e.g. Wooton and Scruton (1970); Novak and Tanaka (1972); de Grenet and Ricciardelli (2005)], as Fig. 2.5 shows for a circular cylinder. The comparison between Fig. 2.5(a) and 2.5(b) highlights the effect of the oncoming turbulence intensity which strongly reduces the fluctuating forces due to vortex shedding.

It is very important to point out that lock-in instability is self-limited, so that limit-cycle

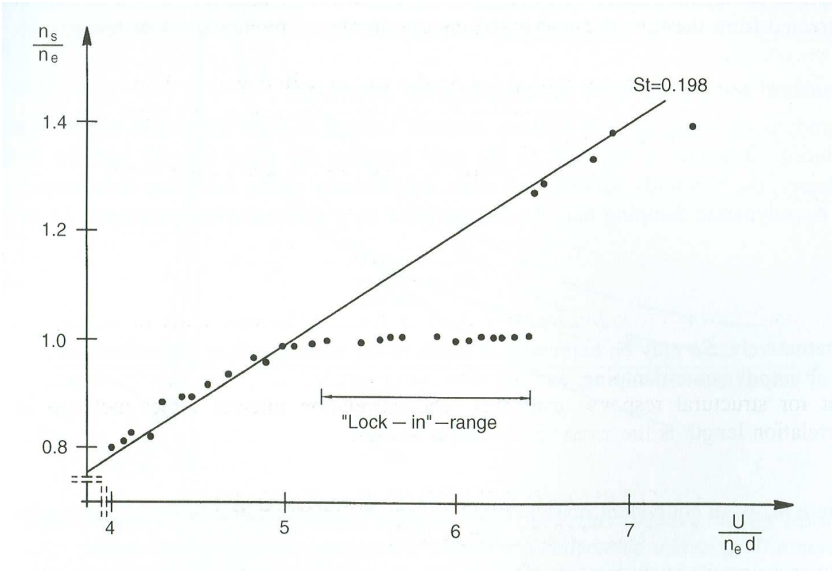

Figure 2.2: Experimental investigation of lock-in after Feng (1968). [From Dyrbye and Hansen (1997)]

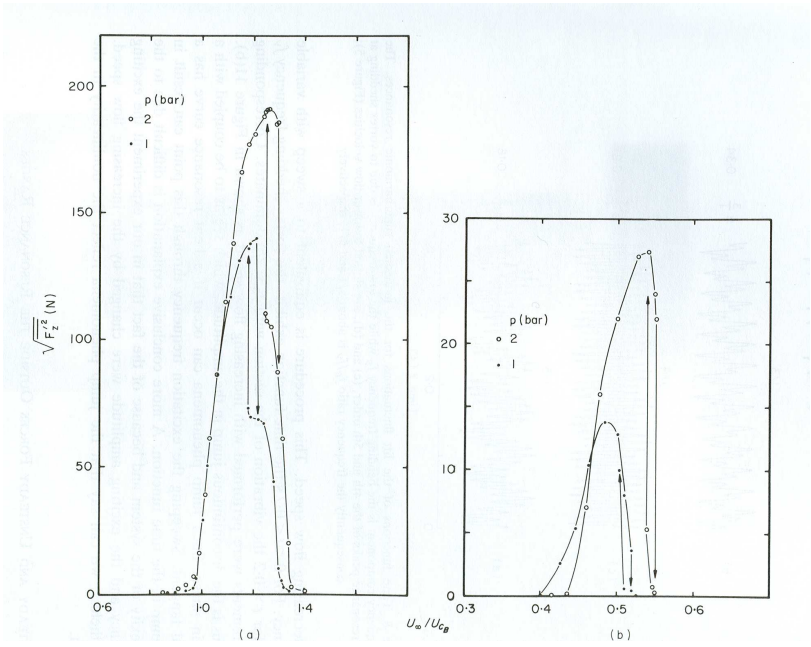

Figure 2.3: (a) Main resonance in bending for an H-shaped cylinder taken at two different wind-tunnel pressures, for increasing and decreasing wind speed. (b) Same as (a) but for the super-harmonic resonance of the second order [from Schewe (1989)]

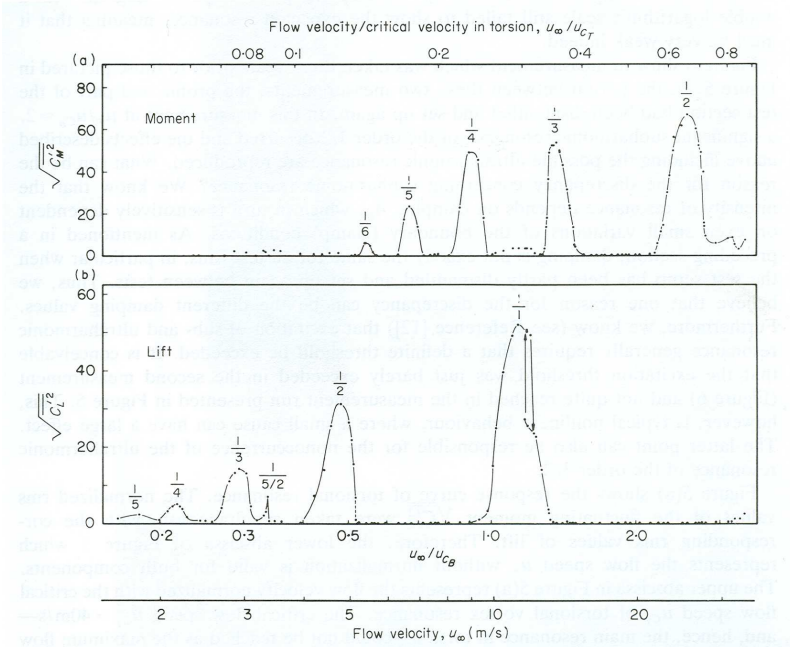

Figure 2.4: Response diagram for moment (a) and lift (b) in the case of an H-shaped cylinder. The quotients denote the order of the resonance [from Schewe (1989)]

oscillations are always reached and the phenomenon quickly disappears as soon as the lock-in range is overcome. The limit-cycle amplitude in bending or torsional modes is strongly dependent on a nondimensional parameter called Scruton number, defined as follows:

$$S_{cr}^{h} = \frac{\zeta_h m}{\rho D^2} \tag{2.14}$$

$$S_{cr}^{\alpha} = \frac{\zeta_\alpha I}{\rho D^4} \tag{2.15}$$

where ζ_h is the bending damping ratio, ζ_α is the torsional damping ratio, m and I are the mass and mass moment of inertia per unit length, D is the cross-wind dimension of the body and ρ the air density. That means that the lock-in vibration amplitude can be very large in light structures with low damping level. An example of the strong dependence of motion amplitude on Scruton number is reported in Fig. 2.6.

Several semi-empirical linear and nonlinear model to calculate lock-in motion amplitude for linelike structures and bridges have been proposed and examples can be found in Scanlan (1998), Simiu and Scanlan (1996), Dyrbye and Hansen (1997), Noè *et al.* (2004) and Pastò (2005).

In particular, concerning bridge decks it was observed that the presence of some secondary structures and non-structural details (fairings, barriers, longitudinal plates, etc.) as well as the level of oncoming turbulence can dramatically influence the strength of the resonance phenomenon both in bending and torsion [e.g. Flamand and Grillaud (1993, 1996); Grillaud

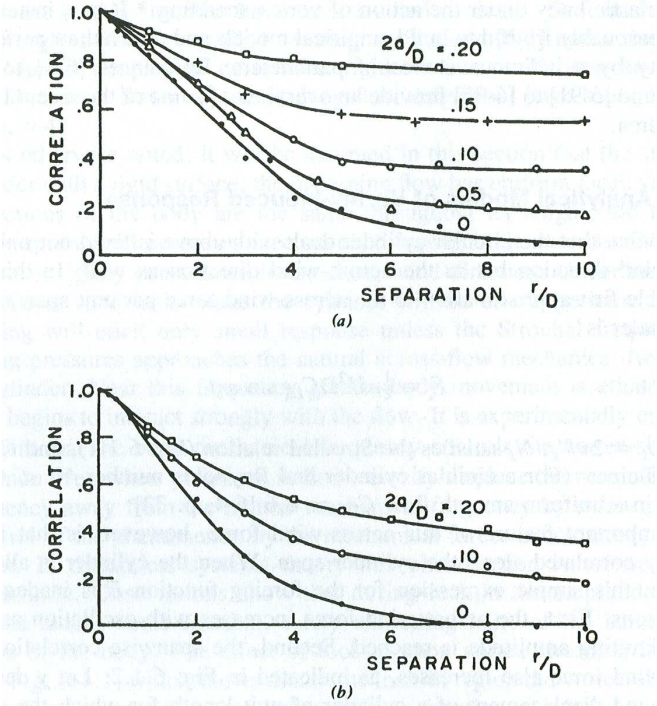

Figure 2.5: The effect of increasing the oscillation amplitude $a/2$ of a circular cylinder of diameter D ($Re = 2.0{\cdot}10^4$) on the correlation between pressures at points separated by distance r along the cylinder axis; (a) smooth flow; (b) flow with turbulence intensity 11 %. Experimental data by Novak and Tanaka (1972). [From Simiu and Scanlan (1996)]

and Flamand (1998)]. In particular, turbulence often reduces the lock-in intensity and in some instances, especially when a mild synchronization is observed in smooth flow, is even able to suppress it.

Vortex-shedding lock-in is very concerning for the fatigue limit state of bridges and especially line-like structures (Pastò, 2005), since this phenomenon often arises for moderate and therefore frequent wind speeds. In addition, in case of bridges, the serviceability limit state is also affected, as the lock-in vibrations can require the interruption of the traffic on the structure.

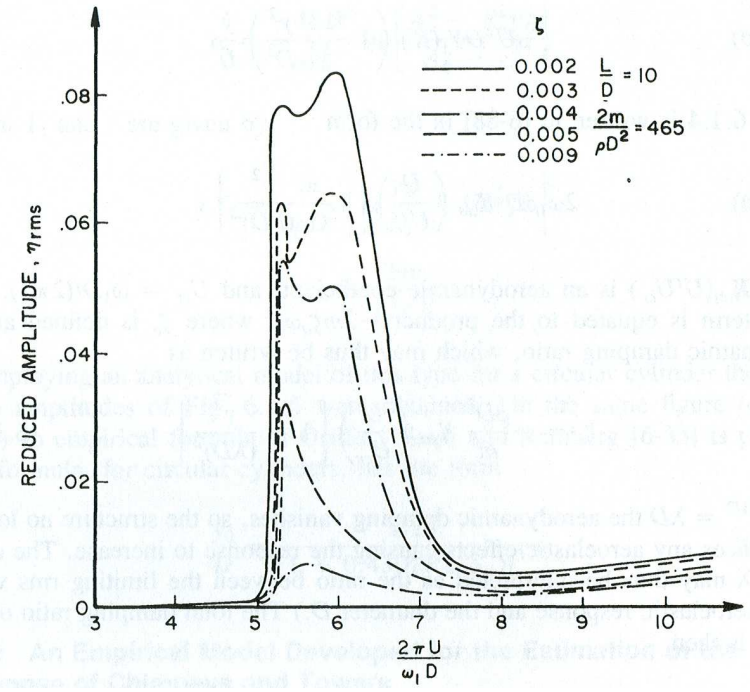

Figure 2.6: The response of a model stack of circular cross section for different values of structural damping (*Re* subcritical). Experimental data by Wooton (1969). [From Simiu and Scanlan (1996)]

2.2.4 Flutter

Flutter is a dynamic instability which can imply divergent oscillations and therefore the collapse of the structure. It has originally been studied for airfoils but after the Tacoma Narrows Bridge collapse in 1940 and more recently with the advent of superlong suspended-span bridges [e.g. Larsen (1993); Larsen and Astiz (1998)], among which the proposal for Messina Crossing is the most outstanding example [e.g. Brancaleoni and Diana (1993); Diana *et al.* (1995); D'Asdia and Sepe (1998); Caracoglia (2000)], careful studies about flutter have become extremely important for civil engineers too.

Generally speaking flutter is a multi-degree-of-freedom instability but in most cases two eigenmodes, a vertical bending and a torsional one, are known to be responsible for its onset (see Chapter 5). The basic idea standing behind this phenomenon is that when a structure vibrates in an airflow there is an energy exchange with the fluid. This exchange is basically driven by the phase shift between heaving and torsional motions and between forces and motion. The energy extracted from or added to an oscillatory motion by the airstream is very sensitive to certain of these phase angles (Bisplinghoff *et al.*, 1996). At low wind speeds usually the structure releases energy to the flow so that the total damping of the structure (structural + aerodynamic) increases. After a certain wind speed this exchange reverses its direction so that the vibrating structure extracts energy from the fluid. When the aerodynamic power

equates the dissipated power a condition of marginal stability (critical condition) is reached and the structural oscillations are characterized by zero total damping. Further increasing the wind speed, heaving and torsional motions tend to diverge (negative total damping). The effect of the aforementioned energy exchange is not only a variation in the total damping but in frequency as well. In particular the torsional frequency tends to decrease more or less monotonously while the bending frequency remains almost constant but little before flutter it sharply increases, jumping to the same value as the torsional one (indeed it is more correct to say that the torsional frequency suddenly appears as dominant frequency in the vertical bending spectrum; see section 3.5.2). At this point the structure vibrates with the same frequency in bending and torsion but it is still stable. A small increase in the wind speed produces the onset of flutter [e.g. Righi (2003)]. Matsumoto and co-workers (Matsumoto, 1996; Matsumoto *et al.*, 1999, 2002; Matsumoto, 2005) have extensively studied this mechanism especially in order to understand which original mode (or "branch") is responsible for the instability. Flutter mechanism is strongly dependent on the unsteadiness of the wake, that is on what is called "fluid memory" and consequently unsteady methods of calculation are generally needed. Flutter boundaries (critical wind speed and coupling frequency) are dependent on the unsteady aerodynamic behavior of the cross-sectional geometry and on some dimensionless structural dynamic parameters such as the relative mass $\gamma_m = \frac{m}{\rho B^2}$, relative mass moment of inertia $\gamma_I = \frac{I}{\rho B^4}$, damping coefficients in bending and torsion and the frequency ratio between bending and torsional modes [see section 2.4.1, Chapter 6 and Dyrbye and Hansen (1997)]. In particular the instability is extremely sensitive to the frequency separation and coupled flutter is not possible when the bending frequency is larger than the torsional one. As it can be observed in Fig. 2.7 for a thin flat plate, the flutter wind speed decreases as the frequency ratio decreases, reaches a minimum around a value of $\gamma_\omega = \omega_\alpha/\omega_h = 1.1$ and then sharply increases again as γ_ω tends to unity. This behavior suggests that the flutter critical wind speed of a very long suspended-span bridge, which is necessarily characterized not only by low frequencies but also by low frequency ratio, cannot be too high. The design of a bridge with torsional frequency lower than the corresponding bending one, apart from practical design problems, could be an appealing innovative solution but it has to be verified that torsional divergence does not arise at a wind speed lower than the design one [e.g. Dyrbye and Hansen (1997)].

The mechanism previously described is that of "classical" or "coupled" flutter which is typical of airfoils and quasi-streamlined bridge decks. Conversely bluffer cross sections are prone to a single-degree-of-freedom torsional instability which is called torsional flutter or torsional galloping, as it has already been mentioned in section 2.2.2. Basically in the neighborhood of the critical condition the flow tends to put energy mainly in a torsional mode. The tendency of a cross-sectional geometry to undergo this kind of single-degree-of-freedom instability is shown by the pattern of the flutter derivative A_2^* (see section 2.4.1), which has the physical meaning of aerodynamic damping in pitch and which tends to reverse its sign little before the instability onset.

The inability of the quasi-steady theory, typical of galloping, to reasonably explain bridge deck torsional flutter has already been mentioned. In Nakamura and Mizota (1975) and Nakamura (1979) it is observed that fluid-memory effect is essential for the onset of torsional

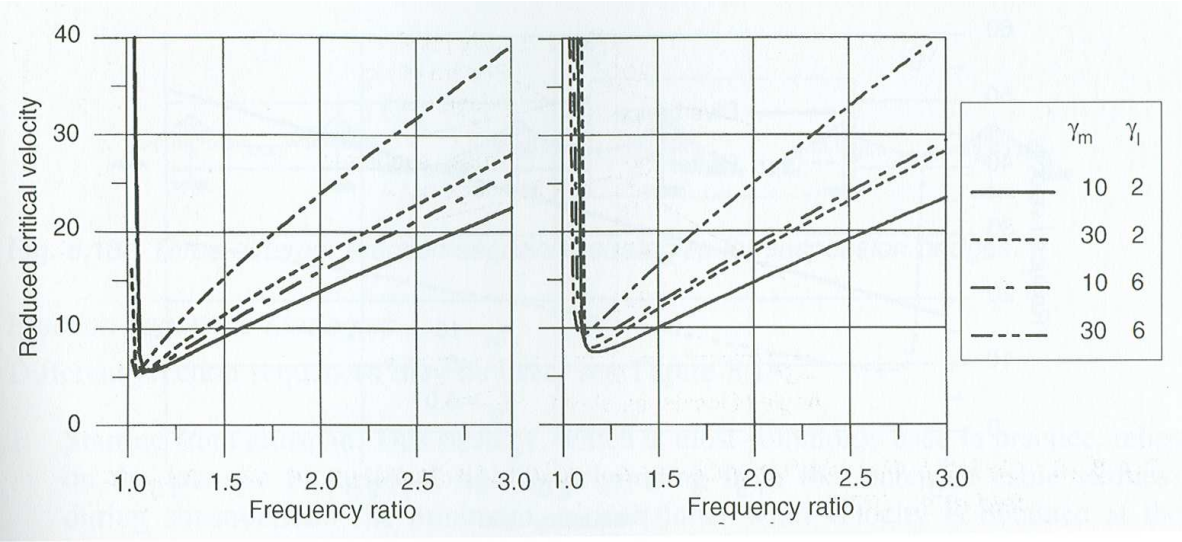

Figure 2.7: Reduced critical flutter wind speed for a theoretical thin flat plate as a function of the frequency ratio γ_ω in still air for four several combinations of the mass ratio γ_m and mass moment of inertia ratio γ_I. The structural damping ratio is assumed to be equal to 0 % on the left and 1 % on the right. [From Dyrbye and Hansen (1997)]

flutter of bluff structures. Sometimes the quasi-steady theory predicts coupled flutter while the unsteady approach correctly shows the possibility of torsional flutter to occur as well. Simple examples for that are the rectangular cylinders with a chord-to-thickness ratio of 8.0 and 10.0 (respectively R8 and R10) which were studied by Matsumoto (1996). These cylinders are found to be prone to torsional flutter, as the negative-to-positive reverse of sign of A_2^* clearly shows. Conversely, the moment coefficient (Matsumoto, 2004), differently from R5 and similarly to R12.5, is characterized by positive slope around zero angle-of-attack, therefore excluding the possibility to detect torsional flutter through the quasi-steady approach.

Beside classical flutter, whose mechanism is mainly driven by the phase shift between bending and torsion, and single-degree-of-freedom torsional flutter, in which the damping in the torsional mode plays a key role, Nakamura during his investigations about bridge deck flutter observed an intermediate type of instability, in which aerodynamic damping and phase shift have comparable effects (Nakamura and Yoshimura, 1976; Nakamura, 1978). He also observed that, in case of bridge decks, coupled flutter usually arises with very small phase shift between heaving and pitching motions, that is with almost fixed center of rotation, normally located upstream with respect to midchord (Nakamura and Yoshimura, 1976; Nakamura, 1978). This fact, probably due to the lack of inertial coupling between heave and pitch, is confirmed by the experimental results presented in Chapter 3.

Generally speaking, more than one or two modes could be involved in the flutter instability mechanism in real bridge structures. The corresponding theory, known as multimodal flutter approach [e.g. Jain *et al.* (1996); D'Asdia and Sepe (1998); Katsuchi *et al.* (1999)], and its

actual relevance will be discussed in Chapter 5.

Flutter is often considered a divergent phenomenon but it is well known that, due to aerodynamic nonlinearities, a limit cycle should be expected if the structure does not collapse before a new equilibrium is reached. It has also been shown that the structural nonlinear behavior of a suspended-span bridge can suppress the flutter tendency to divergent oscillation, although a linear model is assumed for the self-excited load (Salvatori and Spinelli, 2006b). Nevertheless, in bridge engineering the post-critical flutter behavior is not of practical interest since the vibrations induced by this phenomenon can be considered at least "catastrophic" and a significant safety margin with respect to incipient instability has always to be provided. In any case, from the designer's point of view it can be claimed that flutter oscillations concern the ultimate limit state.

2.2.5 Buffeting

Buffeting denotes the loading mechanism due to the oncoming turbulence present in the wind flow in which the structure is immersed. It is basically a problem of random loading but the reason why it is classically described in the framework of aeroelasticity is that the response of the bridge to the wind gusts is strongly influenced by the change of its modal properties as well as the mode coupling due to the airflow.

The simplest way to treat buffeting is the quasi-steady theory [see section 2.4.3; Simiu and Scanlan (1996)]. The assumption which stands behind this approach is that the gust scale is much larger than the characteristic dimension of the deck. Consequently this assumption is not acceptable for small scale turbulence and the quasi-steady approach leads to a significant overestimation of the buffeting load. This model can be corrected with the introduction of the aerodynamic admittance functions [e.g. Davenport (1962); Dyrbye and Hansen (1997); Larose (2005); Peil and Clobes (2005, 2006)], which express how the turbulent wind fluctuations are transformed by the section into aerodynamic loads according to their frequency. With this modification, the buffeting forces can be written as follows:

$$F_x^b(t) = qB\{2C_D(\alpha_0)\chi_x^u(f)\frac{u(t)}{U} + [\frac{dC_D}{d\alpha}(\alpha_0) - C_L(\alpha_0)]\chi_x^w(f)\frac{w(t)}{U}\} \tag{2.16}$$

$$F_z^b(t) = qB\{2C_L(\alpha_0)\chi_z^u(f)\frac{u(t)}{U} + [\frac{dC_L}{d\alpha}(\alpha_0) + C_D(\alpha_0)]\chi_z^w(f)\frac{w(t)}{U}\} \tag{2.17}$$

$$M^b(t) = qB^2\{2C_M(\alpha_0)\chi_M^u(f)\frac{u(t)}{U} + \frac{dC_M}{d\alpha}(\alpha_0)\chi_M^w(f)\frac{w(t)}{U}\} \tag{2.18}$$

where x and z are respectively the horizontal (positive downstream) and the vertical (positive upward) directions; C_D, C_L, C_M are the drag, lift and moment aerodynamic coefficients expressed in the usual reference system reported in section 2.4.3; $u(t)$ and $w(t)$ are respectively the horizontal and the vertical fluctuating component of the wind velocity; $\chi_x^u(f)$, $\chi_x^w(f)$, $\chi_z^u(f)$, $\chi_z^w(f)$, $\chi_M^u(f)$, $\chi_M^w(f)$ are the aerodynamic admittance functions, f is the wind fluctuation frequency and the other symbols have the same meaning previously explained.

The aerodynamic admittances can be measured experimentally in several ways [e.g. Jakobsen (1995)], also using flutter derivatives (Hatanaka and Tanaka, 2002), or they can be approximated with the Sears function (Sears, 1941), which was calculated in closed form for a

thin flat plate (see section 2.3.2). Some authors also explored the possibility to use indicial functions as the time-domain counterpart of the aerodynamic admittance functions in time domain (Scanlan, 1984; Scanlan and Jones, 1999; Borri and Costa, 2004; Costa, 2006).

The aerodynamic admittance functions are expected to tend to unity, like Sears function, as the gust frequency approaches zero and the quasi-steady assumption becomes verified. Nevertheless this is true only for fully correlated gusts which do not exist in the real world. Consequently a coherence function have to be introduced in order to account for the actual correlation of the gusts in the spanwise direction (Simiu and Scanlan, 1996; Dyrbye and Hansen, 1997). Alternatively the aerodynamic admittances can be defined not only as a function of the reduced gust frequency but also of the ratio of the characteristic gust scale to the bridge deck width (Graham, 1970; Larose, 2005).

As previously mentioned, when a buffeting analysis is performed, either in frequency or time domain, it is very important to take into account the contribution of self-excited forces (see section 2.4) due to the deck motion. If the strong (and questionable) assumption of superposition of effects holds and self-excited forces are transferred to the left-hand side of the equations of motion, their contribution can be read as either aerodynamic damping or stiffness and cannot be neglected if realistic estimations of the bridge deck displacements due to buffeting are sought. Even the contribution of cross terms in self-excited forces (see section 2.4.1) should not be forgotten if the reference wind speed is not much smaller than the flutter critical wind speed (Dyrbye and Hansen, 1997).

Buffeting involves both serviceability and ultimate limit states. As a matter of fact, the vibrations due to turbulent wind can prevent the regular traffic on bridges and at the same time the maximum stresses induced by buffeting have to be considered in order to verify that the limit capacity of the structural elements is not exceeded. In some cases buffeting should also be considered for fatigue risk-assessment.

2.2.6 Rain-wind induced vibrations

Rain-wind induced vibration is a very complex fluid-structure interaction phenomenon which appears when rain and wind act simultaneously on cables, hangers and ropes and is particularly concerning for fatigue problems, since it usually arises at low wind speed. It was first consciously observed in 1986 on the cables of Meikonishi Bridge in Japan (Hikami and Shiraishi, 1988). The vibrations can reach large amplitude and usually concern both the in-wind and across-wind degrees of freedom. Important examples of wind-tunnel tests for this phenomenon can be found in Flamand (1994) or in Matsumoto *et al.* (1998).

The actual fluid-dynamic mechanism which leads to rain-wind induced vibration is not completely clear yet. An interesting discussion about the physics of the phenomenon can be found in Matsumoto *et al.* (1992). The restriction of the vibrations to a limited wind speed range suggests resonance phenomena induced by vortex shedding but the large amplitudes, the independence of the eigenfrequencies and the usually wider velocity range invoke a different explanation. Galloping is excluded too for several reasons and especially because the wind-speed range of occurrence is limited, i.e. the phenomenon suddenly stops beyond a certain wind speed. In addition, the very small size of water rivulets with respect to the cable diameter does not seem able to induce galloping. The fact that water flows over the cable according to

the gravity forming a rivulet instead of a film is the basic feature of the phenomenon. Beyond a critical wind speed a second rivulet forms on the cable surface and the existence of both rivulets oscillating around a state of equilibrium is very significant (Seidel and Dinkler, 2006).

Several nonlinear mechanical models for rain-wind induced vibrations of cables are available in the literature. The first model was proposed by Yamaguchi (1990) on the base of a sort of 2-DoF galloping (across-wind translation of the cable and tangential motion of the rivulet). Peil and co-workers developed first a 3-DoF model considering in-wind and across-wind translation of the cable and tangential position of one rivulet (Peil *et al.*, 2002, 2003; Peil and Nahrath, 2003) and then introduced a fourth degree of freedom considering the position of a second rivulet and extended the investigation to 3D-cables (Peil *et al.*, 2003). Seidel and Dinkler's formulation is based on Prandtl's tripwire phenomena and considers two rivulets as movable disturbances (Seidel and Dinkler, 2006). In-wind and across-wind motions of the cable as well as the polar rotations of the rivulets are the considered degrees of freedom. In all the aforementioned approaches the aerodynamic forces are modelled by means of the quasi-steady theory.

2.3 Theoretical approach for a thin flat plate

The main subject of this dissertation is vulnerability analysis of bridges with respect to flutter. That is the reason why the flutter phenomenon is more deeply described in the second part of this chapter. Bridge deck flutter analysis has been based since the first pioneering papers of Selberg (1961), Frandsen (1966) and Scanlan and Tomko (1971) on the analogy with the aeroelastic behavior of airfoils, for which a great deal of theoretical and experimental results are available in the aeronautical engineering literature.

In order to develop an analytical theory, airfoils can be idealized as two-dimensional flat plates with infinitesimal thickness and zero angle-of-attack. Only two degrees of freedom, heave and pitch, are considered. The flat plate is supposed to undergo *very small amplitude oscillations* (small disturbance theory), so that the equations of motion can be linearized and the principle of superposition of effects holds. For airfoils with finite small thickness, small camber and small angle of attack, the actual solution is given by the superposition of the unsteady solution for the oscillating thin flat plate and a steady-state solution for the airfoil of the given thickness and camber at the given angle of attack [e.g. Fung (1993)]. Moreover the flow is assumed to be *inviscid* (no boundary layer development and separation can occur), *incompressible* (density is constant) and *isentropic* (entropy is constant). In addition, the phenomenological rule that the flow velocity remains finite and tangent to the flat plate at the sharp trailing edge, called *Kutta-Joukowski condition* [e.g. Theodorsen (1934); Fung (1993)], is assumed. Under the aforementioned conditions the Helmholtz theorem [e.g. Fung (1993)] applies outside the flat plate and the plane of its wake, so that the flow can be considered *irrotational* there and velocity and acceleration potential exist. Conversely in the region occupied by the flat plate and in the wake behind it, circulation is not zero and vorticity may exist. The problem can be analytically solved through non-stationary potential flow theory in several ways, such as conformal transformations and doublets sink-source method (Theodorsen, 1934; Bisplinghoff *et al.*, 1996), or the definition of the acceleration potential (Fung, 1993).

2.3.1 Self-excited forces: Theodorsen and Wagner's functions

Assuming that the flat plate undergoes small harmonic oscillations in heave and pitch with the same circular frequency ω (critical condition at flutter), the solution of the previously described problem was given in the frequency domain for the first time by Theodorsen (1934).

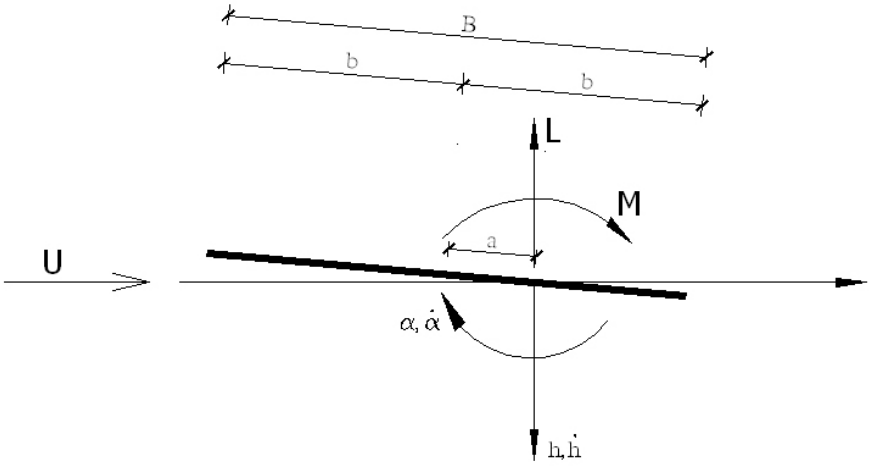

Figure 2.8: Reference system for oscillating flat plate theory

According to the reference system for displacements and forces shown in Fig. 2.8, unsteady self-excited lift and moment can be expressed as follows (Bisplinghoff *et al.*, 1996):

$$L = \pi\rho b^2[\ddot{h} + U\dot{\alpha} - ba\ddot{\alpha}] + 2\pi\rho UbC(k)[\dot{h} + U\alpha + b(\frac{1}{2} - a)\dot{\alpha}] \tag{2.19}$$

$$M = \pi\rho b^2[ba\ddot{h} - Ub(\frac{1}{2} - a)\dot{\alpha} - b^2(\frac{1}{8} + a^2)\ddot{\alpha}] + 2\pi\rho Ub^2(a + \frac{1}{2})C(k)[\dot{h} + U\alpha + b(\frac{1}{2} - a)\dot{\alpha}] \tag{2.20}$$

$C(k)$ is Theodorsen's circulatory function, which can be regarded as a measure of the unsteadiness of the forces, that is of the fluid memory: when $C(k) = 1$ there is no fluid memory and the self-excited load is quasi-steady (see section 2.4.3). This complex function of the reduced frequency of oscillation $k = \omega b/U$ only, where b is half-chord length, can be expressed analytically through Henkel functions $H_n^{(2)}(k)$ or Bessel functions of first and second kind $J_n(k)$, $Y_n(k)$:

$$C(k) = F(k) + iG(k) = \frac{H_1^{(2)}(k)}{H_1^{(2)}(k) + iH_0^{(2)}(k)} \tag{2.21}$$

where

$$H_n^{(2)}(k) = J_n(k) - iY_n(k)$$

The pattern of the real and imaginary part of Theodorsen's circulatory function $C(k)$ is shown in Fig. 2.9.

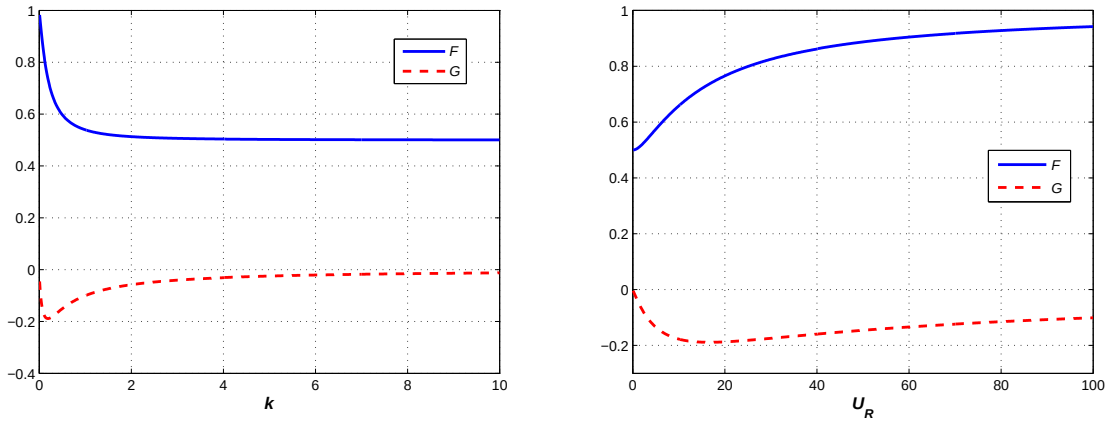

(a) (b)

Figure 2.9: Real and imaginary parts of Theodorsen's circulatory function $C(k) = F(k) + iG(k)$, plotted as a function of the reduced frequency of oscillation k (a) and of the reduced wind speed $U_R = \frac{U}{Bf} = \frac{\pi}{k}$, being $\omega = 2\pi f$ (b)

Unsteady lift and moment in that form are considered as applied to the flat plate elastic axis, whose horizontal distance from mid-chord is indicated with a [for a discussion about the rigorous definition of elastic axis and shear center see for instance Fung (1993)]. Obviously no unsteady drag is expected. The terms in $\ddot{h}$ and $\ddot{\alpha}$ in Eqs. (2.19)-(2.20) have noncirculatory origin, that means they are not due to the vortex sheets on the flat plate and in the wake, but they are apparent mass forces. The lift term $\pi\rho b^2(\ddot{h} - ba\ddot{\alpha})$ has its center of pressure at mid-chord and correspond to the apparent mass $\rho\pi b^2$ of an air cylinder with the diameter equal to the flat plate chord. Conversely the pure nose-down couple $-\frac{1}{8}\rho\pi b^4\ddot{\alpha}$ corresponds to one fourth of the mass moment of inertia of the same air cylinder. If the relative density is very large, as usually is, these aerodynamic inertial terms can be neglected without significant errors (Bisplinghoff *et al.*, 1996). The quasi-steady lift term $\rho\pi b^2 U\dot{\alpha}$ has circulatory nature and corresponds to a centrifugal force with the same magnitude as the apparent mass $\rho\pi b^2$ times $U\dot{\alpha}$, with center of pressure at 3/4-chord point. Neglecting this term may occasionally lead to a marked underestimation of stability (Bisplinghoff *et al.*, 1996). All the other lift terms have circulatory origin and the forward quarter-chord point as center of pressure.

Bridge sections usually are symmetric with respect to the vertical plane so that $a = 0$ (the elastic axis intersects the cross section at mid-chord) and Eqs. (2.19)-(2.20) can be simplified as follows:

$$L = \pi\rho b^2[\ddot{h} + U\dot{\alpha}] + 2\pi\rho UbC(k)[\dot{h} + U\alpha + \frac{b}{2}\dot{\alpha}] \tag{2.22}$$

$$M = -\frac{1}{2}\pi\rho b^3[U\dot{\alpha} + \frac{b}{4}\ddot{\alpha}] + \pi\rho Ub^2C(k)[\dot{h} + U\alpha + \frac{b}{2}\dot{\alpha}] \tag{2.23}$$

In the time domain the equivalent problem had been solved some years before by Wagner (1925). Consider the flat plate with an infinitesimal angle of attack α starting impulsively to move at time $t = 0$ from rest to a uniform velocity U. Taking into account the growth of circulation about the flat plate after the impulsive motion, one obtains (Fung, 1993):

$$L_1(\tau) = 2\pi b \rho U v \Phi(\tau) \tag{2.24}$$

where

$$\tau = \frac{Ut}{b} \tag{2.25}$$

is the nondimensional time (distance travelled in semichords) and $v = U \sin\alpha \cong U\alpha$ is the so called downwash, that is the vertical velocity component of the fluid on the flat plate, considering that the flow must be tangent to the airfoil. The function $\Phi(\tau)$, called Wagner's function, is displayed in Fig. 2.10 and analytically defined in Eq. (2.26):

$$\Phi(\tau) = 1 - \int_0^\infty \{[K_0(x) - K_1(x)]^2 + \pi^2[I_0(x) + I_1(x)]^2)\}^{-1} e^{-x\tau} x^{-2} dx \qquad \text{if } \tau \geq 0 \tag{2.26}$$

$$\Phi(\tau) = 0 \qquad \text{if } \tau < 0 \tag{2.27}$$

where K_0, K_1; I_0, I_1 are modified Bessel functions of the second and first kind, respectively.

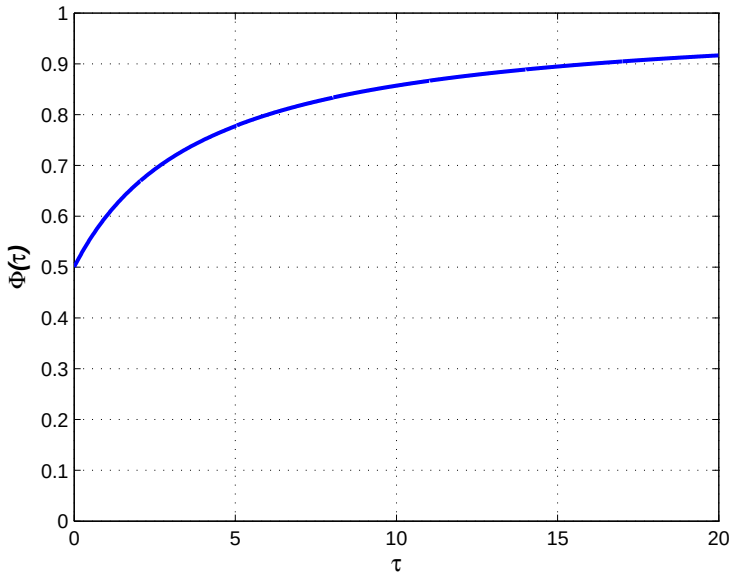

Figure 2.10: Wagner's function after Garrick's rational approximation [e.g. Fung (1993)]

Wagner's function expresses the growth of circulation about the flat plate for a sudden increase of the downwash which is uniform over the plate. For a general motion with two degrees of freedom h and α, the downwash over the airfoil is not uniform but the theory of oscillating airfoils shows that for heaving and pitching oscillations the downwash velocity is

determined by the 3/4-chord point from the leading edge of the flat plate, which can be defined as follows:

$$v(\tau) = U\alpha(\tau) + \frac{U}{b}h'(\tau) + (\frac{1}{2} - a)U\alpha'(\tau) \tag{2.28}$$

where $(\,)'$ denotes differentiation with respect to the nondimensional time τ, while $\dot{(\,)}$ with respect to the physical time t. It results $\dot{(\,)} = \frac{U}{b}(\,)'$.

The lift for a general motion (of small amplitude) is given by Fung (1993):

$$L_1(\tau) = 2\pi b\rho U \int_{-\infty}^{\tau} \Phi(\tau - \sigma)\frac{dv}{d\sigma}(\sigma)d\sigma \tag{2.29}$$

In addition, if the motion is considered to start at time $\tau = 0$, that is $v = 0$ for $\tau < 0$, Eq. (2.29) becomes:

$$L_1(\tau) = 2\pi b\rho U[v_0\Phi(\tau) + \int_0^{\tau} \Phi(\tau - \sigma)\frac{dv}{d\sigma}(\sigma)d\sigma] \tag{2.30}$$

where v_0 is the limiting value of $v(\tau)$ when $\tau \to 0$ from the positive side.

$L_1(\tau)$ has the flat plate forward quarter-chord point as center of pressure. It is worth noting that in order to obtain a general expression for lift and moment of an oscillating flat plate, the apparent inertial terms (noncirculatory) and the centrifugal term (circulatory) previously discussed have to be added.

It is also interesting to note that, as it may have been expected, Wagner's function is a close relative of the inverse Fourier transform of Theodorsen's function (Bisplinghoff *et al.*, 1996):

$$\Phi(\tau) = \frac{1}{2\pi}\int_{-\infty}^{+\infty} \frac{C(k)}{ik}e^{ik\tau}dk \tag{2.31}$$

2.3.2 Gust loading: Sears and Küssner's functions

Let us consider a sinusoidal vertical gust of small amplitude W, positive upward, travelling with circular frequency ω and investing a stationary flat plate, normally immersed in a uniform flow of velocity U. We are interested in the lift and moment generated on the plate by the gust. This problem presents a strong analogy with Theodorsen's one for an oscillating airfoil.

If the equation of the vertical velocity distribution of the gust can be written as follows:

$$w(x,t) = We^{i\omega(t-\frac{x}{U})} \tag{2.32}$$

The resulting lift, acting at the forward quarter-chord point, is given by [e.g. Fung (1993)]:

$$L = 2\pi\rho bUW\chi(k)e^{i\omega t} \tag{2.33}$$

where $\chi(k)$, known as Sears' function (Sears, 1941), is plotted in Fig. 2.11. Eq. (2.34) shows Sears' function analytical expression and its clear relationship with Theodorsen's circulatory function:

$$\chi(k) = [J_0(k) - iJ_1(k)]C(k) + iJ_1(k) \tag{2.34}$$

where $J_n(k)$ are Bessel functions of the first kind.

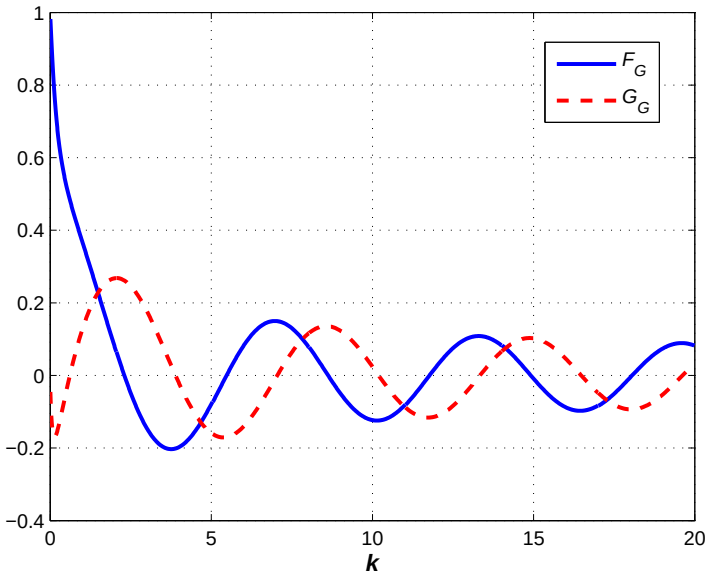

Figure 2.11: Real and imaginary part of Sears' function $\chi(k) = F_G(k) + iG_G(k)$

The same problem can be approached in the time domain considering the flat plate entering in a sharp-edged gust [e.g. Bisplinghoff *et al.* (1996)]. In this case the lift development can be expressed in the following way:

$$L(\tau) = 2\pi\rho bUW\psi(\tau) \tag{2.35}$$

$\psi(\tau)$ is the Küssner's function (Küssner, 1936), which is plotted in Fig. 2.12 along with Wagner's function (2.26) for comparison and whose analytical expression is given in Eq. (2.36).

$$\psi(\tau) = \frac{1}{2\pi}\int_{-\infty}^{+\infty} \frac{\chi(k)}{ik} e^{ik(\tau-1)} dk \tag{2.36}$$

That means that between Küssner's function $\psi(\tau)$ and $\chi(k)e^{-ik}$ there is the same relationship of inverse transformation previously remarked between Wagner's function $\Phi(\tau)$ and Theodorsen's function $C(k)$.

Finally, if an arbitrary $w_G(\tau)$ is defined, for $\tau \geq 0$, as the gust vertical velocity encountered by the flat plate leading edge at the instant $t = \frac{\tau b}{U}$, the resulting lift can be expressed through a Duhamel's integral (Bisplinghoff *et al.*, 1996):

$$L(\tau) = 2\pi b\rho U[w_G(0)\psi(\tau) + \int_0^\tau \psi(\tau-\sigma)\frac{dw}{d\sigma}(\sigma)d\sigma] \tag{2.37}$$

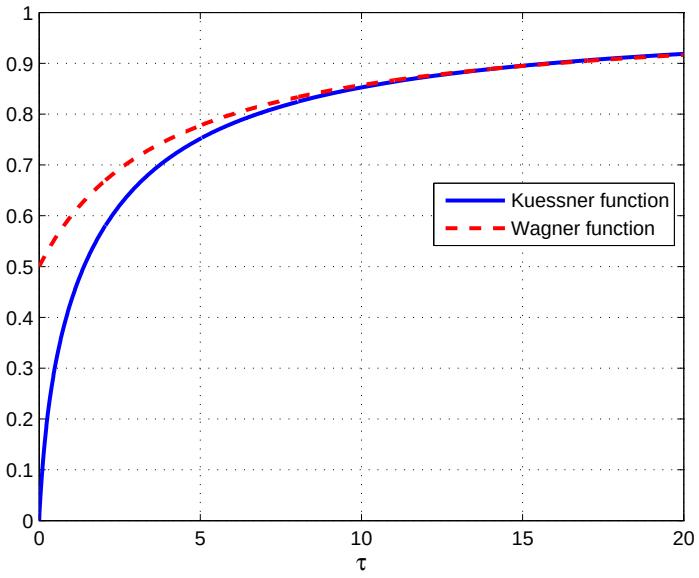

Figure 2.12: Küssner's function in the rational approximation [e.g. Bisplinghoff *et al.* (1996)] and comparison with Wagner's function

2.4 Bridge flutter models

2.4.1 Frequency-domain approach

The airflow around an oscillating bridge deck is much more complicate than around a simple flat plate and an analytical theory giving a closed solution is not possible. In particular the flow is characterized by complex features such as massive separations, reattachments, bubbles, shear layer instability, shedding of eddies and possible merging of some of them. In this case the viscous effects play a prominent role and the assumption of inviscid flow must be removed in order to understand certain phenomena. Nevertheless the analogy with the flat plate has always been kept as a reference, correcting the theoretical result with an experimental parameter called Aerodynamic Stability Performance Index (Selberg, 1961; Frandsen, 1966; Gimsing, 1997; Dyrbye and Hansen, 1997; Righi, 2003; Bartoli and Righi, 2004a,b, 2006) or substituting the Theodorsen's circulatory function with a few experimental functions depending on the bridge deck geometry and on the reduced frequency of oscillation (Scanlan and Tomko, 1971).

If we follow the second approach and consider the reference system of Fig. 2.13, self-excited forces con be expressed in the following way (Simiu and Scanlan, 1996):

$$L(t,K) = qB[KH_1^*(K)\frac{\dot{h}(t)}{U} + KH_2^*(K)\frac{B\dot{\alpha}(t)}{U} + K^2H_3^*(K)\alpha(t) + K^2H_4^*(K)\frac{h(t)}{B}] \quad (2.38)$$

$$M(t,K) = qB^2[KA_1^*(K)\frac{\dot{h}(t)}{U} + KA_2^*(K)\frac{B\dot{\alpha}(t)}{U} + K^2A_3^*(K)\alpha(t) + K^2A_4^*(K)\frac{h(t)}{B}] \quad (2.39)$$

where $q = \frac{1}{2}\rho U^2$ is the kinematic pressure, $B = 2b$ is the bridge chord, $K = 2k = B\omega/U =$

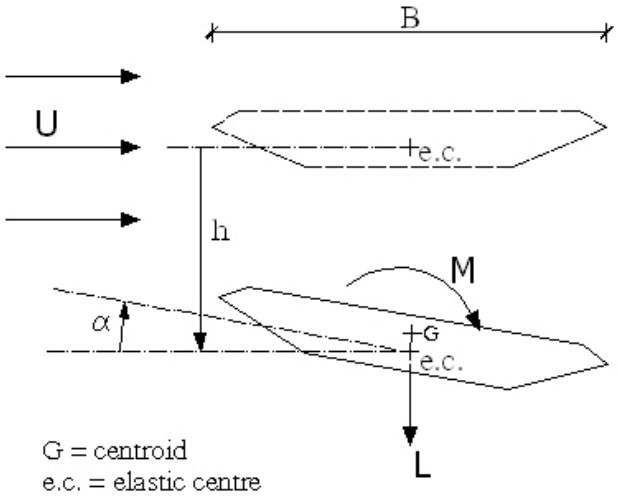

Figure 2.13: Scanlan's reference system for bridge self-excited forces

$= 2\pi/U_R$ is the reduced frequency of oscillation defined on the base of the chord B and the functions H_i^* and A_i^* are the flutter derivatives, which have to be experimentally measured through wind-tunnel tests for every bridge deck geometry. It is worth noting that Scanlan's formulation, according to Eqs. (2.38)-(2.39), is mixed since terms depending on time and frequency coexist. Nevertheless, the model becomes completely frequency-dependent if harmonic motion in heave and pitch is assumed.

This formulation of the self-excited forces considers two degrees of freedom only, as if the bridge deck was an ideal wind-tunnel section model, being therefore convenient for experimental identification of flutter derivatives. The extension to real bridge decks is possible through the so-called *strip-theory assumption* [e.g. Fung (1993)]. However the actual applicability to bridge structures of this 2-DoF model will be discussed in Chapter 5.

Comparing Eqs. (2.38)-(2.39) and Eqs. (2.22)-(2.23) for the thin flat plate, it can be observed that the self-excited forces are still linear functions of the displacements and their first derivatives but now eight functions of the reduced frequency of oscillation instead of two [the real and imaginary part of Theodorsen function $C(k) = F(k) + iG(k)$] are needed. The following theoretical relationship between $C(k)$ and flutter derivatives can be established:

$$H_1^*(K) = -\pi \frac{F(k)}{k} \tag{2.40}$$

$$H_2^*(K) = -\frac{\pi}{4k}[1 + F(k) + \frac{2G(k)}{k}] \tag{2.41}$$

$$H_3^*(K) = -\frac{\pi}{2k^2}[F(k) - \frac{kG(k)}{2}] \tag{2.42}$$

$$H_4^*(K) = \frac{\pi}{2}[1 + \frac{2G(k)}{k}] \tag{2.43}$$

$$(2.44)$$

$$A_1^*(K) = \pi \frac{F(k)}{4k} \tag{2.45}$$

$$A_2^*(K) = -\frac{\pi}{16k}[1 - F(k) - \frac{2G(k)}{k}] \tag{2.46}$$

$$A_3^*(K) = \frac{\pi}{8k^2}[\frac{k^2}{8} + F(k) - \frac{kG(k)}{2}] \tag{2.47}$$

$$A_4^*(K) = -\pi \frac{G(k)}{4k} \tag{2.48}$$

The terms not containing $F(k)$ and $G(k)$ in the previous equations are those with noncirculatory origin (apparent inertial forces) or with circulatory centrifugal nature (see section 2.3.1). The pattern of the flutter derivatives for the theoretical flat plate are shown in Fig. 2.14.

The terms H_4^* and A_4^* are usually considered as negligible for bridges and as a matter of fact Scanlan had not introduced them in its first formulation of self-excited forces (Scanlan and Tomko, 1971). A_2^* conversely has the physical meaning of aerodynamic damping in torsion and it is known to play a key role in flutter instability. In particular when it quickly reverses its sign and become positive (that is the aerodynamic damping becomes negative), it means that the cross section is prone to single-degree-of-freedom torsional flutter.

As we have already said, flutter derivatives are not universal functions but they strongly depend on the cross-sectional geometry. They can be identified in wind tunnel on section models via free-vibration tests [e.g. Scanlan and Tomko (1971); Ibrahim and Mikulcik (1977); Sarkar (1992); Sarkar *et al.* (1994); Gu *et al.* (2000); Chowdhury and Sarkar (2003); Contri (2003); Righi (2003)] and forced-vibration tests [e.g. Li (1995); Matsumoto (1996); Diana *et al.* (2004)] but some attempts have also been done adopting ambient vibration tests [e.g. Jakobsen (1995); Brownjohn and Jakobsen (2001); Jakobsen *et al.* (2003); Ricciardelli and de Grenet (2002); Zhang *et al.* (2003); Zhang and Brownjohn (2004); Fathi (2003)]. In some cases these functions have been tentatively identified on taut-strip models and full aeroelastic models as well (Zasso *et al.*, 1996).

Concerning the possible conventions for the flutter derivatives, that proposed in Eqs. (2.38)-(2.39) is for sure the most used but many others can be found in the literature [e.g. Zasso (1996); Jensen and Höffer (1998); Caracoglia (2000)].

The validity of a linear model for bridge deck self-excited forces is one of the most discussed problems in bridge aeroelasticity, especially concerning the dependence of flutter derivatives on the amplitude of motion (see Chapter 3). Nevertheless a sure source of nonlinearity is the strong dependence of these functions on the mean angle of attack [e.g. Flamand (2001); Diana *et al.* (2005a,b) and section 3.5.2 in the present dissertation]. The mean angle of attack can be due to a possible inclination of the flow, to the static deck torsional deformation and to large scale turbulence (Diana *et al.*, 2005a,b; Chen and Kareem, 2000). Conversely, small scale turbulence can influence directly the pattern of flutter derivatives increasing the mixing in the separated shear layers and therefore changing the flow field around the body (Scanlan and Lin, 1978; Nakamura and Ohya, 1984; Lin, 1996; Righi, 2003; Bartoli and Mannini, 2005).

The 2-DoF equations of motion for the flutter problem in the case of a linear structure can

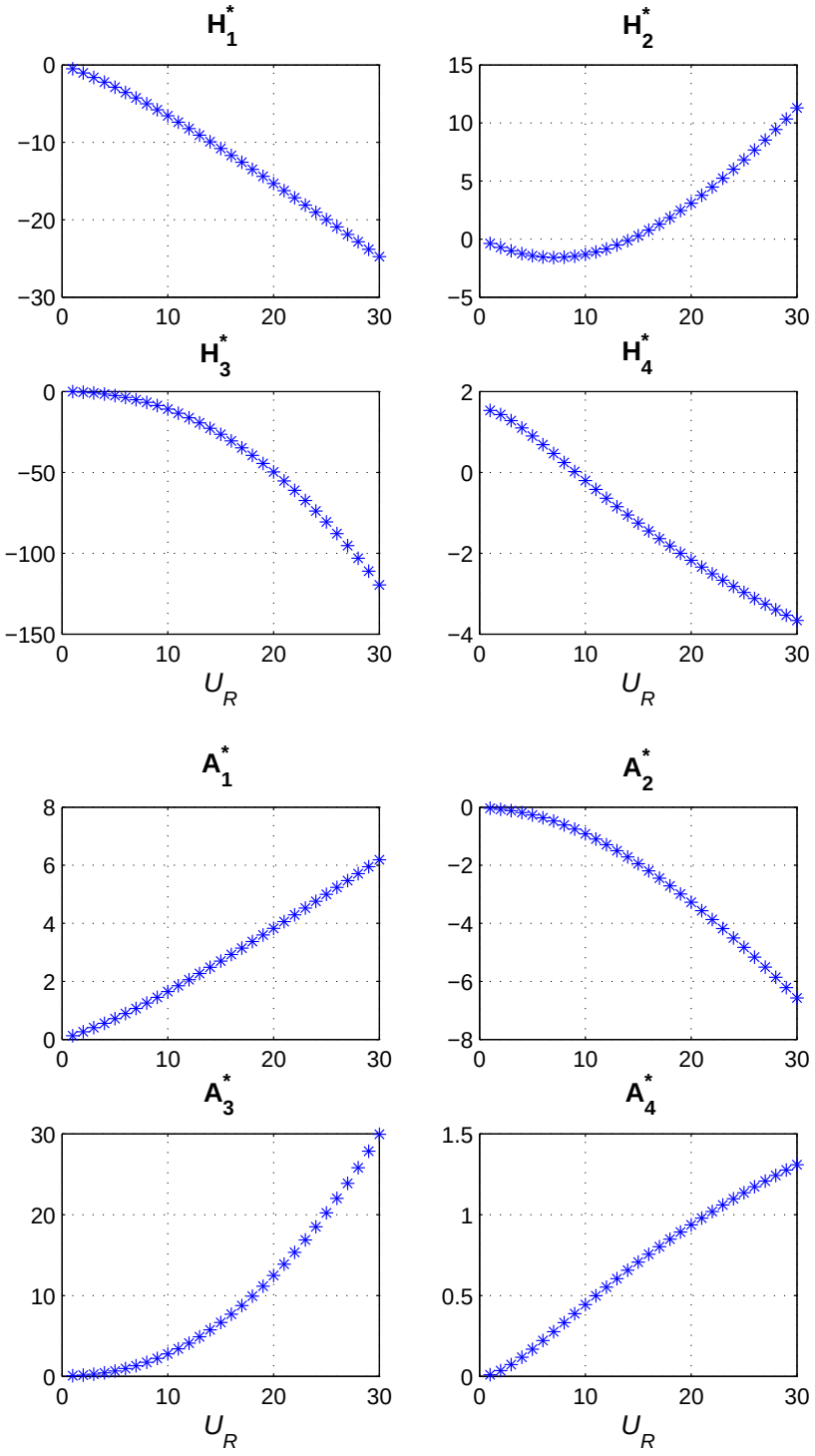

Figure 2.14: Flutter derivatives for a theoretical thin flat plate according to Eqs. (2.40)-(2.48)

be written as follows:

$$m[\ddot{h}(t) + 2\zeta_h\omega_h\dot{h}(t) + \omega_h^2 h(t)] = L(t) \tag{2.49}$$

$$I[\ddot{\alpha}(t) + 2\zeta_\alpha\omega_\alpha\dot{\alpha}(t) + \omega_\alpha^2\alpha(t)] = M(t) \tag{2.50}$$

where $L(t)$ and $M(t)$ are given by Eqs. (2.38)-(2.39), m and I are the mass and mass moment of inertia per unit length, ζ_h and ζ_α are the structural damping ratios and ω_h and ω_α the still-air circular frequencies in heave and pitch.

At the coupled flutter critical condition, heave and pitch can be considered harmonic motions with the same circular frequency ω:

$$h(t) = \bar{h}e^{i\omega t} \qquad \bar{h} \in \mathbb{C} \tag{2.51}$$

$$\alpha(t) = \bar{\alpha}e^{i\omega t} \qquad \bar{\alpha} \in \mathbb{C} \tag{2.52}$$

Substituting Eqs. (2.51) and (2.52) in the equations of motion, one obtains:

$$[2\gamma_m(-1 + \frac{1}{X^2} + i2\zeta_h\frac{1}{X}) - (H_4^* + iH_1^*)]\frac{\bar{h}}{B} - (H_3^* + iH_2^*)\bar{\alpha} = 0 \tag{2.53}$$

$$-(A_4^* + iA_1^*)\frac{\bar{h}}{B} + [2\gamma_I(-1 + \frac{\gamma_\omega^2}{X^2} + i2\zeta_h\frac{\gamma_\omega}{X}) - (A_3^* + iA_2^*)]\bar{\alpha} = 0 \tag{2.54}$$

where:
$\gamma_m = \frac{m}{\rho B^2}$ is the nondimensional mass;
$\gamma_I = \frac{I}{\rho B^4}$ is the nondimensional mass moment of inertia;
$\gamma_\omega = \frac{\omega_\alpha}{\omega_h}$ is the frequency ratio between pitching and heaving motions;
$X = \frac{\omega}{\omega_h}$ is the unknown coupling frequency, adimensionalized with the heaving frequency.

Eqs. (2.53) and (2.54) form a homogeneous linear system in $\bar{h}$ and $\bar{\alpha}$ and in order to obtain a non trivial solution (heaving and pitching motion with non-zero amplitude) the determinant must vanish. Equating to zero the real and imaginary part of the determinant the so called real [Eq. (2.55)] and imaginary [Eq. (2.56)] flutter equations are obtained:

$$R_4X^4 + R_3X^3 + R_2X^2 + R_1X + R_0 = 0 \tag{2.55}$$

$$I_3X^3 + I_2X^2 + I_1X + I_0 = 0 \tag{2.56}$$

where:

$$R_0 = \gamma_\omega^2$$

$$R_1 = 0$$

$$R_2 = -1 - \gamma_\omega^2 - 4\zeta_h\zeta_\alpha\gamma_\omega - \frac{\gamma_\omega^2}{2\gamma_m}H_4^* - \frac{1}{2\gamma_I}A_3^*$$

$$R_3 = \zeta_\alpha\frac{\gamma_\omega}{\gamma_m}H_1^* + \zeta_h\frac{1}{\gamma_I}A_2^*$$

$$R_4 = 1 + \frac{1}{2\gamma_m}H_4^* + \frac{1}{2\gamma_I}A_3^* + \frac{1}{4\gamma_m\gamma_I}(H_4^*A_3^* - H_1^*A_2^* - H_3^*A_4^* + H_2^*A_1^*)$$

$$
\begin{aligned}
I_0 &= 2\zeta_h\gamma_\omega^2 + 2\zeta_\alpha\gamma_\omega \\
I_1 &= -\frac{\gamma_\omega^2}{2\gamma_m}H_1^* - \frac{1}{2\gamma_I}A_2^* \\
I_2 &= -2\zeta_h - 2\zeta_\alpha\gamma_\omega - \zeta_\alpha\frac{\gamma_\omega}{\gamma_m}H_4^* - \zeta_h\frac{1}{\gamma_I}A_3^* \\
I_3 &= \frac{1}{2\gamma_m}H_1^* + \frac{1}{2\gamma_I}A_2^* + \frac{1}{4\gamma_m\gamma_I}(H_4^*A_2^* + H_1^*A_3^* - H_3^*A_1^* - H_2^*A_4^*)
\end{aligned}
$$

The unknowns in Eqs. (2.55)-(2.56) are the coupling flutter frequency, contained in X, and the critical reduced wind speed U_R which is the argument of the flutter derivatives. The two equations can be solved numerically [e.g. Simiu and Scanlan (1996); Dyrbye and Hansen (1997)], plotting the real X solutions of both equations against U_R: the actual flutter boundaries are given by the intersection of these two curves (or the intersection for the lowest physical wind speed, if it is not unique). The flutter coupling frequency has to be larger than the heaving frequency and smaller than the pitching frequency. It is worth noting that the flutter equations allow to calculate the flutter critical wind speed and the coupling frequency and then, introducing this solution in Eqs. (2.51) and (2.52), the ratio between the complex amplitudes of pitching and heaving motions $\bar{\alpha}$ and $\bar{h}$ can be found as well. Nevertheless their actual values are undetermined given the linearity of the model.

2.4.2 Time-domain approach

Self-excited forces can also be expressed in the time domain, following the analogy with the lift formulation for the thin flat plate of Eq. (2.29) or Eq. (2.30). For bridge decks several indicial functions are employed instead of Wagner's function. Again these functions are not universal and they are usually determined from the corresponding flutter derivatives [e.g. Borri and Höffer (2000); Caracoglia and Jones (2003b); Costa (2004); Costa and Borri (2006)], which are easier to be measured through wind-tunnel tests. In few cases tentatively indicial functions have been directly identified by experiments (Caracoglia, 2000; Caracoglia and Jones, 2003a). Several formulations, not very different one from the other, are available in the literature [e.g. Scanlan *et al.* (1974); Borri and Höffer (2000); Caracoglia and Jones (2003b); Costa (2004); Costa and Borri (2006)]; in Eqs. (2.57)-(2.58) that after Costa (2004) is reported:

$$
\begin{aligned}
L(t) = &- qB\frac{dC_L}{d\alpha}(0)[\Phi_{Lh}(0)\frac{\dot{h}(t)}{U} + \Phi_{L\alpha}(0)\alpha(t) + \\
&+ \int_0^t \dot{\Phi}_{Lh}(t-\sigma)\frac{\dot{h}(\sigma)}{U}d\sigma + \int_0^t \dot{\Phi}_{L\alpha}(t-\sigma)\alpha(\sigma)d\sigma]
\end{aligned}
\tag{2.57}
$$

$$
\begin{aligned}
M(t) = &\, qB^2\frac{dC_M}{d\alpha}(0)[\Phi_{Mh}(0)\frac{\dot{h}(t)}{U} + \Phi_{M\alpha}(0)\alpha(t) + \\
&+ \int_0^t \dot{\Phi}_{Mh}(t-\sigma)\frac{\dot{h}(\sigma)}{U}d\sigma + \int_0^t \dot{\Phi}_{M\alpha}(t-\sigma)\alpha(\sigma)d\sigma]
\end{aligned}
\tag{2.58}
$$

where $\Phi_{Ly}(t)$, $\Phi_{L\alpha}(t)$, $\Phi_{My}(t)$, $\Phi_{M\alpha}(t)$ are the indicial functions and $\dot{\Phi}_{Ly}(t)$, $\dot{\Phi}_{L\alpha}(t)$, $\dot{\Phi}_{My}(t)$, $\dot{\Phi}_{M\alpha}(t)$ their time derivatives. In this case the reference system for unsteady forces and motion is the one shown in Fig. 2.13, whereas classically for the static coefficients C_L and C_M the convention of Fig. 2.8 (lift positive upward) is followed.

The main advantage of the time-domain approach is its larger flexibility: for instance it can be adopted for supercritical analyses and above all it is much more convenient than frequency-domain approach to deal with subcritical problems such as the buffeting response of bridge decks. In addition, time-domain self-excited forces can be better implemented in finite-element models [e.g. Salvatori and Spinelli (2006a,b)]. Conversely, when only the flutter boundaries are sought, the frequency-domain approach is much more direct and fast.

2.4.3 Quasi-steady approach

When the reduced frequency of oscillation is small (that is the reduced wind speed is large) the time needed by the fluid particles to travel the bridge width (B/U) is small with respect to the period of oscillation of the structure ($2\pi/\omega$). Consequently the fluid-memory effects tend to become small and the quasi-steady theory can be used instead of the unsteady theory (Bisplinghoff *et al.*, 1996; Miyata *et al.*, 1995; Minh *et al.*, 1999; Diana *et al.*, 1999). In the quasi-steady approach at each time the forces do not depend on what happened before and the structure is seen by the flow as it was stationary with its instantaneous values of displacements and velocities. The quasi-steady approach can be used to determine both self-excited and buffeting forces.

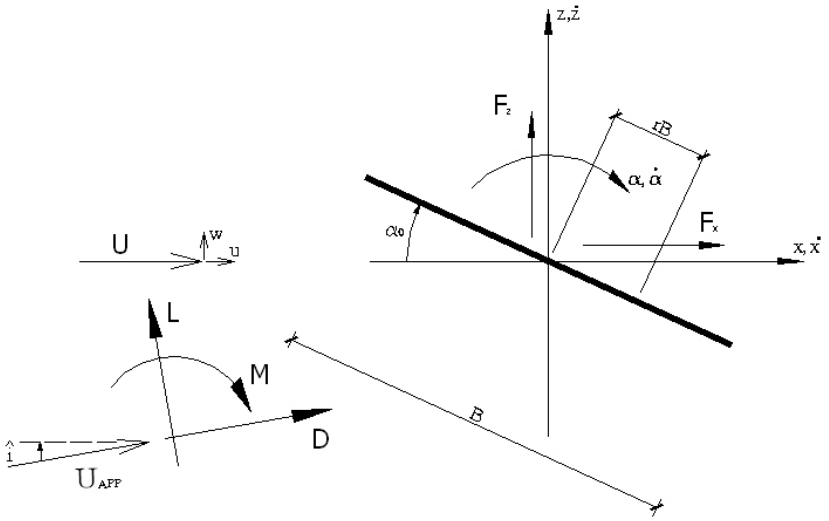

Figure 2.15: Reference system for the quasi-steady theory

Considering the reference system of Fig. 2.15, drag, lift and moment can be expressed as functions of the apparent wind speed U_{APP}, apparent wind incidence $\hat{i}$ and instantaneous

pitching angle α with respect to the mean position α_0:

$$D = \frac{1}{2}\rho U_{APP}^2 B C_D(\alpha_0 + \hat{i} + \alpha) \tag{2.59}$$

$$L = \frac{1}{2}\rho U_{APP}^2 B C_L(\alpha_0 + \hat{i} + \alpha) \tag{2.60}$$

$$M = \frac{1}{2}\rho U_{APP}^2 B^2 C_M(\alpha_0 + \hat{i} + \alpha) \tag{2.61}$$

where

$$U_{APP}^2 = (U + u - \dot{x})^2 + (w - \dot{z} + rB\dot{\alpha})^2 \tag{2.62}$$

$$\hat{i} = \arctan\frac{w - \dot{z} + rB\dot{\alpha}}{U + u - \dot{x}} \tag{2.63}$$

It is immediately worth noting that with respect to sections 2.3.1, 2.4.1 and 2.4.2, the meaning of L is slightly different here. This is the reason why the notation F_z is introduced to denote the force in the direction of the vertical displacement. The angle of attack due to the angular motion of the structure is not constant over the chord but, in analogy with the unsteady airfoil theory, it is assumed here that there is a point at a distance rB from midchord, which is representative for the whole section. Nevertheless, this point can be different for drag ($r = r_D$), lift ($r = r_L$) and moment ($r = r_M$). If the wind speed fluctuations are small with respect to the mean wind speed and the structure undergoes small displacements, Eqs. (2.62)-(2.63) can be linearized:

$$U_{APP}^2 \cong U^2 + 2Uu - 2U\dot{x} = U^2(1 + \frac{2u}{U} - \frac{2\dot{x}}{U}) \tag{2.64}$$

$$\hat{i} \cong \frac{w}{U} - \frac{\dot{z}}{U} + \frac{rB\dot{\alpha}}{U} \tag{2.65}$$

If the aerodynamic coefficients are developed in Taylor's series around the mean angle of attack α_0, retaining the linear terms only and neglecting the products of small quantities as higher-order infinitesimals, drag, lift and moment can be written as follows:

$$\begin{aligned} D \cong & qB(1 + \frac{2u}{U} - \frac{2\dot{x}}{U})[C_D(\alpha_0) + \frac{dC_D}{d\alpha}(\alpha_0)(\hat{i} + \alpha)] \\ \cong & qBC_D(\alpha_0)(1 + \frac{2u}{U} - \frac{2\dot{x}}{U}) + qB\frac{dC_D}{d\alpha}(\alpha_0)(\hat{i} + \alpha) \end{aligned} \tag{2.66}$$

$$\begin{aligned} L \cong & qB(1 + \frac{2u}{U} - \frac{2\dot{x}}{U})[C_L(\alpha_0) + \frac{dC_L}{d\alpha}(\alpha_0)(\hat{i} + \alpha)] \\ \cong & qBC_L(\alpha_0)(1 + \frac{2u}{U} - \frac{2\dot{x}}{U}) + qB\frac{dC_L}{d\alpha}(\alpha_0)(\hat{i} + \alpha) \end{aligned} \tag{2.67}$$

$$\begin{aligned} M \cong & qB^2(1 + \frac{2u}{U} - \frac{2\dot{x}}{U})[C_M(\alpha_0) + \frac{dC_M}{d\alpha}(\alpha_0)(\hat{i} + \alpha)] \\ \cong & qB^2C_M(\alpha_0)(1 + \frac{2u}{U} - \frac{2\dot{x}}{U}) + qB^2\frac{dC_M}{d\alpha}(\alpha_0)(\hat{i} + \alpha) \end{aligned} \tag{2.68}$$

where, as usual, $q = \frac{1}{2}\rho U^2$ is the kinematic pressure. Drag and Lift can be composed in order to obtain horizontal and vertical forces:

$$F_x = D\cos\hat{i} - L\sin\hat{i} \cong D - L\hat{i} \tag{2.69}$$

$$F_z = D\sin\hat{i} + L\cos\hat{i} \cong D\hat{i} + L \tag{2.70}$$

Discarding again the higher-order terms one obtains:

$$F_x \cong qBC_D(\alpha_0)(1 + \frac{2u}{U} - \frac{2\dot{x}}{U}) + qB[\frac{dC_D}{d\alpha}(\alpha_0) - C_L(\alpha_0)]\hat{i} + qB\frac{dC_D}{d\alpha}(\alpha_0)\alpha \tag{2.71}$$

$$F_z \cong qBC_L(\alpha_0)(1 + \frac{2u}{U} - \frac{2\dot{x}}{U}) + qB[\frac{dC_L}{d\alpha}(\alpha_0) + C_D(\alpha_0)]\hat{i} + qB\frac{dC_L}{d\alpha}(\alpha_0)\alpha \tag{2.72}$$

$$M \cong qB^2C_M(\alpha_0)(1 + \frac{2u}{U} - \frac{2\dot{x}}{U}) + qB^2\frac{dC_M}{d\alpha}(\alpha_0)\hat{i} + qB^2\frac{dC_M}{d\alpha}(\alpha_0)\alpha \tag{2.73}$$

It is now possible to split the aerodynamic forces we found in mean, buffeting and self-excited contributions:

$$F_x = \bar{F}_x + F_x^b + F_x^{se} \tag{2.74}$$

$$F_z = \bar{F}_z + F_z^b + F_z^{se} \tag{2.75}$$

$$M = \bar{M} + M^b + M^{se} \tag{2.76}$$

- *Mean aerodynamic forces*

$$\bar{F}_x = qBC_D(\alpha_0) \tag{2.77}$$

$$\bar{F}_z = qBC_L(\alpha_0) \tag{2.78}$$

$$\bar{M} = qB^2C_M(\alpha_0) \tag{2.79}$$

- *Buffeting forces*

$$F_x^b = qB\{2C_D(\alpha_0)\frac{u}{U} + [\frac{dC_D}{d\alpha}(\alpha_0) - C_L(\alpha_0)]\frac{w}{U}\} \tag{2.80}$$

$$F_z^b = qB\{2C_L(\alpha_0)\frac{u}{U} + [\frac{dC_L}{d\alpha}(\alpha_0) + C_D(\alpha_0)]\frac{w}{U}\} \tag{2.81}$$

$$M^b = qB^2\{2C_M(\alpha_0)\frac{u}{U} + \frac{dC_M}{d\alpha}(\alpha_0)\frac{w}{U}\} \tag{2.82}$$

- *Self-excited forces*

$$F_x^{se} = qB\{-2C_D(\alpha_0)\frac{\dot{x}}{U} + [\frac{dC_D}{d\alpha}(\alpha_0) - C_L(\alpha_0)](-\frac{\dot{z}}{U} + \frac{r_xB\dot{\alpha}}{U}) + \frac{dC_D}{d\alpha}(\alpha_0)\alpha\} \tag{2.83}$$

$$F_z^{se} = qB\{-2C_L(\alpha_0)\frac{\dot{x}}{U} + [\frac{dC_L}{d\alpha}(\alpha_0) + C_D(\alpha_0)](-\frac{\dot{z}}{U} + \frac{r_zB\dot{\alpha}}{U}) + \frac{dC_L}{d\alpha}(\alpha_0)\alpha\} \tag{2.84}$$

$$M^{se} = qB^2\{-2C_M(\alpha_0)\frac{\dot{x}}{U} + \frac{dC_M}{d\alpha}(\alpha_0)(-\frac{\dot{z}}{U} + \frac{r_MB\dot{\alpha}}{U} + \alpha)\} \tag{2.85}$$

Coming back now to the Scanlan's convention for forces and displacements (Fig. 2.13), considering drag and sway motion as well (see section 5.1), the following equivalences with the quasi-steady theory can be established when $K \longrightarrow 0$:

$$KP_1^* \longrightarrow -2C_D(\alpha_0) \qquad KH_1^* \longrightarrow -[\frac{dC_L}{d\alpha}(\alpha_0) + C_D(\alpha_0)] \qquad KA_1^* \longrightarrow \frac{dC_M}{d\alpha}(\alpha_0)$$

$$KP_2^* \longrightarrow r_x[\frac{dC_D}{d\alpha}(\alpha_0) - C_L(\alpha_0)] \qquad KH_2^* \longrightarrow -r_z[\frac{dC_L}{d\alpha}(\alpha_0) + C_D(\alpha_0)] \qquad KA_2^* \longrightarrow r_M\frac{dC_M}{d\alpha}(\alpha_0)$$

$$K^2P_3^* \longrightarrow \frac{dC_D}{d\alpha}(\alpha_0) \qquad K^2H_3^* \longrightarrow -\frac{dC_L}{d\alpha}(\alpha_0) \qquad K^2A_3^* \longrightarrow \frac{dC_M}{d\alpha}(\alpha_0)$$

$$K^2P_4^* \longrightarrow 0 \qquad K^2H_4^* \longrightarrow 0 \qquad K^2A_4^* \longrightarrow 0$$

$$KP_5^* \longrightarrow \frac{dC_D}{d\alpha}(\alpha_0) - C_L(\alpha_0) \qquad KH_5^* \longrightarrow 2C_L(\alpha_0) \qquad KA_5^* \longrightarrow -2C_M(\alpha_0)$$

$$K^2P_6^* \longrightarrow 0 \qquad K^2H_6^* \longrightarrow 0 \qquad K^2A_6^* \longrightarrow 0$$

A very important point is the best value to attribute to r_x, r_z and r_M and in particular to r_M since it is strictly connected to the aerodynamic damping in torsion. For a symmetrical thin flat plate the quasi-steady forces can be obtained imposing $C(k) = 1$ in Eqs. (2.22)-(2.23):

$$L = \pi\rho b^2[\ddot{h} + U\dot{\alpha}] + 2\pi\rho Ub[\dot{h} + U\alpha + \frac{b}{2}\dot{\alpha}] \tag{2.86}$$

$$M = -\frac{1}{2}\pi\rho b^3[U\dot{\alpha} + \frac{b}{4}\ddot{\alpha}] + \pi\rho Ub^2[\dot{h} + U\alpha + \frac{b}{2}\dot{\alpha}] \tag{2.87}$$

Apparent inertial contributions (terms in $\ddot{h}$ and $\ddot{\alpha}$) can be neglected. In addition, it is well known that for a zero-degree-angle-of-attack flat plate it results [e.g. Bisplinghoff *et al.* (1996); Dyrbye and Hansen (1997)]:

$$C_D(0) = 0 \qquad \frac{dC_D}{d\alpha}(0) = 0$$

$$C_L(0) = 0 \qquad \frac{dC_L}{d\alpha}(0) = 2\pi$$

$$C_M(0) = 0 \qquad \frac{dC_M}{d\alpha}(0) = \frac{\pi}{2}$$

Consequently it is possible to conclude that:

$$r_x = 0 \tag{2.88}$$

$$r_z = \frac{1}{2} \tag{2.89}$$

$$r_M = 0 \tag{2.90}$$

Unfortunately there is no evidence that this conclusion can be extended to real bridge decks. As a matter of fact the reference point for the angular velocity motion is assumed as coincident with the aerodynamic center both in Miyata *et al.* (1995) and in the textbook of the Association Française de Génie Civil (AFGC, 2002), with the leading edge according to Farquharson (1949)

or with a point placed at a chord distance upstream with respect to the midchord in Diana *et al.* (2004).

It is also important to understand when the quasi-steady theory can actually be used instead of the unsteady theory. To the writer's knowledge no clear studies are available in the literature for real bridge decks. Conversely for airfoils in Bisplinghoff *et al.* (1996) it is said that also for reduced frequency values $k < 0.1$ (that is $U_R > 30$) the fluid-memory effects on the flutter instability can be remarkable. As a matter of fact $C(k)$ is responsible for a phase lag between forces and motions (along with a magnitude reduction of forces), which is extremely important for the flutter mechanism. Fig. 2.16 shows a polar plot of Theodorsen's function and it can be easily noted that the maximum phase-shifting effect occurs around $k = 0.2$ and for $k = 0.1$ this is definitely not negligible. A similar conclusion may be drawn observing in Fig. 2.9(b) how the real and imaginary part of $C(k)$ slowly approach their asymptotic values.

In order to quantify the actual effect of fluid memory, a particular study case is considered. The modal properties of the proposed design of Messina Strait Bridge (D'Asdia and Sepe, 1998) and the flutter derivatives of the theoretical flat plate are combined, while the chord length B is considered as a free parameter in order to increase as much as possible the flutter reduced critical wind speed. In Tab. 2.1 the comparison between unsteady and quasi-steady results [Eqs. (2.86)-(2.87)] is outlined. It is worth noting that also for large reduced wind speed ($U_R \cong 100$) the difference between the results given by the two theories is not negligible. In addition, it is confirmed that the contribution of apparent inertial forces is small.

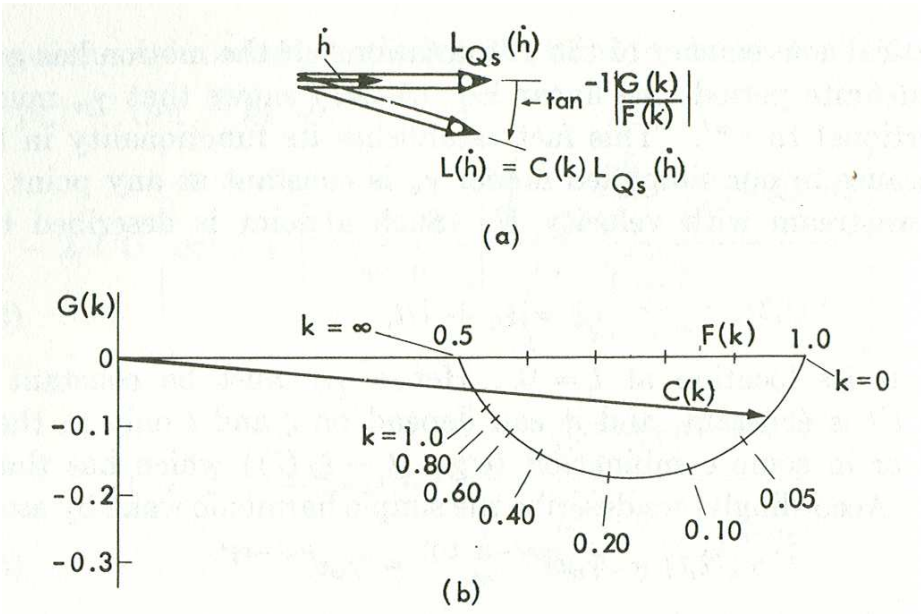

Figure 2.16: Relationship between quasi-steady and unsteady lift (a) and polar plot of the Theodorsen's circulatory function $C(k)$ (b). [From Bisplinghoff *et al.* (1996)]

Table 2.1: Comparison between unsteady and quasi-steady (QS) results

B [m]	k_c	U_{Rc}	U_{Rc} (QS)	ΔU_{Rc} [%]
25	0.1407	22.3	13.8	-38.3
15	0.0625	50.2	37.6	-25.1
10	0.0313	100.3	84.5	-15.7
3	0.0033	960.5	934.5	-2.7
1	0.0004	8444	8410	-0.4

Chapter 3

Wind-tunnel tests

3.1 Motivations for these tests

The main purpose of this experimental campaign is to increase the number of available data concerning bridge deck flutter derivatives. The choice of the cross-sectional geometry, namely a trapezoidal single-box girder with lateral cantilevers [Fig. 3.5(b)], is due to the fact that it is common for medium-span cable-stayed bridges, for which the simplified method of flutter assessment outlined in this dissertation could be particularly appealing. In addition, for this geometry just few sets of data are available in the literature and in some cases only three functions are measured (Barré *et al.*, 1996a,b).

Another important motivation for these tests is the need to give a probabilistic description of flutter derivatives, in order to apply the method of probabilistic flutter assessment described in Chapter 4.

The relevance of this experimental work also concerns several other issues, such as the identification of flutter derivatives at different angles of attack via free-vibration tests. In fact it is well known that the aeroelastic coefficients can be very sensitive to the mean angle of flow incidence [e.g. ONERA (1989); Flamand (2000, 2001); Diana *et al.* (2005a,b)] and how important this effect can be on flutter and buffeting calculations (Diana *et al.*, 2005a,b; Chen and Kareem, 2000). Nevertheless, flutter derivatives are only rarely measured at different angles of attack and usually via forced-vibration tests.

Another point discussed in the following is the supposed linearity of self-excited forces with respect to the amplitude of the motion [Eqs. (2.38)-(2.39)], that being still an open issue in bridge aeroelasticity.

Besides aeroelastic tests, static tests are performed in order to measure the aerodynamic force coefficients. In addition to their direct use (static load, buffeting analysis, quasi-steady self-excited load), their knowledge is useful to determine indicial functions [Eqs. (2.57)-(2.58)] and their patterns can say much about the aerodynamic behavior of the cross section. Moreover, with stationary configurations it is easier than with aeroelastic suspension systems to investigate Reynolds number effects.

The results of a few Computational Fluid Dynamics simulations, performed by the writer at the Institute of Aeroelasticity of the German Aerospace Center (DLR) of Göttingen are

compared with the experimental data, helping to better understand them and to explain the significant differences with the results obtained in the Western Ontario Wind-Tunnel Laboratory in Canada (Ricciardelli and Hangan, 2001).

3.2 CRIACIV-DIC Boundary Layer Wind Tunnel

All the static and aeroelastic tests are performed in the CRIACIV[1]-DIC[2] Boundary Layer Wind Tunnel (http://windlab.ing.unifi.it), located in Prato, Italy (Figs. 3.1-3.2).

It is an Eiffel-type open-circuit wind tunnel with a cross section slightly divergent from the inlet to the test section, which is 2.42 m large and 1.60 m high. The total length of the wind tunnel is about 22 m. The wind speed is regulated both by adjusting the pitch of the ten blades constituting the fan and by controlling the rotating speed. The maximum wind speed attainable is as high as about 30 m/s. More details concerning the wind tunnel can be found in Augusti *et al.* (1995).

Figure 3.1: View of the CRAICIV-DIC Boundary Layer Wind Tunnel in Prato

3.3 Instrumentation

For the static and aeroelastic tests discussed herein the following instruments are adopted:

- Two Pitot tubes
- A two-components hot-wire anemometer

[1]Centro di Ricerca Interuniversitario di Aerodinamica delle Costruzioni e Ingegneria del Vento (Inter-university Research Center of Building Aerodynamics and Wind Engineering)

[2]Dipartimento di Ingegneria Civile (Department of Civil Engineering)

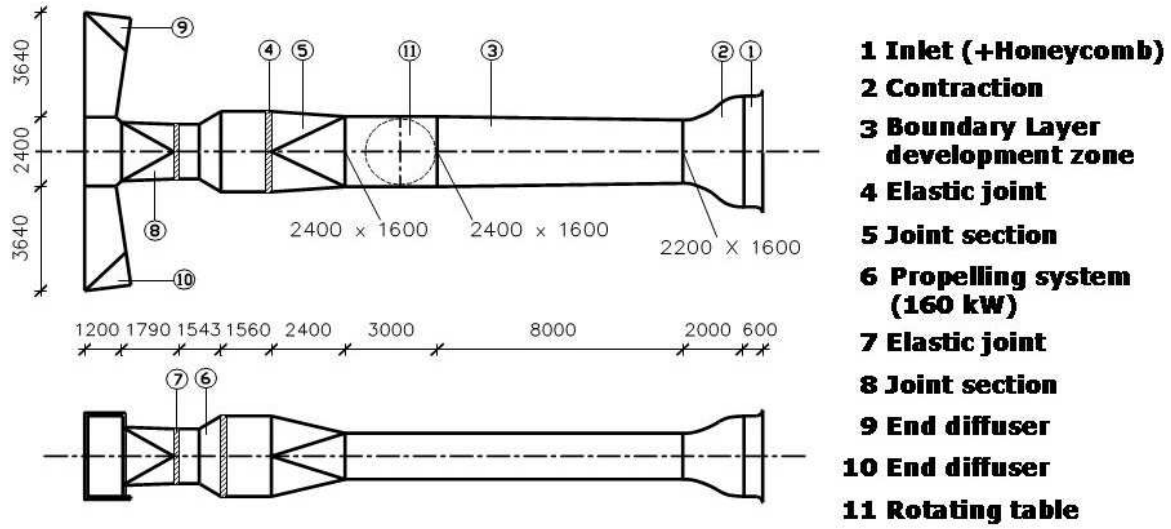

Figure 3.2: Schematic view of the wind tunnel (position 11 also indicates the test section)

- Two accelerometers
- Six strain-gauges load cells
- Three displacement laser transducers

The Pitot tube allows to measure the mean kinetic pressure of the incoming flow and therefore indirectly the mean wind speed. The position of the pitot tube upstream of the model can be freely chosen. The instrument is connected to a pressure transducer (Setra System, model 239) whose voltage signal is acquired by a PC by means of a data acquisition card.

The hot-wire anemometer allows to measure the component of the instantaneous wind speed in the plane perpendicular to the wire. It is a thermic transducer with a platinum plated tungsten wire sensor. Electricity warms the sensor up by Joule effect, whereas the wind flow with its local instantaneous speed cools it down by convection. The voltage necessary to keep constant the wire temperature is measured.

A set of ICP® accelerometers produced by PCB Piezotronics, model 353B34, are used in the laboratory. They can measure frequencies in the range 1 to 4000 Hz with a sensitivity tolerance of $\pm 5\%$. Their conversion factor is 10.19 mV/(m/s^2). Their resonant frequency is larger than 22 kHz and their non-linearity smaller than 1 %.

Six 535 QD strain-gauges load cells produced by DS EUROPE s.r.l., are used to measure the aerodynamic forces on the stationary section model [Fig. 3.3(a)]. Their technical characteristics are reported in Tab. 3.1. The actual linearity of these instruments is checked as shown in Fig. 3.3(b).

Three non-contact optical laser transducers (Micro-epsilon Model OptoNCDT 1605) are available to determine the displacements of the model in the aeroelastic set-up or the angle

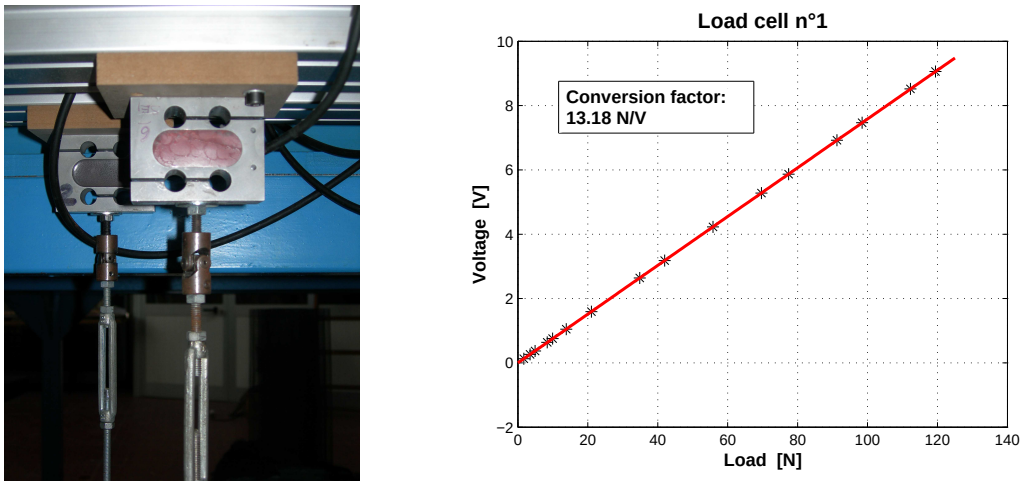

(a) (b)

Figure 3.3: (a) View of a load cell; (b) Relationship between load cell output voltage and actual force applied.

Table 3.1: Main technical characteristics of the strain-gauges load cells

Measure range	$0 \div 120$ N
Sensitivity	2 mV/V at end scale (FS)
Repeatability error	$\leq \pm 0.033\%$ FS
Error for non-linearity and hysteresis	$\leq \pm 0.023\%$ FS
Error of thermic variation of the zero-point	$\leq \pm 0.033\%$ FS
Creep error after 8 hours	$\leq \pm 0.033\%$ FS
Zero unbalancing	$\leq \pm 2\%$ FS
Maximal deflection at FS	≤ 0.6 mm
Safety limit load	50% FS
Coaxial fixing holes	IP65
Out of axis loads	insensitive until 10 cm

of attack in the static set-up [Fig. 3.4(a)]. These lasers use a semiconductor with 675 nm wavelength and a maximum output power of 1 mW and their functioning principle is based on triangulation. The output voltage range is ±10 V which corresponds to a displacement of roughly ±100 mm. The lasers are connected to a PC acquisition card. The characteristics of the lasers are reported in Tab. 3.2. The actual linearity of these transducers and their conversion factor is checked for each laser by means of a high precision mechanical distantiometry [Fig. 3.4(b)].

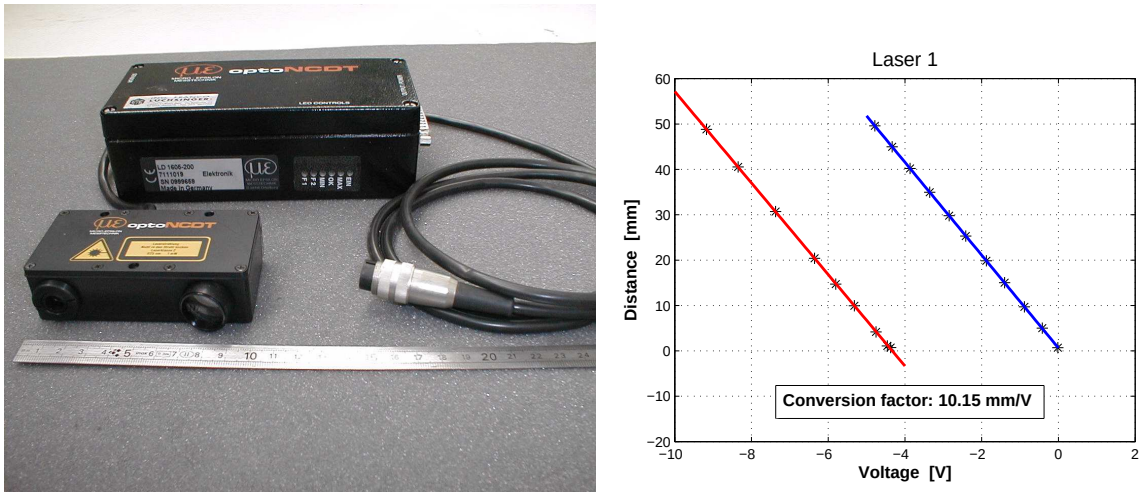

(a) (b)

Figure 3.4: (a) View of a laser triangulator device for displacement measurement; (b) Relationship between laser output voltage and actual object distance.

3.4 Static tests

3.4.1 Experimental set-up

The same section model is used for static and aeroelastic tests. The model is made of aluminium and its weight (without supporting system) is as high as 9.2 kg. The model is build around a circular tube with a diameter of 45 mm, 16 ribs (8 mm thick) supporting the external 0.5 mm sheet-aluminium. The model, whose main geometric features can be seen in Fig. 3.5, is 2380 mm long (the tube is 2800 mm long), 450 mm wide and 70 mm deep. Therefore the chord-to-thickness ratio is $B/D = 6.43$ and the length-to-chord ratio is $l/B = 5.29$. The model is tested in the bare-deck configuration, i.e. without non-structural details.

The model is placed in the wind tunnel test section as shown in Fig. 3.6(a) and six load cells (three on each side) are assembled to form a force measuring system according to the scheme of Figs. 3.6-3.7. Before starting the tests the whole system is calibrated applying known drag, lift and torque loads in order to build a calibration matrix.

The model ends are very close to the wind-tunnel walls (the distance is only 20 mm), which work as end-plates, imposing approximately a two-dimensional flow around the section model.

Table 3.2: Micro-epsilon Model OptoNCDT 1605 laser characteristics

Sensor type	Laser-Sensor
Model	LD 1605
Type	200
Measuring range	±100 mm
Stand-off midrange	340 mm
Non-linearity $\leq \pm 0.3\%$ d.M.	600 μm
Resolution (noise) static	60 μm
Measuring spot dia. midrange	2 mm
Light source	Laser 1 mW, wavelength: red 675 nm
Sampling frequency	40 kHz
Laser class	2
Analogical Output	
Displacement	±10 V
Output impedance	appr. 0 Ohm (10 mA max.)
Angle dependance	appr. 0.5 % when turning ± 30° about longitudinal axis
Rise time	0.1/0.2/2 or 20 msec selectable
Frequency response	10 kHz, 3 kHz, 250 Hz or 25 Hz
Temperature stability	0.03 %/°K
Intensity of reflecting light	1 V bis 10 V/max; 0 V bis +13 V
Permissible ambient light	20000 Lux
Life time	50000 h for laser-diode
Insulation	200 VDC, 0 V against housing
Max. vibration	10 g to 1 kHz
Operation temperature	0 to 50 °C

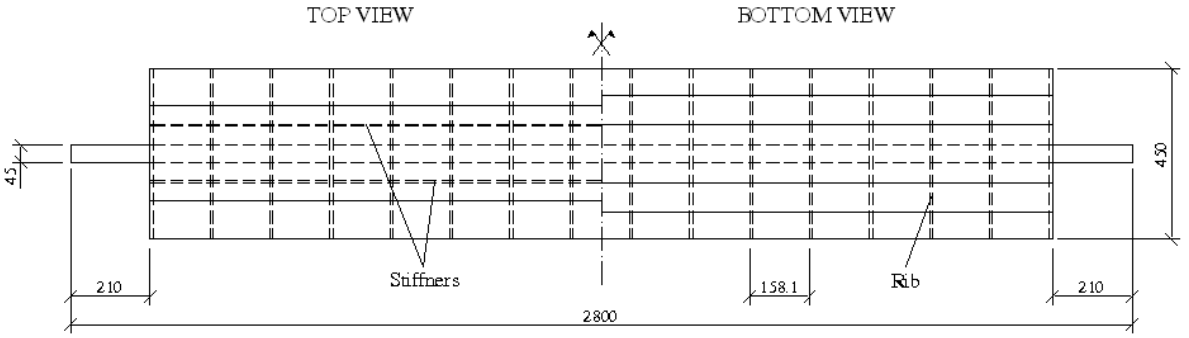

(a)

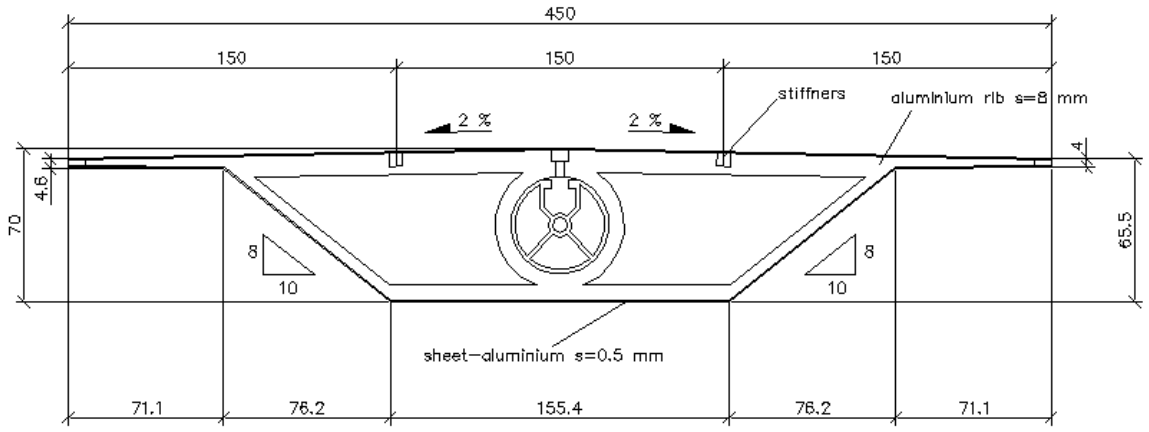

(b)

Figure 3.5: Geometric characteristics of the bridge deck section model: (a) plan view; (b) cross section. All dimensions are in mm.

Finally, the natural frequencies of the model and the balance are measured by means of two accelerometers placed at the midspan and at one support of the model [Fig. 3.7(b)] and exciting the system with symmetric [Fig. 3.8(a)] and eccentric dynamic loads [Fig. 3.8(b)]. Clearly the first natural frequency of the model is that corresponding to the symmetric vertical bending mode and is as high as about 16 Hz, while the first torsional frequency is about 42 Hz.

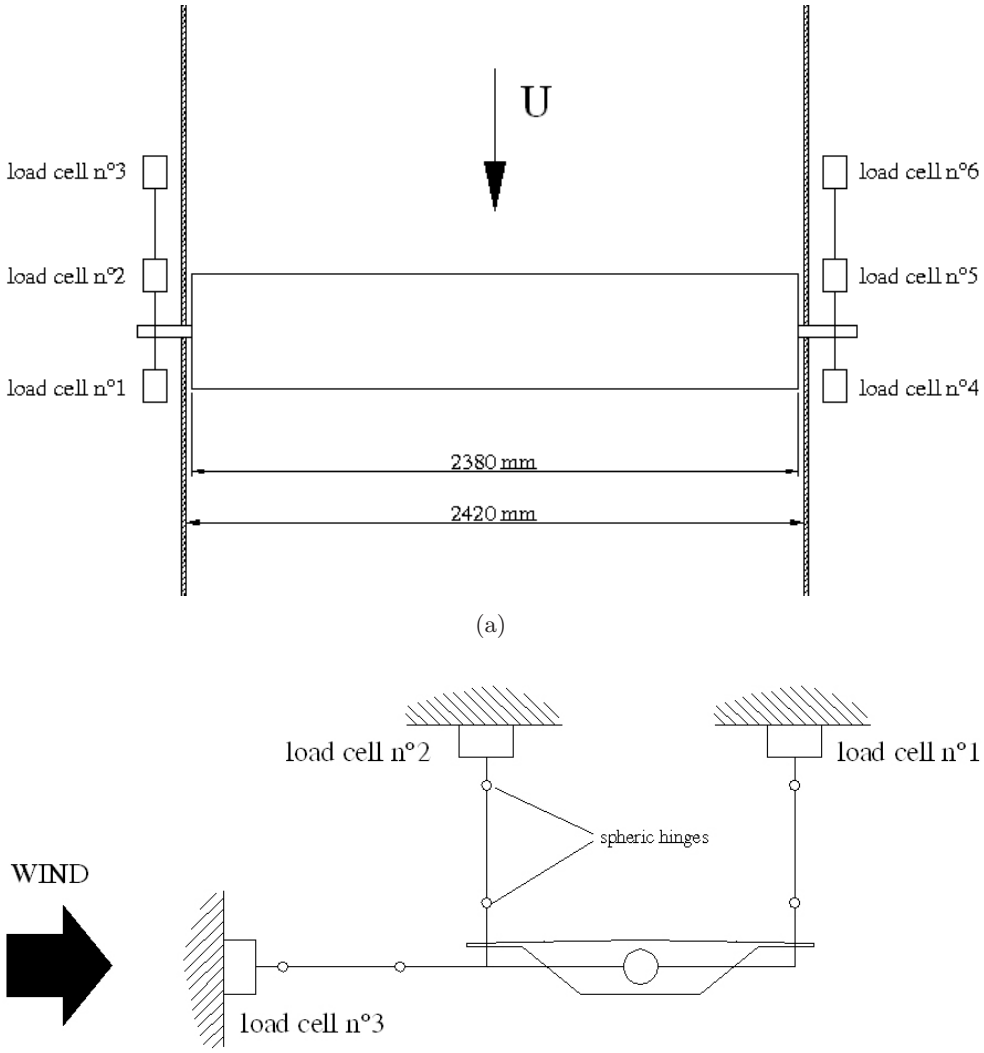

Figure 3.6: Sketch of the set-up for the static measurements: (a) top view; (b) lateral view

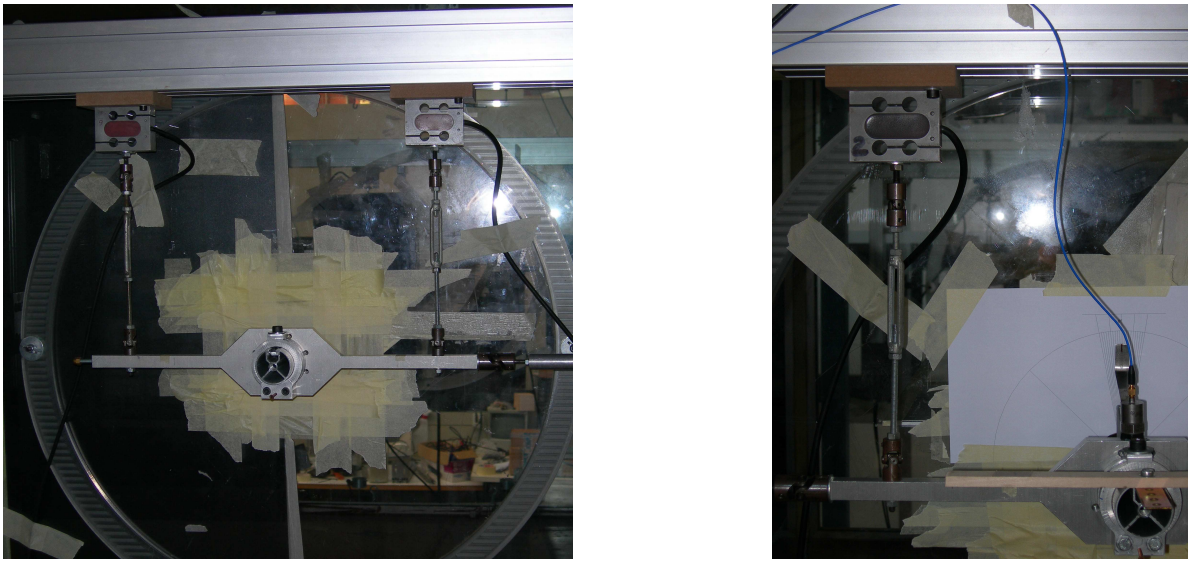

(a) (b)

Figure 3.7: Set-up for the static measurements. In (b) the accelerometer placed at the support can be seen.

3.4.2 Results

The influence of Reynolds number on the static behavior of the section model is investigated at three different angles of attack (-5°, 0°, +5°) increasing the wind speed approximately in the range 3 - 28 m/s ($9 \cdot 10^4 < Re < 8 \cdot 10^5$) and measuring the aerodynamic force coefficients. Reynolds number is defined according to Eq. (3.1), physically being a measure of the ratio of inertial forces to viscous forces in the flow.

$$Re = \frac{\rho B U}{\mu} = \frac{B U}{\nu} \tag{3.1}$$

where ρ is the air density, U the undisturbed mean flow speed, B is a characteristic reference length (in our case the section-model chord), μ is the air dynamic viscosity and $\nu = \mu/\rho$ is the air kinematic viscosity ($\nu = 1.5 \cdot 10^{-5}$ m^{2}s^{-1} at 20°C). The air density is calculated measuring the temperature and static pressure according to the perfect gas law:

$$p = \rho R T \tag{3.2}$$

where p is the air static pressure, R=287 J kg^{-1}K^{-1} is the universal gas constant and T is the absolute temperature (in K). The air dynamic viscosity is calculated following the Sutherland's law:

$$\mu(T) = \mu_0 (\frac{T}{T_0})^{\frac{3}{2}} \frac{T_0 + S_u}{T + S_u} \tag{3.3}$$

where $\mu_0 = \mu(T_0) = 1.716 \cdot 10^{-5}$ kg m^{-1}s^{-1} is the reference viscosity, T_0=273 K is the reference temperature and S_u=110.4 K is the Sutherland's constant.

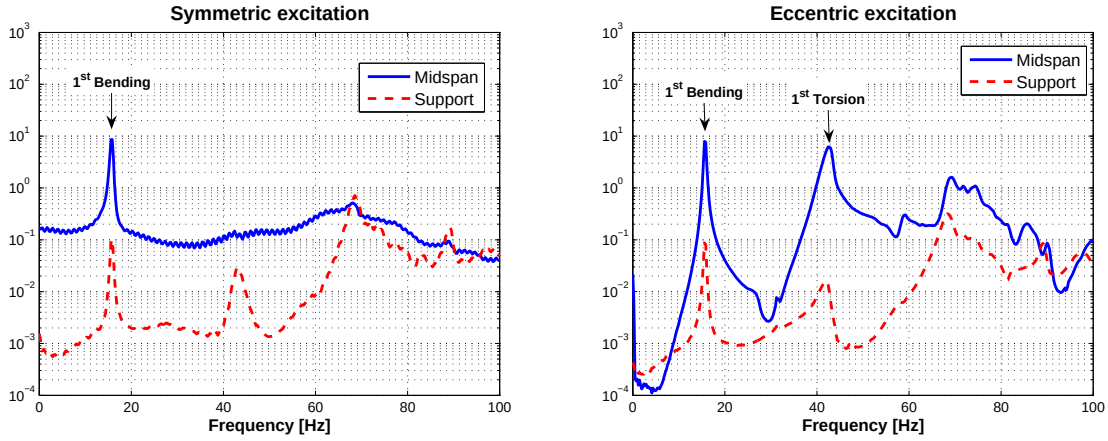

(a) (b)

Figure 3.8: Power spectral density of the signals registered by the accelerometers placed at the midspan and at the right support of the model. (a) Symmetric excitation: both accelerometers are placed on the longitudinal symmetry plane; (b) Eccentric excitation: the accelerometer at midspan is eccentric as well.

The definition of the aerodynamic force coefficients is reported in Eqs. (3.4)-(3.6):

$$C_D(t) = \frac{D(t)}{qBl} \tag{3.4}$$

$$C_L(t) = \frac{L(t)}{qBl} \tag{3.5}$$

$$C_M(t) = \frac{M(t)}{qB^2l} \tag{3.6}$$

where $D(t)$, $L(t)$ and $M(t)$ are the instantaneous total drag, lift and moment respectively acting on the section model, $q = \frac{1}{2}\rho U^2$ is the kinetic pressure and l is the section-model length on which the aerodynamic forces act. It is worth noting that strictly speaking l is not as large as the whole length of the section model, since a boundary layer develops on the lateral walls of the wind tunnel, which play the role of end-plates, being very close to the section-model ends. Nevertheless, in some preliminary tests it was observed that the thickness of this boundary layer is relatively small and consequently this complication can be neglected here. $M(t)$ is measured with respect to the pitching rotation center of the section model, which coincides with the center of the circular tube in Fig. 3.5(b). The forces are represented according to the "aeronautical convention", as shown in Fig. 3.9.

The dependence on Reynolds number of the mean force coefficients and their rms-value is shown in Figs. 3.10(a)-3.10(f) for zero-degree angle of attack. The same diagrams for $\pm 5^\circ$ are reported in the Appendix. It is evident that Reynolds number has a non-negligible influence on the aerodynamic forces. For low values of the wind speed the forces are small and the

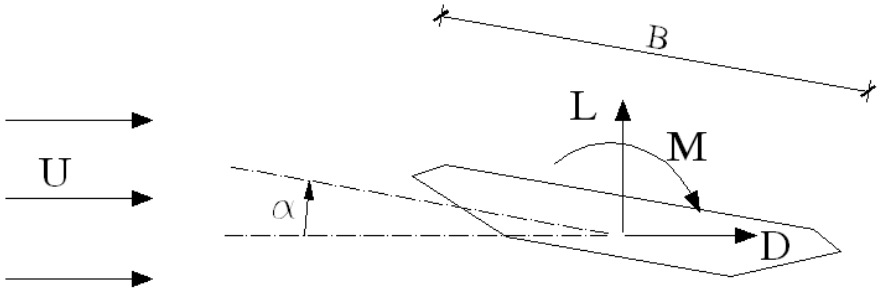

Figure 3.9: Reference system for the aerodynamic force coefficients

measurements are not very reliable, nevertheless a clear and regular trend can be unequivocally detected. It is worth noting that the mean values of the aerodynamic coefficients do not reach a plateau, especially C_D at all the considered angles of attack and C_M at -5° and 0°. For instance, in case of zero flow incidence, both drag and moment coefficients significantly increase with Reynolds number, reach a peak around $Re = 4.5 \cdot 10^5$ and then start to decrease (smoothly C_D, more rapidly C_M). The rms-value of all force coefficients is much higher at low Reynolds number, then in most cases it tends to stabilize (apart from the lift coefficient at 0°).

The explanation for these pronounced Reynolds number effects can be partially found in the work of Schewe and Larsen (1998) and Schewe (2001) for the approaching-span cross section of the Great Belt East Bridge, where it is found that the reattachment of one of the shear layers on the lower surface of the profile is responsible for a sudden reduction of the width of the wake, with consequent crisis of the drag coefficient and increase of the Strouhal number. Nevertheless, in this case the Reynolds number effects are not characterized by sharp jumps limited to a small interval of Re-values but they are continuous and much smoother. A key role could be played by the lower corners of the box which, in contrast with the theoretical design of the model, are not manufacturing as perfectly sharp. This degree of roundness could be responsible for an enhancement and a "smoothing" of the scale effects. This important point is further discussed in section 3.4.3.

This non-negligible Reynolds-number dependance can be expected to affect also the aeroelastic behavior of the model and in particular the flutter derivative values. Nevertheless, the conclusion for the stationary body cannot be directly translated to the oscillating case, where it is mainly the motion of the body which drives the dynamics of the flow. Additional remarks on this point can be found in section 3.4.3 but more investigations are still needed to clarify this issue.

The previously shown load-cell measurements at different wind speeds cannot be used to measure the shedding frequencies and therefore to determinate the Strouhal number, because in the signal spectra only the natural frequencies of the model are visible, as shown in Fig. 3.11. It is worth noting that at low wind speed several peaks due to the electrical noise are also evident in the spectrum. Consequently, in order to measure the shedding frequency, a hot-wire

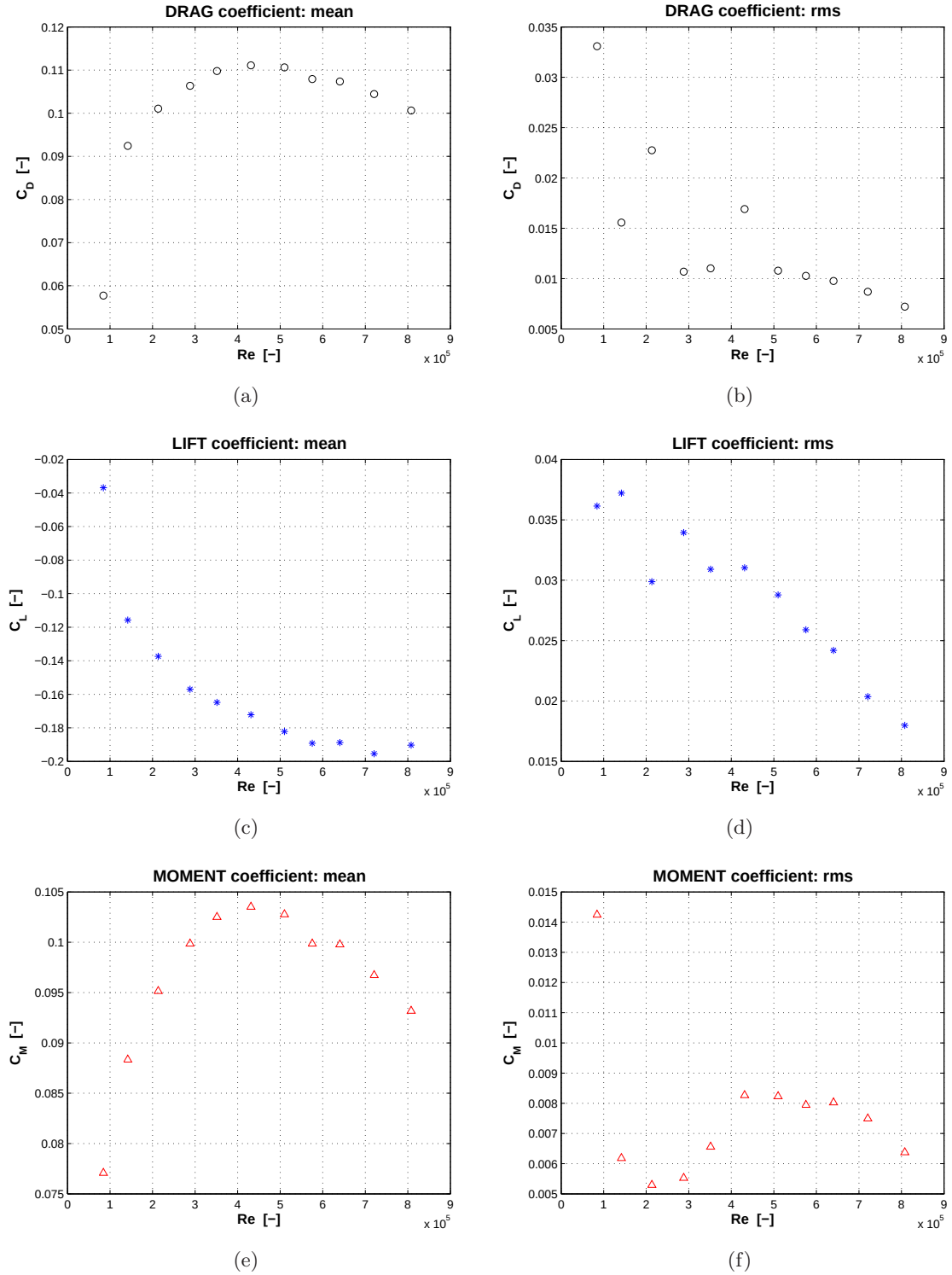

Figure 3.10: Mean and rms-values of the aerodynamic force coefficients depending on Reynolds number at 0° angle of attack (frequency of acquisition: 2000 Hz; length of the signals: 120 s)

anemometer is placed in the lower region of the wake and the measured spectra are analyzed in order to find one or more peaks proportional to the wind speed. The uncertainties in the determination of the Strouhal number are due to the fact that the spectra are broad-banded (especially for $\alpha = 0°$) and disturbed by the electrical noise. Consequently, the Strouhal number is identified for $\alpha = 0°$ and $\pm 5°$ averaging the supposed shedding frequencies at different wind speeds. The results are reported in Tab. 3.3 and four examples of Strouhal peaks in the spectra are shown in Fig. 3.12. The complete series of spectra used to determine the Strouhal numbers are reported in the Appendix. In Tab. 3.3 we see that for this bridge section the Strouhal number can be estimated to be around 0.20-0.25 and that a significant scatter affects the values which are averaged. Nevertheless, Fig. 3.13 clearly shows that this variability is not the result of the Reynolds number effects, since there is no well defined trend. In addition, the slightly smaller mean value of the Strouhal number for $\alpha = 0°$ with respect to $\alpha = \pm 5°$, could be due only to the larger uncertainty concerning the position of the Strouhal peak in the spectra. It seems reasonable to state that the Strouhal number does not change much for a wide range of angles of attack (-5°$\leq \alpha \leq$ +5°).

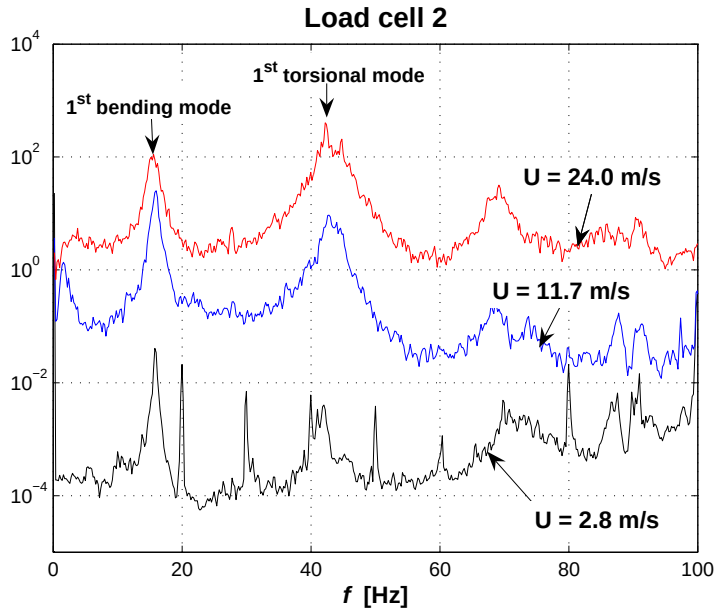

Figure 3.11: Example of power spectral density of load cell signal (zero degree angle of attack)

Given that the first bending and torsional natural frequencies of the model are respectively 16 Hz and 42 Hz, significant resonance effects are expected around 4-6 m/s and 12-15 m/s. Therefore, the aerodynamic force coefficients at different angles of attack should be measured at a wind speed far from these ranges. In addition, in view of the previously discussed Reynolds number effects, a wind speed as high as possible is desirable. Finally, since a convenient safety margin has to be provided, a wind speed of 19.2 m/s is chosen ($Re = 5.76 \cdot 10^5$), except in the range $+8 \div 10°$ where, in order to reduce the very high aerodynamic forces, wind speeds of 14.3 m/s (+8°) and 9.5 m/s (+9° and +10°) are selected. The measured mean aerodynamic

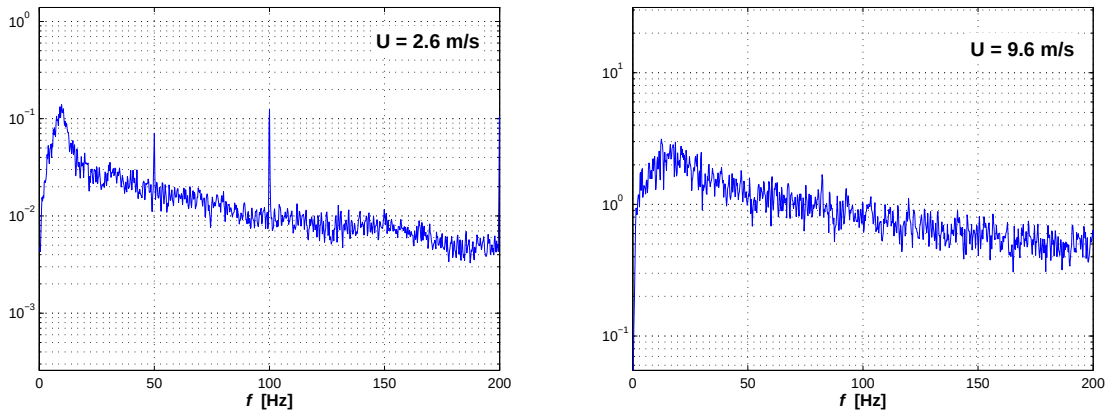

(a)

(b)

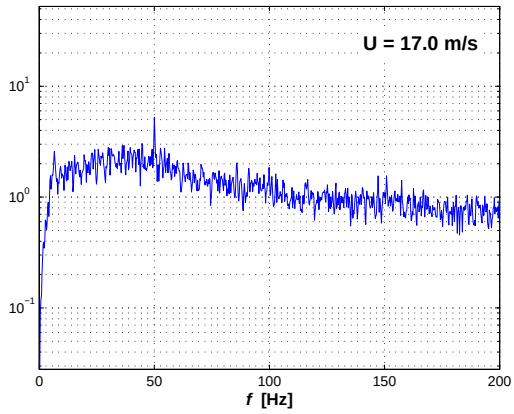

(c)

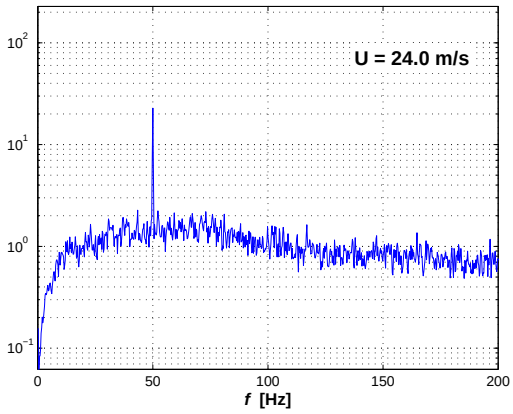

(d)

Figure 3.12: Power spectral density of the wind speed fluctuation signals registered by the hot-wire anemometer placed in the wake of model at zero degree angle of attack (frequency of acquisition: 2000 Hz; length of the signals: 120 s)

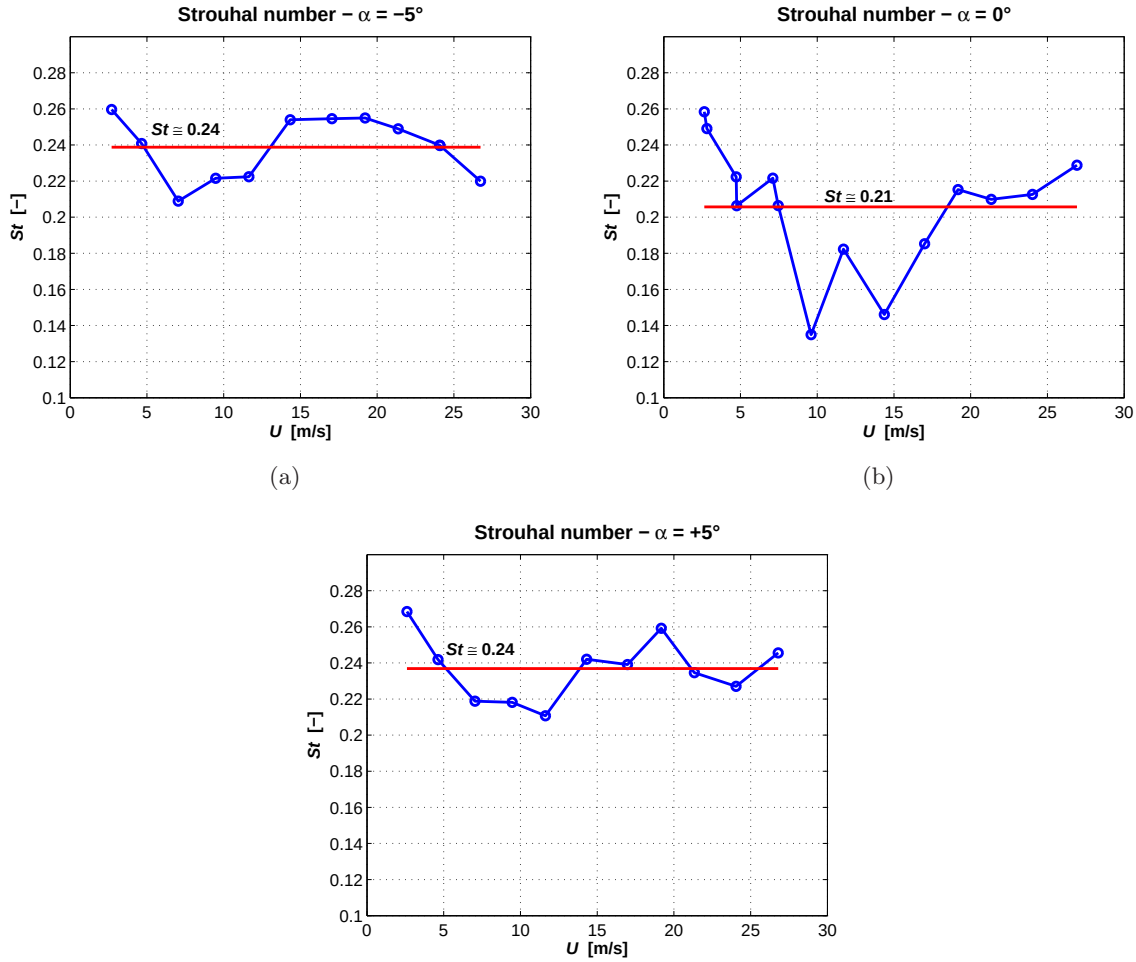

Figure 3.13: Measured and mean values of the Strouhal number

Table 3.3: Strouhal number evaluation from hot-wire anemometer measures

$\alpha = 0°$			$\alpha = -5°$			$\alpha = +5°$		
U [m/s]	f_s [Hz]	St [-]	U [m/s]	f_s [Hz]	St [-]	U [m/s]	f_s [Hz]	St [-]
2.64	9.75	0.258	2.70	10	0.260	2.61	10	0.268
2.81	10	0.249	4.65	16	0.241	4.63	16	0.242
4.72	15	0.222	7.04	21	0.209	7.04	22	0.219
4.75	14	0.206	9.48	30	0.222	9.46	29.5	0.218
7.11	22.5	0.222	11.64	37	0.222	11.62	35	0.211
7.46	22	0.206	14.33	52	0.254	14.31	49.5	0.242
9.60	18.5	0.135	17.05	62	0.255	16.98	58	0.239
11.71	30.5	0.182	19.22	70	0.255	19.17	71	0.259
14.37	30	0.146	21.37	76	0.249	21.33	71.5	0.235
17.00	45	0.185	24.07	82.5	0.240	24.05	78	0.227
19.18	59	0.215	24.09	82.5	0.240	26.80	94	0.246
21.34	64	0.210	26.73	84	0.220			
24.03	73	0.213						
26.93	88	0.229						
Mean		**0.21**			**0.24**			**0.24**

force coefficients are reported in Fig. 3.14.

In the aerodynamic coefficients a regular pattern can be remarked except in the range from -2.5° to 0° where some significant changes in the flow around the profile seems to appear. As a matter of fact the lift coefficient follows a linear trend from -10° to -2.5° and then again from 0° to +8° with only a small difference in the slope. Conversely, for the moment the slope seems to be exactly the same in the two ranges. At +6° the moment coefficient shows a stalling behavior, although the lift coefficient continues to follow a linear pattern until +8°. In order to better understand what happens in the range from -2.5° to 0° the rms-values of the aerodynamic force coefficients are shown in Fig. 3.15. It can be observed that these mean fluctuations are nearly constant except in the range from about -3° to +1° and near the stall (it is worth reminding that the force coefficients corresponding to the last three positive angles of attack are measured at lower wind speed that in all the other cases), where a significant increase in the aerodynamic force fluctuations is evident. This local behavior cannot be explained with resonance effects, because it appears at different wind speeds, as Fig. 3.16 clearly shows. Here again some Reynolds number effects can be recognized.

Clearly, excluding the stall at high angles of attack, two main flow regimes can be distinguished. The first regime corresponds to the ranges approximately from -10° to -2.5° and from 0° to +6°, where the aerodynamic coefficients show a very regular behavior and a linear pattern with respect to the angle of attack. The second regime, which looks like a local "instability" of the flow, is limited to the range from -2.5° to 0° (or to -3° to +1° if we look at the rms-values in Fig. 3.15), where the aforementioned linear pattern is lost, the slope of the curves completely changes and much higher fluctuations affect the aerodynamic forces. In addition, it seems that the transition between the two regimes is fairly smooth around 0° whereas it shows a

sudden jump around -2.5°. It is also worth noting that the aerodynamic coefficients measured with the static set-up and above all the behavior in the range -2.5°$\lesssim \alpha \lesssim$ 0° are confirmed by the measurements with the aeroelastic set-up (Fig. 3.31), as shown in the next section. In particular, when the section model is free to vibrate, the difference between the discussed flow regimes is even more evident.

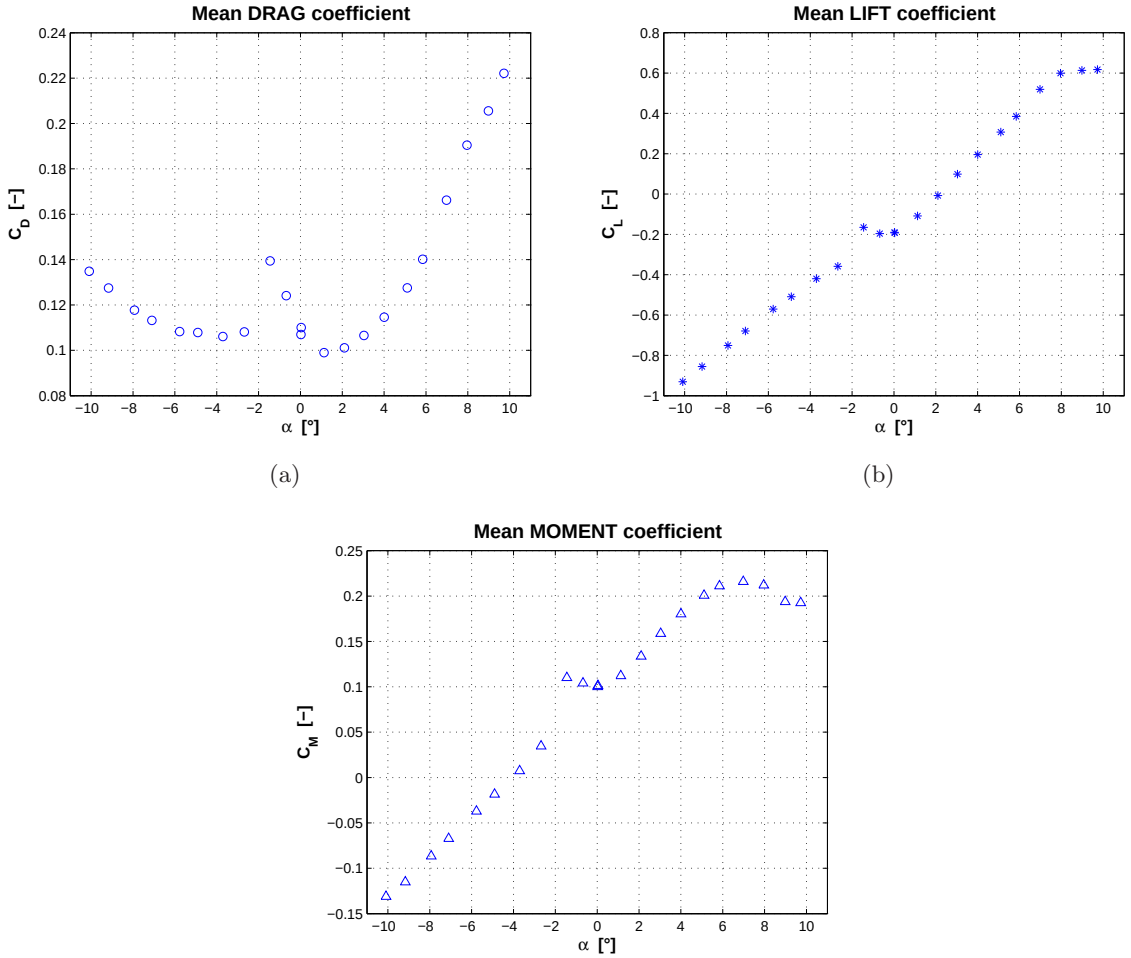

(a) (b)

(c)

Figure 3.14: Mean aerodynamic force coefficients at different angles of attack (frequency of acquisition: 1000 Hz; length of the signals: 60 s)

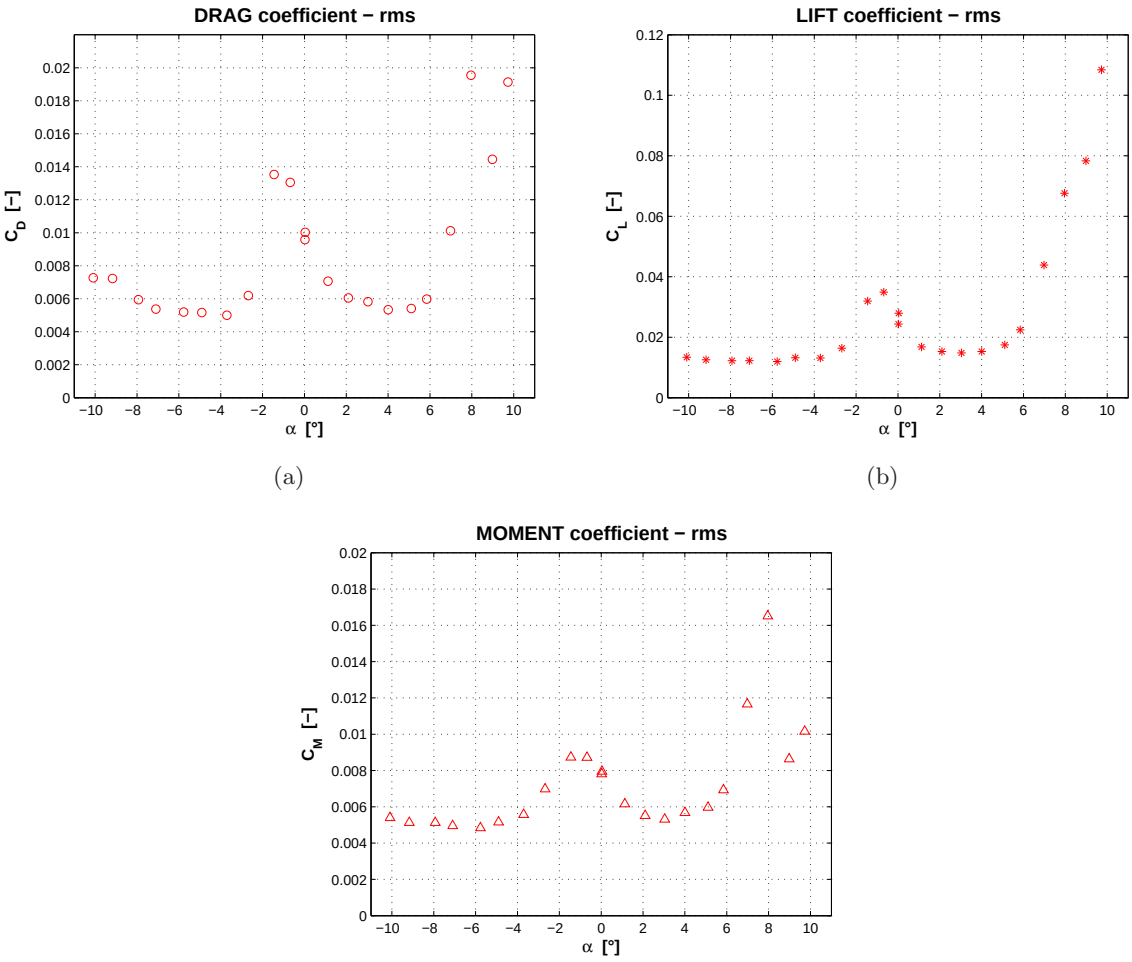

(a)

(b)

(c)

Figure 3.15: Mean fluctuation of the aerodynamic force coefficients at different angles of attack

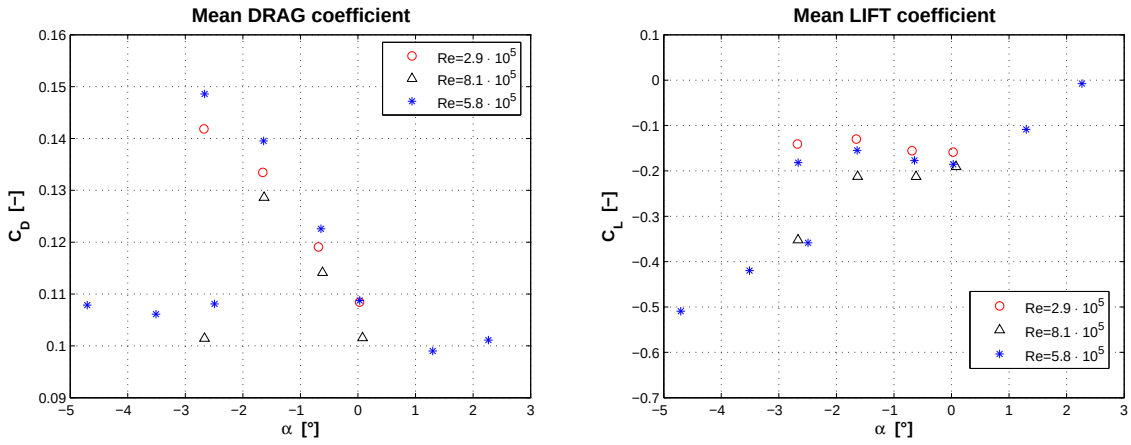

(a)

(b)

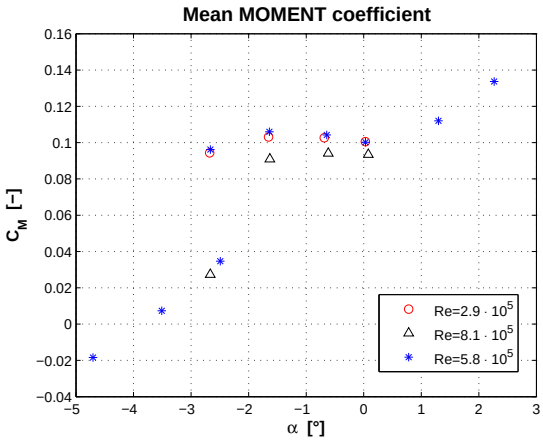

(c)

Figure 3.16: Aerodynamic coefficients in the range -3°$\lesssim \alpha \lesssim$ 0° for three different wind speeds

3.4.3 Comparison with CFD simulations

Very similar to the section model tested by the writer (from now on called "CRIACIV section") is the one of the Sunshine Skyway Bridge (SSB) in Florida, in the bare-deck configuration, tested at Western Ontario Wind-Tunnel Laboratory in Canada (Davenport and King, 1982; Ricciardelli and Hangan, 2001). The two cross sections are compared in Figs. 3.17 and 3.18 and at first glance they appear to be very similar, with only minor differences in the geometry (for instance $B/D = 6.43$ for the CRIACIV section and $B/D = 6.80$ for the SSB section). Nevertheless, the aerodynamic force coefficients and Strouhal numbers measured for the two profiles result to be very different (Fig. 3.19). For instance, the mean lift coefficient at 0° is definitely positive for the Sunshine Skyway Bridge ($C_L = +0.29$), while it is negative for the CRIACIV section ($C_L = -0.20$), as confirmed by the measurements performed with the aeroelastic set-up (see Fig. 3.31 in the next section). Also in order to shed some light on these discrepancies, the CRIACIV section is investigated through Computational Fluid Dynamics (CFD) simulations (Mannini *et al.*, 2006a,b). It is worth noting that in the following no attempt has been made to reproduce the exact geometry of the SSB section.

The flow around the stationary cross section is calculated through the Navier-Stokes code Tau [e.g. Gerhold *et al.* (1997)], developed at the Deutsches Zentrum für Luft- und Raumfahrt (DLR), an unstructured solver based on finite volume approach. This code, normally used for aeronautical applications and transonic flows, has been validated for low Mach number flows around both streamlined and bluff bodies such as square (B/D=1) and rectangular (B/D=5) cylinders (Mannini *et al.*, 2006a,b). The code solves the compressible governing equations with second-order accuracy in both space and time. The diffusive terms are approximated with the central differencing scheme, while the convective terms can be modelled with central or upwinding algorithms: in the computations discussed herein the central differencing scheme with classical dissipation is adopted. The flow variables are stored in the nodes of the primary grid (cell-vertex scheme). For time-accurate simulations the dual-time-stepping technique is used, along with the explicit residual smoothing and a multi-grid technique based on agglomeration of the dual-grid volumes. All computations are performed on the computer cluster of the Institut für Aeroelastik, DLR-Göttingen.

The two-dimensional Unsteady Reynolds-Averaged Navier-Stokes (URANS) approach is adopted along with the Linearized Explicit Algebraic (LEA) turbulence model (Rung *et al.*, 1999) based on the two-equation $k-\omega$ model of Wilcox. The one-equation turbulence model of Spalart and Allmaras (1992) is also tested but discarded because it gives an unrealistic steady flow solution and less accurate results.

The spatial domain is discretized with a hybrid grid, composed of body-aligned structured quadrilateral cells near the body, in order to better capture boundary layer development, separation and reattachment, and unstructured triangular cells in the remaining part of the domain (Fig. 3.20). A non-reflecting circular farfield is assumed at one-hundred chord distance from the solid body. Concerning time discretization, the expected period of vortex shedding is resolved with 500 time steps ($\Delta s = U\Delta t/B = 2.8 \cdot 10^{-3}$) and 100 inner iterations per time step.

In order to obtain a flow solution independent of the spatial and temporal discretization, grid- and time-convergence studies are performed for the case $\alpha = 0°$. In particular, in Fig. 3.21

and Tabs. 3.4-3.5 the results of the grid-convergence study are reported. Four meshes with different levels of refinement (Tab. 3.4) are tested. The use of the so-called "Coarsest grid") implies a steady solution (Fig. 3.21 and Tab. 3.5), while in the case of the "Fine grid") the observed high-frequency oscillations with small amplitude (Fig. 3.21) are probably the result of numerical instabilities due to the lack of numerical dissipation. Finally, it seems possible to consider the "Medium grid" (Fig. 3.20) solution as a converged result and therefore this computational mesh is used in all the following simulations.

Two angle-of-attack configurations (0° and +5°) are simulated for $Re = 6.0 \cdot 10^5$ and the results are in good agreement with the aerodynamic force coefficients and Strouhal number measured for the bare-deck configuration of the Sunshine Skyway Bridge, as clearly shown in Fig. 3.19 and Tab. 3.6. The most significant geometrical difference between the two section models compared in Figs. 3.17 and 3.18 are the lower corners of the trapezoidal box, which are intentionally made sharp in the SSB case by means of small triangular appendices. Conversely, in the CRIACIV section a small roundness is present, due to the bending of the aluminium-sheet during the manufacturing of the model, and this feature is believed to be responsible for such a big difference in the results, since there the separation of the boundary layer occurs (Fig. 3.22). A small radius of curvature can move forward or backward the separation point and that is critical for the possible shear layer reattachment. In the computations the corners are simulated as perfectly sharp and this explains the agreement with the Sunshine Skyway Bridge data, as confirmed by Fig. 3.23(a) where the calculated mean pressure coefficient distribution shows an outstanding agreement with the experimental measures (Ricciardelli and Hangan, 2001). Conversely, concerning the mean fluctuations of the pressure coefficient [Fig. 3.23(b)] the agreement is only qualitative, being the measured values significantly underestimated by the numerical simulation. The reasons for this discrepancy are not clear yet (limits of the URANS approach, difference in the Reynolds number and so forth). In addition, the perfect sharpness of the lower edges could be the cause for the Reynolds number insensitivity suggested by the results reported in Figs. 3.19 and 3.23 and Tab. 3.6.

In order to prove these speculations, another computation is run modifying the cross-sectional geometry introducing a small radius of curvature ($R = 0.05B$) in correspondence of the lower corners. As a result, the flow field around the body dramatically changes, as clearly shown in Fig. 3.22: the lower shear layer, which is fully separated at the intrados of the profile in case of perfectly sharp edges [Fig. 3.22(a)], now quickly reattaches on the bottom surface [Fig. 3.22(b)]. Consequently, the width of the wake is reduced and the frequency of vortex shedding increases. In addition, the aerodynamic coefficients and the Strouhal number approach the values measured for the CRIACIV section (Fig. 3.19 and Tab. 3.6): in particular the lift at 0° becomes negative and the moment coefficient perfectly matches the experimental value. In order to obtain an even better agreement with the experiments, probably it would be necessary to simulate the actual radius of curvature which characterizes the lower edges of the section model. Unfortunately, this parameter is very difficult to be measured and perhaps even not constant along the span of the model. Therefore, a parametric study may be the best way to address the problem. As a future development, it could be also interesting to understand if the smooth corners completely change the aerodynamic behavior of the profile or just anticipate a Reynolds-dependent wake transition, like it was observed in Schewe and Larsen (1998) and Schewe (2001) for the Great Belt East Bridge, which would occur anyway

but at higher Reynolds number in case of sharp corners.

Although this CFD investigation still needs to be completed, these first computational results and their comparisons with different sets of experimental data seem to warn both experimental and numerical analysts about the importance of "minor" details in the geometry of the models, such as the degree of sharpness of the edges.

Finally, a comment is in order concerning the two sets of aerodynamic force coefficients presented in Fig. 3.19. The curves are different and also the aerodynamic stall occurs at different angles of attack. Nevertheless, the lift and moment slopes are very close for a wide range of angles of attack. Since the slope of the aerodynamic coefficients is correlated to the aeroelastic behavior of the section according to the quasi-steady theory, as widely discussed in section 2.4.3, it could be deduced that, when the body motion governs the wake, details such as the corner sharpness become less critical than in the case of stationary cross sections. Obviously this conjecture needs further numerical and experimental validation in the future.

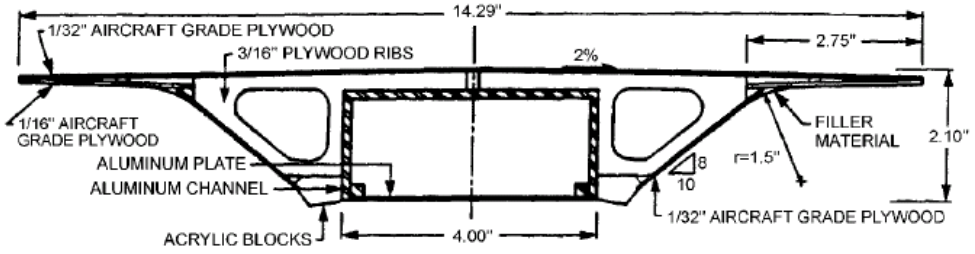

Figure 3.17: Sunshine Skyway Bridge section model (unit dimensions in inches) [From Davenport and King (1982)]

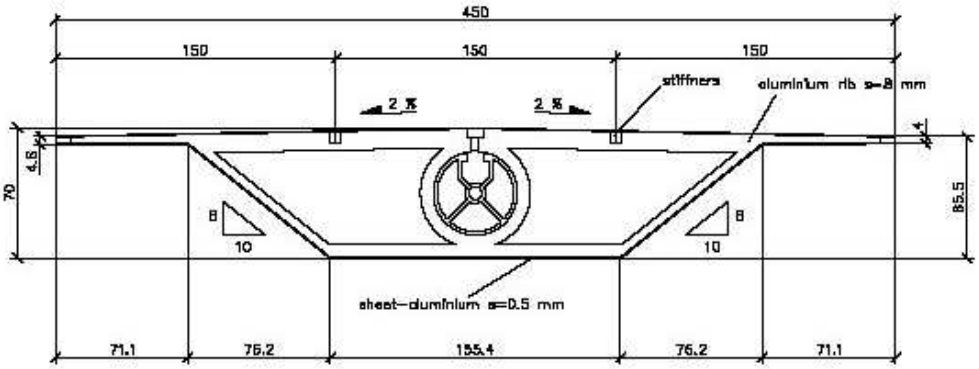

Figure 3.18: CRIACIV section model (unit dimensions in mm)

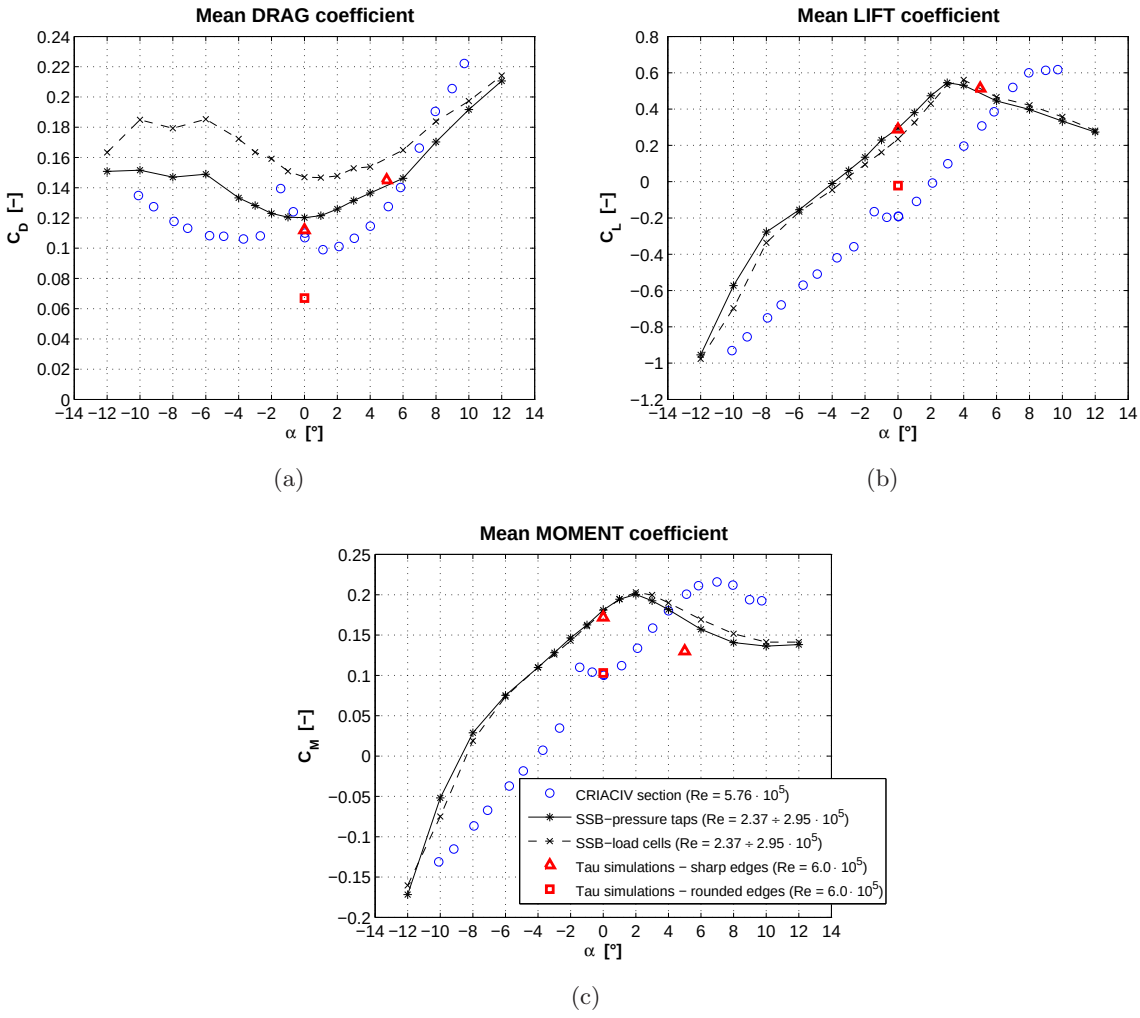

Figure 3.19: Experimental and numerical aerodynamic force coefficients for Sunshine Skyway Bridge (SSB) and CRIACIV section

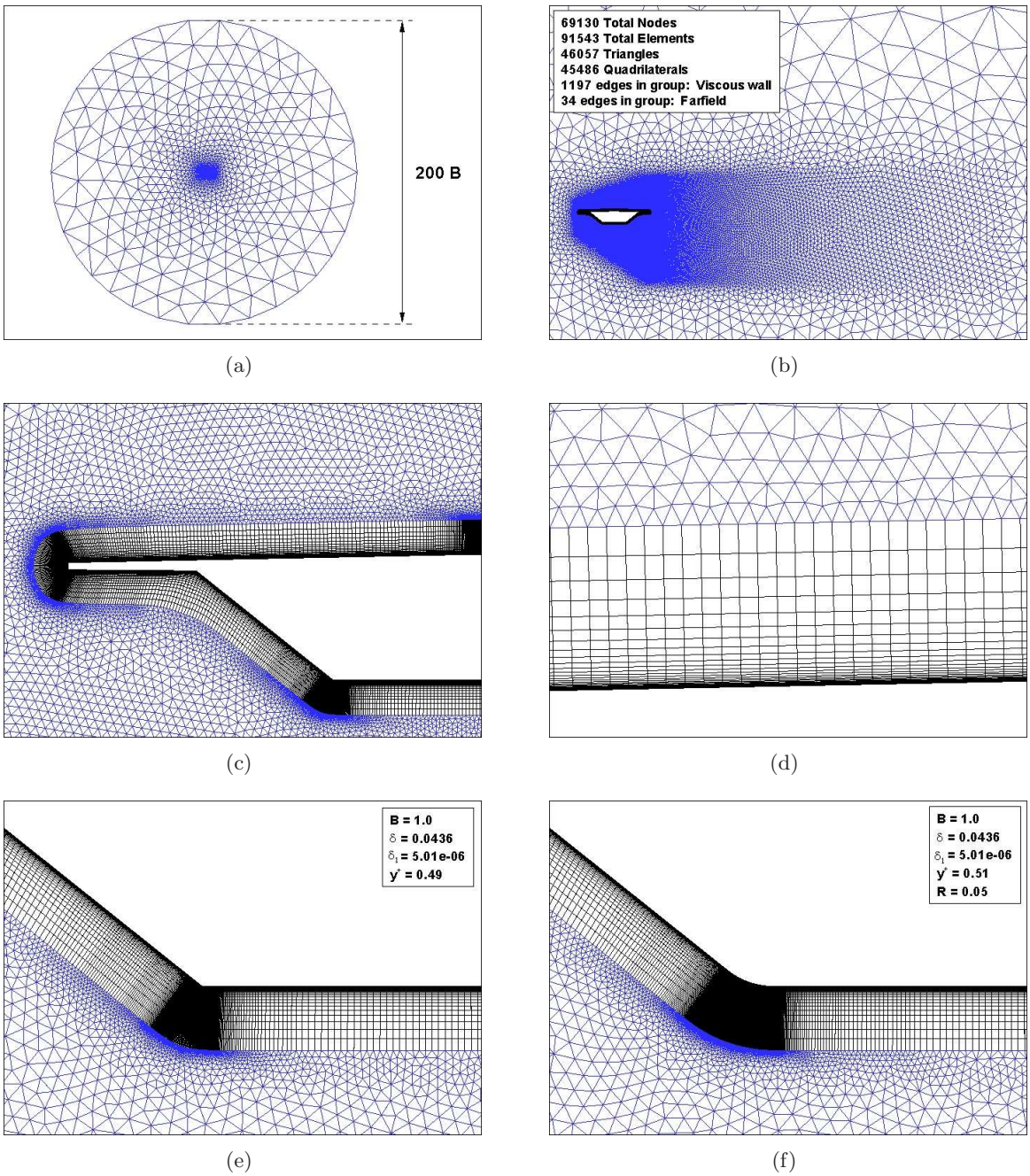

(a) (b)

(c) (d)

(e) (f)

Figure 3.20: Hybrid "Medium" mesh used in the CFD simulations: (a) computational domain; (b) refinement around the body and in the wake; (c) near body grid; (d) structured-unstructured grid transition; (e) detail of one of the lower edges in the configuration with sharp corners; (f) detail of one of the lower edges in the configuration with rounded corners. δ is the total height of the structured portion of the grid, δ_1 is the height of the first structured layer, R is the radius of curvature of the lower corners, y^+ is a computational variable correlated to δ_1

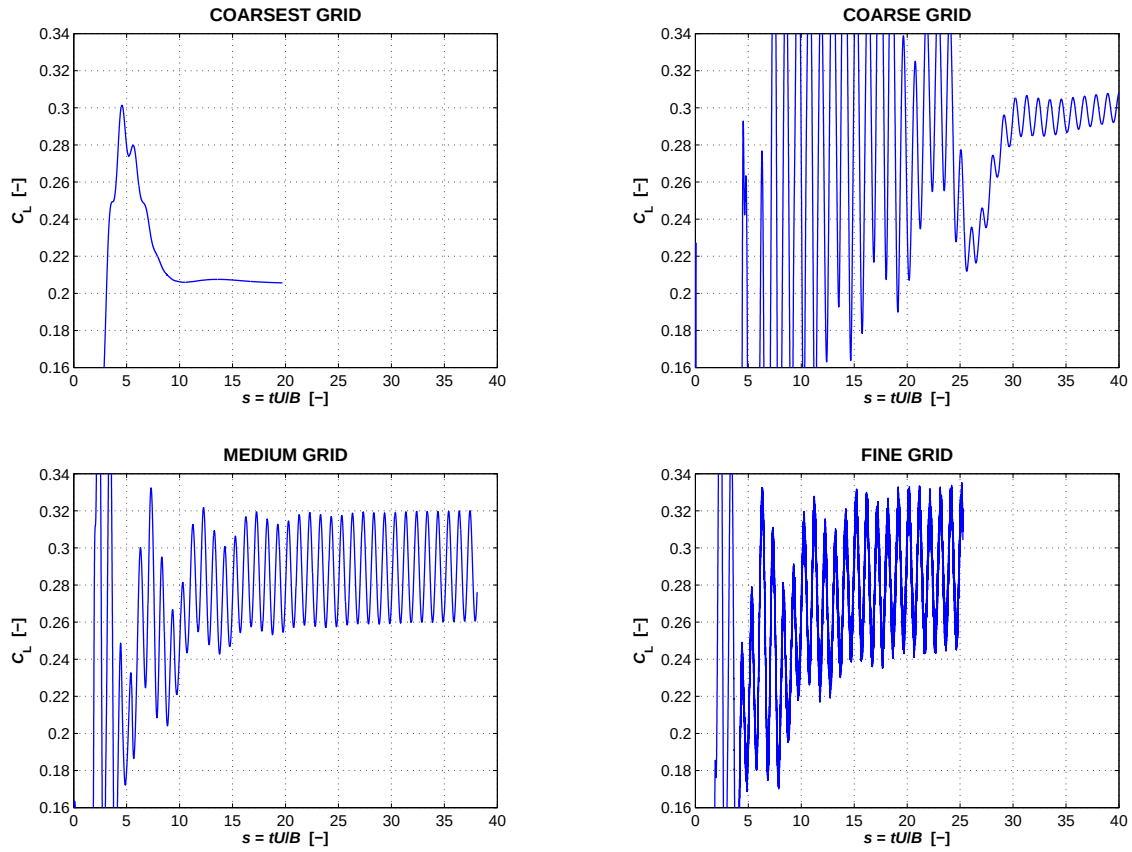

Figure 3.21: Grid-convergence study relative to the meshes described in Tab. 3.4

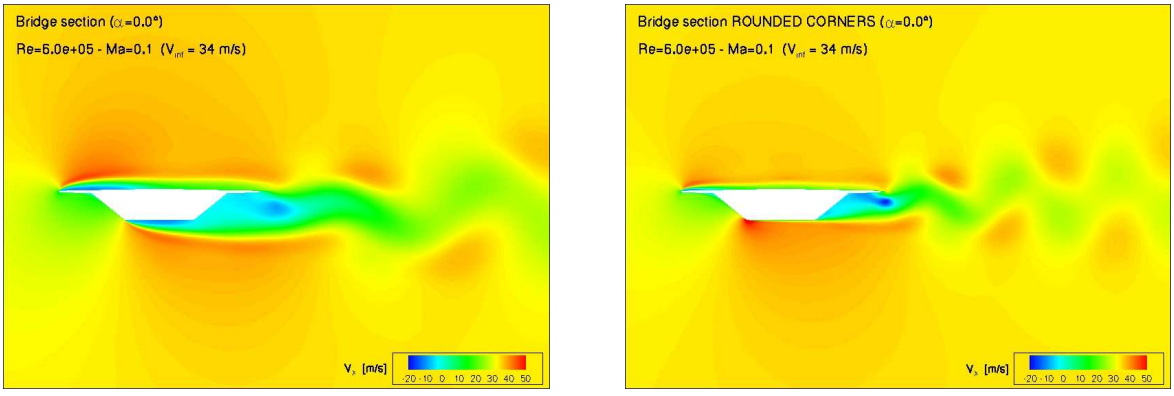

(a) (b)

Figure 3.22: Computed horizontal velocity flow field corresponding to the instant of maximum lift: (a) configuration with sharp edges; (b) configuration with rounded lower edges [$\alpha = 0°$, $Re = 6.0 \cdot 10^5$, $Ma = 0.1$ ($U_\infty = 34$ m/s)]

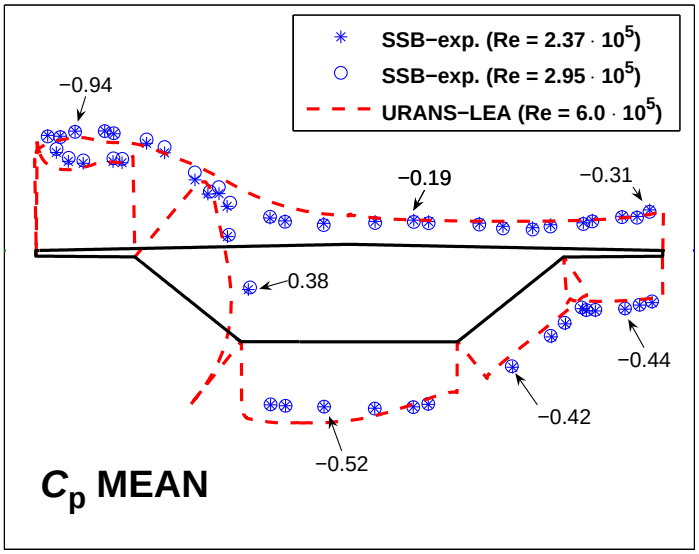

(a)

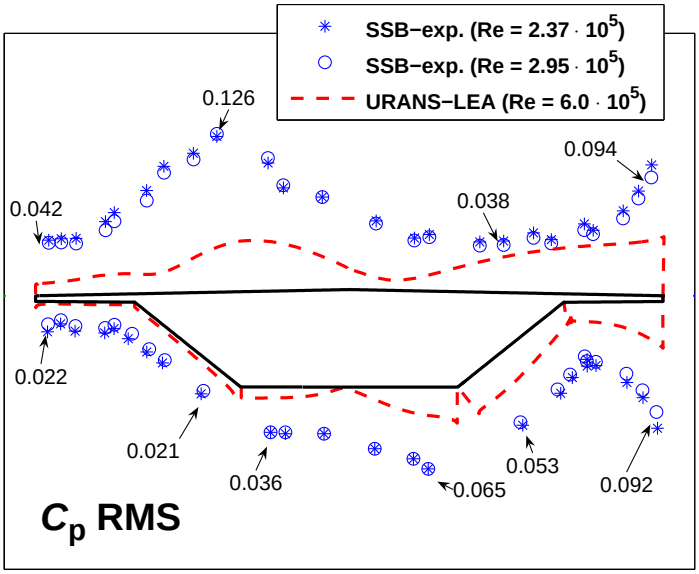

(b)

Figure 3.23: Pressure coefficient distribution over the bridge deck surface (configuration with perfect sharp edges): (a) mean values; (b) rms values. Experimental data from Ricciardelli and Hangan (2001)

Table 3.4: Main properties of the meshes used in the grid-convergence study. δ_1 represents the height of the first structured grid layer (relative to the chord B). $\Delta s = U\Delta t/B$ is the non-dimensional time step

Grid	Δs [-]	δ_1 [-]	Total nodes	Total cells	Surface points	Farfield points	Quadrilateral cells	Triangular cells
Coarsest	2.8e-03	5.02e-06	27654	34994	520	34	19760	15234
Coarse	2.8e-03	5.02e-06	42535	55162	766	34	29108	26054
Medium	2.8e-03	5.01e-06	69130	91543	1197	34	45486	46057
Fine	2.8e-03	1.00e-06	103476	133262	1674	34	71982	61280

Table 3.5: Grid-convergence study results ($\alpha = 0°$). y^+ is a computational variable correlated to δ_1

Grid	y^+ [-]	St [-]	C_L [-]	C_D [-]	C_M [-]	$C_{L\,RMS}$ [-]	$C_{D\,RMS}$ [-]	$C_{M\,RMS}$ [-]
Coarsest	0.36	-	0.206	0.107	0.164	-	-	-
Coarse	0.47	0.142	0.305	0.106	0.170	0.0047	0.0004	0.003
Medium	0.49	0.154	0.288	0.112	0.169	0.021	0.002	0.014
Fine	0.11	0.160	0.288	0.114	0.168	0.026	0.003	0.017

Table 3.6: Comparison between the Strouhal numbers measured for the CRIACIV and Sunshine Skyway Bridge section models (Ricciardelli and Hangan, 2001) and the numerically simulated values [Strouhal numbers are calculated according to Eq. (2.13)]

α [°]	Present work	Tau simulation (rounded lower edges)	Sunshine Skyway Bridge	Tau simulation (sharp edges)
0	~ 0.21	0.255	0.146	0.154
+5	~ 0.24		0.091	0.081

3.5 Aeroelastic tests

3.5.1 Experimental set-up

For the aeroelastic tests a set-up in which the section model is elastically suspended and both the heaving and pitching modes are allowed, is necessary. This is obtained by clamping the core-tube of the model to rigid suspension arms and then connecting eight springs to them. Each suspension arm consists of two aluminium plates connected together, in order to be as light as possible but very stiff with respect to the bending in the vertical plane. The connection between the springs and the suspension arms is realized with thin steel cables, in order to minimize the mechanical friction and allow the springs to work as regularly as possible. The springs are placed at a transversal distance of 500 mm and prestressed in order to behave always linearly. Those springs which are mounted above the section model (T42630) are stiffer than those mounted below it (T42150), since they have to bear also the weight of the model and the suspension arms. The main properties of the two sets of springs employed in the tests, produced by D.I.M. s.r.l., are reported in Tab. 3.7.

Table 3.7: Main properties of the springs used for the aeroelastic set-up (k = stiffness; L_0 = total length at rest; f_1 = maximum allowable displacement)

	Material	k [N/m]	L_0 [mm]	f_1 [mm]
T42630	stainless steel	800	102.0	139.0
T42150	stainless steel	380	87.7	137.0

Since only two degrees of freedom should be allowed, it is necessary to restrain the oscillation of the model in the along wind direction, as well as the rotation about a vertical axis. This is obtained by means of four long steel anti-drag cables which are connected to the model by means of two low-friction pillow blocks, in order not to interfere with the pitching degree of freedom [Fig. 3.24(d)]. Some pictures and a sketch of the set-up are reported in Figs. 3.24-3.25.

Finally, since the flutter derivatives are identified by measuring the heaving-pitching free-decay motion under wind, a system to impose a controlled and as regular as possible heaving-pitching initial condition is necessary. This consists of two magnets and two iron devices that are able to release two steel cables which are connected to the model suspension arms [Fig. 3.24(f)]. In order to limit as much as possible the rolling motion (rotation with respect to a horizontal axis perpendicular to the model longitudinal axis), it is important that the two magnets release the steel ropes at same time and that the initial vertical displacements are the same on both sides of the model.

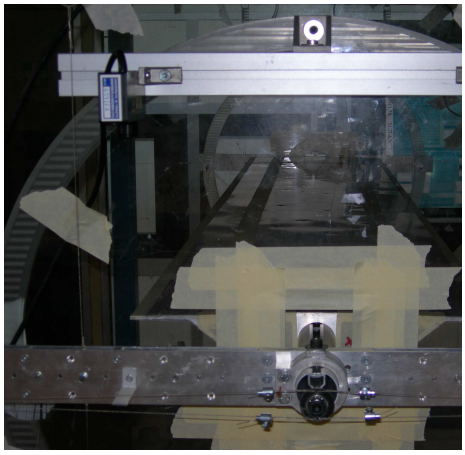

(a)

(b)

(c)

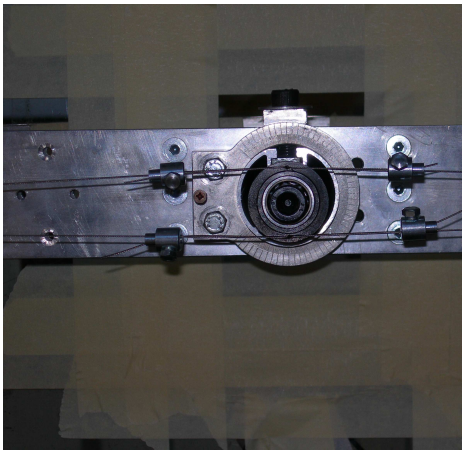

(d)

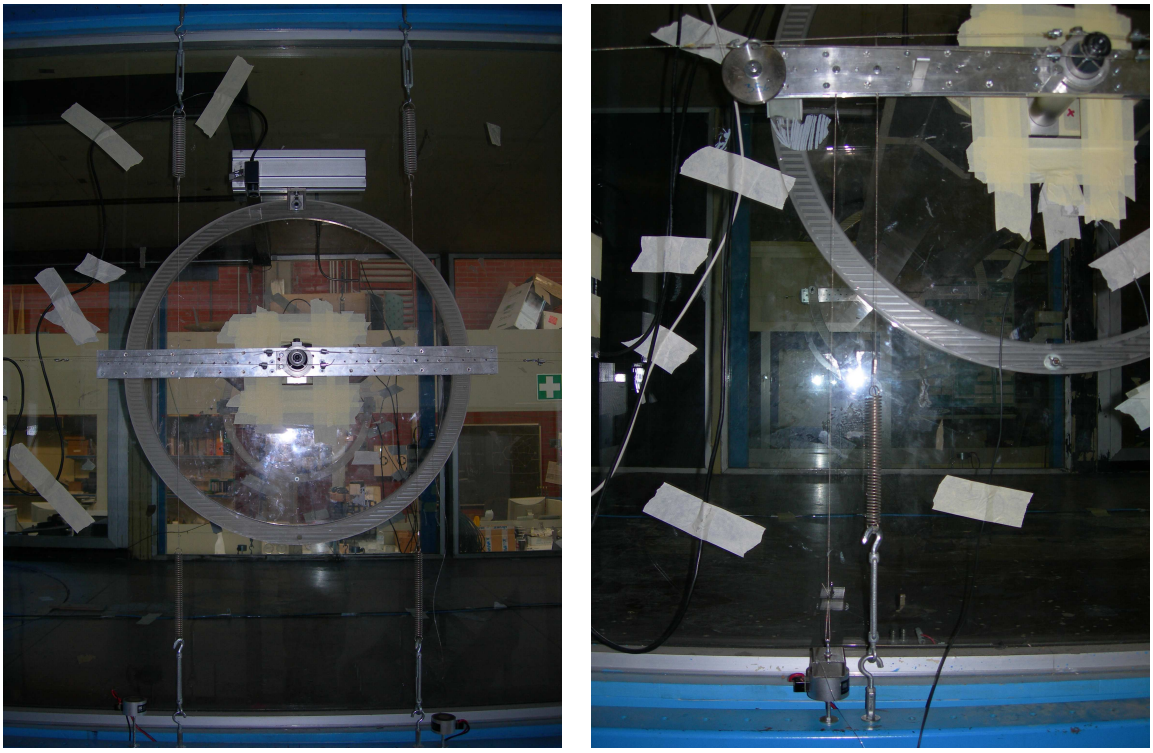

(e) (f)

Figure 3.24: Set-up for the aeroelastic measurements

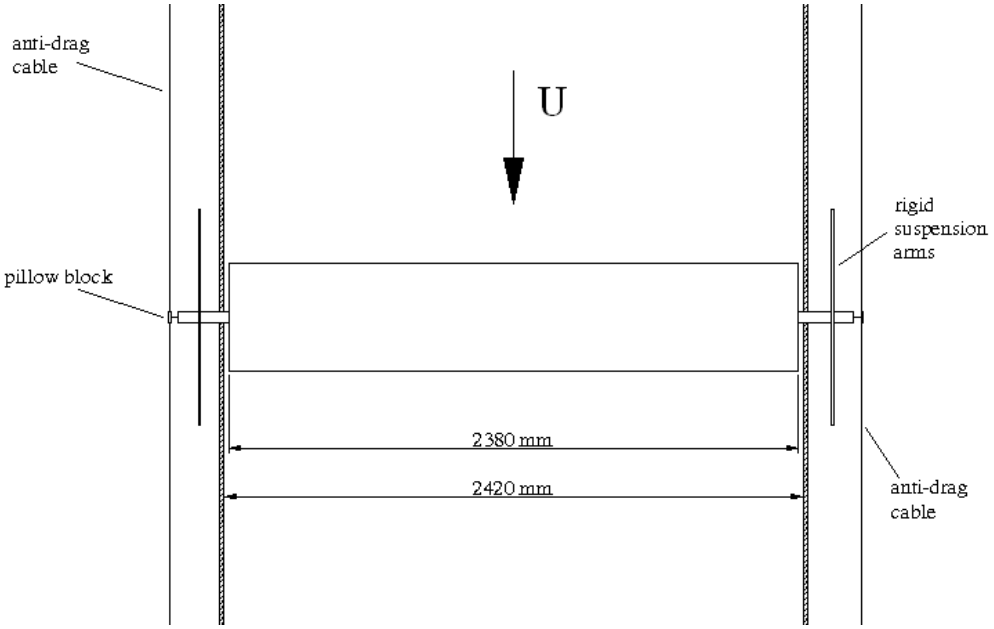

(a)

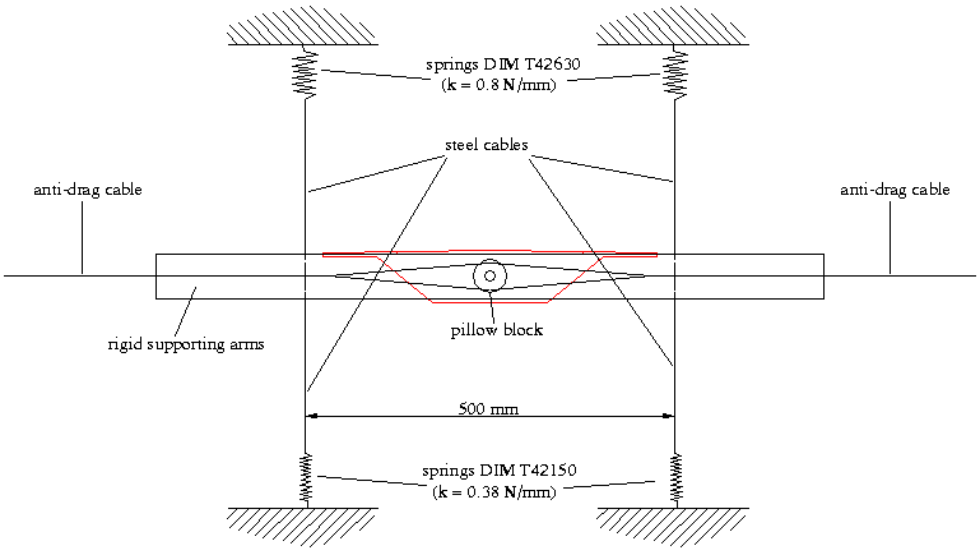

(b)

Figure 3.25: Sketch of the set-up for the aeroelastic measurements: (a) top view; (b) lateral view

3.5.2 Results

Still-air measurements

The first measurements are done in still air in order to obtain the exact static and dynamic parameters of the mechanical system. The static stiffness is measured by hanging to the model some known weights and measuring the consequent displacements. Fig. 3.26 shows the perfect linearity of the system. In Tab. 3.8 the resulting heaving and pitching stiffness under static conditions are compared with the theoretical values, showing that the eight springs have a stiffness very close to the one officially declared by the manufacturer, at least on average, and no additional stiffness seems to affect the system.

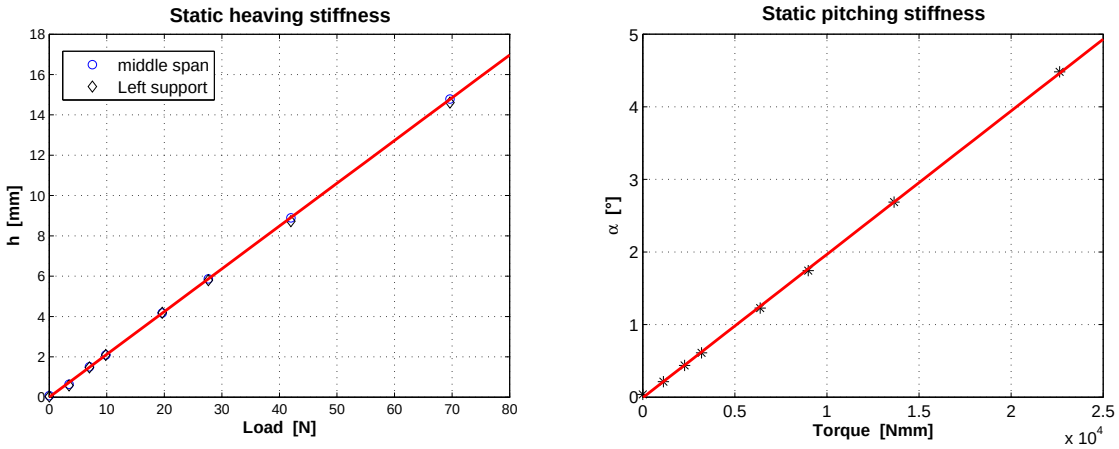

(a) (b)

Figure 3.26: Heaving (a) and pitching (b) static stiffness of the elastically suspended section model (frequency of acquisition: 500 Hz; signal length: 30 s)

Table 3.8: Comparison between measured and theoretical static stiffness

	Heave [N/m]	Pitch [Nm]
Measured	4714.4	290.07
Theoretical	4720.0	295.00

Afterwards, a combined heaving-pitching initial condition is imposed to the model and then released and the still-air free-decay motion is monitored in order to measure the eigenfrequencies and the modal damping. In Fig. 3.27 an example of free-decay heaving and pitching signals are shown with the corresponding power spectral density diagrams. In particular, in Fig. 3.27(a) it is clearly shown how the vibrations in the rolling mode (rotation about the wind-tunnel longitudinal axis, i.e. the midspan horizontal axis perpendicular to the longitudinal axis of the model) are small with respect to those in the heaving mode. This contribution,

due to small asymmetries in the system and in the initial condition, is not accounted for in the mathematical model [Eqs. (2.38)-(2.39)] we refer to and consequently should be kept as small as possible. It is worth noting that for this experimental set-up the frequency ratio between pitching and heaving modes is $\gamma_\omega = 1.95$.

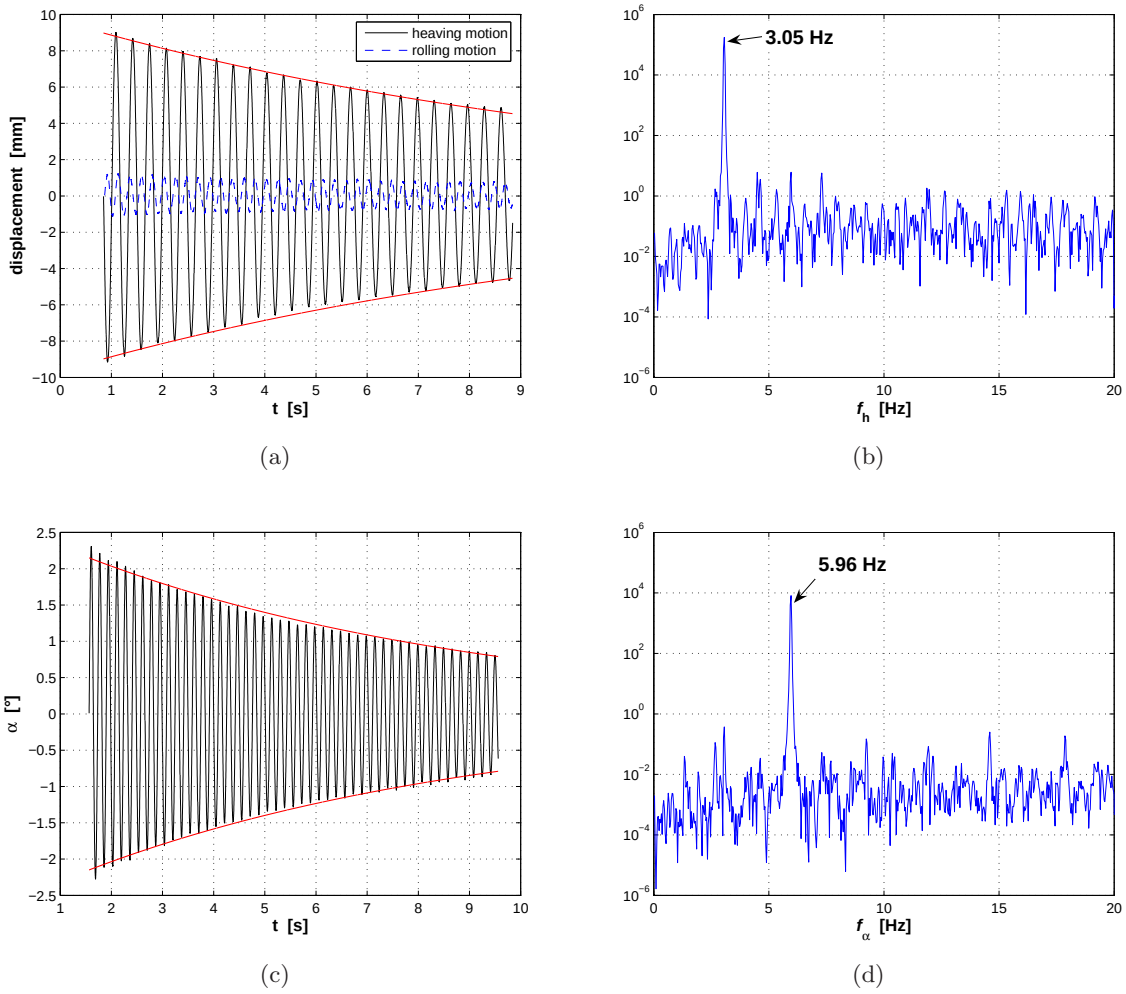

Figure 3.27: Still-air free-decay heaving and rolling signals (a) and heaving power spectral density (b); still-air free-decay pitching signal (c) and its power spectral density (d) (frequency of acquisition: 1000 Hz)

A first problem we have to deal with is the non-viscous damping contribution of the air resistance. As a matter of fact, increasing the length of the signal the least-square estimated value of the damping tends to decrease and the harmonic oscillations no longer show an exponential decay (Fig. 3.28 and Tab. 3.9). Therefore the damping is not linear, depending on the oscillation amplitude. Conversely, if the section model is turned of 90°, drastically reducing the air resistance, this non-linearity becomes absolutely negligible. The time-domain

Table 3.9: Damping ratios in the heaving (ζ_h) and pitching (ζ_α) modes as a function of the considered length of the signal

Signal length [s]	ζ_h [%]	ζ_α [%]
5	0.47	0.37
8	0.42	0.33
10	0.40	0.31
15	0.35	0.27
30	0.26	0.19
58	0.17	0.13

identification procedure we use to estimate the flutter derivatives is the Unified Least-Square (ULS) method (Gu *et al.*, 2000) in the modified version proposed in Righi (2003), which is based on a linear model. Consequently, the effect of non-viscous damping, which cannot be avoided in the experiments, represents a source of uncertainty in the flutter derivative identification. Nevertheless, being the "structural" damping (perhaps it would be better to say "still-air damping") very small with respect to the aerodynamic damping (Tab. 3.9), minor errors are expected. This is confirmed by the fact that the measured flutter derivatives do not depend, within certain limits, on the initial condition amplitude and that no appreciable difference in their values is observed when the considered length of the signals is sensibly varied, as it is shown later in this section.

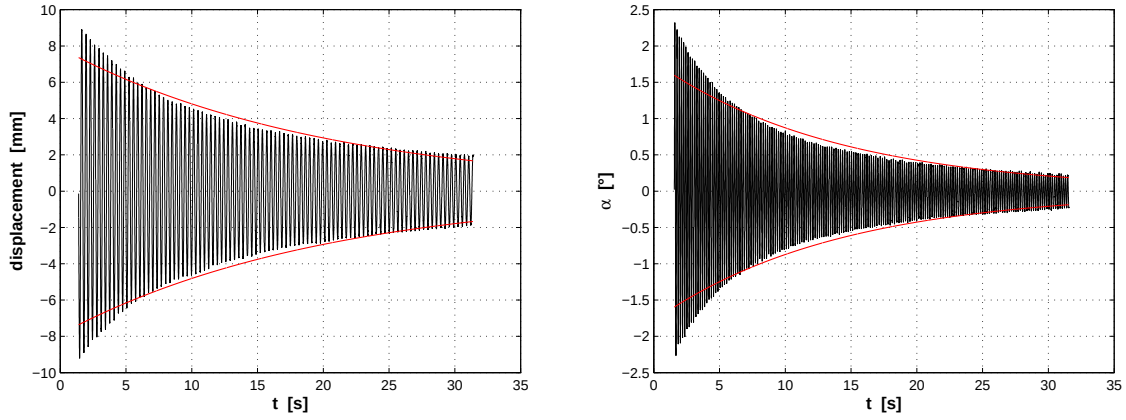

(a) (b)

Figure 3.28: Still-air free-decay heaving (a) and pitching (b) motions with the corresponding viscous damping envelope when a 30-seconds signal is taken into account

The last still-air measurement is finalized to estimate the mass and mass moment of inertia of the mechanical system. As a matter of fact it is necessary to add to the contribution of the model and the suspension arms also that of the whole suspension system and in particular of the

Table 3.10: Comparison between static and dynamic measured stiffness and theoretical stiffness

	Heaving [N/m]	Pitching [Nm]
Dynamic	4811.0	310.51
Static	4714.4	290.07
Theoretical	4720.0	295.00

eight springs which take part in the motion, although they do not rigidly move with the model. Their contribution consists of a portion of their mass which is usually quite small as compared to the total mass but often non-negligible with respect to the total mass moment of inertia. In addition, it is possible that the dynamic stiffness of the springs does not exactly coincide with their static stiffness (Tab. 3.10). In order to obtain this total mass and inertia a series of known masses are added and the corresponding frequencies of the system are measured. If we call ω_{h0} the heaving circular frequency when no additional masses are present and ω_{h1} the circular frequency when the mass Δm_1 is added to the actual system mass m, it is possible to write:

$$\frac{1}{\omega_{h1}^2} = \frac{1}{\omega_{h0}^2} + \frac{1}{m\omega_{h0}^2}\Delta m_1 \tag{3.7}$$

Analogous equation can be written for the pitching mode:

$$\frac{1}{\omega_{\alpha 1}^2} = \frac{1}{\omega_{\alpha 0}^2} + \frac{1}{I\omega_{\alpha 0}^2}\Delta I_1 \tag{3.8}$$

m and I can be estimated with the least square method, as shown in Fig. 3.29.

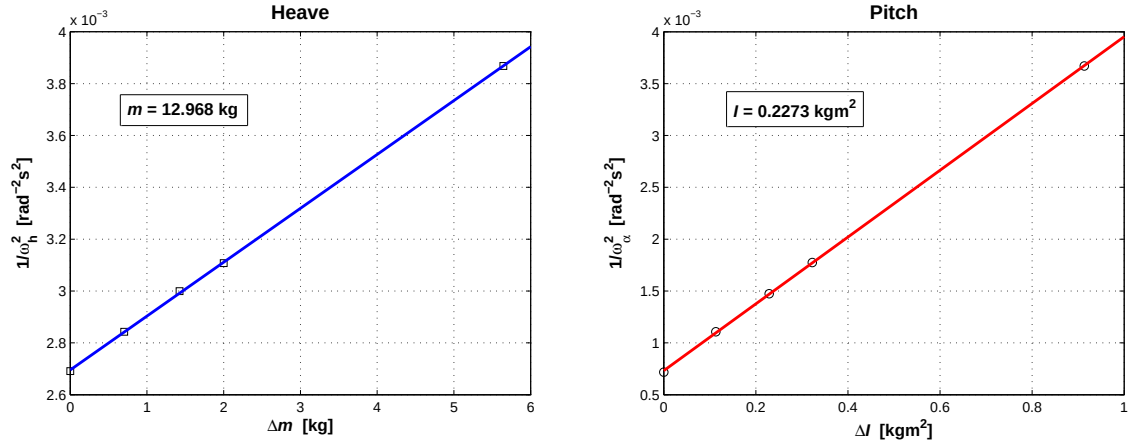

(a) (b)

Figure 3.29: (a) Mass and (b) mass moment of inertia measurements

Table 3.11: Summary of the mechanical parameters of the aeroelastic system

B [m]	0.45	model chord
D [m]	0.07	model thickness
l [m]	2.38	model span
B/D [-]	6.43	chord-to-thickness ratio
l/B [-]	5.29	span-to-chord ratio
l/D [-]	34.0	span-to-thickness ratio
St [-]	$\sim$ 0.20 - 0.25	Strouhal number
K_h [N/m]	4714.4	static heaving stiffness
K_α [Nm]	290.07	static pitching stiffness
m [kg]	12.968	mass of the dynamic system
I [kgm^2]	0.2273	mass moment of inertia of the dynamic system
f_h [Hz]	3.05	heaving eigenfrequency
f_α [Hz]	5.96	pitching eigenfrequency
γ_ω [-]	1.954	frequency ratio
ζ_h [%]	0.42	heaving modal damping ($t = 8$ s)
ζ_α [%]	0.33	pitching modal damping ($t = 8$ s)

Ambient vibrations

After the still-air measurements the behavior of the section model let free to vibrate under wind is studied. In particular, mean displacements and rms-values of the vibrations are monitored with increasing wind speed until the flutter instability onset. Three different configurations, with $\alpha_0 = 0°$, -1.7° and -3.7°, where α_0 is the angle of attack of the model when the wind tunnel is switched off (i.e. in still air), are tested. The results for the case $\alpha_0 = 0°$ are reported in Fig. 3.30 according to the reference system of Fig. 3.34.

It is worth noting that in Figs. 3.30(b) and 3.30(d) the graphs do not show any peak suggesting vortex-shedding lock-in. In view of the Strouhal number around 0.20 - 0.25, $D = 0.07$ m and the system eigenfrequencies $f_h = 3.05$ Hz and $f_\alpha = 5.96$ Hz, lock-in is expected around 1 m/s in the heaving mode and 2 m/s in the pitching mode. Probably for such low wind speeds the energy involved is not enough to observe significant amplitudes of oscillation.

Now an important point needs to be discussed. Increasing the wind speed, the mean angle of attack progressively changes [in Fig. 3.30(c) it increases from 0° to +3.35°]. This means that the aerodynamics changes both because of the increasing flow speed and angle of attack. This problem affects all the non symmetric cross sections (with respect to the horizontal plane), as bridge deck profiles usually are. The mean pitching angle of the model at a given wind speed depends not only on the moment coefficient but also on the torsional stiffness of the elastic suspension system. As a result, the measured flutter derivatives are not unique for that geometry but depend on the particular set-up too. In order to overcome this problem different initial angles of attack α_0 are tested, so that the flutter derivatives can be expressed as functions of the reduced wind speed and the current angle of attack. Finally, this procedure allows to reconstruct by interpolation the aeroelastic functions in the range of interest of angles

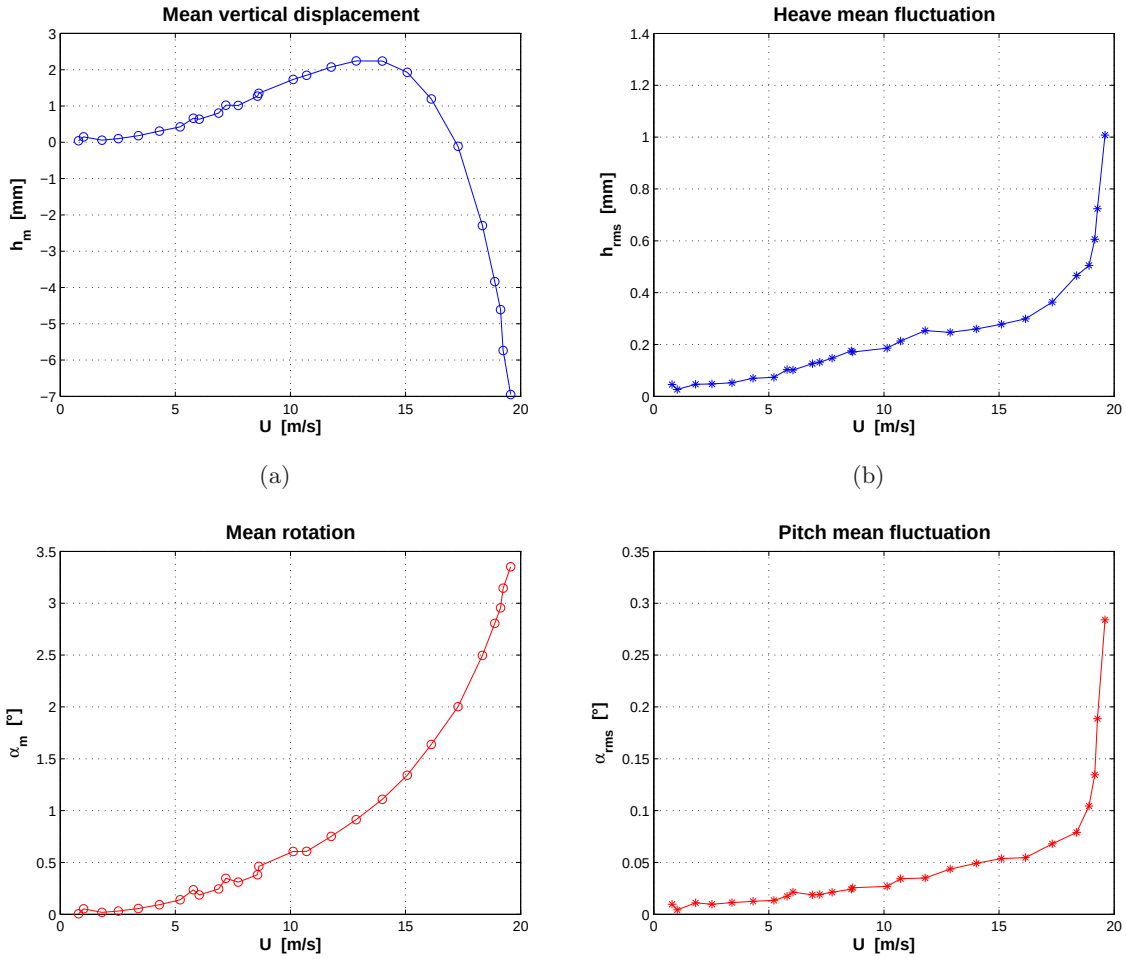

(a) (b)

(c) (d)

Figure 3.30: Mean and rms-value of the heaving and pitching displacements of the model under ambient vibrations ($\alpha_0 = 0°$; signal length: 60 s; frequency of acquisition: 1000 Hz)

of attack and reduced wind speeds. Also the initial condition changes with the wind speed as a consequence of the mean pitching angle and mean vertical displacement. However the results, within certain limits, seem to be insensitive to the amplitude of the initial condition, as it will be shown later on.

In order to check the aerodynamic force coefficients measured via static tests, the same coefficients can be calculated on the basis of the mean displacements obtained with the aeroelastic set-up [Figs. 3.30(a)-3.30(c)]:

$$C_L = -\frac{K_h \cdot h_m}{qBl} \tag{3.9}$$

$$C_M = \frac{K_\alpha \cdot \alpha_m}{qB^2 l} \tag{3.10}$$

where K_h and K_α are the section-model static stiffness in heave and pitch (Tab. 3.10), h_m and α_m the mean vertical displacement and pitching rotation, q the kinetic pressure, B and l respectively the chord and length of the model. The minus in Eq. 3.9 is due to the different reference system for lift in case of static and aeroelastic tests (see Figs. 3.9-3.34). In Fig. 3.31 the lift and moment coefficients obtained in these two different ways are compared. A perfect superposition cannot be expected given the non-negligible Reynolds number effects shown in Fig. 3.10 and in the Appendix. Nevertheless, except few values affected by some measurement errors at low wind speed [the points corresponding to small irregularities in the curves of Figs. 3.30(a)-3.30(c)], the three sets of results are in good agreement and the small distance between them seems to follow the previously discussed Reynolds number effects. This result confirms the validity of the measures of the aerodynamic force coefficients reported in Fig. 3.14, in particular concerning the irregular behavior observed for small negative angles of attack.

Particular attention must be paid to the configuration with $\alpha_0 = -3.72°$ since the system becomes unstable when the mean angle of attack is in the "critical" range between -2.5° and 0°. In this case the instability arises much earlier than expected and two equilibrium states are reached: the first one characterized by large positive (downward) mean vertical displacement and large negative (nose-down) mean angle of attack, which is stable; the second one with smaller positive mean vertical displacement and smaller negative mean angle of attack, which is unstable. As shown in Fig. 3.32, the model continuously switches between these two states so that the oscillations do not diverge for a wide range of wind speeds. Also the heaving frequency continuously changes, coupling to the pitching frequency when the model undergoes diverging oscillations. It is quite difficult to determine precisely the mean displacements (and consequently the mean aerodynamic coefficient values) corresponding to the two different states but it seems that, when the model is unstable, the mean angle of attack is around -2° and the mean aerodynamic coefficients assume a value which belongs to the previously discussed irregular branch. Conversely, when the model is in the stable state, the mean angle of attack is around -3° and the corresponding mean aerodynamic coefficients fall at the end of the regular straight branch or in the steep transition zone of the curves.

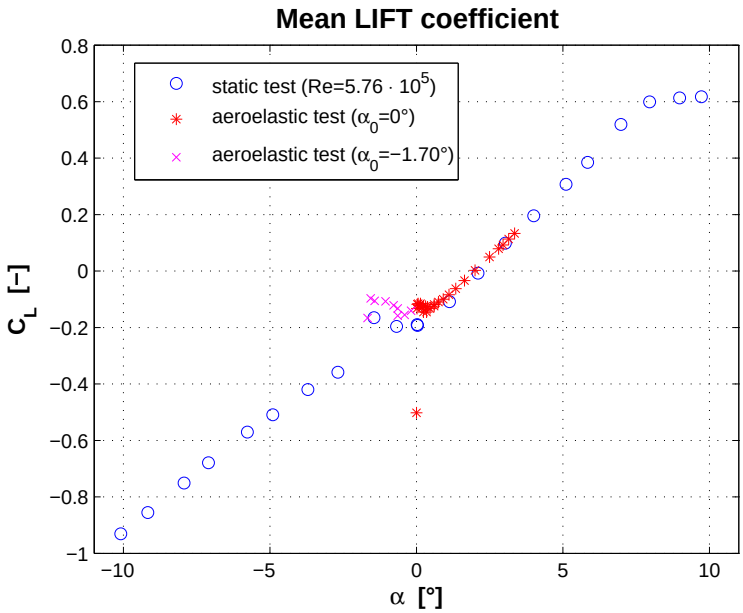

(a)

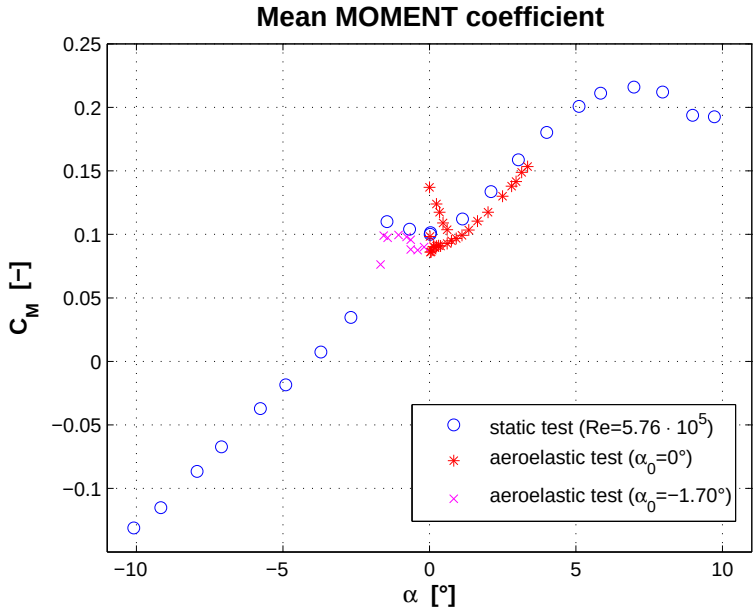

(b)

Figure 3.31: Comparison between lift and moment coefficients measured via static and aeroelastic tests

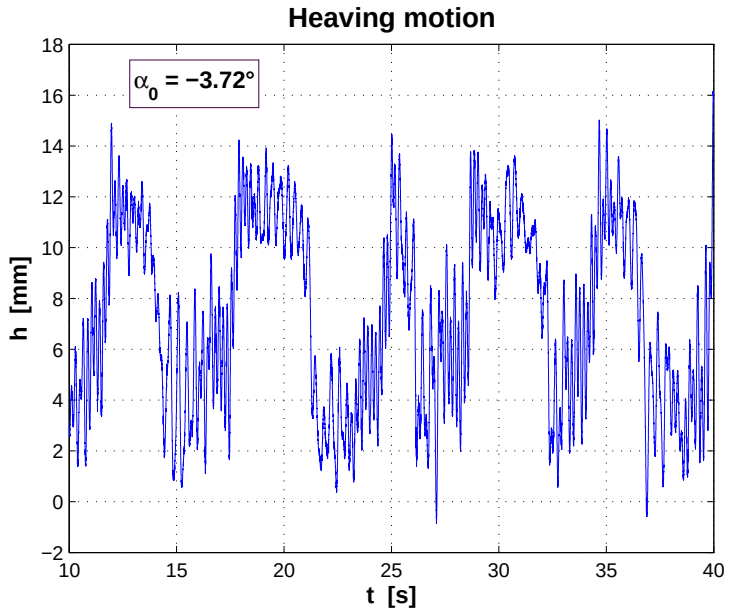

(a)

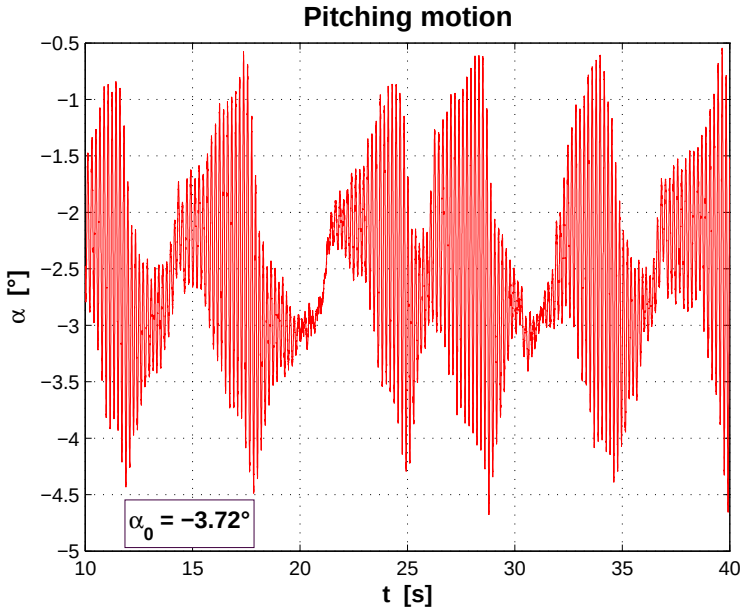

(b)

Figure 3.32: Particular behavior at high wind speed ($U = 17.19$ m/s) of the section model for the configuration with still-air angle of attack $\alpha_0 = -3.72^\circ$

Flutter derivatives

Flutter derivatives are identified in the time domain measuring the mechanical parameters of the in-wind free-decay heaving and pitching signals and comparing them to the still-air values. The adopted procedure is called Unifying Least-Square (ULS) proposed by Gu *et al.* (2000), according to the modified algorithm explained in Righi (2003). This method is based on complex modal analysis and it is therefore linear. It allows to identify at the same time all the eight flutter derivatives. Consequently a combined heaving-pitching initial condition has to be imposed. The capability of the model standing behind this method to reproduce the measured signals is shown in Fig. 3.33, where for different wind speeds the wind-tunnel signals and those reconstructed with the identified parameters are compared. It is evident that the ULS method is able to well capture the main features of the section-model motion, apart from some irregularities probably due to oncoming turbulence [e.g. Fig. 3.33(g)-3.33(h)]. The possibility to correctly simulate the signals measured in the wind tunnel with a linear model also suggests the independence of the flutter derivatives of the amplitude of the oscillations. As a matter of fact, if the aerodynamic damping was a function of the amplitude of vibration, such a good reconstruction of the signals would not be possible.

In order to better investigate this point, the flutter derivatives are measured for the configuration corresponding to initial (still-air) angle of attack $\alpha_0 = 0°$, applying three different initial conditions (Tab. 3.12). As it can be noted in Fig. 3.35, with the "very small initial condition" the flutter derivatives can be identified only at high reduced wind speeds because for low wind speed the initial condition is so small that it cannot be properly released. At each wind speed the measurement is repeated five times in order to have an idea of the statistical dispersion of the measures. Results for the eight flutter derivatives are presented in Fig. 3.35. It seems that the amplitude of the free-decaying motion does not affect the flutter derivative pattern suggested by the "clouds" of the experimental results, obviously within the limits of small displacements. Nevertheless, with the "large" initial condition the scatter of the identified values is the smallest, probably due to the better definition of the motion. Conversely, it is not easy to explain why the larger dispersion seems to occur with the "small" instead of the "very small" initial condition. This result confirms the linearity of the self-excited forces with respect to the amplitude of vibration (i.e. independence of the flutter derivatives of the initial condition amplitude) and at this regard, at least for this cross-section geometry, the validity of the Scanlan's model [Eqs. (2.38)-(2.39)]. In the following, initial conditions close to the so-called "large" one are chosen. The dispersion of the flutter derivatives increases with the wind speed and becomes particularly significant near the flutter instability. A possible explanation for this last point is that when the total damping approaches zero even small disturbances, such as for instance the low turbulence characterizing the flow in the wind tunnel, can affect the decaying motion of the model very much. Conversely, the identification method does not seem to be significantly responsible for this statistical dispersion, given the good performance shown in Fig. 3.33.

Before continuing in the description of the experimental results, it is worth pointing out that the reference system for self-excited forces and displacements is the one sketched in Fig. 3.34, Scanlan's definition of flutter derivatives is adopted [Eqs. (2.38)-(2.39)] and the reduced wind

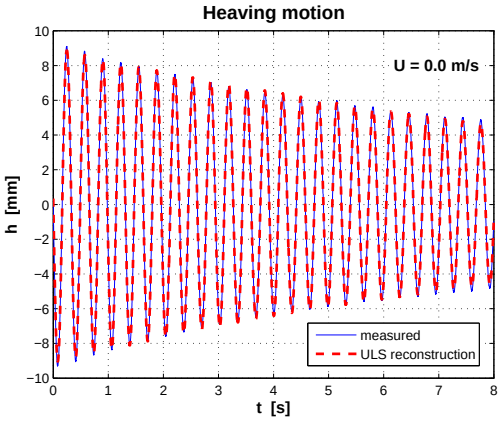
Heaving motion
U = 0.0 m/s
h [mm]
t [s]
measured
ULS reconstruction

(a)

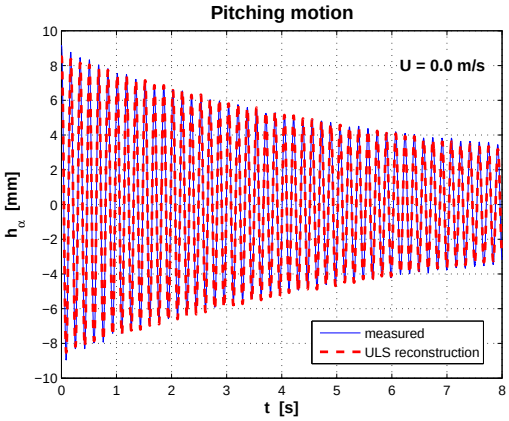
Pitching motion
U = 0.0 m/s
h_α [mm]
t [s]
measured
ULS reconstruction

(b)

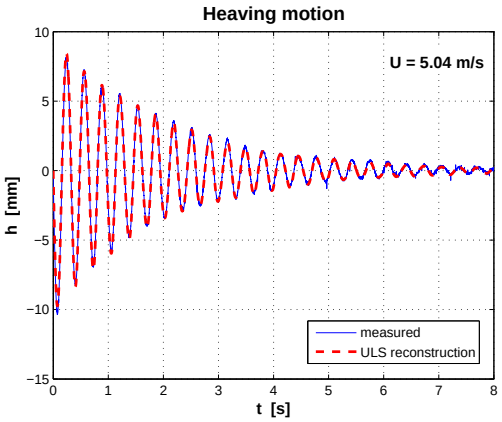
Heaving motion
U = 5.04 m/s
h [mm]
t [s]
measured
ULS reconstruction

(c)

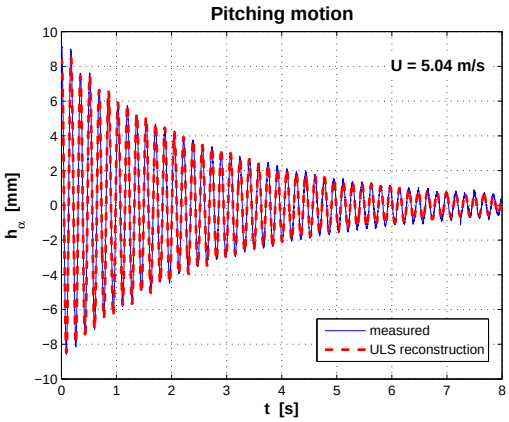
Pitching motion
U = 5.04 m/s
h_α [mm]
t [s]
measured
ULS reconstruction

(d)

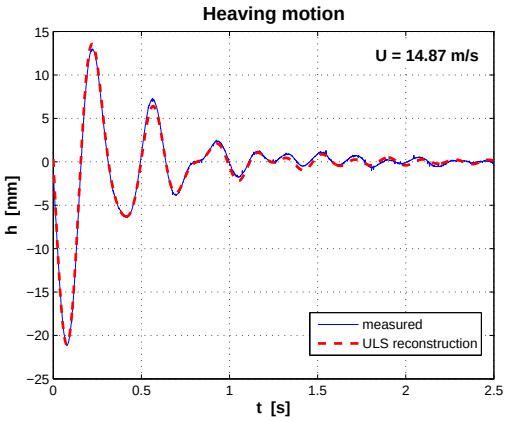
Heaving motion
U = 14.87 m/s
h [mm]
t [s]
measured
ULS reconstruction

(e)

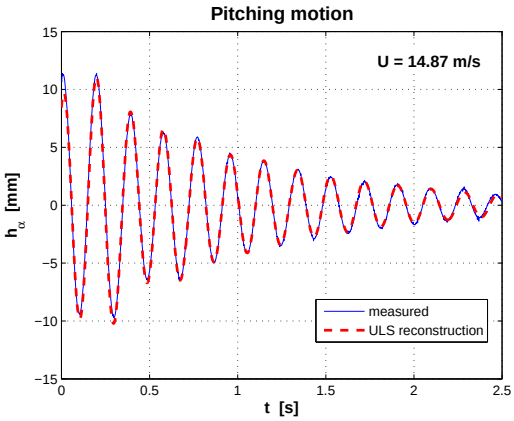
Pitching motion
U = 14.87 m/s
h_α [mm]
t [s]
measured
ULS reconstruction

(f)

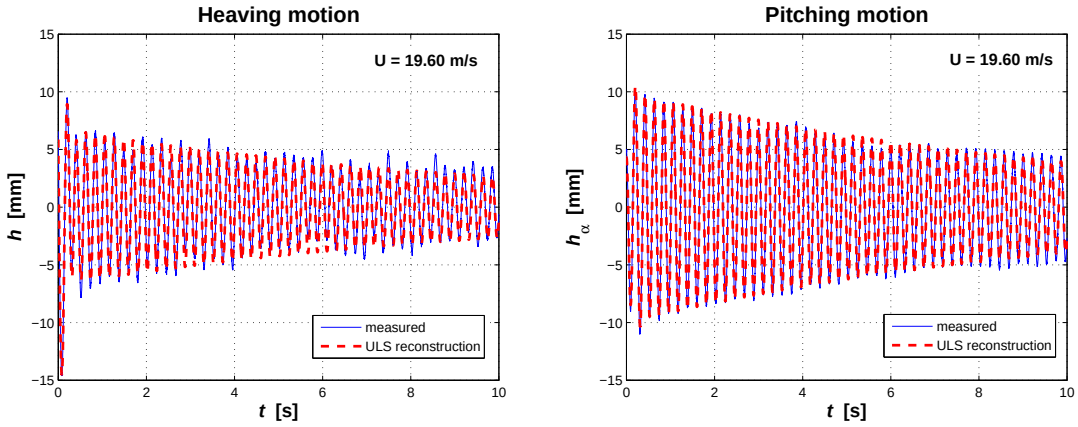

(g) (h)

Figure 3.33: ULS reconstruction of the measured heaving and pitching signals at different wind speeds (frequency of acquisition: 1000 Hz). The pitching signal is expressed as $h_\alpha = B/2 \cdot \alpha$. Signals in (g) and (h) correspond to a wind speed immediately before flutter.

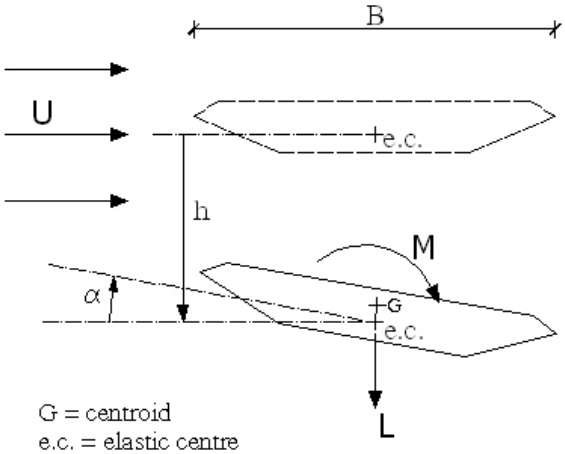

Figure 3.34: Scanlan's reference system for bridge self-excited forces

Table 3.12: Still-air initial conditions for the identification of the flutter derivatives

	$h_{i.c.}$ [mm]	$\alpha_{i.c.}$ [°]
"Large"	+9.6	-2.5
"Small"	+5.5	-1.4
"Very small"	+2.2	-0.6

speed is defined with the in-wind eigenfrequencies f_{hw} and $f_{\alpha w}$ according to Eqs. (3.11)-(3.12):

$$U_R = \frac{U}{f_{hw}B} \qquad (heave) \tag{3.11}$$

$$U_R = \frac{U}{f_{\alpha w}B} \qquad (pitch) \tag{3.12}$$

This last issue is further discussed later in this section.

After the first tests reported in Fig. 3.35 the experimental set-up is dismounted and remounted a few days later using new springs of the same type. The test is repeated this time with ten measures for each wind speed. As an example of the repeatability of the measurements four flutter derivatives are reported in Fig. 3.36, while in the Appendix the complete set of functions is shown. Practically identical results are obtained with the exception of a difference in the values of H_1^* and A_2^* immediately before flutter. It seems that near the critical condition ($13 < U_{Rh} < 14$ for H_1^* and $8 < U_{R\alpha} < 9.5$ for A_2^*) with the second set-up the aerodynamic damping in the heaving mode and even more in the pitching is slightly lower. This discrepancy could be due to a small difference in the still-air angle of attack α_0, since one of the defects of this set-up is the difficulty to suspend the section model in perfectly horizontal position. On the whole, the measures can be said repeatable but attention must be paid if the data are extrapolated for reduced wind speeds beyond the measurement range.

It is also important to check the sensitivity of the flutter derivatives to the length of the transient signals considered for the identification with the ULS-method. Therefore, the identification is first performed isolating the transient signal in the most reasonable way and then doubling this length. Results are reported in Fig. 3.37. It can be claimed that the identified values are insensitive to this choice (within reasonable limits). Only near flutter the results do not perfectly coincide but seem to be characterized by the same mean value. The scatter of the data immediately before flutter seems to be slightly larger if longer signals are processed.

The analysis of the results reported in Fig. 3.37 (but also in Fig. 3.35 and Fig. 3.36) needs some comments. First, it is evident that the flutter derivatives H_4^* and A_4^* are the most scattered functions. Nevertheless, their contribution to buffeting and flutter prediction is known to be marginal and indeed they were not present in the first Scanlan's formulation of flutter derivatives (Scanlan and Tomko, 1971). Conversely, the coefficients related to the rotation α (H_3^* and A_3^*) are easy to be identified, with small dispersion even near flutter. In addition, their patterns are close to those resulting from the Theodorsen's theory for thin airfoils. H_1^*, A_1^* and A_2^* present a well-defined pattern with large dispersion only near the instability onset. Their values are also fairly close to the Theodorsen's curves (especially A_1^*).

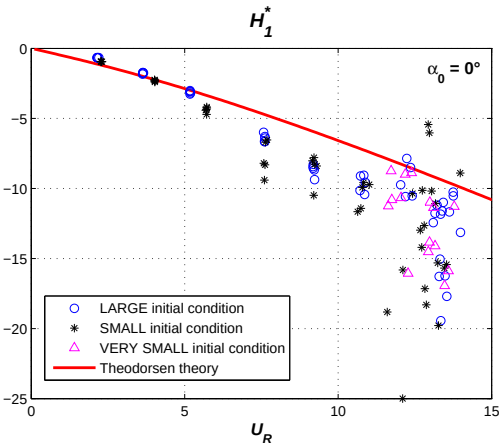
H_1^*
α_0 = 0°
LARGE initial condition
SMALL initial condition
VERY SMALL initial condition
Theodorsen theory
U_R

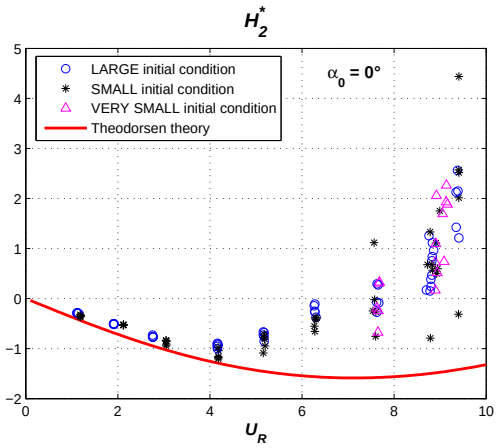
H_2^*
α_0 = 0°
LARGE initial condition
SMALL initial condition
VERY SMALL initial condition
Theodorsen theory
U_R

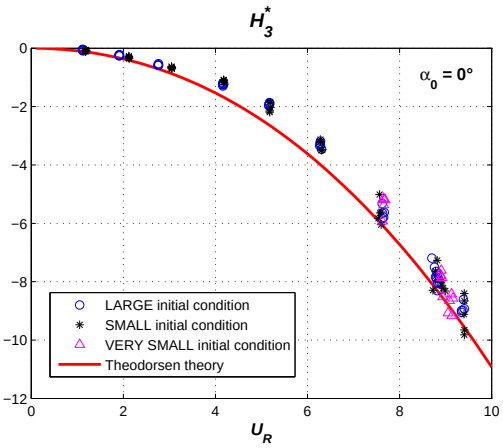
H_3^*
α_0 = 0°
LARGE initial condition
SMALL initial condition
VERY SMALL initial condition
Theodorsen theory
U_R

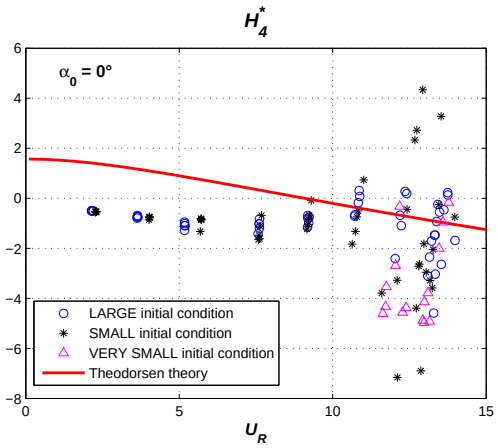
H_4^*
α_0 = 0°
LARGE initial condition
SMALL initial condition
VERY SMALL initial condition
Theodorsen theory
U_R

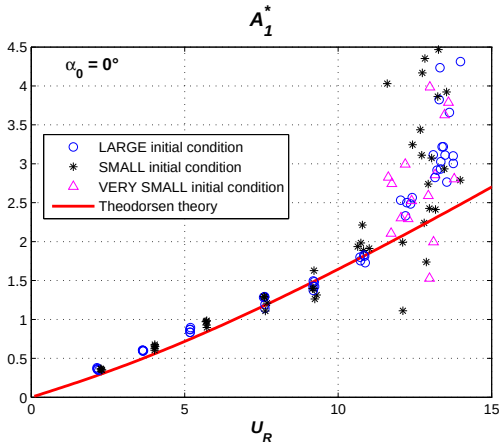
A_1^*
α_0 = 0°
LARGE initial condition
SMALL initial condition
VERY SMALL initial condition
Theodorsen theory
U_R

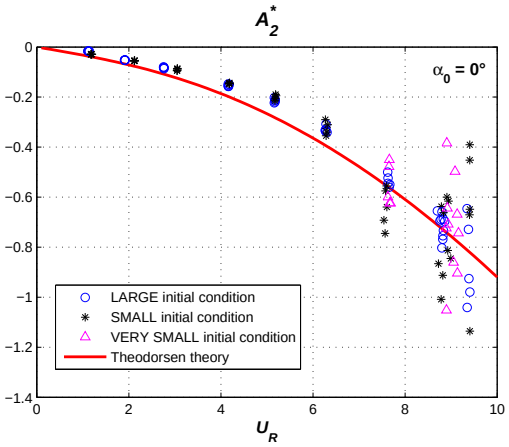
A_2^*
α_0 = 0°
LARGE initial condition
SMALL initial condition
VERY SMALL initial condition
Theodorsen theory
U_R

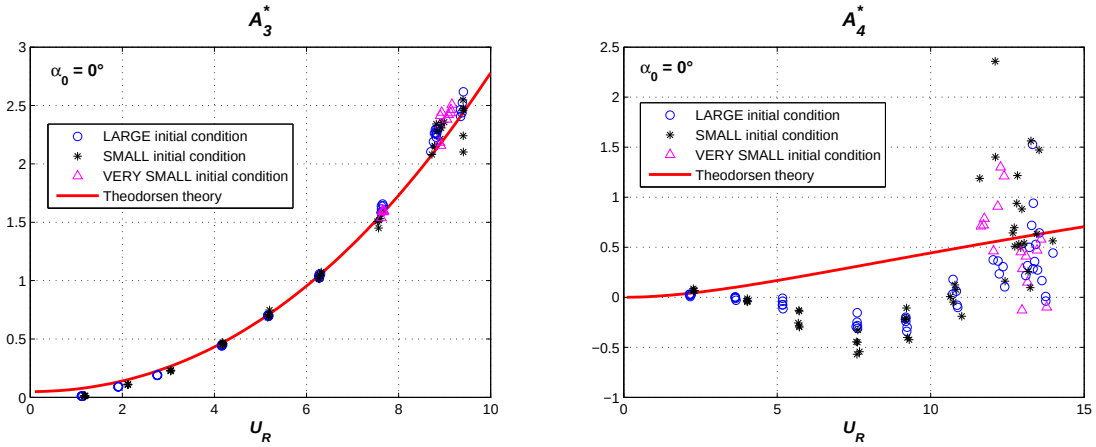

Figure 3.35: Flutter derivatives for three different initial conditions. In still air the section model is horizontal ($\alpha_0 = 0°$)

Finally, the pattern of H_2^* is well defined but very different from the theoretical one.

Fig. 3.38 shows the evolution of the eigenfrequencies and modal damping (structural+aerodynamic) with the wind speed. Due to the symmetries of the mechanical system, in still air the heaving and pitching motions are decoupled and coincide with the eigenmodes of the system (Mode #1 and Mode #2 in Figs. 3.38 and 3.39, which for this reason can be denoted respectively as "heaving-branch" and "pitching-branch" modes). Conversely, as a result of the fluid-structure interaction and in particular of the cross flutter derivatives, significant off-diagonal terms appear in the damping and stiffness matrices which also lose their symmetry. Consequently, for $U > 0$ m/s the eigenmodes no longer coincide with the heaving and pitching degrees of freedom but are a linear combination of them. This means that in the spectra of the heaving and pitching signals two peaks, corresponding to the two eigenfrequencies, should be visible. Fig. 3.39 shows that far from flutter this is just a secondary effect since only Mode #1 frequency in the heaving signal and Mode #2 frequency in the pitching signal are discernable. Nevertheless, near flutter the pitching-branch component in the heaving signal suddenly starts to acquire energy and quickly becomes dominant (Fig. 3.39). Therefore, the heaving and pitching motions result to be coupled through the pitching-branch eigenmode. In Fig. 3.40, which displays the heaving signal immediately before flutter, it can be observed that the first high-amplitude oscillation after the initial condition release is at a lower frequency (heaving-branch frequency) but this component is immediately damped out [as shown in Fig. 3.38(b) the damping ratio is as large as about 25 %] and low-damping higher frequency oscillations appear (pitching-branch frequency). This behavior is confirmed by the experimental results reported in Righi (2003) for two rectangular cylinders: if the frequencies corresponding to the dominant peaks in the spectra of the heaving and pitching signals are plotted for various wind speeds, it can be remarked that these frequencies slightly tend to approach and then, immediately before flutter, the dominant frequency in the heaving signal suddenly jumps at the corresponding value of the pitching signal. In Fig. 3.38(a), where the pure eigenmodes are

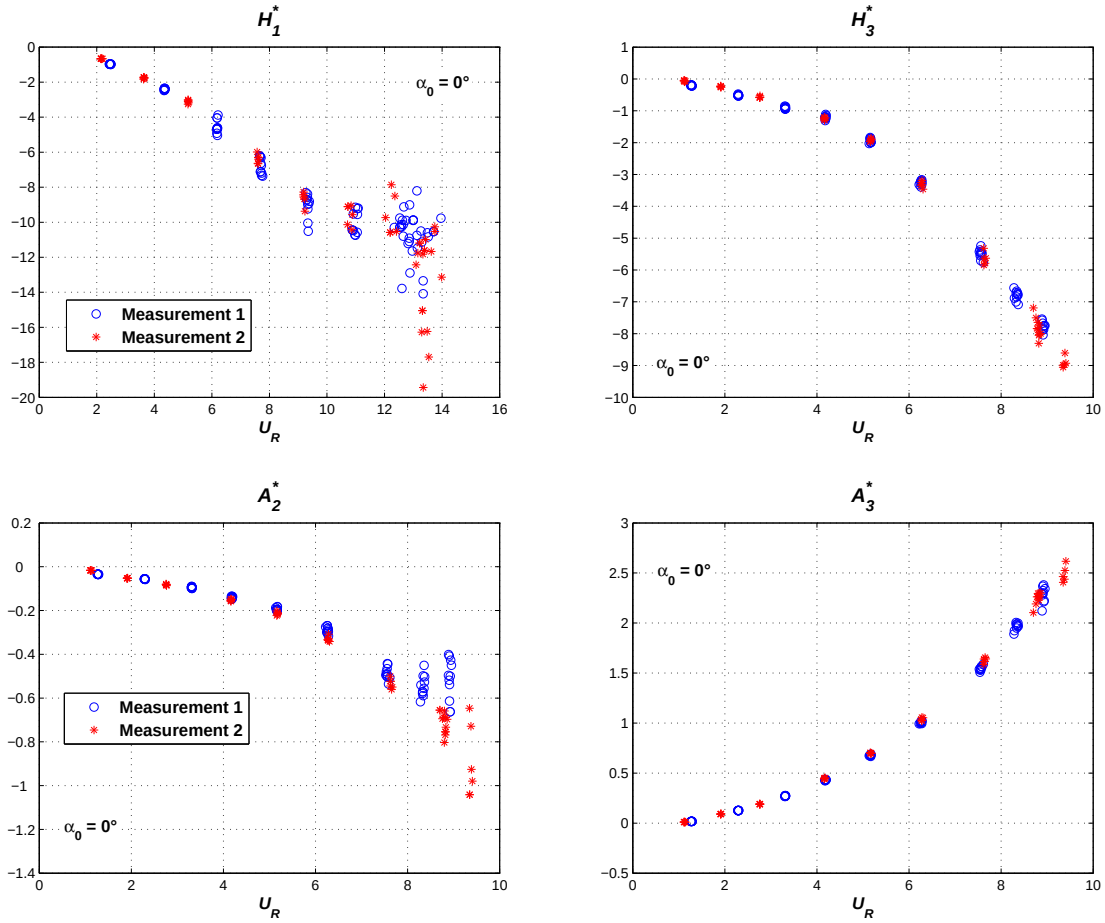

Figure 3.36: Repeatability of the flutter derivative measurements

analyzed, it is possible to observe that the heaving-branch frequency (Mode #1) stays almost constant for a wide range of flow speed and only near flutter tends to moderately increase, whereas the pitching-branch frequency (Mode #2) monotonously decreases until flutter (as far as about 20 %). Concerning the modal damping it is worth noting that it is the pitching branch to become negatively damped and therefore unstable [Fig. 3.38(b)]. Increasing the flow speed, for both eigenmodes the modal damping increases with respect to the still-air value but near flutter the pitching-branch damping starts to decrease and then becomes negative while the heaving-branch one continues to increase. This behavior for the eigenfrequencies and the modal damping is in agreement with the experimental results observed by Matsumoto and co-workers for some rectangular cylinders and other cross sections (Matsumoto, 1996; Matsumoto *et al.*, 1997, 1999, 2001, 2002; Matsumoto, 2005). The higher dispersion of damping and frequency values for the heaving branch near instability is due to the short heaving signal (or heaving-branch component of the signal) available for the identification, given the very high aerodynamic damping. Finally, it is now clear why the observed non-viscous effects due

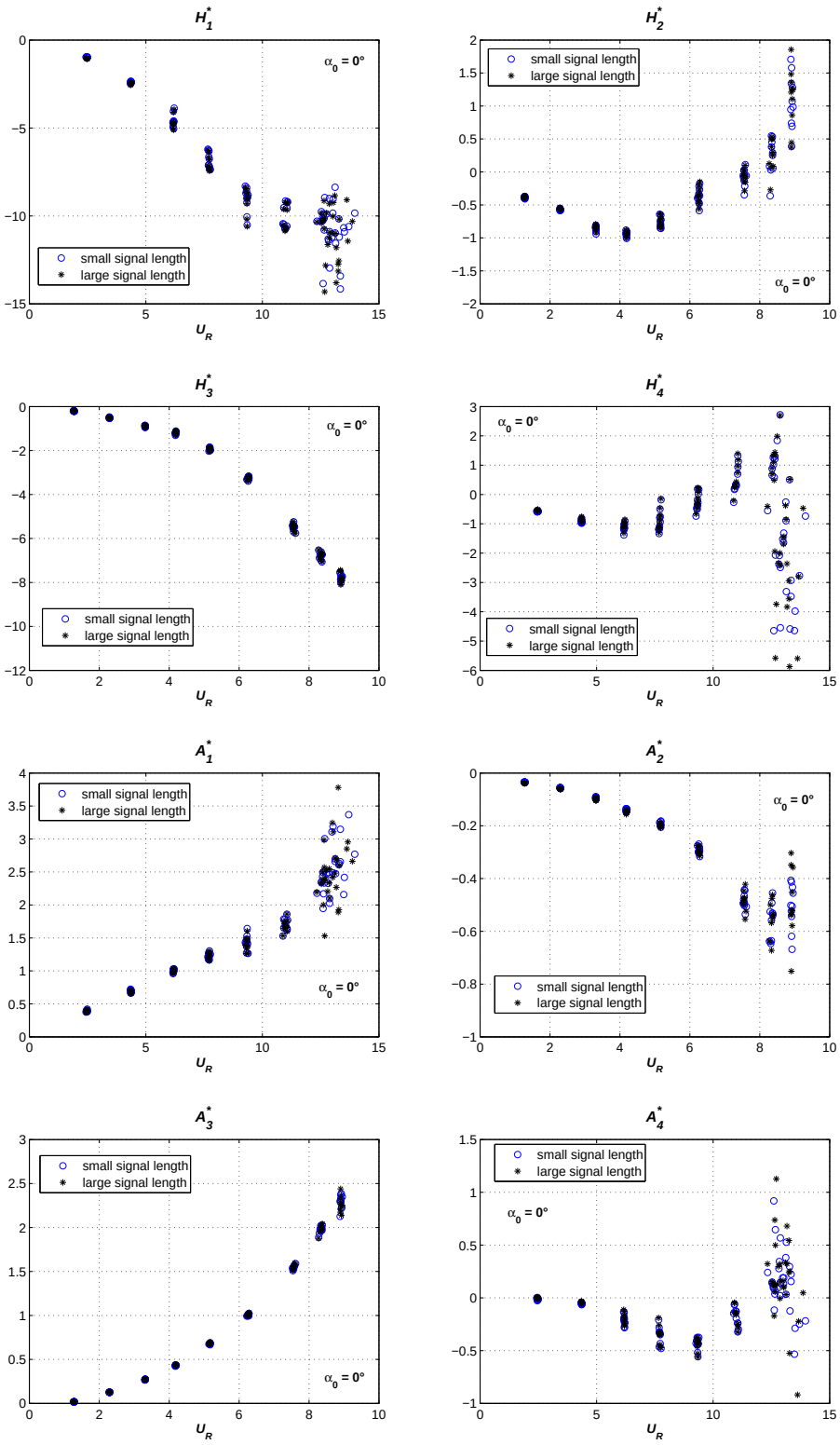

Figure 3.37: Flutter derivatives for two different choices of the length of the processed signals

to the still-air resistance do not affect the flutter derivative values: Fig. 3.38(b) shows that the structural damping ($U = 0$ m/s) is definitely negligible with respect to the aerodynamic damping, even at low wind speed.

At this point, some discussion is necessary concerning the definition of the reduced wind speed. For a free-vibration set-up, if one wants to keep the analogy to the thin airfoil theory, from which the flutter derivative concept is derived, the frequency appearing in the expression of U_R should be interpreted as the one of the heaving-pitching coupled mode of vibration at the current wind speed. Unfortunately it is practically impossible to arrange an experimental set-up characterized by heaving and pitching modes with the same frequency. It is often difficult even to reduce much the frequency separation in order not to experience flutter too early. Therefore, a coupled mode usually appears only near the onset of the aeroelastic instability. In addition, as it was previously noted, the heaving-pitching reference system, which is principal in still air, it is no longer when the model is immersed in the airflow, although this rotation of the principal reference system can be appreciated in the spectra only near flutter. Therefore, an inconsistency between basic theory and experimental set-up is evident. In the writer's opinion the more correct solution is to normalize the flutter derivatives and the reduced wind speed on the basis of the dominant frequencies in the heaving and pitching signals, since those modes mainly contribute to the generation of the aerodynamic forces. It means that far from flutter the heaving-branch and pitching-branch eigenfrequencies can be considered for the flutter derivatives related respectively to the heaving and pitching degree of freedom, whereas near flutter, when suddenly the peak relative to the pitching-branch mode appears in the spectrum of the heaving signal, this eigenfrequency should be used to normalize all the eight functions. Consequently, there could be a limited wind speed interval wherein an ambiguous situation originates due to the comparability of the two peaks in the heaving spectrum. Nevertheless, as expressed by Eqs. 3.11-3.12, here the flutter derivatives and the reduced wind speed corresponding to the heaving degree of freedom are normalized by means of the heaving-branch eigenfrequency also after coupling for practical reasons. As a matter of fact, if one adopted the pitching-branch frequency (dominant after coupling in the heaving signal), the reduced wind speed would become smaller but the values of the function would not coincide with the that measured at lower wind speed and equivalent U_R because the mean angle of attack is now higher, thus implying a problem of graphical representation. However, it must be remarked that this choice has no consequence in the flutter calculations because it concerns reduced wind speeds higher than the critical one.

It is also quite common to express the reduced wind speed by means of the still-air frequencies. This is not correct since it is equivalent to consider flutter derivatives as dependent just on the wind speed instead of the reduced wind speed. Nevertheless, this procedure does not imply large errors whenever the frequencies do not change much due to the aeroelastic coupling. Sarkar (1992) investigated the effect of interchanging the frequencies of normalization both for reduced wind speed and flutter derivative values. The curves in several cases do not differ much, although large discrepancies are found for instance for the function H_2^*. However, this result cannot be generalized and it can be easily demonstrated that it does not apply for those aeroelastic functions whose modulus does not grow monotonically with the reduced wind speed.

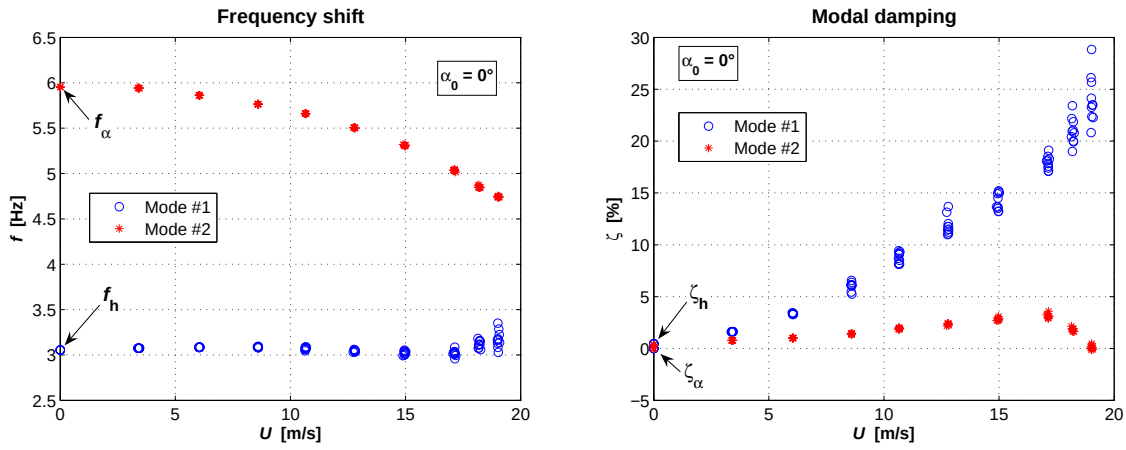

(a) (b)

Figure 3.38: (a) Frequency and (b) modal damping evolution with the wind speed ($\alpha_0 = 0°$). Mode #1 and Mode #2 denote respectively the heaving- and pitching-branch modes

Since the main application of the flutter derivatives is the flutter prediction through eigenvalue analysis, the validity of the identified functions is checked by averaging their values for each reduced wind speed, performing a shape-preserving piecewise cubic interpolation and then estimating the flutter critical wind speed. Besides the basic configuration on which the flutter derivatives are identified ("test case 0"), other two test cases are taken into account, changing the frequency ratio, the mass and mass moment of inertia by adding eccentric masses in correspondence of the model suspension arms. The results are reported in Tabs. 3.13-3.14. It is worth noting that it is difficult to specify the actual damping ratios due to the previously discussed non-viscosity of the still-air resistance contribution. Consequently, the same calculation is performed both with the damping ratio estimated for 15 s-free-decay signals and for zero-damping level. However, the contribution to flutter of the structural damping, at least in this case, is negligible. Limited extrapolations are necessary for the flutter derivatives corresponding to the pitching degree of freedom (H_2^*, H_3^*, A_2^* and A_3^*). This is done by fitting the experimental data with second, third or fourth-order polynomial functions.

The results of the flutter calculations for "test case 0" and "test case 1" are extremely accurate with respect to the experiments. Conversely, for "test case 2" the eigenvalue analysis leads to an overestimation of the flutter critical wind speed of about 20 %. The reasons for this discrepancy are not clear yet but a possible explanation could be that the critical reduced wind speed in "test case 0" and "test case 1" is fairly close (or coincident) to the value at which flutter instability occurred in the system on which the aeroelastic functions are identified. Conversely this is not true for "test case 2". Considering that the measurements are more reliable far from flutter, in the sense that their scatter is much smaller (e.g. Fig. 3.35, 3.36 and 3.37), a less accurate result should not be expected unless we suppose that some of the functions we identify through free-vibrations, probably among the cross-derivatives, though

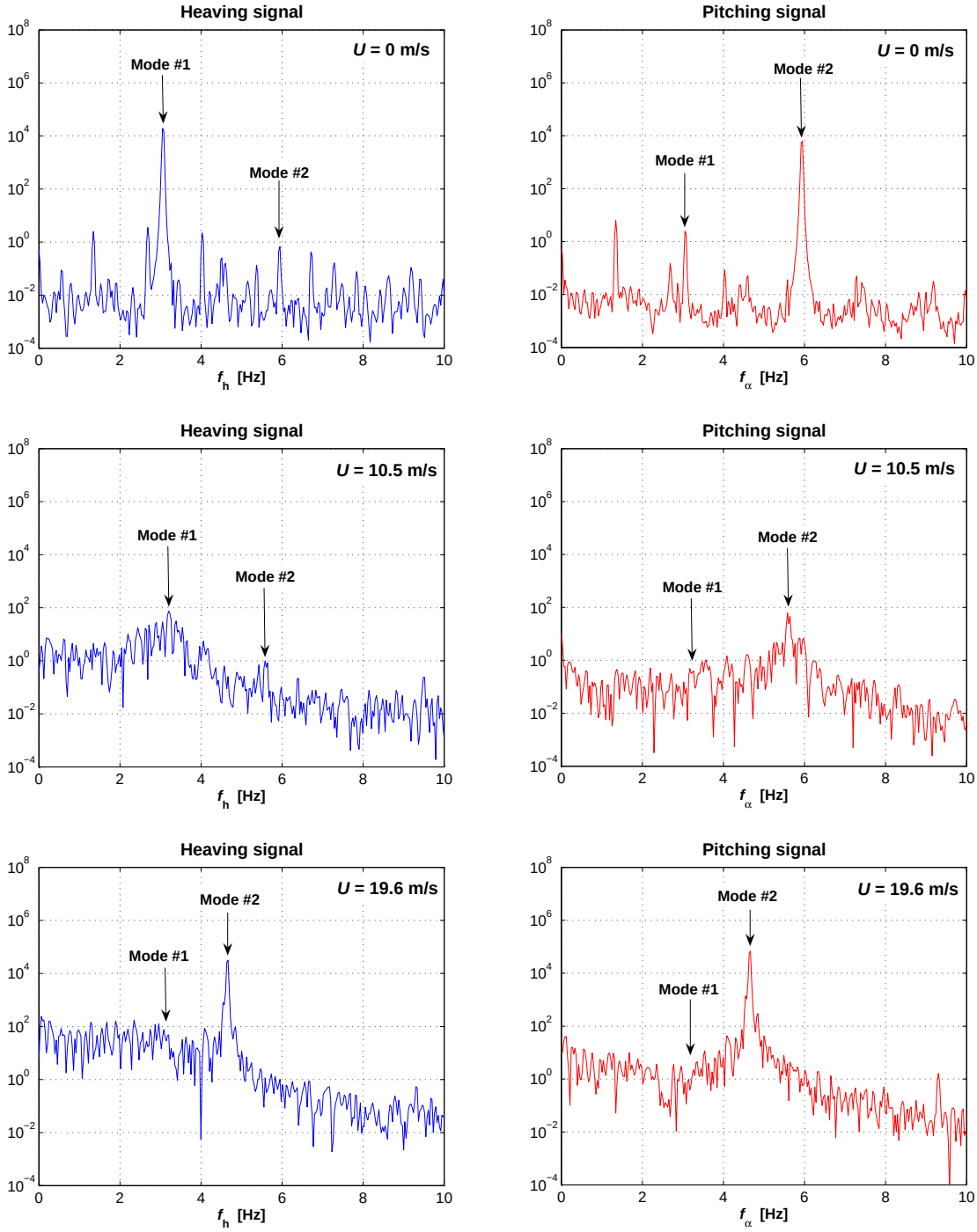

Figure 3.39: Power spectral density of heaving and pitching signals at different wind speeds

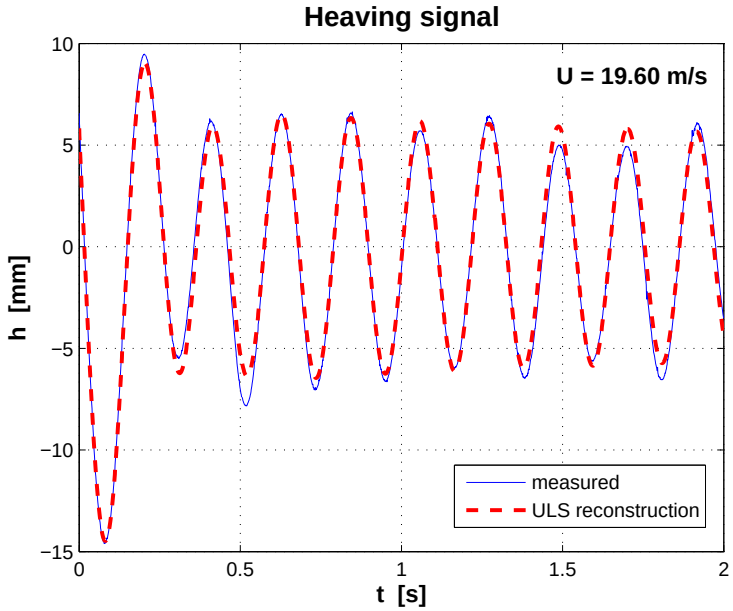

Figure 3.40: First cycles of oscillation of the heaving signal immediately before flutter [detail of Fig. 3.33(g)]

well defined, are not actual flutter derivatives in the Scanlan's sense, because measured far from coupling between heaving and pitching modes. Further discussion of this issue can be found in section 6.6.

It is also worth noting in Tab. 3.14 that the flutter critical wind speeds calculated with the Theodorsen's theory overestimate the measured values and those obtained with the experimental flutter derivatives but they are not very far from them. This result is not surprising given the previously discussed similarity between the measured flutter derivatives and the thin-flat-plate theoretical functions.

Now, in order to be able to express the flutter derivatives as functions of the reduced wind speed and mean angle of attack, the still-air angle of attack is varied and the in-wind free-decay tests repeated for α_0 = -3.72°, -1.70°, +1.24°, +2.61°, +4.32°. For each wind speed the measurement is repeated five times. The resulting flutter derivatives are shown in Fig. 3.41.

Table 3.13: Dynamic parameters of the test cases for flutter calculation. In "test case 0" the experimental set-up is the one on which the flutter derivatives are identified

Test case	ρ [kg/m^3]	m [kg/m]	I [kgm^2/m]	f_h [Hz]	f_α [Hz]	γ_ω [-]
0	1.195	5.449	0.0955	3.055	5.953	1.948
1	1.212	6.047	0.1917	2.906	4.165	1.433
2	1.212	6.289	0.2311	2.847	3.788	1.331

Table 3.14: Measured and calculated flutter critical reduced wind speed (U_{Rc}), frequency (f_c) and dimensional wind speed (U_c). The damping ratios for "test case 0" are quite different from those reported in Tab. 3.9, since they refer to the "remounted" set-up (see Fig. 3.36)

			Measured			Eig. analysis			Theodorsen's theory		
	ζ_h	ζ_α	U_{Rc}	f_c	U_c	U_{Rc}	f_c	U_c	U_{Rc}	f_c	U_c
Test case	[%]	[%]	[-]	[Hz]	[m/s]	[-]	[Hz]	[m/s]	[-]	[Hz]	[m/s]
0	0.24	0.18	9.30	4.74	19.86	9.42	4.69	19.89	11.24	4.35	22.00
	0.0	0.0				9.38	4.70	19.85	11.13	4.37	21.87
1	0.35	0.17	9.13	3.70	15.20	9.19	3.69	15.27	9.83	3.63	16.04
	0.0	0.0				9.08	3.70	15.13	9.64	3.64	15.79
2	0.34	0.17	7.24	3.56	11.60	9.10	3.44	14.08	9.28	3.42	14.27
	0.0	0.0				8.96	3.45	13.90	9.04	3.43	13.95

The aeroelastic functions related to the rotation α (H_3^* and A_3^*) are always well defined, with small dispersion and close to the thin-flat-plate theoretical functions. In addition, they do not seem very sensitive to the angle of attack. The flutter derivatives which express the heaving and pitching aerodynamic damping (H_1^* and A_2^*) are more sensitive to the angle of attack. The patterns are similar for zero and positive angles of attack, whereas they change even qualitatively for negative angles of attack. This fact is particularly evident for A_2^*: for positive angles of attack this function monotonously increases, closely following the Theodorsen's theoretical values until a reduced wind speed, little before flutter, where it suddenly starts to increase. The position of the minimum of the A_2^*-curve depends on the mean angle of attack, corresponding to lower reduced wind speed as α_0 increases (Fig. 3.41). This means that also the flutter critical wind speed is lower for configurations with larger α_0. Conversely, for negative angles of attack the pattern of A_2^* is completely different and quite far from the flat-plate theoretical one, with smaller values of the pitching aerodynamic damping. A_1^* is not very sensitive to the angle of attack, at least outside the particular flow regime for small negative angles of incidence. Similarly to A_2^*, except for α_0 = -3.72°, H_2^* is characterized by similar patterns, with first decreasing and then increasing values, but the reduced wind speed at which the sign of the slope changes depends on the angle of attack.

The analysis of the flutter derivatives for several initial angles of attack shows that the aeroelastic behavior for small negative mean flow incidence (configurations with α_0 = -3.72° and -1.70° in Fig. 3.41) is completely different from the one for positive mean angles of attack, thus confirming the idea suggested by the static tests that this cross-section profile is characterized by two completely different flow regimes. In order to qualitatively show the different flutter mechanism for small negative angles of attack, in Fig. 3.43 the in-wind frequency shift and modal damping diagrams for the configuration with $\alpha_0 = -1.70°$ are reported. It is worth noting that the heaving branch frequency remains constant for a wide range of reduced wind speed and near flutter starts to slightly decrease instead of increasing as in the case of positive angles of attack (Fig. 3.38). In addition, the modal damping corresponding to the pitching branch does not increase much for low wind speed, then approaches zero and remains constant

(flutter limit cycle oscillations).

In addition, the position of the rotation center x_0 and the phase angle ϕ between heaving and pitching motion are plotted against the wind speed for different angles of attack in Fig. 3.42. Significant coupling is observed only for the pitching-branch mode, which becomes unstable at flutter and is therefore taken into account in the graphs. For the same reason the results shown in Fig. 3.42 are particularly relevant for wind speeds near flutter. The position of the rotation center, positive downstream, is defined as:

$$x_0 = -\frac{h_0}{\alpha_0} \tag{3.13}$$

where h_0 and α_0 are the amplitudes respectively of the heaving- and pitching-branch modes. It can be remarked that the rotation center is placed always upstream with respect to the midchord, its distance increasing with the wind speed, following roughly the same pattern for all the considered angles of attack. In the case $\alpha_0 = 0°$, at flutter the rotation center is placed nearly 14 cm from the midchord. The pitching motion lags behind the heaving motion but the phase angle is fairly small near flutter for zero and positive angles of attack (for $\alpha_0 = 0°$ $\phi \cong -10°$), thus confirming the assumption discussed by Nakamura (1978). Conversely, for negative incidence [Figs. 3.42(d) and 3.42(f)] the phase lag is much larger.

Finally, the flutter derivative values we measured could be thought as functions of two variables, the reduced wind speed and the mean angle of attack [$\alpha(U)$ instead of α_0]. Consequently, if a two-dimensional interpolation is performed, then it could be possible to extract the flutter derivatives corresponding to a constant angle of attack in the range of interest. This manipulation would significantly widen the practical applicability of the data presented in this chapter.

3.6 Conclusions

Static and aeroelastic tests are performed on a bridge deck section model (bare-deck configuration) whose cross section is common for medium-span cable-stayed bridges (closed-box girder with lateral cantilevers).

The static tests allow to measure the aerodynamic force coefficients for several angles of attack as well as the Strouhal number. These tests show a certain sensitivity to Reynolds number, whereas the comparison with other tests on a similar cross section and with CFD simulations highlighted the strong dependence of the flow field around the deck on the degree of sharpness of the lower corners of the trapezoidal box.

The aeroelastic tests confirm the static results concerning the mean lift and moment coefficients and allow the identification of the flutter derivatives for several initial angles of attack. The dependency of these functions on the amplitude of the motion, the repeatability of the measures as well as the sensitivity with respect to the considered length of the transient signals, showing the robustness of the results. It is also shown the capability of the Unifying Least-Square method to properly interpret and reproduce the measured signals. Furthermore, the critical flutter wind speed calculated with the flutter derivatives is compared with the directly measured value for three different test cases.

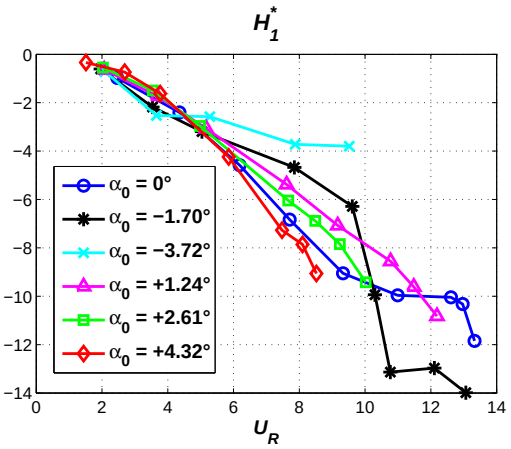
H_1^*
α_0 = 0°
α_0 = −1.70°
α_0 = −3.72°
α_0 = +1.24°
α_0 = +2.61°
α_0 = +4.32°
U_R

(a)

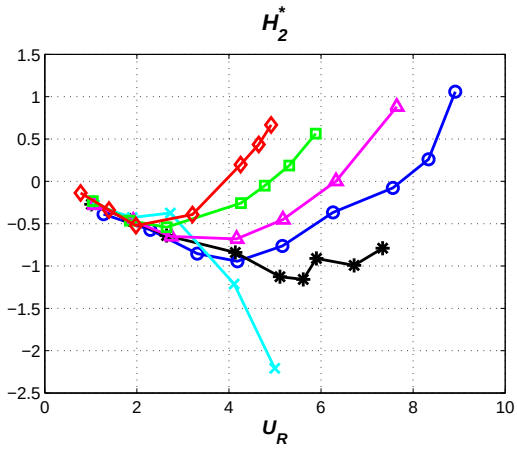
H_2^*
U_R

(b)

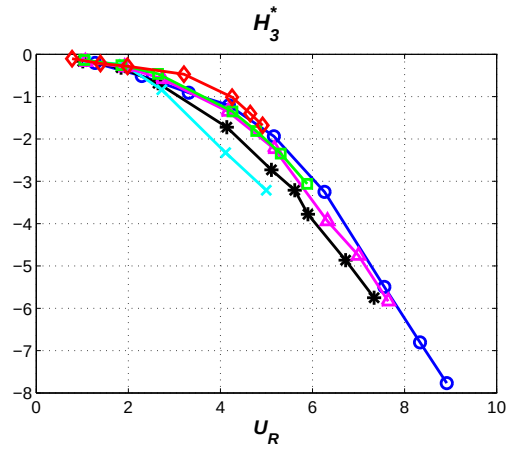
H_3^*
U_R

(c)

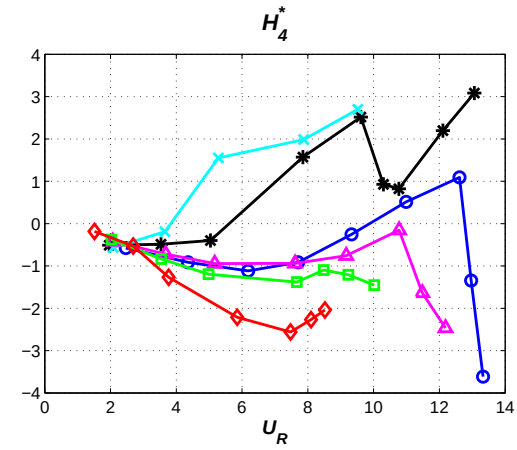
H_4^*
U_R

(d)

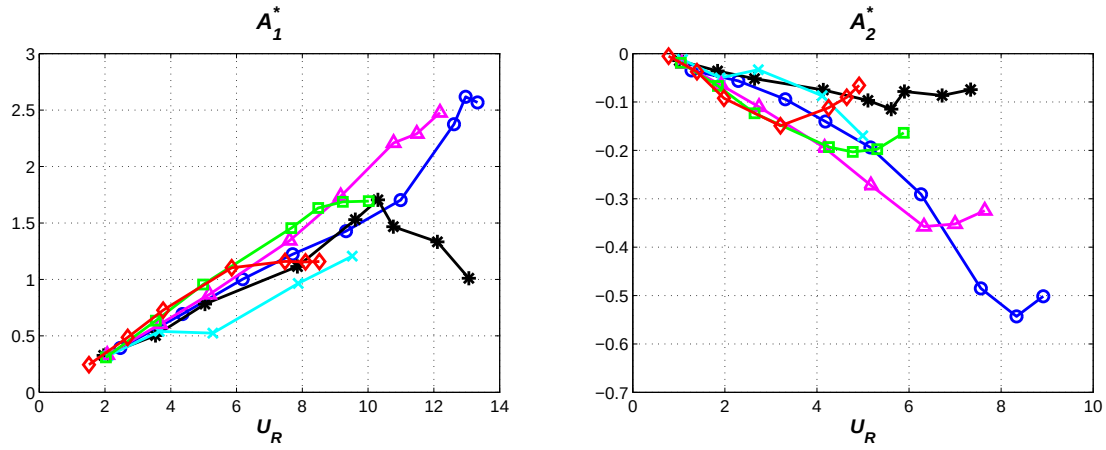

(e) (f)

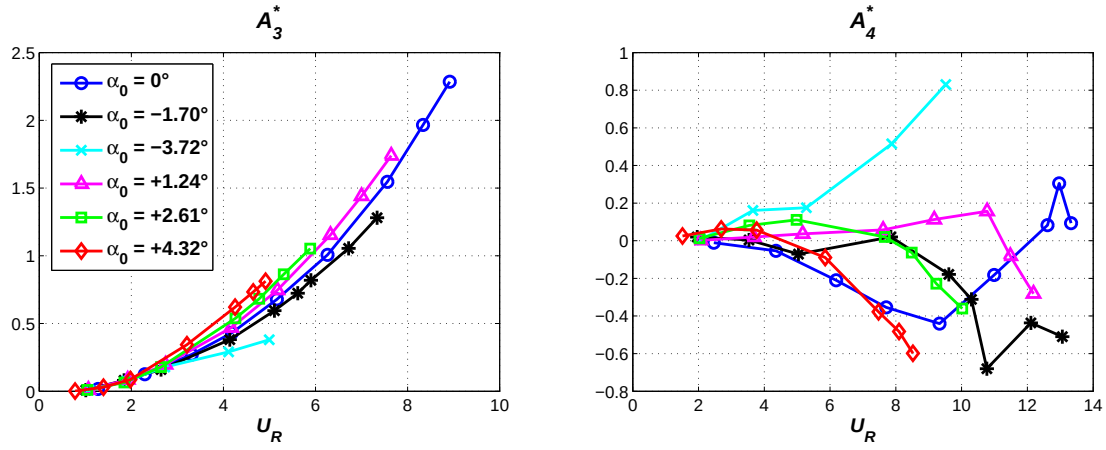

(g) (h)

Figure 3.41: Mean values of the flutter derivative for different still-air angles of attack α_0

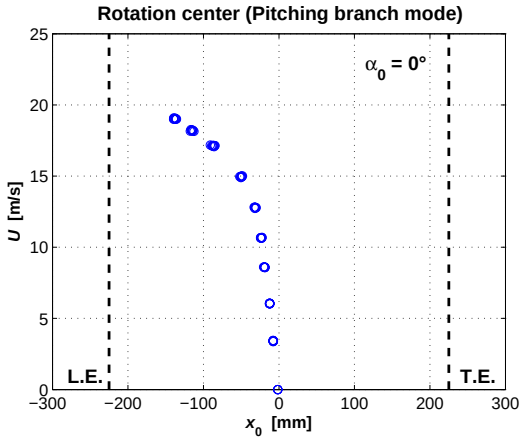
Rotation center (Pitching branch mode)
α0 = 0°
L.E.
T.E.
U [m/s]
x0 [mm]

(a)

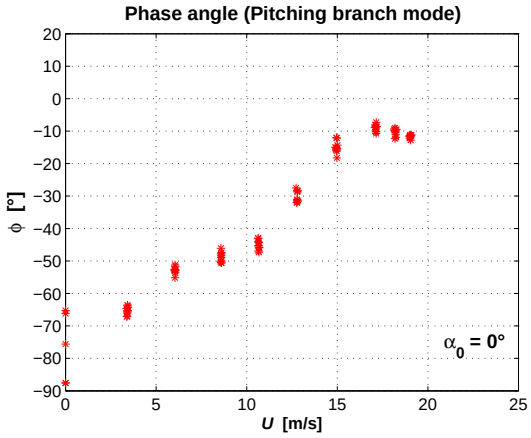
Phase angle (Pitching branch mode)
α0 = 0°
ϕ [°]
U [m/s]

(b)

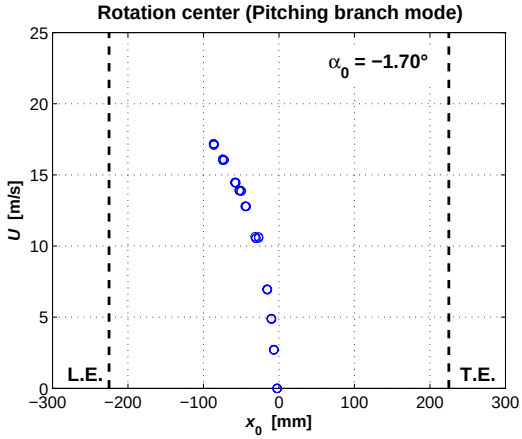
Rotation center (Pitching branch mode)
α0 = −1.70°
L.E.
T.E.
U [m/s]
x0 [mm]

(c)

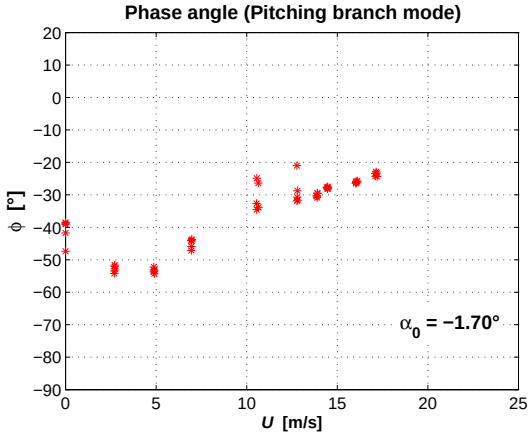
Phase angle (Pitching branch mode)
α0 = −1.70°
ϕ [°]
U [m/s]

(d)

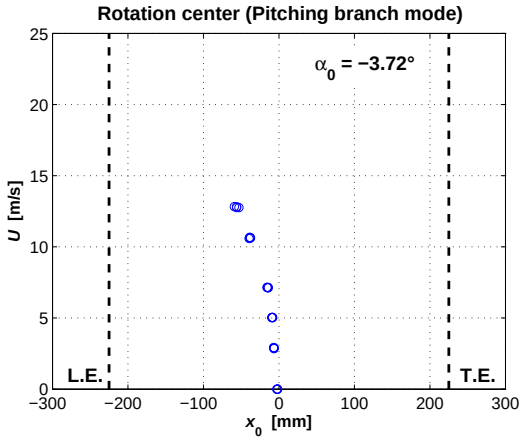
Rotation center (Pitching branch mode)
α0 = −3.72°
L.E.
T.E.
U [m/s]
x0 [mm]

(e)

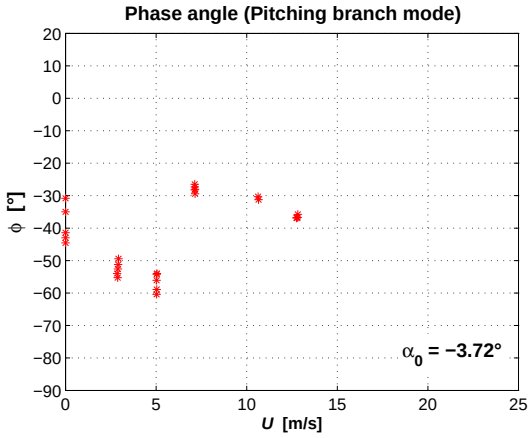
Phase angle (Pitching branch mode)
α0 = −3.72°
ϕ [°]
U [m/s]

(f)

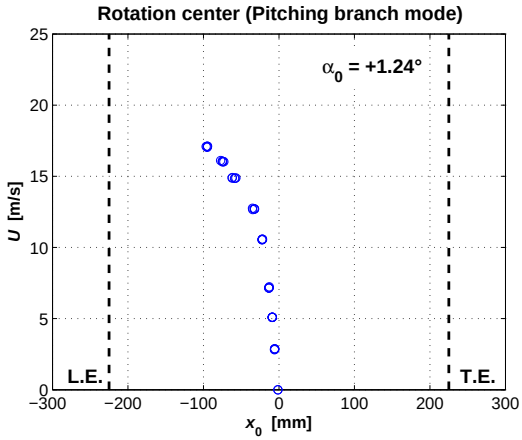

(g)

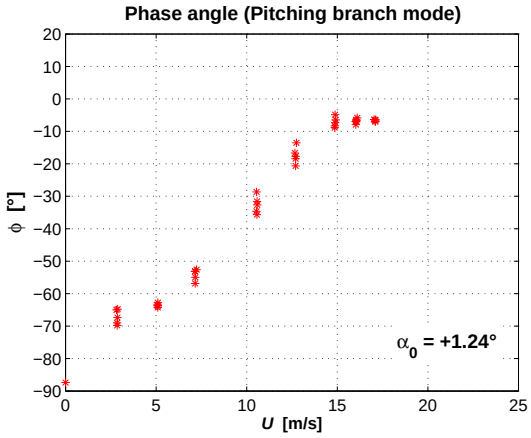

(h)

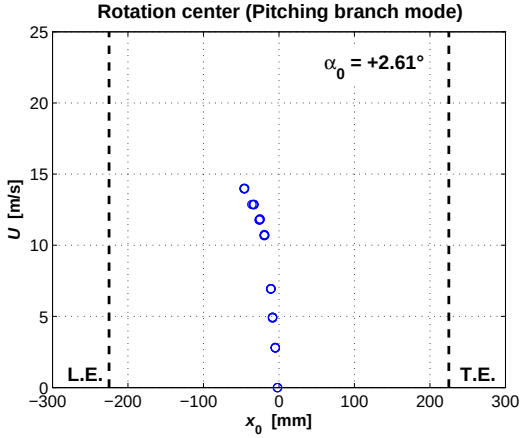

(i)

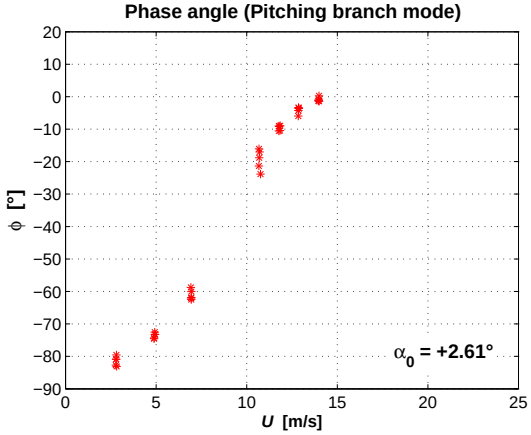

(j)

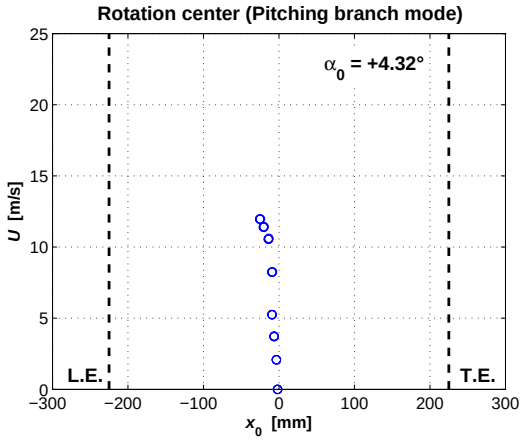

(k)

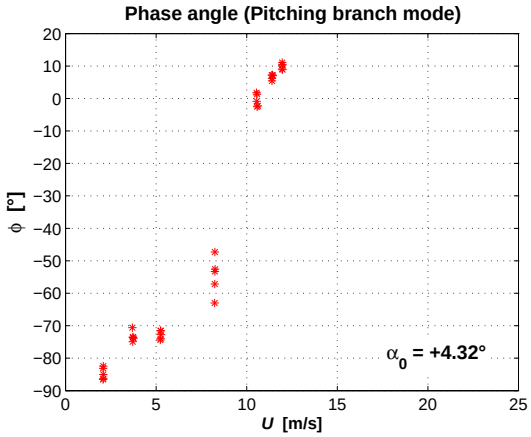

(l)

Figure 3.42: Rotation center and phase angle relative to the pitching-branch mode. L.E. and T.E. denote respectively the leading and trailing edge

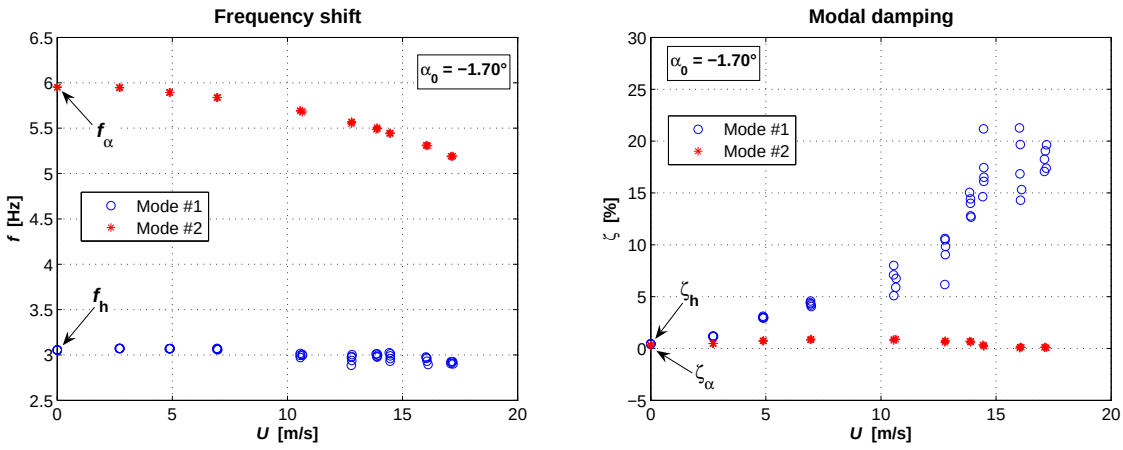

(a) (b)

Figure 3.43: (a) Frequency and (b) modal damping evolution with the wind speed ($\alpha_0 = -1.70°$)

The influence on the aeroelastic behavior of the mean angle of attack is studied in order to express the flutter derivatives as functions of both the reduced wind speed and the mean angle of attack. With the exception of small negative angles of attack, for which, in agreement with the static measurements, the characteristics of the flow seems to change completely, the flutter derivatives show qualitatively similar patterns changing the mean angle of attack. In addition, the trends are in most cases close to that of the theoretical thin flat plate. This last observation and some considerations discussed at the end of section 3.4.3 suggest that the bridge deck aeroelastic behavior may be less sensitive to Reynolds number and small geometrical details (such as the degree of sharpness of the lower corners) than the static aerodynamic force coefficients. Nevertheless, our research is not able to demonstrate this conjecture and further investigation is needed about this issue.

Finally, it is important to remind that in our experimental work particular attention is paid to give a statistical description of the measured flutter derivatives, in order to use them in a probabilistic approach to flutter (see Chapter 4), in view of a flutter vulnerability assessment.

Chapter 4

Probabilistic flutter approach

4.1 Flutter derivative measurements and uncertainty

It has been said several times in the previous chapters that flutter derivatives can be considered as functions of the cross-sectional geometry, reduced wind speed and mean angle of attack. The role played by small scale turbulence is still not clear but it seems to act as if the shape of the bluff body was slightly different, usually more streamlined (Scanlan and Lin, 1978; Lin, 1996; Righi, 2003; Bartoli and Mannini, 2005).

Flutter derivatives are usually considered as deterministic functions but the dispersion which always characterizes their values, as shown in the previous chapter for the single-box girder deck section or in Righi (2003) for two rectangular cylinders, demonstrates that they have to be treated as not deterministic. Many sources of uncertainties can be enumerated:

- experimental measurement errors
- non-perfect capability of the mathematical model to explain the physical phenomenon
- imperfections in the identification procedure
- turbulence

It has already been shown that the identification method ULS is able to reproduce very well the measured signals. Therefore its contribution to the scatter of data does not seem very significant. Conversely, Righi (2003) highlighted the important contribution to uncertainty given by turbulence, which strongly increases the dispersion of the measured values, even at low wind speeds. It is important to bear in mind that the contribution of turbulence cannot be avoided as natural wind is always turbulent and wind-tunnel flows are never really "smooth", especially in the case of boundary layer wind tunnels for civil engineering applications where a minimum turbulence intensity of about 1 % is quite common. It is also worth noting that in case of forced-vibration set-ups the scatter affecting the aeroelastic coefficients is expected to be smaller than for free-vibration tests but it cannot be avoided.

Hence flutter derivatives have to be considered probabilistic functions of the reduced wind speed (and mean angle of attack) and the uncertainties which affect their values are necessarily

somehow transferred to the calculated flutter critical wind speed and frequency. A model of probabilistic flutter assessment is then necessary to find the probability distribution of the flutter wind speed and consequently to evaluate the reliability of the calculated flutter boundaries and indirectly of the measured flutter derivatives. It is important to understand that if the dispersion affecting the flutter calculation output is very large, the number one calls critical wind speed is not very meaningful. Practically, in this chapter a method to estimate the variance of this variable is proposed.

In addition, the probabilistic approach outlined herein is consistent with the vulnerability assessment in a Performance-Based Design scheme. As a matter of fact, repeating here the previously discussed PEER equation [Eqs. (1.4),(1.6), (4.1) and (4.2)], the proposed approach can be considered as a method to define the term $p(EDP|IM)$, that is the exceedance probability to have a certain structural response EDP (flutter oscillations) given a certain Intensity Measure IM (mean wind speed). Even though aerodynamic and structural [e.g. Salvatori and Spinelli (2006b)] nonlinearities could lead to large-amplitude limit-cycle oscillations, as a first approximation and in any case to be conservative, flutter can be regarded as a divergent phenomenon and consequently the collapse limit state is concerned. Therefore, with reference to what is said in section 1.3, also the term $p(SL|IM)$ can be calculated with respect to the ultimate limit state for flutter instability.

$$p(DV) = \int\int\int p(DV|DM) \cdot |dp(DM|EDP)| \cdot |dp(EDP|IM)| \cdot dp(IM) \tag{4.1}$$

$$p(SL) = \int p(SL|IM) \cdot dp(IM) \tag{4.2}$$

In the following the main assumptions standing behind the proposed probabilistic model are presented and discussed, the results obtained for two rectangular cylinders are summarized, then the probabilistic method is applied to the bridge deck section analyzed in Chapter 3 and finally some conclusions are drawn.

4.2 Model assumptions

The probabilistic model is based on the following assumptions:

1. each flutter derivative is a random variable independent from the corresponding variable at a different reduced wind speed;

2. given the reduced wind speed, the eight flutter derivatives are independent between them;

3. these random variables are normally-distributed with the same mean and variance as the experimental samples.

The first point to discuss is the independency of the random variables. The measurements at different wind speeds absolutely do not depend on each other because, after a measure is done, the initial condition is imposed again and then released, therefore the previous measure has no

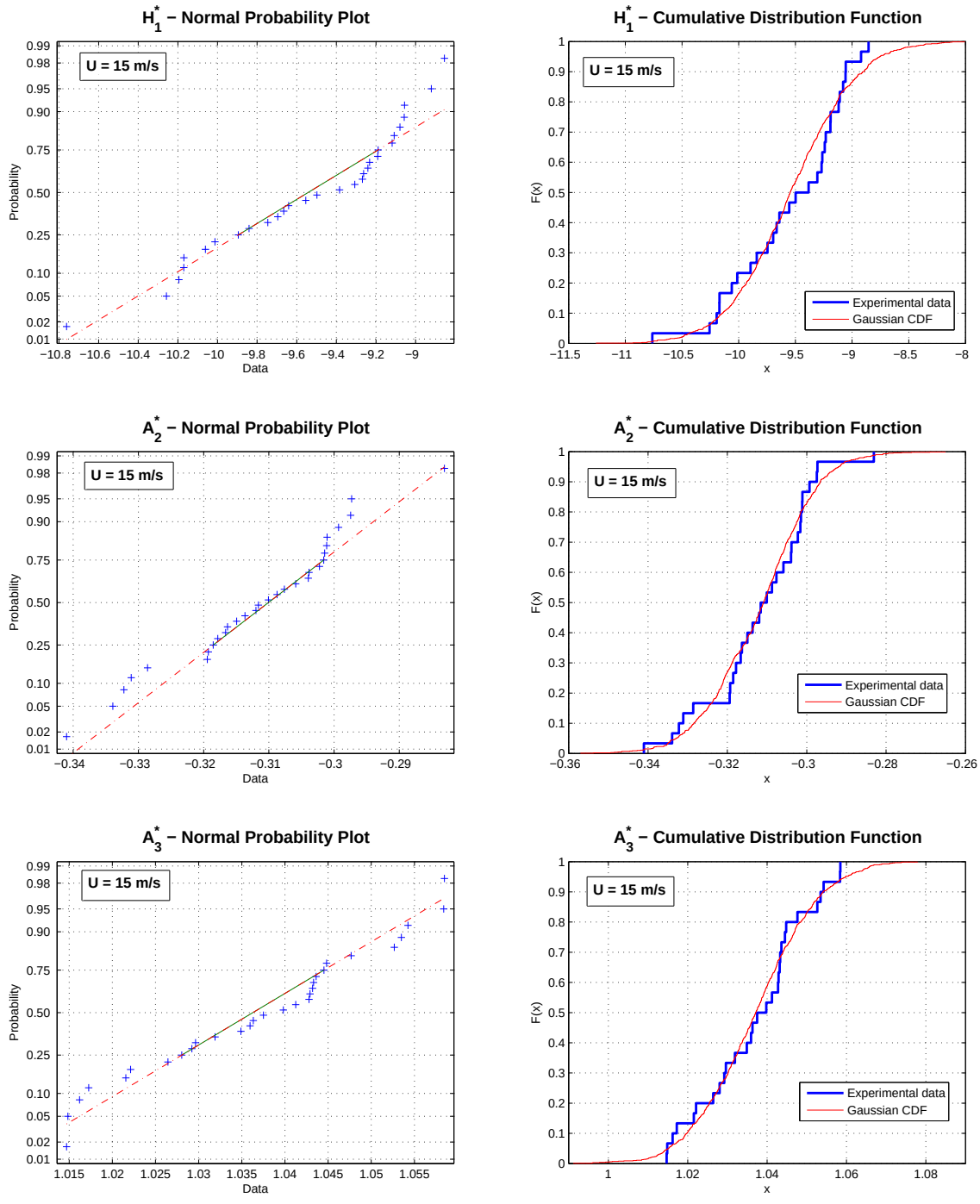

Figure 4.1: Probability plot and cumulative distribution function for the flutter derivatives H_1^*, A_2^*, A_3^* measured at a wind speed of 15 m/s (sample size $N = 30$)

influence at all on the following one. Despite that, due to the physics of the phenomenon, the flutter derivative values at different reduced velocities are supposed to follow a certain pattern. This means that, if one performed just a measurement per wind speed, the current measure would not be influenced by the previous value, but patterns far from the "physical" one would be less probable than patterns close to the ideal, and a priori unknown, curve. Hence the assumption of independency does not fully hold. To accept that is equivalent to spread out the "clouds" or random points, which substitute the deterministic curves (see Figs. 4.3 and 4.11), consequently increasing the actual variance of the input.

The second assumption states that at the same reduced wind speed the different flutter derivatives are independent random variables. This point is questionable because for instance the contribution to uncertainty of turbulence is likely to have an effect which is correlated, especially for some aeroelastic coefficients. Nevertheless, first investigations on the experimental data seem to show a weaker correlation than it could have been expected. Furthermore, to account for that would require the estimation of a large number of joint probability functions, therefore complicating very much the probabilistic model. As further development of this work, we would like to better investigate this aspect of the problem and consequently improve the model.

The fact that the flutter derivative values follow a normal distribution should be proved. A first attempt was done in Bartoli and Mannini (2005) for the flutter derivatives measured for two rectangular cylinders in smooth and turbulent flow by Righi (2003). Statistical tests are performed on the hypothesis of Gaussian distribution at the significance level of 5 % and in most cases positive answers are obtained. Nevertheless the samples are too small to draw robust conclusions. During the experimental campaign described in Chapter 3, for three different wind speeds large samples are produced (30 measures for each wind speed), in order to perform meaningful tests. The first series of measurements is performed at a wind speed of about 4 m/s when the aerodynamic damping is not very high; the second series at 15 m/s when the aerodynamic damping is very high and the flutter instability limit is still far; finally the last series of measurements are performed at a wind speed of 19.2 m/s, that is immediately before the flutter onset. The initial angle of attack is always $\alpha_0 = 0°$. Two different tests are performed to check the goodness of fit to a normal distribution: Lilliefors and Jarque-Bera tests. The Lilliefors test is very similar to a Kolmogorov-Smirnov test but it adjusts for the fact that the parameters of the normal distribution are estimated from the sample rather than specified in advance. The empirical distribution of the variable is compared with a normal distribution having the same mean and variance as the sample. Conversely, the Jarque-Bera test determines whether the sample skewness and kurtosis are unusually different than their expected values for a normal distribution (0 and 3 respectively), as measured by a chi-square statistic. The Jarque-Bera test is an asymptotic test and is not recommended when small samples are available, in which cases the Lilliefors test has to be preferred. For the three series of measures for all the eight flutter derivatives both tests with significance level of 5 % give positive answers with the only exception of the Jarque-Bera test for H_3^* at low wind speed. Therefore it is possible to conclude that the measured flutter derivatives at each reduced wind speed are normally-distributed random variables. As visual examples of the distributions of the flutter derivatives and of the corresponding normal distributions, normal probability plots and cumulate distribution functions for H_1^*, A_2^*, A_3^* at 15 m/s are reported in Fig. 4.1. For

the other wind speeds the same graphs can be found in the Appendix.

Given the statistical distribution of the flutter derivatives, it is now possible to determine how the uncertainty in the input (flutter derivatives) is transferred into the output (flutter boundaries) through Monte-Carlo simulations. Random generations of the flutter derivatives are performed and then these functions are used to calculate the critical flutter wind speed and frequency via the usual eigenvalue analysis. This procedure is repeated many times (100000 simulations) so that the probability distributions of the flutter boundaries are obtained. In Bartoli and Mannini (2005) flutter derivatives are generated in correspondence of the reduced velocities at which measurements are performed and then interpolated with a shape-preserving piecewise cubic function. This interpolation has the effect to reduce the actual data dispersion, statistically forcing the generated curves to approach the mean curve. This procedure is somehow accounting for the "physical correlation" between flutter derivatives at different wind speeds but in an uncontrolled way. Conversely here the flutter derivative mean values and standard deviations are first interpolated and then Monte-Carlo simulations are performed at all the reduced velocities considered for the calculation (the discretization step is $\Delta U_R = 0.01$). This procedure perfectly fits assumption 1.

4.3 Results for two rectangular cylinders

A first attempt to apply this probabilistic flutter approach to realistic test cases is performed for two rectangular cylinders with chord-to-thickness ratio $B/D = 5.0$ (R5) and $B/D = 12.5$ (R12.5), whose wind-tunnel test results in smooth and turbulent flow are reported in Righi (2003). More details about the statistical characterization of the flutter derivatives and previous probabilistic calculations can be found in (Bartoli and Mannini, 2005). It is important to remark that only for R12.5 in turbulent flow reasonable samples of ten measures are available. For R12.5 in smooth flow on average five measurements at each reduced wind speed are performed, whereas for R5 in smooth and turbulent flow only samples of three measures are available. It is obvious that the statistical description of the flutter derivatives cannot be accurate.

The probability distribution of the reduced critical wind speed, frequency and dimensional wind speed, as well as the corresponding normal probability plots are reported in Figs. 4.2-4.7. In order to be meaningful these frequency histograms are characterized by a number of intervals defined according to Sturges' rule:

$$1 + \frac{10}{3}\log_{10} N \leq n_{int} \leq 10\log_{10} N \tag{4.3}$$

where $N = 100000$ is the available number of data. The upper limit ($n_{int} = 50$) is always chosen except in some cases for the reduced critical wind speed, due to the discretization of this variable in the calculation ($\Delta U_R = 0.01$), which requires a slightly smaller number of intervals (between 30 and 40 instead of 50) to obtain clearly readable distributions. If the probability density functions are needed, it is just necessary to divide each probability value by the corresponding bar width. In Tabs. 4.2-4.3 the statistics of the results are compared with the deterministic flutter results and experimentally measured values. The section-model dynamic parameters are reported in Tab. 4.1.

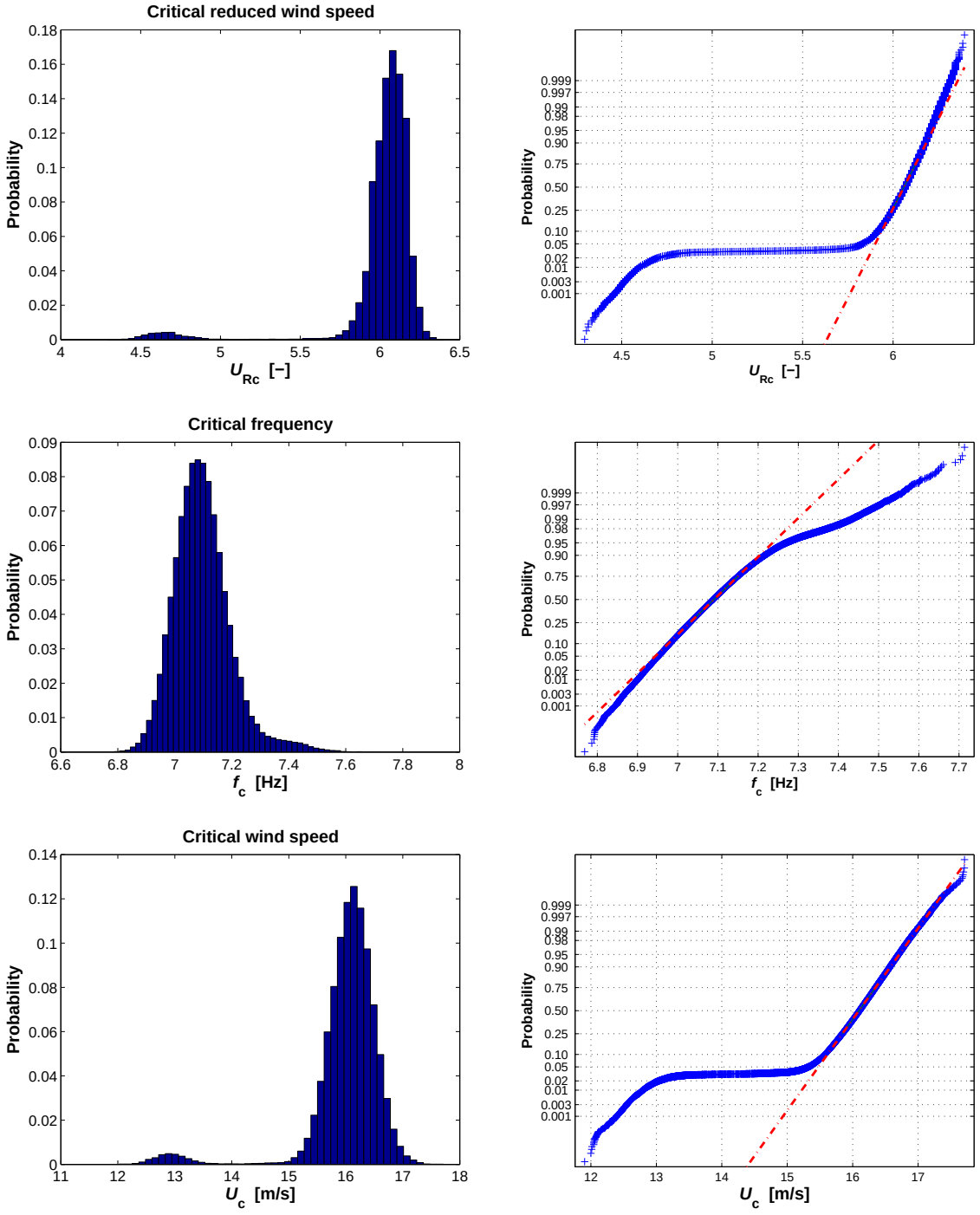

Figure 4.2: Probability distribution and normal probability plot ($N = 100000$) of the critical reduced wind speed (U_{Rc}), frequency (f_c) and dimensional wind speed (U_c) for the rectangular cylinder R12.5 in smooth flow

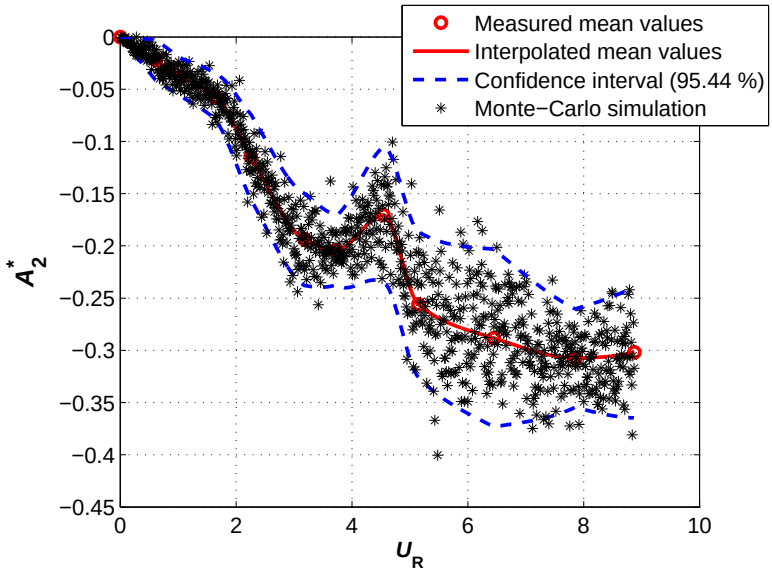

Figure 4.3: Mean values and 95.44 % confidence interval for the flutter derivative A_2^* for the rectangular cylinder R12.5 in smooth flow. An example of Monte-Carlo generated function is shown as well

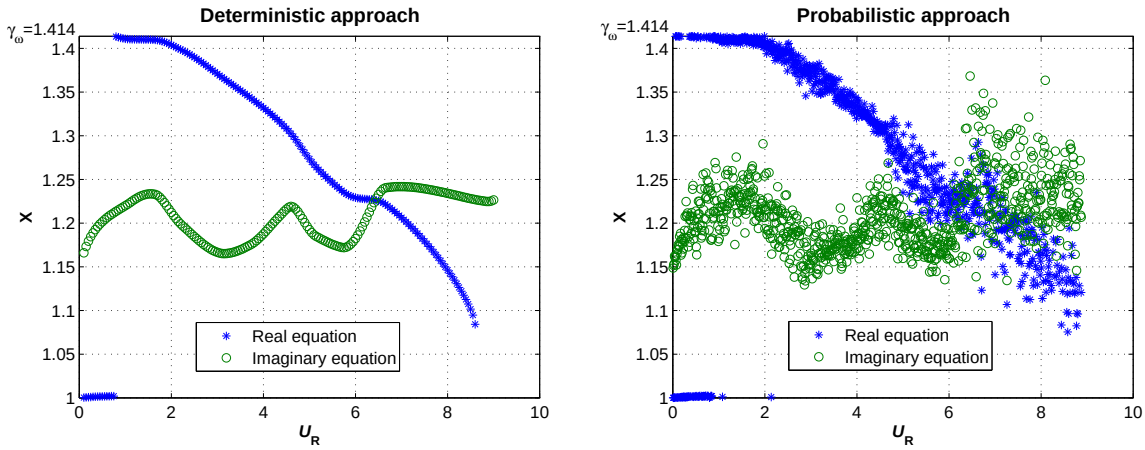

Figure 4.4: Deterministic and probabilistic flutter solution (see section 2.4.1): R12.5 in smooth flow

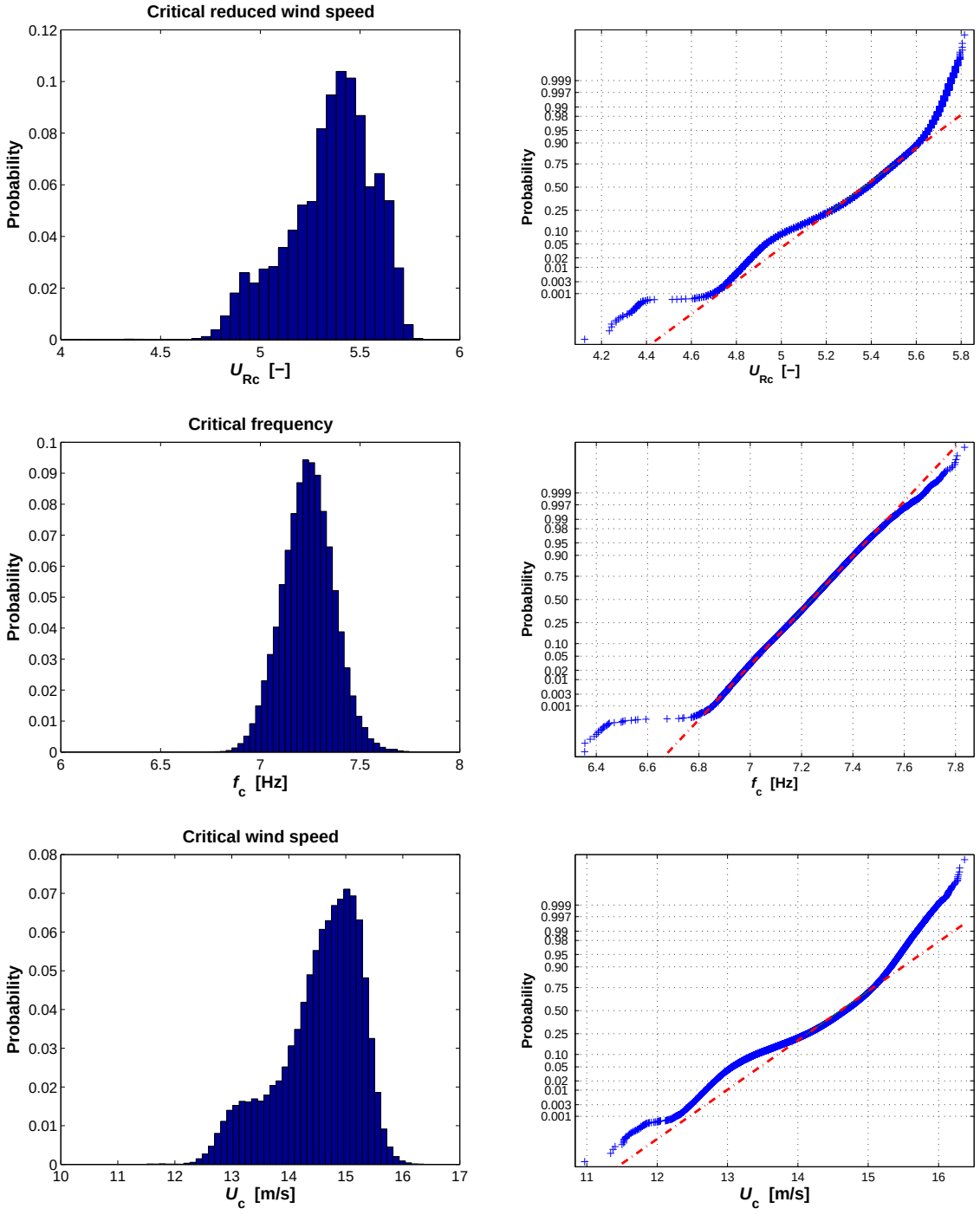

Figure 4.5: Probability distribution and normal probability plot ($N = 100000$) of the critical reduced wind speed (U_{Rc}), frequency (f_c) and dimensional wind speed (U_c) for the rectangular cylinder R12.5 in turbulent flow

Table 4.1: Dynamic parameters of the two rectangular cylinders ($\rho = 1.25$ kg/m^3)

B/D	m [kg/m]	I [kgm^2/m]	ζ_h [%]	ζ_α [%]	f_h [Hz]	f_α [Hz]	γ_ω [-]
12.5	3.810	0.037	0.18	0.28	5.87	8.30	1.414
5.0	3.157	0.010	0.16	0.55	3.90	7.70	1.974

Table 4.2: Measured and deterministically calculated flutter critical reduced wind speed (U_{Rc}), frequency (f_c) and dimensional wind speed (U_c) for two rectangular cylinders [N/R = Not Reached]

		Measured			Deterministic calculation		
B/D	Flow	U_c (divergence) [m/s]	U_c (coupling) [m/s]	f_c [Hz]	U_{Rc} [-]	f_c [Hz]	U_c [m/s]
12.5	Smooth	16.90	15.54	7.37	6.43	7.20	17.35
	Turbulent	N/R	N/R	N/R	5.79	7.01	15.22
5.0	Smooth	6.90	N/R	7.47	5.37	7.45	8.00
	Turbulent	N/R	N/R	N/R	N/R	N/R	N/R

In the case of the rectangular cylinder R12.5 in smooth flow bimodal distributions are found for the flutter boundaries (Fig. 4.2). The mode corresponding to larger critical wind speed is close to the deterministic result and experimentally measured values. Conversely the second mode in the distributions, corresponding to a reduced wind speed slightly larger than 4.5, is due to the particular characteristics of the A_2^* flutter derivative. In Fig. 4.3 it is possible to see that around $U_{Rc} = 4.5$ the pattern of the mean values of A_2^* shows a hump, which implies a sudden reduction of the aerodynamic damping in pitch. For the same reduced wind speed the standard deviation also increases and these two factors imply a certain probability that the eigenvalue analysis gives a flutter wind speed falling in this range. This fact is evident from Fig. 4.4, where the deterministic solution of the flutter equations is compared to the one relative to a Monte-Carlo simulation of the flutter derivatives. The origin of this hump is not known but, if it is physical, that means that in the aforementioned range of reduced velocity the total damping becomes very small and the flutter instability limit is close. Therefore, even though

Table 4.3: Results of the probabilistic flutter calculation for two rectangular cylinders (μ = mean; CoV = Coefficient of Variation; skw = skewness; krt = kurtosis)

		U_{Rc}				f_c				U_c			
		μ [-]	CoV [%]	skw [-]	krt [-]	μ [Hz]	CoV [%]	skw [-]	krt [-]	μ [m/s]	CoV [%]	skw [-]	krt [-]
12.5	smooth	6.02	4.35	-4.33	23.09	7.10	1.43	0.90	5.07	16.01	4.16	-3.07	15.42
12.5	turb.	5.35	4.00	-0.61	2.96	7.24	1.78	-0.01	3.44	14.53	4.95	-0.78	3.05
5.0	smooth	5.11	2.59	0.14	2.85	7.23	2.11	-0.02	2.31	7.38	3.92	0.14	2.59

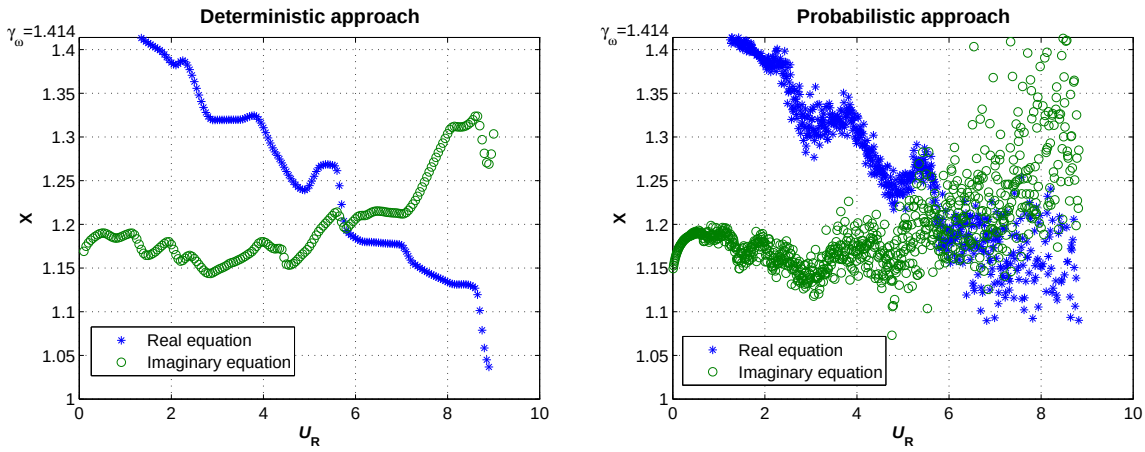

Figure 4.6: Deterministic and probabilistic flutter solution: R12.5 in turbulent flow

in the experimental tests for that reduced wind speed the section model was stable, a small change in the actual dynamic parameters could be enough for the onset of flutter oscillations at a wind speed much lower than expected. The probabilistic approach with the resulting bimodal probability distributions warns about this unusual situation. Conversely, if the local behavior of the flutter derivative A_2^* is only due to measurement errors, the deterministic flutter calculation, especially if only one or few measurements are performed at each wind speed (as it is often the case), could lead to a large underestimation (in this particular case) of the flutter critical wind speed. Obviously, the probabilistic approach is not able to explain the origin of the two modes in the probability distributions but in any case it warns about this peculiar behavior and suggests that more investigations are needed. The large kurtosis and negative skewness for this case study, reported in Tab. 4.3, is due to the significant bimodality of the probability distributions of the reduced and dimensional critical wind speed. The mean value of the calculated flutter velocity slightly underestimates the measured one, while the deterministic result moderately overestimates it (Tab. 4.2). The coefficients of variation are smaller than 5 %.

The probability distributions obtained for the same rectangular cylinder R12.5 in turbulent flow are more regular and tend to concentrate close to the deterministic result, as shown in Fig. 4.6 and Tab. 4.3. Nevertheless, a small tendency to bimodality is still present in the distribution of the critical wind speed (Fig. 4.5). In spite of the large scatter affecting the flutter derivatives, the coefficients of variation of the critical wind speed and frequency are definitely small (between 1.78 % and 4.95 %).

Finally, the case of the bluffer rectangular cylinder R5 in smooth flow, which is prone to single-degree-of-freedom torsional flutter, seems to show the higher degree of reliability of the results. As a matter of fact the probability distributions are the most regular with a mean values which still overestimates the measured flutter critical wind speed but less than the deterministic result. Conversely the critical frequency is slightly underestimated (see Tabs. 4.2-4.3 and Fig. 4.8). The coefficient of variations are small (less than 4 %), the skewness is very

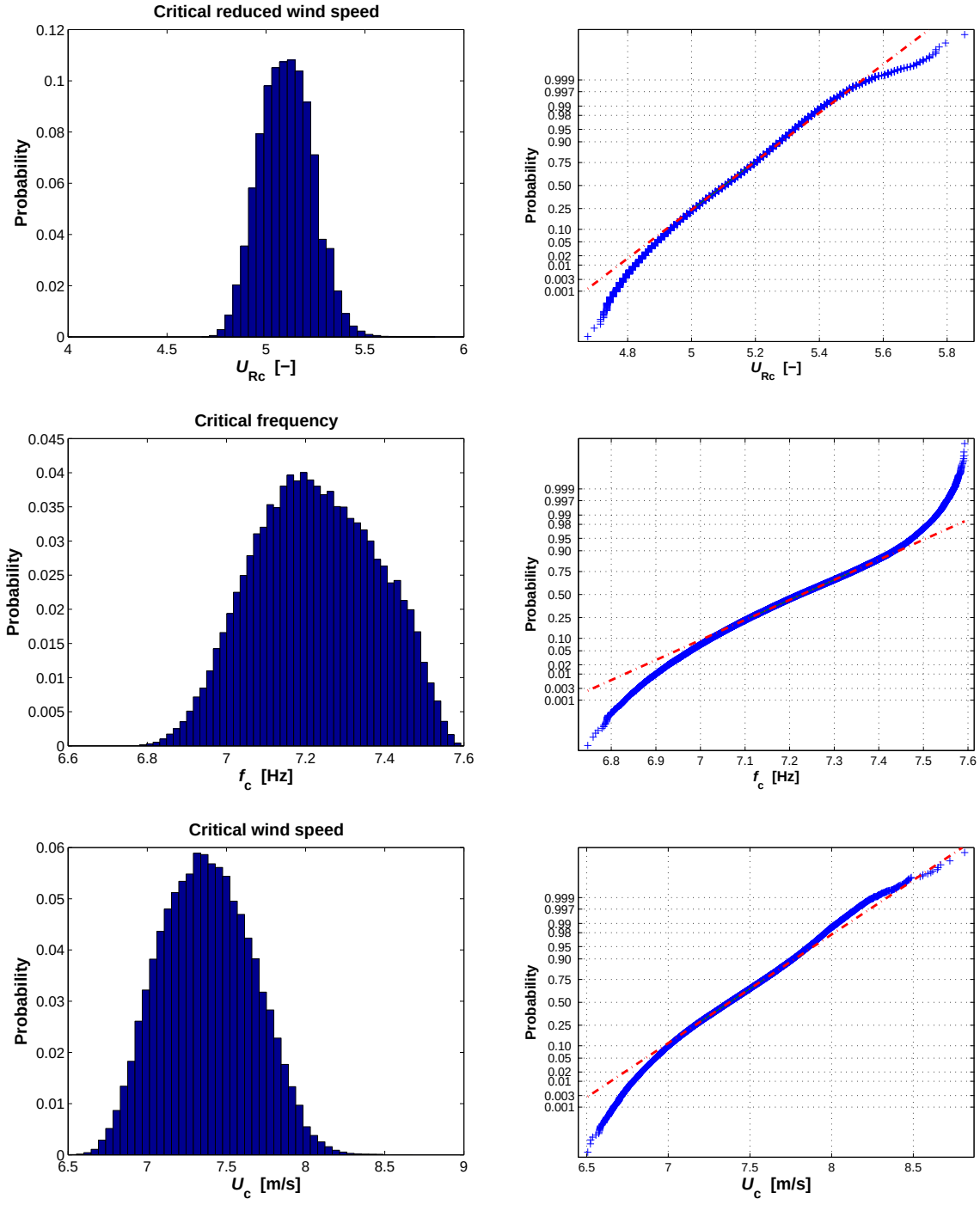

Figure 4.7: Probability distribution and normal probability plot ($N = 100000$) of the critical reduced wind speed (U_{Rc}), frequency (f_c) and dimensional wind speed (U_c) for the rectangular cylinder R5 in smooth flow

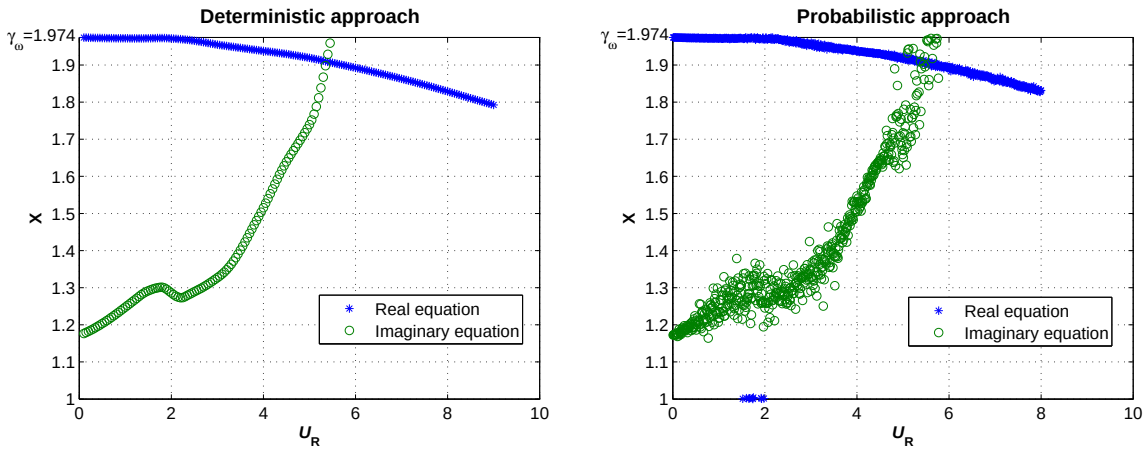

Figure 4.8: Deterministic and probabilistic flutter solution: R5 in smooth flow

small and the kurtosis not far from 3. It must be pointed out that a limited extrapolation is needed for the flutter derivatives corresponding to the pitching degree of freedom. This is done by fitting the mean values with appropriate polynomial curves. In addition, at the highest wind speed only one measure is available, therefore an "average" standard deviation is associated to this point and then kept constant for the extrapolated ones. It is then worth reminding that for the other reduced wind speeds only three measurements are available and consequently the significance of the results for this last test case is only partial.

The case R5 in turbulent flow is not analyzed because flutter was not reached in the wind speed range experimentally tested and above all because with the logical extrapolation of the flutter derivatives no solution is found in the eigenvalue analysis neither (Tab. 4.2).

Finally, the hypothesis of Gaussian distribution for the Monte-Carlo simulation results is tested via Lilliefors and Jarque-Bera tests (5 % significance level) which always give negative answer. The fact that the distributions of the flutter critical wind speed and frequency are not Gaussian, even though the flutter derivatives are normally distributed, is due to the high nonlinearity of the flutter equations [Eqs. (2.53)-(2.54)] and it can be appreciated in the normal probability plots in Figs. 4.2-4.7. In Fig. 4.9 the Cumulative Distribution Function (CDF) of the critical wind speed in the three case studies is compared to the corresponding Gaussian distribution. Remarkable differences can be appreciated for R12.5 in smooth and turbulent flow, whereas for R5 in smooth flow, in spite of the statistical tests, the two distributions are very similar.

4.4 Application to the tested bridge section

The probabilistic flutter approach is now applied to the tested single-box girder bridge section, whose flutter derivatives are presented and discussed in Chapter 3. At this stage the dependence of flutter derivatives on mean angle of can be waived since the measured aeroelastic functions are used to calculate the flutter wind speed for "test case 0", that is the configura-

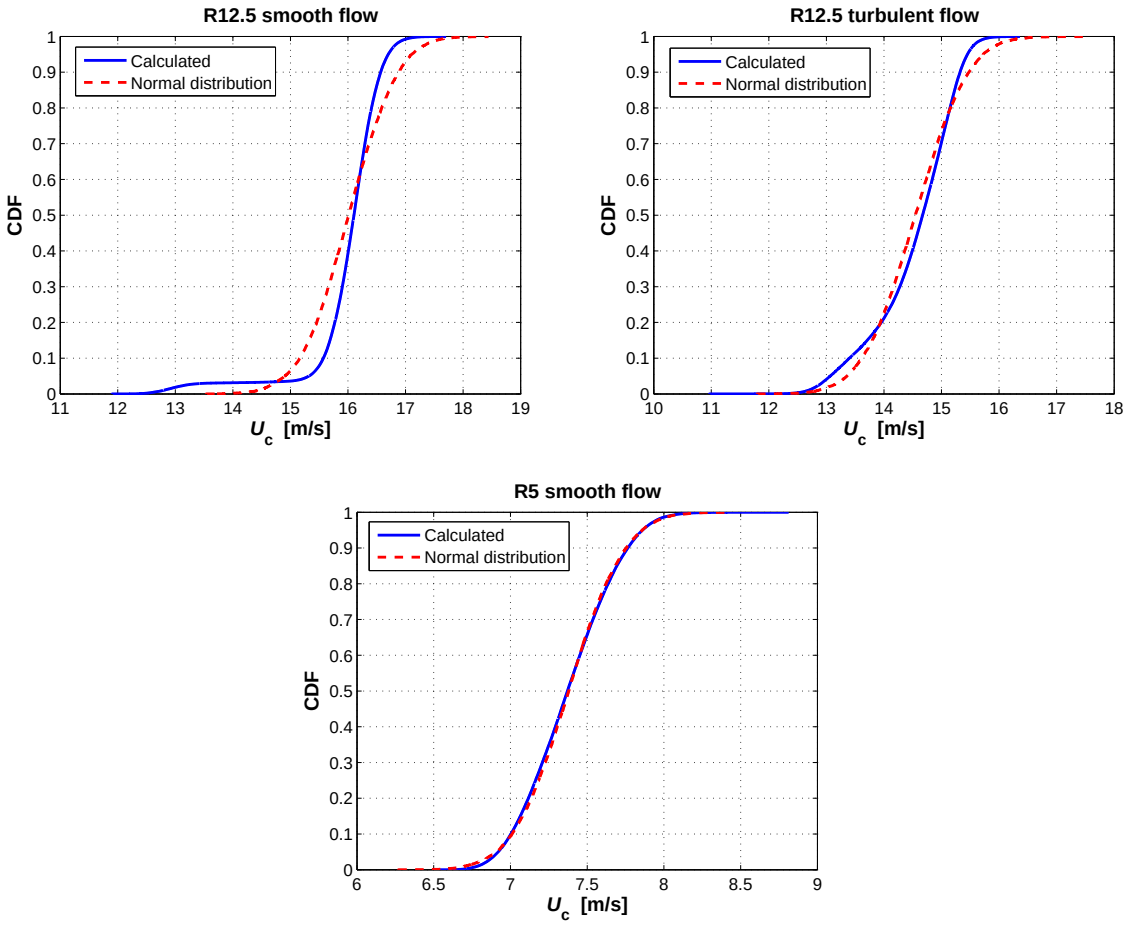

Figure 4.9: Cumulative Distribution Function (CDF) of the flutter critical wind speed for the studied rectangular cylinders

tion on which they are measured, and "test case 2", where the suspension system is the same but eccentric masses are added. It means that, once the wind speed is fixed, the mean angle of attack is the same in the two cases. Therefore only the derivatives corresponding to the still-air angle of attack α_0=0° are needed. The dynamic parameters for the two test cases are repeated here in Tab. 4.4. The flow is smooth in both cases, that means characterized by a wind-tunnel physiologic turbulence intensity of about 1 %.

The statistical properties of the flutter derivatives has already been discussed in section 4.1, showing that a Gaussian distribution is appropriate. Here it is worth reminding that samples of ten measures are available for each reduced wind speed. In Fig. 4.10 the flutter derivatives for the bridge section are reported, showing the interpolated mean values and the 95.44 % confidence interval, defined by $\pm 2\sigma$, where σ is the standard deviation. Very limited extrapolations for the flutter derivatives corresponding to the pitching degree-of-freedom (H_2^*, H_3^*, A_2^* and A_3^*) are needed to perform correctly the computations. This is obtained by fitting the data with second, third or fourth-order polynomial functions. The same standard deviation as for the last reduced wind speed measurement is attributed to the extrapolated values. An example of Monte-Carlo generated flutter derivatives H_1^* and A_2^* is shown in Fig. 4.11.

The probabilistic flutter calculation results for "test case 0" are shown in Fig. 4.12-4.13 and Tab. 4.6. The probability distributions are regular and tend to concentrate close to the deterministic results and measured values. The mean of the distribution of the critical wind speed is slightly smaller than the deterministically calculated value but still very close to the measured one (Tab. 4.5). The coefficients of variation of the critical parameters are very small (less than 2 %) and that allows to conclude that the flutter derivatives are characterized by a high degree of reliability. The distributions show small values of the skewness and kurtosis close to 3. Lilliefors and Jarque-Bera tests at the significance level of 5 % suggest that the hypothesis of Gaussian distribution should be refused but it is clear from the probability plots in Fig. 4.12 and above all the cumulative distribution function in Fig. 4.14 that a normal approximation is in this case reasonable.

For "test case 2" the results are shown in Fig. 4.15-4.16 and Tab. 4.6. Also in this case the probability distributions are quite regular and tend to distribute close to the deterministic results. The mean values are only moderately closer to the measured critical wind speed and frequency but a significant discrepancy still remains, showing that it does not depend on the averaging process performed before starting the deterministic eigenvalue analysis. The variance of the distributions is even smaller than in the previous test case (the coefficient of variation is always smaller than 1.4 %), coherently with the fact that the scatter of the flutter derivatives decreases while moving towards smaller reduced wind speed. Conversely the distributions are slightly skewer than before, with also larger values of the kurtosis, showing that the output random variables are not normally distributed, as confirmed by Lilliefors and Jarque-Bera tests. Fig. 4.17 displays the CDF of the calculated critical wind speed and it puts in evidence the limited difference with respect to the corresponding Gaussian distribution.

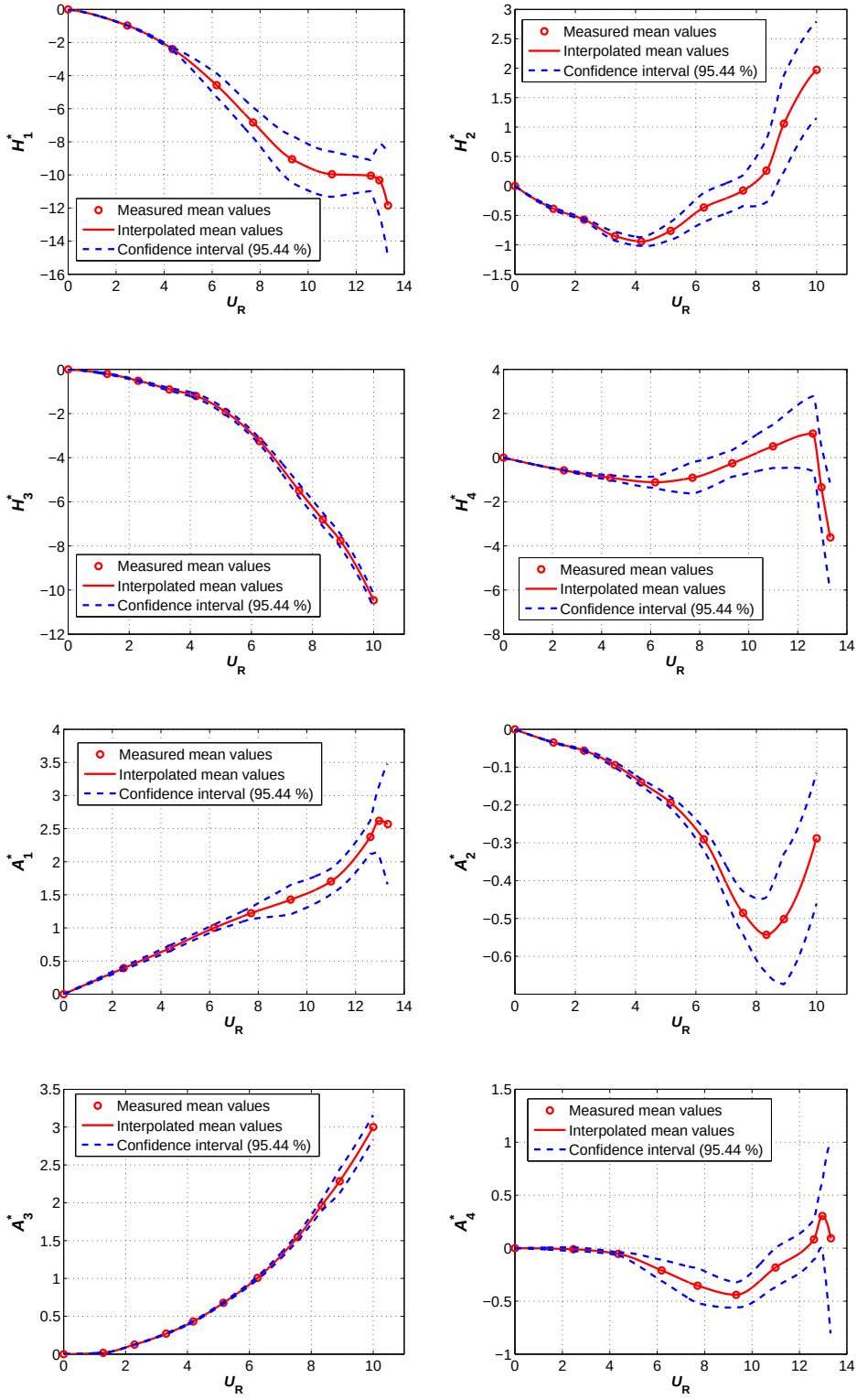

Figure 4.10: Flutter derivative mean values and 95.44 % confidence intervals (α_0=0°)

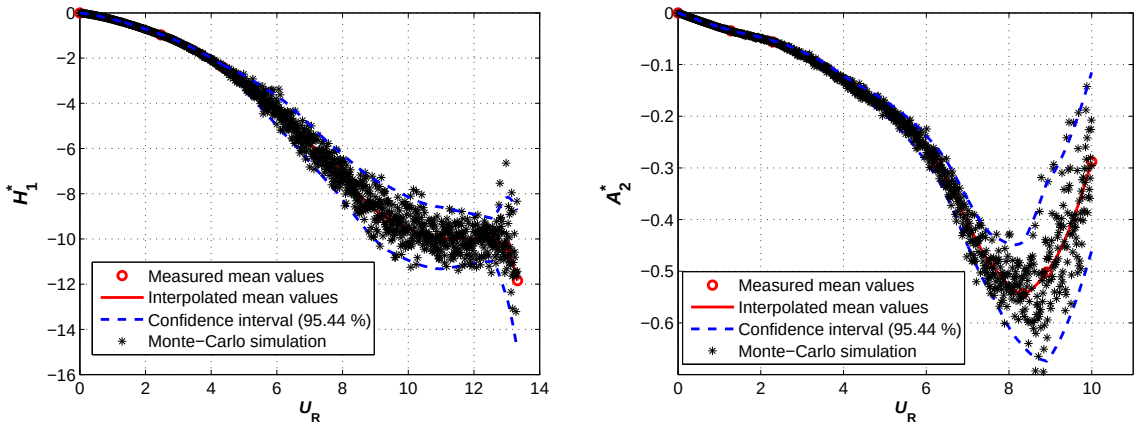

(a) (b)

Figure 4.11: Example of flutter derivatives obtained via Monte-Carlo simulations

Table 4.4: Dynamic parameters for flutter calculation. In "test case 0" the experimental set-up is the same as the one on which the flutter derivatives are measured

	ρ [kg/m^3]	m [kg/m]	I [kgm^2/m]	ζ_h [%]	ζ_α [%]	f_h [Hz]	f_α [Hz]	γ_ω [-]
Test case 0	1.195	5.449	0.0955	0.24	0.18	3.055	5.953	1.948
Test case 2	1.212	6.289	0.2311	0.0	0.0	2.847	3.788	1.331

Table 4.5: Measured and deterministically calculated flutter critical reduced wind speed (U_{Rc}), frequency (f_c) and dimensional wind speed (U_c) for the single-box girder bridge cross section

	Measured			Deterministic calculation		
	U_{Rc} [-]	f_c [Hz]	U_c [m/s]	U_{Rc} [-]	f_c [Hz]	U_c [m/s]
Test case 0	9.30	4.74	19.86	9.42	4.69	19.89
Test case 2	7.24	3.56	11.60	8.96	3.45	13.90

Table 4.6: Results of the probabilistic flutter calculation for the single-box girder bridge cross section (μ = mean; CoV = Coefficient of Variation; skw = skewness; krt = kurtosis)

	U_{Rc}				f_c				U_c			
	μ [-]	CoV [%]	skw [-]	krt [-]	μ [Hz]	CoV [%]	skw [-]	krt [-]	μ [m/s]	CoV [%]	skw [-]	krt [-]
Test case 0	8.97	1.40	-0.16	2.86	4.73	0.98	0.11	3.09	19.12	1.53	-0.03	2.89
Test case 2	8.54	1.38	-0.75	4.32	3.47	0.34	-0.07	3.05	13.33	1.30	-0.66	4.09

4.5 Conclusions

In this chapter a probabilistic model of flutter assessment is proposed. The model is based on three assumptions which are extensively discussed in section 4.2. Three applications on rectangular cylinders in smooth and turbulent flow and two on the single-box girder bridge cross section whose experimental results are presented in this dissertation, are discussed. The method, based on Monte-Carlo simulation, gives the probability distribution of the critical flutter wind speed and frequency and therefore their coefficient of variation. This statistic is very important because it allows to estimate the actual degree of reliability of the calculated flutter boundaries and indirectly of the measured flutter derivatives, which is completely unknown if a deterministic approach is followed. One of the most interesting results of the analyses performed in this chapter is the fact that, despite the large dispersion of the measured flutter derivatives, the coefficient of variation of the critical wind speed and frequency is always very small. This outcome could be due to the high nonlinearity of the flutter equations and to the fact that only few aeroelastic coefficients actually contribute to the flutter instability mechanism (see Chapter 6). Nevertheless, in the case of the rectangular cylinder R12.5 in smooth flow, the probabilistic approach shows the limited reliability of the deterministic result, suggesting more investigation about the reason of the bimodal shape of the probability distributions. A slightly bimodal distribution is obtained also for R12.5 in turbulent flow but in this case its origin is not clear. In addition it can be remarked that, despite the normal distribution of the flutter derivatives, the output random variables are found to be generally non-Gaussian, as the effect of the nonlinear structure of the flutter equations. Nevertheless, in some cases the normal approximation seems to work quite well.

It is worth noting that in the previous analyses, the mean value of the flutter critical wind speed is smaller than the one calculated through the deterministic approach, although very close to it. This is due to the fact that the intersection between the "clouds" of solutions of the imaginary and real equations is searched by increasing the reduced wind speed and therefore approaching the solution from above. In any case this means the the probabilistic approach offers a slightly more conservative solution the the deterministic calculation.

The probabilistic model can also be implemented in a Performance-Based Design application to deal with the vulnerability ring in the risk-assessment chain. As a matter of fact the cumulative distribution function of the flutter critical wind speed (Figs. 4.9, 4.14 and 4.17) can be read as the probability of collapse of a bridge due to flutter, given a certain measure of the hazard, that is the mean wind speed in the specific site at the height of the deck, which is in turn defined by another probability distribution. In other words this method allows to calculate the term $p(SL|IM)$ in the modified PEER convolution integral [Eq. (4.2)], accounting for the uncertainty in the self-excited forces. It is worth noting that, although the degree of randomness of the aeroelastic coefficients seems to be much higher and effective than the one of the structural parameters, strictly speaking also the uncertainty on the bridge structural properties should be considered. However, this is out of the scopes of the present research work and therefore this complication of the model is waived.

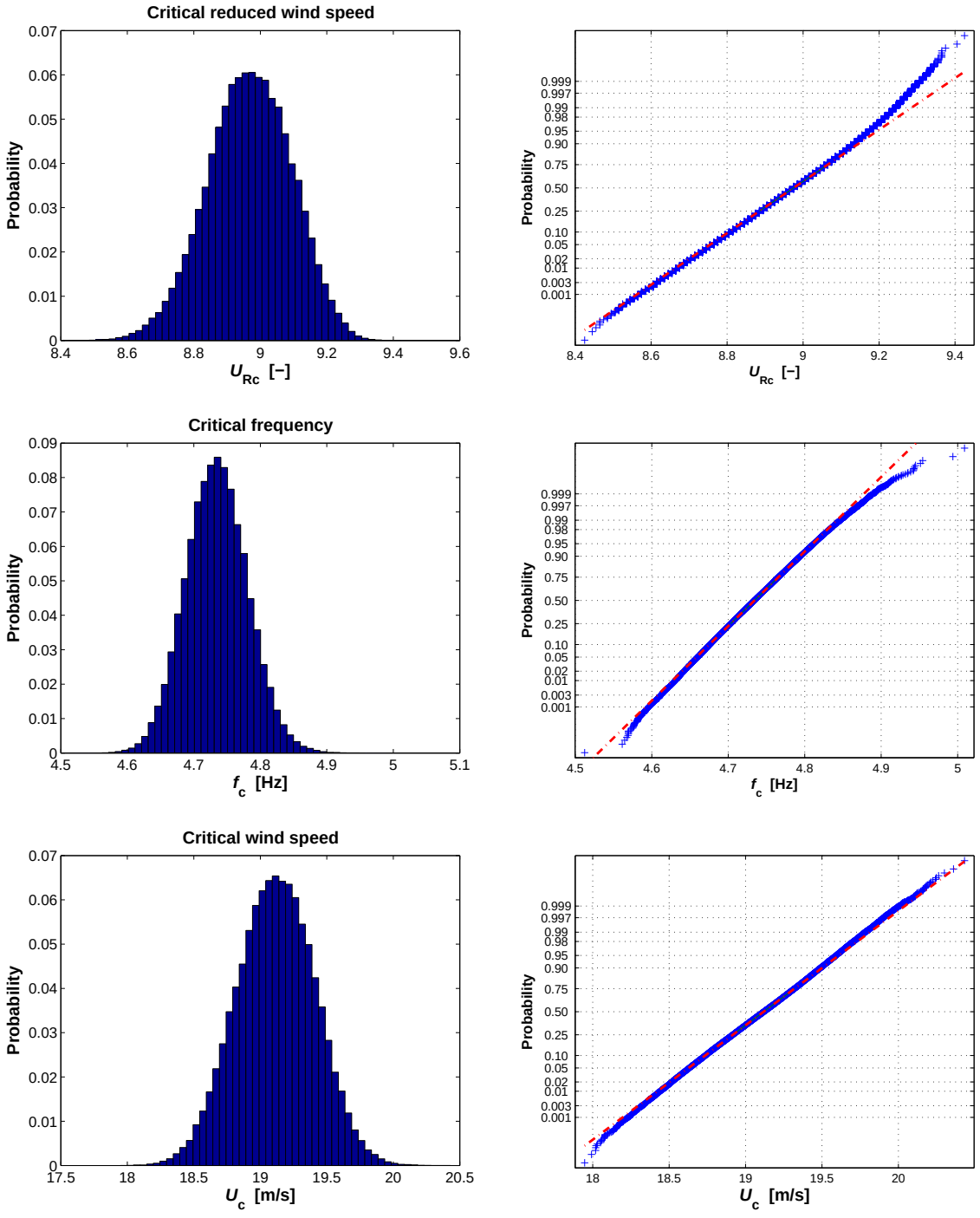

Figure 4.12: Probability distribution and normal probability plot ($N = 100000$) of the critical reduced wind speed (U_{Rc}), frequency (f_c) and dimensional wind speed (U_c) for "test case 0"

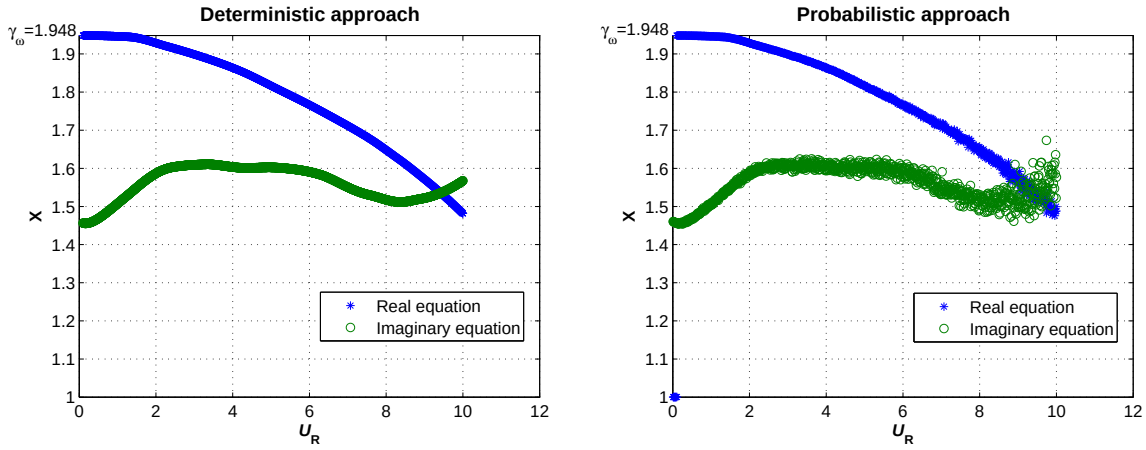

Figure 4.13: Deterministic and probabilistic flutter solution: "test case 0"

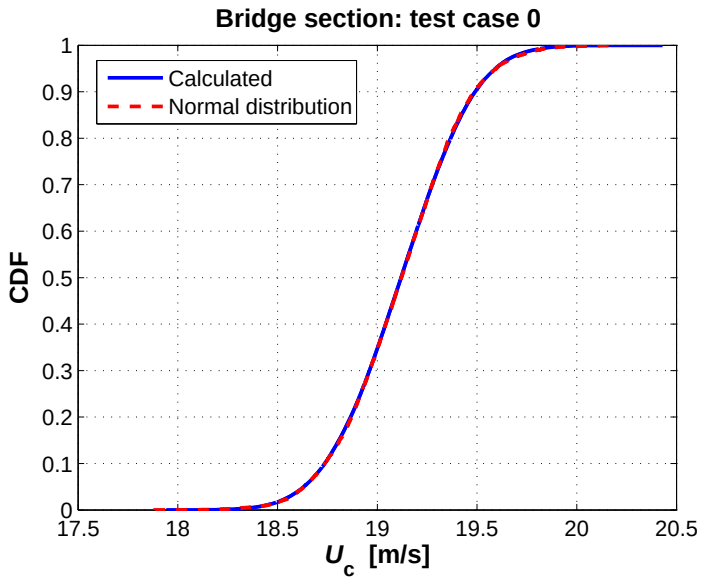

Figure 4.14: Cumulative Distribution Function (CDF) of the critical flutter wind speed for "test case 0"

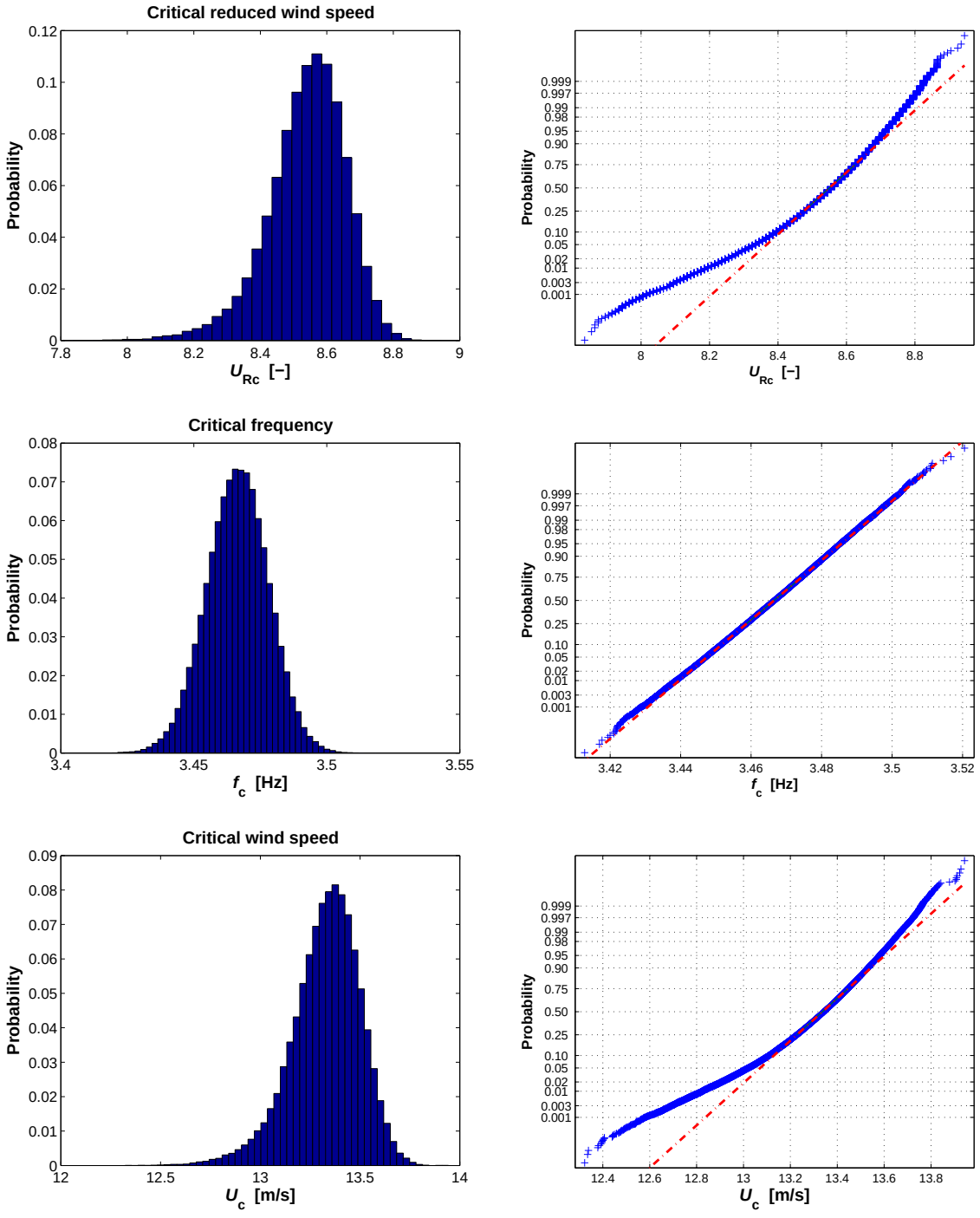

Figure 4.15: Probability distribution and normal probability plot ($N = 100000$) of the critical reduced wind speed (U_{Rc}), frequency (f_c) and dimensional wind speed (U_c) for "test case 2"

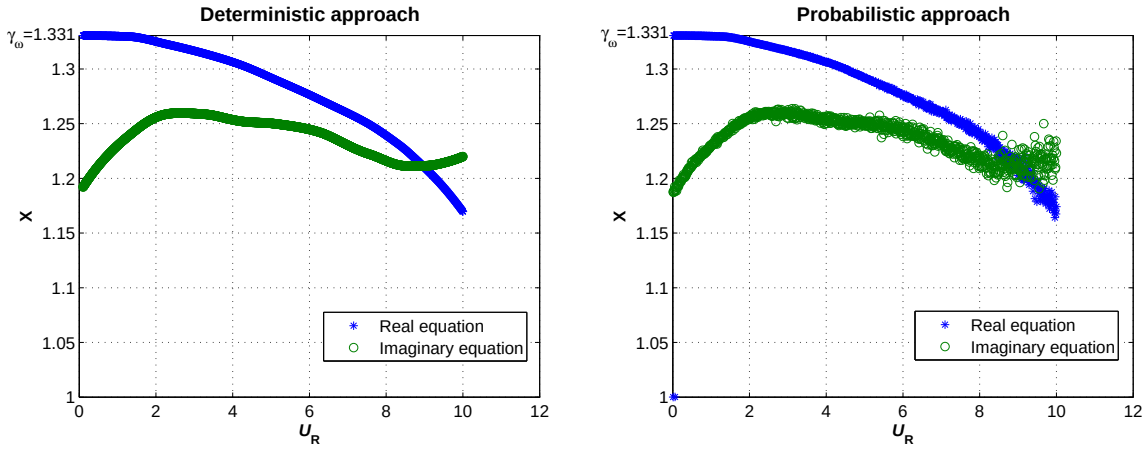

Figure 4.16: Deterministic and probabilistic flutter solution: "test case 2"

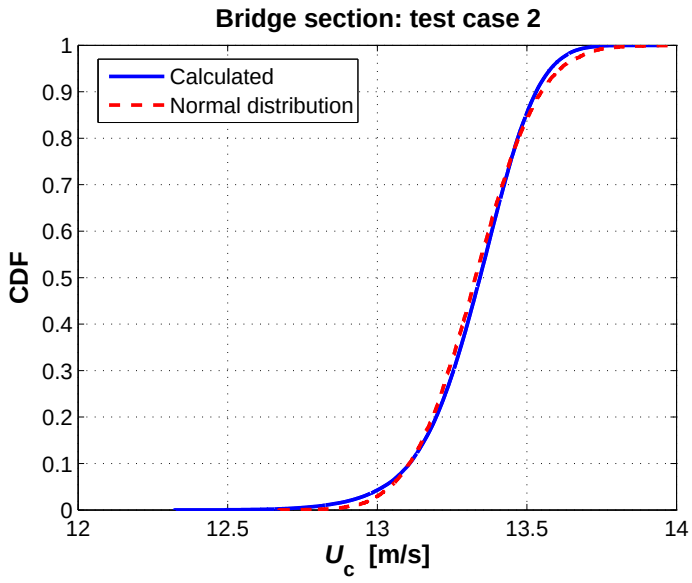

Figure 4.17: Cumulative Distribution Function (CDF) of the critical flutter wind speed for "test case 2"

Chapter 5

From multimodal to bimodal approach to flutter

5.1 Introduction

In the section 1.4 it is stated that code-implementation can be an effective strategy of risk mitigation and in Fig. 1.4 the procedure we are following to set up a simplified method of flutter assessment is schematized. The simplified formulas and the discussion about flutter derivative generalization are treated in the next two chapters. Here only the first box of the flow chart is analyzed, that is the simplification from multimodal to bimodal approach to flutter. This step is crucial because it implies a strong simplification of the model, reducing the number of experimental functions from 18 to 8 and the number of modes from n to 2. In this way the flutter calculation becomes much easier to handle, reducing the possibilities of error and allowing a better understanding of the basic features of the phenomenon. Nevertheless, the most important consequence of this simplification is that the identification of ten flutter derivatives, namely H_5^*, H_6^*, A_5^*, A_6^*, P_1^*,...,P_6^*, which are extremely difficult to be measured in wind tunnel and whose reliability is known to be poor, is no longer necessary.

The bimodal approach to flutter is often adopted instead of the multimodal one in practical applications but it is not completely clear which is the approximation which it actually introduces. Since the simplified formulas we are proposing in Chapter 6 are directly based on the assumption of binary flutter, it is crucial to check accurately the validity of this model.

Several investigations about the multimodal approach to flutter seem to suggest that the nature of the phenomenon is less complicated and that generally only a bending and a torsional mode give rise to the instability. This seems to be true even for such a peculiar structure like Messina Strait Bridge, where, according to D'Asdia and Sepe (1998) and Caracoglia (2000), only the first antisymmetric vertical bending and torsional modes couple in the neighborhood of the critical wind speed.

The scope of the present chapter is to discuss and clarify the relationship between multimode and binary flutter, highlighting the individual steps that lead to the simplified model and the possible limits in their validity. Finally two examples of bridge structures are analyzed to support the theoretical investigations.

5.2 Multimodal approach to flutter

The basic assumptions whereon the theory of flutter usually stands are:

1. the structure undergoes small displacements around a static deformed configuration so that linear elastic behavior can be postulated;

2. the structural vibrations are viscously damped;

3. linearized self-excited forces are assumed for the condition of incipient instability;

4. the self-excited forces act on the 3D-vibrating deck depending only on the instantaneous local angle of attack [strip theory; e.g. Fung (1993)].

Moreover, the following commonly accepted assumptions are retained in the present formulation:

5. large-scale turbulence does not affect the flutter instability mechanism;

6. the flow mean velocity is constant along the bridge span;

7. the external deck geometry is constant along the span and, for the evaluation of the flutter derivatives, the mean angle of attack due to the static wind load can be considered as constant too.

The fifth point is particularly critical and it will be discussed later on in the chapter. The last assumption is dropped in Katsuchi *et al.* (1999), with the consequent heavy numerical complications.

For each deck strip the equations of motion can be written for the three components of the displacement which define the vibration of the structure:

$$m\ddot{h}(x,t) + S_x\ddot{\alpha}(x,t) + c_h\dot{h}(x,t) + K_h h(x,t) = L_{se}(x,t,K) \tag{5.1}$$

$$I\ddot{\alpha}(x,t) + S_x\ddot{h}(x,t) + S_z\ddot{p}(x,t) + c_\alpha\dot{\alpha}(x,t) + K_\alpha\alpha(x,t) = M_{se}(x,t,K) \tag{5.2}$$

$$m\ddot{p}(x,t) + S_z\ddot{\alpha}(x,t) + c_p\dot{p}(x,t) + K_p p(x,t) = D_{se}(x,t,K) \tag{5.3}$$

where h, α and p denote the vertical bending, torsional and lateral bending displacements (Fig. 5.1); m, I, S_x and S_z are respectively the mass, mass moment of inertia and the lateral and vertical static unbalance per unit length; c_h, c_α, c_p are the coefficients of viscous damping; K_h, K_α and K_p are the stiffness values related to the three degrees of freedom. x is the abscissa along the span and the dot denotes the derivative with respect to time t; $K = B\omega/U$ is the reduced frequency of oscillation, being as usual B the deck chord, ω the circular frequency of oscillation and U the mean wind speed.

The self-excited lift, moment and drag can be expressed in the frequency domain through the Scanlan's formulation with eighteen flutter derivatives [e.g. Jain *et al.* (1996); Katsuchi *et al.* (1999)]:

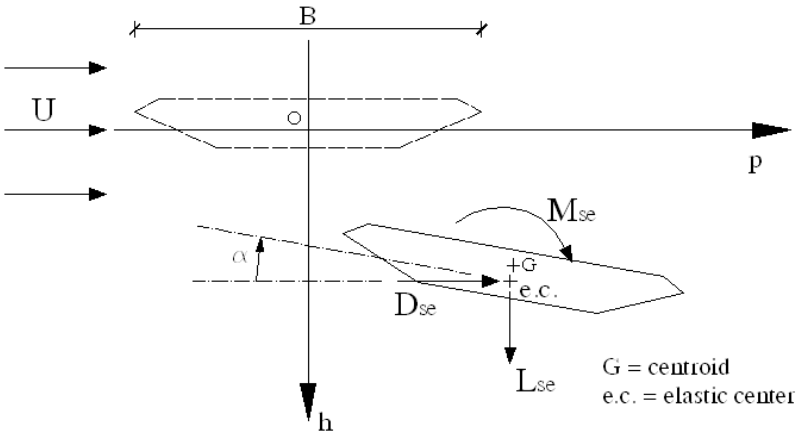

Figure 5.1: Reference system for displacements and self-excited forces

$$L_{se}(x,t,K) = \frac{1}{2}\rho U^2 B[KH_1^*\frac{\dot{h}}{U} + KH_2^*\frac{B\dot{\alpha}}{U} + K^2H_3^*\alpha + K^2H_4^*\frac{h}{B} + KH_5^*\frac{\dot{p}}{U} + K^2H_6^*\frac{p}{B}] \quad (5.4)$$

$$M_{se}(x,t,K) = \frac{1}{2}\rho U^2 B^2[KA_1^*\frac{\dot{h}}{U} + KA_2^*\frac{B\dot{\alpha}}{U} + K^2A_3^*\alpha + K^2A_4^*\frac{h}{B} + KA_5^*\frac{\dot{p}}{U} + K^2A_6^*\frac{p}{B}] \quad (5.5)$$

$$D_{se}(x,t,K) = \frac{1}{2}\rho U^2 B[KP_1^*\frac{\dot{p}}{U} + KP_2^*\frac{B\dot{\alpha}}{U} + K^2P_3^*\alpha + K^2P_4^*\frac{p}{B} + KP_5^*\frac{\dot{h}}{U} + K^2P_6^*\frac{h}{B}] \quad (5.6)$$

where ρ is the air density. The buffeting forces due to turbulence are not included here since they are supposed not to affect the stability of the bridge.

By means of the following modal decomposition:

$$h(x,t) = \sum_{r=1}^{N} h_r(x)B\xi_r(t) \quad (5.7)$$

$$\alpha(x,t) = \sum_{r=1}^{N} \alpha_r(x)\xi_r(t) \quad (5.8)$$

$$p(x,t) = \sum_{r=1}^{N} p_r(x)B\xi_r(t) \quad (5.9)$$

where N is the number of modes taken into account, $h_r(x)$, $\alpha_r(x)$, $p_r(x)$ are the dimensionless mode shapes and $\xi_r(t)$ the generalized coordinates, the model can be switched into the modal space, obtaining a system of N aerodynamically coupled equations:

$$I_j[\ddot{\xi_j}(t) + 2\zeta_j\omega_j\dot{\xi_j}(t) + \omega_j^2\xi_j(t)] = Q_j(t,K) \quad (5.10)$$

where I_j, ω_j and ζ_j are respectively the generalized mass, the circular frequency and the damping ratio-to-critical associated with the j-th eigenmode of the structure (j=1...N). $Q_j(t,K)$ is the frequency-time dependent generalized force given by:

$$Q_j(t,K) = \int_S (L_{se}Bh_j + M_{se}\alpha_j + D_{se}Bp_j)ds \cong \int_D (L_{se}Bh_j + M_{se}\alpha_j + D_{se}Bp_j)dx \quad (5.11)$$

The subscript S in Eq. (5.11) indicates that the integral is extended to the whole structure while D means that it is limited to the deck. In Eq. (5.11) it is assumed that the contribution of the self-excited forces to flutter instability is negligible outside the deck. This seems to be acceptable for lift and moment but is known to be a rough approximation for drag. The generalized mass is given by:

$$I_j = \int_S \eta_j^2(x,y,z) \cdot dm(x,y,z) \quad (5.12)$$

where $\eta_j(x,y,z)$ is the full bridge mode shape and dm the infinitesimal mass. Introducing a reference length L (usually the main span length), the equations of motion can be written in the following way (Jain *et al.*, 1996):

$$\begin{aligned} I_j(\ddot{\xi}_j + 2\zeta_j\omega_j\dot{\xi}_j + \omega_j^2\xi_j) = \frac{1}{2}\rho U^2 B^2 L \cdot [& KH_1^* \sum_{r=1}^{N} \frac{B\dot{\xi}_r}{U} G_{h_r h_j} + KH_2^* \sum_{r=1}^{N} \frac{B\dot{\xi}_r}{U} G_{\alpha_r h_j} + \\ & K^2 H_3^* \sum_{r=1}^{N} \xi_r G_{\alpha_r h_j} + K^2 H_4^* \sum_{r=1}^{N} \xi_r G_{h_r h_j} + KH_5^* \sum_{r=1}^{N} \frac{B\dot{\xi}_r}{U} G_{p_r h_j} + K^2 H_6^* \sum_{r=1}^{N} \xi_r G_{p_r h_j} + \\ & KA_1^* \sum_{r=1}^{N} \frac{B\dot{\xi}_r}{U} G_{h_r \alpha_j} + KA_2^* \sum_{r=1}^{N} \frac{B\dot{\xi}_r}{U} G_{\alpha_r \alpha_j} + K^2 A_3^* \sum_{r=1}^{N} \xi_r G_{\alpha_r \alpha_j} + K^2 A_4^* \sum_{r=1}^{N} \xi_r G_{h_r \alpha_j} + \\ & KA_5^* \sum_{r=1}^{N} \frac{B\dot{\xi}_r}{U} G_{p_r \alpha_j} + K^2 A_6^* \sum_{r=1}^{N} \xi_r G_{p_r \alpha_j} + KP_1^* \sum_{r=1}^{N} \frac{B\dot{\xi}_r}{U} G_{p_r p_j} + KP_2^* \sum_{r=1}^{N} \frac{B\dot{\xi}_r}{U} G_{\alpha_r p_j} + \\ & K^2 P_3^* \sum_{r=1}^{N} \xi_r G_{\alpha_r p_j} + K^2 P_4^* \sum_{r=1}^{N} \xi_r G_{p_r p_j} + KP_5^* \sum_{r=1}^{N} \frac{B\dot{\xi}_r}{U} G_{h_r p_j} + K^2 P_6^* \sum_{r=1}^{N} \xi_r G_{h_r p_j}] \end{aligned} \quad (5.13)$$

where the coefficients denoted by G are the modal integrals:

$$G_{l_r n_j} = \int_D l_r(x) \cdot n_j(x) \frac{dx}{L} \quad (5.14)$$

and l, $n = h$, α, p ; $r, j = 1...N$. It is important to point out that if the deck geometry, the mean wind speed and the mean angle of attack are significantly varying along the span, the flutter derivatives are functions of the position x as well and they have to be kept inside the integral of Eq. (5.14), as shown in Katsuchi *et al.* (1999).

In order to determine the flutter critical condition, harmonic oscillation at the common frequency ω is assumed:

$$\xi_j(t) = \xi_{0j} e^{i\omega t} \tag{5.15}$$

where $i = \sqrt{-1}$ is the imaginary unit. The following equation in matrix notation is finally obtained:

$$\mathbf{E}(\mathbf{X}, K) \cdot \boldsymbol{\xi_0} = [\mathbf{D}(\mathbf{X}, K) + i\mathbf{F}(\mathbf{X}, K)] \cdot \boldsymbol{\xi_0} = 0 \tag{5.16}$$

where it is set:

$$\mathbf{X} = (X_j)_{j=1\ldots N} \tag{5.17}$$

$$\boldsymbol{\xi_0} = (\xi_{0j})_{j=1\ldots N} \tag{5.18}$$

being $\mathbf{E}(\mathbf{X}, K)$ the matrix of the complex system of equations, whose components are given by:

$$\begin{aligned} E_{jr}(X_j, K) =& (1 - 2i\zeta_j X_j - X_j^2) \cdot \delta_{jr} + \gamma_j \cdot [(iH_1^* + H_4^*)G_{h_r h_j} + (iH_2^* + H_3^*)G_{\alpha_r h_j} + \\ & (iH_5^* + H_6^*)G_{p_r h_j} + (iA_1^* + A_4^*)G_{h_r \alpha_j} + (iA_2^* + A_3^*)G_{\alpha_r \alpha_j} + (iA_5^* + A_6^*)G_{p_r \alpha_j} + \\ & (iP_1^* + P_4^*)G_{p_r p_j} + (iP_2^* + P_3^*)G_{\alpha_r p_j} + (iP_5^* + P_6^*)G_{h_r p_j}] \end{aligned} \tag{5.19}$$

where

$$\gamma_j = \frac{\rho B^4 L}{2I_j} \tag{5.20}$$

$$X_j = \frac{\omega_j}{\omega} \tag{5.21}$$

The flutter critical condition can be determined as the lowest value of U such that it exists a real value of ω for which the matrix $\mathbf{E}(\mathbf{X}, K)$ becomes singular. The solution of the problem is quite laborious and it requires the computation of the generalized masses and $3N(3N+1)/2$ modal integrals, given the symmetry of the G terms.

5.3 Model simplification

Starting from the complete multimode system, we want now to introduce a sequence of assumptions in order to finally obtain the binary flutter model. The first generally accepted simplification is to neglect the contribution of lateral displacements and drag forces. In most cases this is not merely an option but is dictated by the difficulty to identify the corresponding flutter derivatives. In addition, it has already been remarked that considering the unsteady drag forces acting on the deck alone might not be correct to describe the actual self-excited

contribution. Despite that, to neglect the drag and the horizontal degree of freedom seems to be reasonable, at least for non-super-long-span bridges characterized by low-drag profiles.

In the flutter analysis of the Akashi Kaikyo Bridge performed by Katsuchi *et al.* (1999), it is found that neglecting the P_2^* and P_3^* the critical wind speed increases of about 70 %. This surprising result is not confirmed by some simple analyses carried out by the writer. As a matter of fact, for the modified cross-section configuration (Katsuchi *et al.*, 1999; Miyata, 1995), practically the same critical wind speed and frequency found by Katsuchi *et al.* (1999) through a complete multimodal analysis, can be calculated with a simple bimodal approach, considering only the first symmetric vertical bending and first symmetric torsional modes (see Tabs. 6.7-6.8 in Chapter 6). However, given the relevance of this issue, an effort should be done by the scientific community in order to shed some light on the actual role played by the flutter derivatives relative to drag and sway motion.

The second simplifying assumption that can be made is that the modes are pure vertical bending or pure torsional. This is absolutely true for symmetric decks (with respect to a longitudinal vertical plane) as the elastic center and the centroid are vertically aligned. Obviously this assumption should be rejected in the very particular case of asymmetric bridge decks. As a consequence, the $\tilde{N}$ coupled equations (N minus the number of lateral modes) can be divided into two groups (N_h relative to the vertical bending modes and N_α to torsional modes). Then normalizing the generalized inertias and modal integrals as follows:

$$m_{eq.r} = \frac{\int_S m(x) h_r^2(x) dx}{\int_D h_r^2(x) dx} \tag{5.22}$$

$$I_{eq.s} = \frac{\int_S I(x) \alpha_s^2(x) dx}{\int_D \alpha_s^2(x) dx} \tag{5.23}$$

$$C_{h_j h_r} = \frac{G_{h_j h_r}}{G_{h_r h_r}} = \frac{\int_D h_j(x) h_r(x) dx}{\int_D h_r^2(x) dx} \tag{5.24}$$

$$C_{\alpha_k h_r} = \frac{G_{\alpha_k h_r}}{G_{h_r h_r}} = \frac{\int_D \alpha_k(x) h_r(x) dx}{\int_D h_r^2(x) dx} \tag{5.25}$$

$$C_{\alpha_k \alpha_s} = \frac{G_{\alpha_k \alpha_s}}{G_{\alpha_s \alpha_s}} = \frac{\int_D \alpha_k(x) \alpha_s(x) dx}{\int_D \alpha_s^2(x) dx} \tag{5.26}$$

$$C_{h_j \alpha_s} = \frac{G_{h_j \alpha_s}}{G_{\alpha_s \alpha_s}} = \frac{\int_D h_j(x) \alpha_s(x) dx}{\int_D \alpha_s^2(x) dx} \tag{5.27}$$

and setting:

$$p_r(t) = B \xi_{h.r}(t) \qquad r = 1...N_h \tag{5.28}$$

$$q_s(t) = \xi_{\alpha.s}(t) \qquad s = 1...N_\alpha \tag{5.29}$$

where $\xi_{h.r}(t)$ and $\xi_{\alpha.s}(t)$ are the generalized coordinates relative to the r-th vertical bending mode and the s-th torsional mode respectively, the following equations can be obtained:

$$m_{eq.r}(\ddot{p_r} + 2\zeta_r\omega_r\dot{p_r} + \omega_r^2 p_r) = \frac{1}{2}\rho U^2 B[KH_1^* \sum_{j=1}^{N_h} \frac{\dot{p_j}}{U} C_{h_j h_r} + KH_2^* \sum_{k=1}^{N_\alpha} \frac{B\dot{q_k}}{U} C_{\alpha_k h_r} + K^2 H_3^* \sum_{k=1}^{N_\alpha} q_k C_{\alpha_k h_r} + K^2 H_4^* \sum_{j=1}^{N_h} \frac{p_j}{B} C_{h_j h_r}] \tag{5.30}$$

$$I_{eq.s}(\ddot{q_s} + 2\zeta_s\omega_s\dot{q_s} + \omega_s^2 q_s) = \frac{1}{2}\rho U^2 B^2[KA_1^* \sum_{j=1}^{N_h} \frac{\dot{p_j}}{U} C_{h_j \alpha_s} + KA_2^* \sum_{k=1}^{N_\alpha} \frac{B\dot{q_k}}{U} C_{\alpha_k \alpha_s} + K^2 A_3^* \sum_{k=1}^{N_\alpha} q_k C_{\alpha_k \alpha_s} + K^2 A_4^* \sum_{j=1}^{N_h} \frac{p_j}{B} C_{h_j \alpha_s}] \tag{5.31}$$

This system can be further simplified supposing that, for the modes wherein the deck is significantly involved, the modal masses are almost equal to the portion relative just to the deck and suspension cables (i.e. the masses of the other structural elements are small or the contribution of these elements to the modal displacement is moderate). This assumption is fairly realistic if the first stages of construction are excluded [e.g. Dyrbye and Hansen (1997)].

Then, if the mass and mass moment of inertia of the deck are constant along the span, one obtains:

$$m_{eq.r} = \frac{m \int_S h_r^2(x)dx}{\int_D h_r^2(x)dx} \cong \frac{m \int_D h_r^2(x)dx}{\int_D h_r^2(x)dx} = m \tag{5.32}$$

$$I_{eq.s} = \frac{I \int_S \alpha_s^2(x)dx}{\int_D \alpha_s^2(x)dx} \cong \frac{I \int_D \alpha_s^2(x)dx}{\int_D \alpha_s^2(x)dx} = I \tag{5.33}$$

m and I have to be interpreted as the mass and mass moment of inertia of the deck alone in the case of cable-stayed bridges, whereas for suspension bridges they must include the contribution of the suspension cables, whose displacements follow those of the deck in the modes of interest for the flutter instability. As a consequence, the mode shapes become orthogonal to each other, that is:

$$C_{h_j h_r} = \frac{G_{h_j h_r}}{G_{h_r h_r}} = \delta_{jr} \tag{5.34}$$

$$C_{\alpha_k \alpha_s} = \frac{G_{\alpha_k \alpha_s}}{G_{\alpha_s \alpha_s}} = \delta_{ks} \tag{5.35}$$

where δ_{jr} and δ_{ks} indicate Kronecker's functions. The resulting $\tilde{N}$ equations are still entirely coupled.

In order to further simplify the problem it can be assumed that the contribution to the modal integrals of the side spans is negligible and that the mode shapes are approximately sinusoidal in the main span of the deck:

$$C_{\alpha_k h_r} = \frac{G_{\alpha_k h_r}}{G_{h_r h_r}} \cong \delta_{kr} \tag{5.36}$$

$$C_{h_j \alpha_s} = \frac{G_{h_j \alpha_s}}{G_{\alpha_s \alpha_s}} \cong \delta_{js} \tag{5.37}$$

The last two assumptions are in most cases quite accurate and lead to the following system:

$$m(\ddot{p_r} + 2\zeta_r \omega_r \dot{p_r} + \omega_r^2 p_r) = \frac{1}{2}\rho U^2 B[KH_1^* \frac{\dot{p_r}}{U} + KH_2^* \frac{B\dot{q_s}}{U} + K^2 H_3^* q_s + K^2 H_4^* \frac{p_r}{B}] \tag{5.38}$$

$$I(\ddot{q_s} + 2\zeta_s \omega_s \dot{q_s} + \omega_s^2 q_s) = \frac{1}{2}\rho U^2 B^2[KA_1^* \frac{\dot{p_r}}{U} + KA_2^* \frac{B\dot{q_s}}{U} + K^2 A_3^* q_s + K^2 A_4^* \frac{p_r}{B}] \tag{5.39}$$

in which the equations are only coupled in pairs. It is worth noting that, when the modal shapes are approximately sinusoidal, Eqs. (5.34) and (5.35) hold also if the mass and mass moment of inertia are not constant along the deck. In this case the only difference in Eqs. (5.38) and (5.39) is that m and I have to be substituted by $m_{eq.r}$ and $I_{eq.s}$. It is also important to observe that only the modes with approximately the same node position along the deck main span are expected to give rise to flutter instability, being otherwise the value of the corresponding modal integral close to zero. Consequently, if the results of a modal analysis are available, on the basis of the frequency values and frequency ratios it is very easy to establish which modes can be the critical ones, and to calculate the flutter critical wind speed and frequency by solving a simple bimodal problem, as if one was dealing with a section model instead of a complete bridge structure. Conversely, when the sinusoidal approximation is not acceptable, it is possible to calculate a coupling coefficient for each pair of torsional and bending modes (Dyrbye and Hansen, 1997).

To sum up, the assumptions which allow to simplify the multimodal approach to flutter and obtain the bimodal one are listed below:

I self-excited drag force and sway degree of freedom do not significantly affect the flutter mechanism;

II the deck is symmetric with respect to a vertical longitudinal plane, so that the modes are pure torsional or vertical bending;

III only the deck (for cable-stayed bridges) or the deck and the suspension cables (for suspension bridges) significantly contribute to the modal masses;

IV the contribution of the side spans to the modal integrals is negligible;

V the deck mode shapes are approximately sinusoidal.

The validity of the assumptions from II to V can be straightforward checked just looking at the results of the modal analysis, so that the degree of approximation they introduce is easily perceived. Conversely, the first assumption cannot be verified unless the whole set of eighteen flutter derivatives is experimentally measured. That assumption is definitely the most questionable point in this analysis and further investigation is needed on this issue.

5.4 Examples

In order to verify the simplifying assumptions discussed in the previous section, through which the multimodal problem is transformed into a bimodal one, two existing structures, a quite large suspension bridge and a small cable-stayed bridge, are taken into account as study cases. For this analysis sets of eighteen flutter derivatives are needed. Therefore the structural characteristics of the bridges are associated to the aerodynamic properties of two cross-sectional profiles for which these aeroelastic data are available. This combination can be done because, as it is remarked in section 2.4.1, flutter derivatives are independent of the modal parameters of the structure on which these functions are measured. Nevertheless, the results of the flutter calculations no longer refer to the considered bridges but to hybrid non-existing (albeit possible) structures.

5.4.1 Bosporus I Strait Bridge

The first study case is the Bosporus I Strait Bridge (Bogazici Bridge, Istanbul, Turkey, 1973), a suspension bridge with a main span of 1074 m [Figs. 5.2(c) and 5.2(a)]. The data about the structure can be found in Martini (2004). The aerodynamic behavior of the deck is simulated considering the flutter derivatives of a thin rectangular box girder section with semi-circular fairings and a chord-to-thickness ratio of 14.3 [Fig. 5.2(d)], reported in Chowdhury and Sarkar (2004).

The modal analysis is performed with the software SAP (CSI, 1999) on the finite-element model displayed in Fig. 5.2(b). The results are listed in Tab. 5.1. As modal damping, given the small influence of this parameter on the flutter instability, an arbitrary value of 1 % is assumed for all modes. The results of the rigorous multimodal (Multimodal I) and bimodal flutter analyses are reported in Tab. 5.2 in terms of critical wind speed and coupling frequency. Other two calculations, both neglecting the lateral bending modes (Multimodal II and III) and the second one considering only the contributions of the deck to the modal masses (Multimodal III), are also included. It is evident that the difference in the results is negligible. Therefore the simplifying assumptions discussed in the previous chapter seem to be in this case largely reasonable, including the one about the negligibility of the flutter derivatives corresponding to drag and sway degree of freedom.

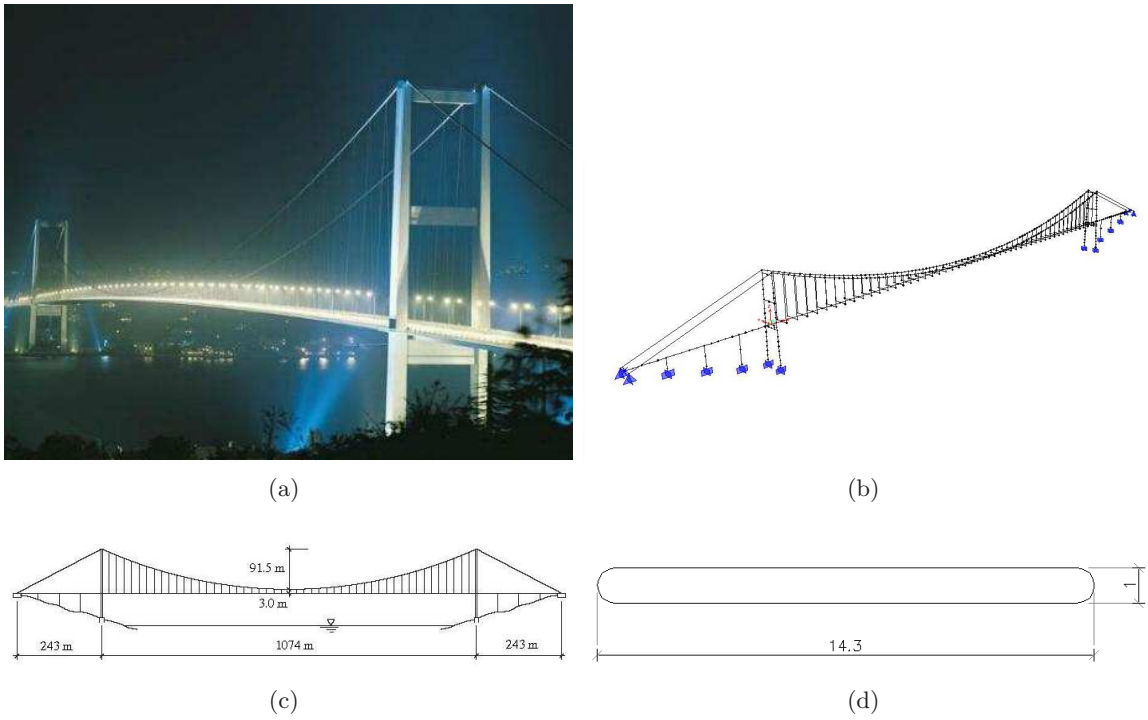

Figure 5.2: Bosporus I Strait Bridge: (a) night view; (b) finite-element model for the modal analysis; (c) main features of the geometry of the structure; (d) cross-sectional profile considered for the aerodynamics

Table 5.1: Modal analysis results for Bosporus Strait Bridge (V = vertical bending, T = torsional, L = lateral bending, long = longitudinal, S = symmetric, A = antisymmetric)

Mode	Type	Frequency [Hz]	Mode	Type	Frequency [Hz]
1	LS1	0.109	12	Cables4	0.381
2	VA1	0.146	13	VA3	0.474
3	VS1	0.162	14	LS2	0.493
4	VS2	0.226	15	Cables5	0.551
5	LA1	0.268	16	Cables6	0.566
6	VA2	0.291	17	TA1	0.567
7	Cables1	0.343	18	VS4	0.582
8	Cables2	0.351	19	VS+long	0.666
9	Cables3	0.361	20	VA+long	0.706
10	TS1	0.371	21	TS2	0.849
11	VS3	0.381	22	TA2	1.104

Table 5.2: Bosporus I Strait Bridge: multimodal and bimodal analyses (ΔU_c and Δf_c are always calculated with respect to the case "Multimodal I")

Analysis	Modes	U_c [m/s]	ΔU_c [%]	f_c [Hz]	Δf_c [%]
Multimodal I	22	83.8	-	0.285	-
Multimodal II	13	83.9	+0.16	0.285	-0.07
Multimodal III	13	83.7	-0.03	0.284	-0.35
Bimodal (VS1+TS1)	2	82.2	-1.87	0.282	-0.95

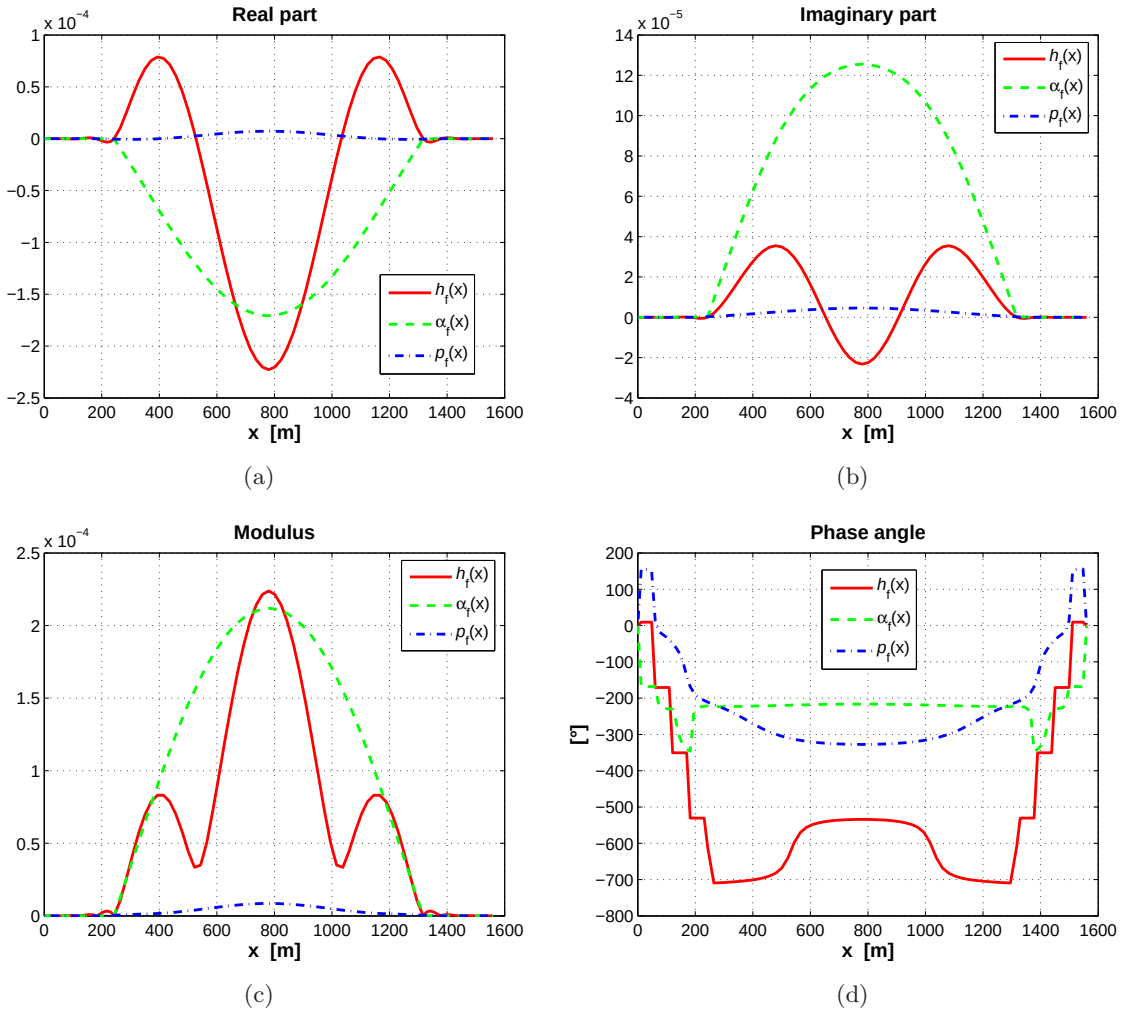

Figure 5.3: Flutter mode shape for Bosporus I Strait Bridge: (a) real part; (b) imaginary part; (c) modulus; (d) phase angle

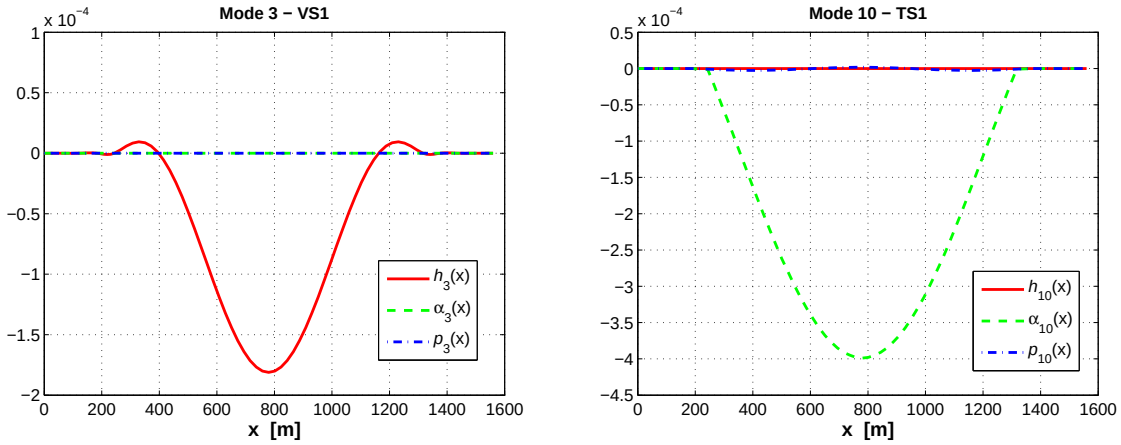

(a)

(b)

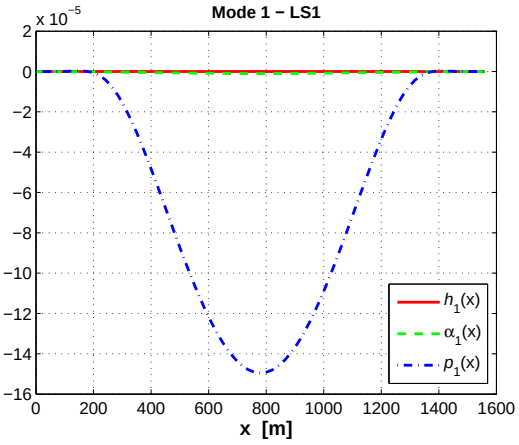

(c)

Figure 5.4: Bosporus I Strait Bridge: still-air modes mainly involved in the flutter coupling; (a) symmetric vertical bending mode; (b) symmetric torsional mode; (c) symmetric lateral bending mode;

The flutter mode shape corresponding to the complete multimodal analysis is shown in Fig. 5.3 and can be compared with the still-air modes mainly involved in the instability process, along with the corresponding lateral mode, reported in Fig. 5.4. In the main span of the bridge, near the pylons, small contribution from some "non-critical" modes can be detected in the vertical component of the flutter mode shape, as confirmed by the non-constant phase angle between the mode components [Fig. 5.3(d)]. Nevertheless, this modification of the flutter mode shape is not traduced into a significant change of the flutter critical wind speed.

5.4.2 Ponte all'Indiano

The second example we are taking into account is Ponte all'Indiano (Florence, Italy, 1978), a single-span cable-stayed bridge of 189.1 m characterized by a fairly complicated and discontinuous cross-section geometry [Figs. 5.5(a)-5.5(c)]. The flutter derivatives of the Tsurumi Fairway Bridge (Japan), reported in Singh *et al.* (1995), whose cross-sectional profile is shown in Fig. 5.5(d), are considered in the flutter calculation. It must be said that the choice of the dynamic behavior of such a small bridge, with high torsional stiffness and consequently large frequency ratio, is not optimal for a flutter analysis, since very high critical wind speed is expected. Nevertheless, this is the only cable-stayed bridge for which all structural parameters are available to the writer and the relevance of the study case for the comparison between multimodal and bimodal approach is not questionable.

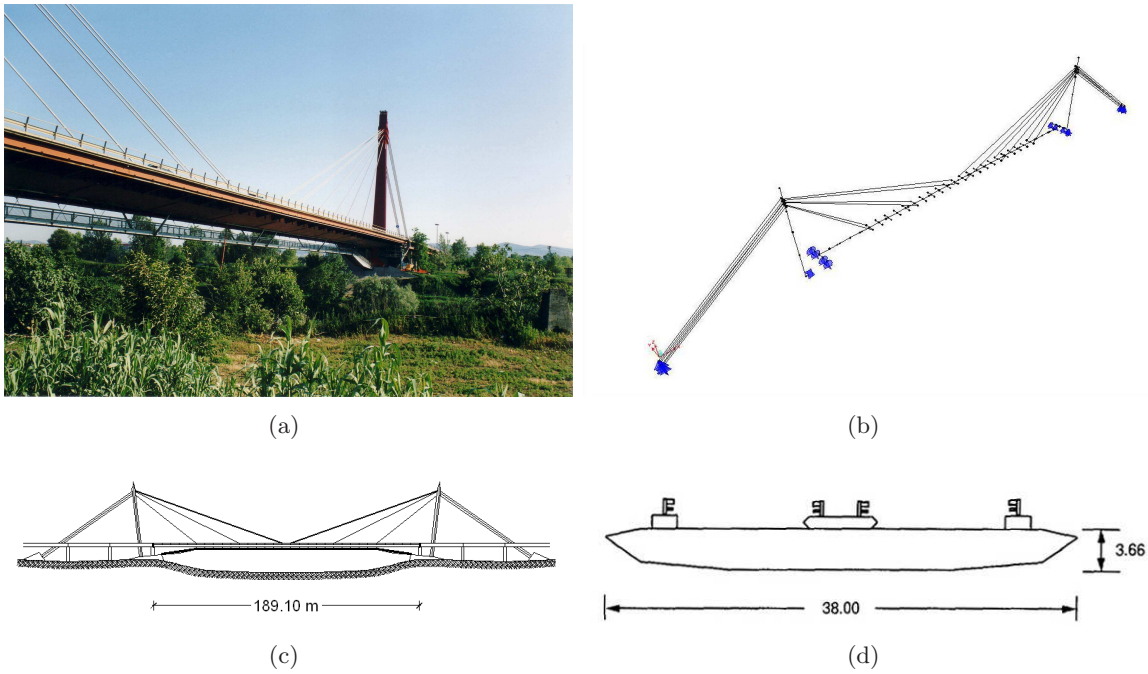

(a) (b) (c) (d)

Figure 5.5: Ponte all'Indiano: (a) view of the bridge; (b) finite-element model for the modal analysis; (c) main features of the geometry of the structure; (d) cross-sectional profile considered for the aerodynamics

Table 5.3: Modal analysis results for Ponte all'Indiano (V = vertical bending, T = torsional, L = lateral bending, long = longitudinal, S = symmetric, A = antisymmetric)

Mode	Type	Frequency [Hz]	Mode	Type	Frequency [Hz]
1	VS1	0.573	12	VS3	3.204
2	VA1	0.616	13	TS2	3.284
3	LS1	0.775	14	TA2	4.293
4	Pylons	0.927	15	VA3	4.502
5	Pylons	0.936	16	TS3	5.313
6	TS1	1.179	17	Pylons	5.616
7	VA1-bis	1.256	18	Pylons	5.639
8	VS2	1.530	19	VS4	6.000
9	TA1	2.213	20	TA3	6.416
10	VA2	2.240	21	LS2	6.878
11	LA1	3.094	22	LA2	12.382

Table 5.4: Ponte all'Indiano: multimodal and bimodal analyses (ΔU_c and Δf_c are always calculated with respect to the case "Multimodal I")

Analysis	Modes	U_c [m/s]	ΔU_c [%]	f_c [Hz]	Δf_c [%]
Multimodal I	22	220.0	-	0.828	-
Multimodal II	18	219.9	-0.03	0.828	+0.06
Multimodal III	14	224.8	+2.22	0.854	+3.18
Bimodal (VS1+TS1)	2	223.1	+1.43	0.856	+3.43

The modal analysis is performed with SAP on the finite-element model displayed in Fig. 5.5(b). The main results are shown in Tab. 5.3. It is worth noting that the first mode frequency is very close to the value measured in situ and reported in Augusti *et al.* (1980). The results of the multimodal and bimodal flutter analysis are reported in Tab. 5.4. Once again only two modes are necessary to correctly calculate the critical wind speed. In addition, in this case the contribution of the other modes is negligible also for the definition of the flutter mode shape, as it can be remarked in Figs. 5.6 and 5.7.

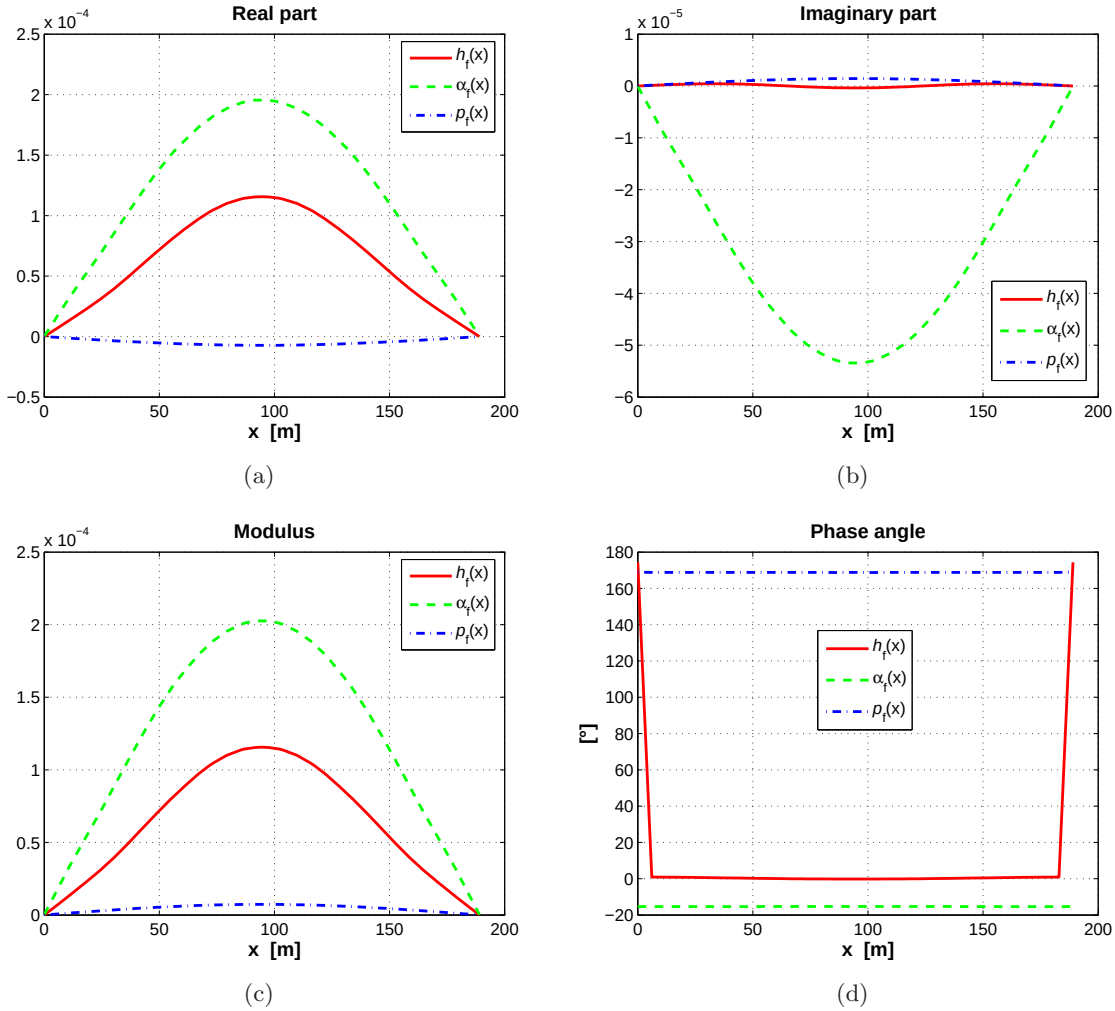

Figure 5.6: Flutter mode shape for Ponte all'Indiano: (a) real part; (b) imaginary part; (c) modulus; (d) phase angle

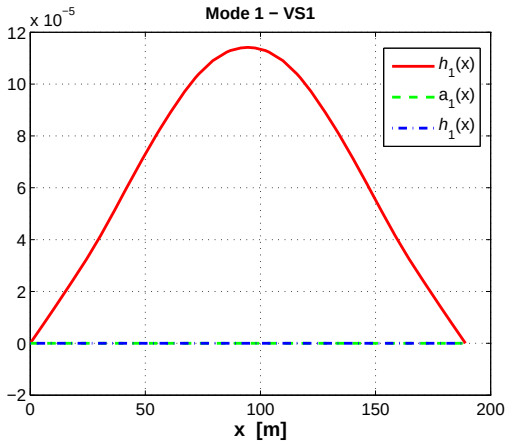

(a)

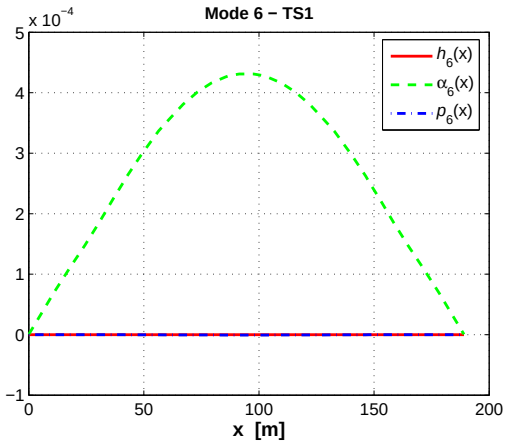

(b)

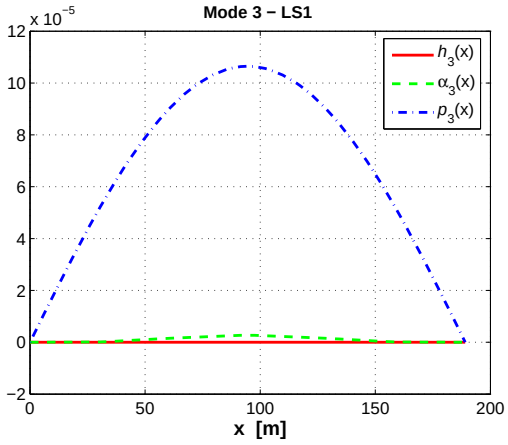

(c)

Figure 5.7: Ponte all'Indiano: still-air modes mainly involved in the flutter coupling; (a) symmetric vertical bending mode; (b) symmetric torsional mode; (c) symmetric lateral bending mode;

5.5 Conclusions

The numerical results reported in the previous section, as well as those showed in D'Asdia and Sepe (1998) and Caracoglia (2000) for Messina Strait Bridge (albeit considering the quasi-steady approach to determine the flutter derivatives corresponding to drag and sway motion), seem to confirm the validity of the assumptions listed in the third section of the present chapter. That means that the contribution of the lateral bending modes to flutter is negligible and there is no significant transfer of energy between modes with different modal shapes.

Nevertheless, the first conclusion needs further investigation since its validity for long-span bridges with high drag, like Akashi Kaikyo Bridge, is still doubtful (Katsuchi *et al.*, 1999). As a matter of fact, the sets of flutter derivatives considered herein for the study cases correspond to deck cross sections with low drag, so that surprising destabilizing effects due to the lateral bending modes are not expected.

Conversely, the second statement, in the case of laminar wind, is based only on some easy assumptions whose validity can be straightforward checked before the calculation. On the other hand, considering non-perfectly correlated turbulent flows and performing a much more sophisticated analysis of stochastic stability, it is known that the energy transfer between modes is enhanced with either stabilizing or destabilizing effects on flutter [e.g. Bucher and Lyn (1988a,b, 1989); Bartoli *et al.* (1995)]. The actual relevance of these effects requires to be better understood even in order to define a simplified procedure of flutter assessment.

Finally, it is important to precise that the fact that basically only two modes seem to be responsible for the flutter instability mechanism does not mean that the same conclusion can be extended to the pre-critical state. In fact, several modes have to be taken into account in order to correctly predict the response of a structure to turbulent wind [e.g. Minh *et al.* (1999); Diana *et al.* (1999); Salvatori and Spinelli (2006b)].

Chapter 6

Simplified formulas

6.1 Introduction

In this chapter we deal with the simplification of the flutter calculation procedure in order to finally achieve an approximate method of flutter assessment which does not require wind-tunnel tests. The importance for risk-mitigation to dispose of simplified tools to treat bridge flutter and aeroelastic phenomena in general and the lack of them both in the national and international codes have already been discussed in section 1.4.

A common simplified method to investigate flutter is the quasi-steady approach [e.g. Miyata *et al.* (1995); Minh *et al.* (1999); Diana *et al.* (1999)], in which the knowledge of static aerodynamic coefficients is required instead of flutter derivatives. Nevertheless, it has already been discussed in section 2.4.3 that this approach does not seem to be appropriate for the relatively low reduced wind speeds which characterize bridge deck flutter. In addition, Nakamura (Nakamura and Mizota, 1975; Nakamura, 1979) pointed out that the quasi-steady result can be not only quantitatively inaccurate but also qualitatively uncorrect in the case of single-degree-of-freedom torsional flutter (see section 2.2.4).

Another simplified method to assess flutter instability consists in the calculation of the critical wind speed for a dynamically equivalent thin flat plate, which is then reduced (usually) or increased (rarely) by introducing an empirical coefficient of "aeroelastic performance" depending on the actual cross-sectional geometry (Frandsen, 1966; Gimsing, 1997; Dyrbye and Hansen, 1997; Righi, 2003; Bartoli and Righi, 2004b, 2006). The main limit of this approach is that the physics of the phenomenon is lost, condensing in one coefficient the whole aerodynamics of the deck section.

The proposed approach is based on the eigenvalue stability analysis and is able to follow the actual mechanism of destabilization. The flutter equations are manipulated on the basis of a large number of dynamic and aerodynamic data in order to find simplified analytical expressions for the coupling frequency and reduced wind speed, depending only on three (H_1^*, A_2^* and A_3^*) or even two (H_1^* and A_2^*) aeroelastic functions instead of the usual eight. It is worth noting that the retained aeroelastic functions are supposed to be the most reliable and easiest to be identified through wind-tunnel tests and those for which more data are available in the literature. The validity and the limits of this approach are investigated through a wide range

of bridge deck flutter derivatives and its applicability comes out to be surprisingly wide, being the degree of approximation usually very good. In particular, although the method is mainly thought for classical coupled flutter, it seems to apply in the case of single-degree-of-freedom torsional instability as well.

It is also worth noting that it is the first time, at least to the knowledge of the writer, that such a wide range of dynamic and aerodynamic data about bridge decks are collected and analyzed in order to study the flutter mechanism and to check the validity of an approximate formula.

6.2 Flutter problem

For two degree-of-freedom structural systems allowed to undergo heaving and pitching vibrations, the equations of motion can be written in the following form, common in the aeronautical field (Fung, 1993):

$$m[\ddot{h} + (1 + ig_h)\omega_h^2 h] = L_h \tag{6.1}$$

$$I[\ddot{\alpha} + (1 + ig_\alpha)\omega_\alpha^2 \alpha] = M_\alpha \tag{6.2}$$

where h and α denote respectively the heaving displacement and the pitching rotation (Fig. 2.13), m and I the mass and mass moment of inertia per unit length, ω_h and ω_α the circular frequencies of the heaving and pitching modes (in still air), L_h and M_α the lift and moment per unit length, i is the imaginary unit and the dot denotes the derivative with respect to time. g_h and g_α are the coefficients of rate-independent damping for the heaving and pitching modes and, in the case of a sinusoidal motion with circular frequency ω, they can be related to the more common ratio-to-critical damping coefficients ζ_h and ζ_α through the simple expressions:

$$g_h = 2\zeta_h \frac{\omega}{\omega_h} \tag{6.3}$$

$$g_\alpha = 2\zeta_\alpha \frac{\omega}{\omega_\alpha} \tag{6.4}$$

The advantage of using rate-independent damping instead of the more familiar notation will result clear later.

Lift and moment can be expressed as the sum of steady forces due to mean wind, buffeting and self-excited forces but only the latter must be retained when flutter stability is concerned. Self-excited forces can be expressed again in the Scanlan's form (Simiu and Scanlan, 1996), as follows:

$$L_{se}(t, K) = qB[KH_1^*(K)\frac{\dot{h}(t)}{U} + KH_2^*(K)\frac{B\dot{\alpha}(t)}{U} + K^2 H_3^*(K)\alpha(t) + K^2 H_4^*(K)\frac{h(t)}{B}] \tag{6.5}$$

$$M_{se}(t, K) = qB^2[KA_1^*(K)\frac{\dot{h}(t)}{U} + KA_2^*(K)\frac{B\dot{\alpha}(t)}{U} + K^2 A_3^*(K)\alpha(t) + K^2 A_4^*(K)\frac{h(t)}{B}] \tag{6.6}$$

where $q = \frac{1}{2}\rho U^2$ is the kinetic pressure, B is the deck chord, K is the reduced frequency of oscillation defined on the base of the chord B and the functions H_i^* and A_i^* are the well known flutter derivatives.

Substituting Eqs. (6.5)-(6.6) in Eqs. (6.1)-(6.2), imposing a sinusoidal motion with coupled frequency (critical condition) and the singularity of the resulting system, as explained in Chapter 2, two flutter equations are then obtained. In particular, following the approach outlined here, they can be written as follows (Fung, 1993):

$$\begin{aligned}&(1-g_h g_\alpha)\frac{r_\alpha^2\mu^2}{\gamma_\omega^2}X^2 - [r_\alpha^2\mu^2(1+\frac{1}{\gamma_\omega^2}) + \frac{\mu}{\gamma_\omega^2}(A_3^* - g_h A_2^*) + r_\alpha^2\mu(H_4^* - g_\alpha H_1^*)]X + \\ &r_\alpha^2\mu^2 + \mu A_3^* + r_\alpha^2\mu H_4^* + H_4^* A_3^* - H_1^* A_2^* - H_3^* A_4^* + H_2^* A_1^* = 0\end{aligned} \tag{6.7}$$

$$\begin{aligned}&(g_h+g_\alpha)\frac{r_\alpha^2\mu^2}{\gamma_\omega^2}X^2 - [r_\alpha^2\mu^2(g_\alpha + \frac{g_h}{\gamma_\omega^2}) + \frac{\mu}{\gamma_\omega^2}(g_h A_3^* + A_2^*) + r_\alpha^2\mu(g_\alpha H_4^* + H_1^*)]X + \\ &\mu A_2^* + r_\alpha^2\mu H_1^* + H_4^* A_2^* + H_1^* A_3^* - H_3^* A_1^* - H_2^* A_4^* = 0\end{aligned} \tag{6.8}$$

where it is set:

$$\mu = \frac{2m}{\rho B^2} \qquad r_\alpha = \sqrt{\frac{I}{mB^2}} \qquad \gamma_\omega = \frac{\omega_\alpha}{\omega_h} \qquad X = \frac{\omega_\alpha^2}{\omega^2}$$

The parameter μ represents the relative mass of the deck, that is proportional to the ratio of the mass of the deck to the mass of the air moved by the deck; r_α is the dimensionless radius of inertia of the deck, γ_ω is the frequency ratio in still air between the torsional and vertical bending modes susceptible to couple and X is the unknown non-dimensional frequency of oscillation at flutter. It is now evident the advantage of writing in Eqs. (6.1)-(6.2) the damping like a complex stiffness, as it allows to deal with flutter equations of second order in X instead of fourth and third order respectively if usual notation for damping is assumed [Eqs. (2.55) and (2.56)]. It is also worth noting that all the modal properties of the 2-DoF system relevant for flutter instability are summarized by the parameters μ, r_α and γ_ω along with the damping coefficients.

Eq. (6.7) is usually called "real equation" as it is obtained imposing the vanishing of the real part of the determinant of the aforementioned system of equations. For analogous reasons Eq. (6.8) is called "imaginary equation". It is important to point out that from Eqs. (6.7)-(6.8) it is possible to calculate the critical reduced wind speed ($U_{Rc} = 2\pi/K_c$, where c stands for "critical"), the coupling frequency and consequently the actual flutter wind speed, which depend only on the aerodynamic parameters (flutter derivatives) and the already mentioned non-dimensional modal parameters (μ, r_α, γ_ω, g_h, g_α).

6.3 Simplification procedure

In order to simplify the flutter equations it can immediately be noted that $g_h g_\alpha \ll 1$ in Eq. (6.7), since hardly the damping coefficients are higher than 0.02. Isolating then in the left hand side of both equations the term $r_\alpha^2\mu^2 X^2/\gamma_\omega^2$ and consequently equating the right hand sides, an equation of first order in X is obtained:

$$
\begin{aligned}
&[\frac{r_\alpha^2\mu^2}{\gamma_\omega^2}(\frac{\gamma_\omega^2 g_h + g_\alpha}{g_h+g_\alpha}) + \frac{\mu A_3^*}{\gamma_\omega^2}(\frac{g_\alpha}{g_h+g_\alpha}) - \frac{\mu A_2^*}{\gamma_\omega^2}(g_h + \frac{1}{g_h+g_\alpha}) + r_\alpha^2\mu H_4^*(\frac{g_h}{g_h+g_\alpha}) + \\
&- r_\alpha^2\mu H_1^*(g_\alpha + \frac{1}{g_h+g_\alpha})]X - r_\alpha^2\mu^2 - \mu A_3^* + \frac{\mu A_2^*}{g_h+g_\alpha} - r_\alpha^2\mu H_4^* + \frac{r_\alpha^2\mu H_1^*}{g_h+g_\alpha} + \\
&- H_4^*A_3^* + H_1^*A_2^* + H_3^*A_4^* - H_2^*A_1^* + \frac{H_4^*A_2^* + H_1^*A_3^* - H_3^*A_1^* - H_2^*A_4^*}{g_h+g_\alpha} = 0
\end{aligned}
\tag{6.9}
$$

In Eq. (6.9) the terms which contain a second power of the damping coefficients can be neglected, giving:

$$
\begin{aligned}
&[\frac{r_\alpha^2\mu^2}{\gamma_\omega^2}(\frac{\gamma_\omega^2 g_h + g_\alpha}{g_h+g_\alpha}) + \frac{\mu}{\gamma_\omega^2}(\frac{g_\alpha A_3^*}{g_h+g_\alpha} - \frac{A_2^*}{g_h+g_\alpha}) + r_\alpha^2\mu(\frac{g_h H_4^*}{g_h+g_\alpha} - \frac{H_1^*}{g_h+g_\alpha})]X + \\
&- r_\alpha^2\mu^2 - \mu A_3^* + \frac{\mu A_2^*}{g_h+g_\alpha} - r_\alpha^2\mu H_4^* + \frac{r_\alpha^2\mu H_1^*}{g_h+g_\alpha} - H_4^*A_3^* + H_1^*A_2^* + H_3^*A_4^* - H_2^*A_1^* + \\
&\frac{H_4^*A_2^* + H_1^*A_3^* - H_3^*A_1^* - H_2^*A_4^*}{g_h+g_\alpha} = 0
\end{aligned}
\tag{6.10}
$$

It is worth noting that Eq. (6.9) relies on the assumption that $g_h + g_\alpha \neq 0$. The case $g_h = g_\alpha = 0$ will be discussed later in section 6.3.2.

6.3.1 Range of variability of the dynamic parameters

Now it is important to understand the range of variability of the non-dimensional modal parameters which appear in the equations above. For this reason they are reported in Tab. 6.1 for some bridge decks with various characteristics. Four suspended-span bridges of different dimensions and cross sections are taken into account: First Tacoma Narrows Bridge, USA (Larsen, 1998), Bosporus Strait Bridge, Turkey (Martini, 2004), Akashi Kaikyo Bridge, Japan (Miyata and Yamaguchi, 1993) and the proposed Messina Strait Bridge, Italy (D'Asdia and Sepe, 1998). In the first part of Table 1 the main geometric and modal properties and the non-dimensional parameters appearing in the flutter equations can be found (L = main span length; f_h, f_α = vertical bending and torsional frequencies susceptible to couple). The same data are reported in the second part of Tab. 6.1 for four cable-stayed bridges: Ponte all'Indiano, Italy (Augusti *et al.*, 1980), Guamà Bridge, Brazil (Rocha *et al.*, 2003), Tsurumi Fairway Bridge, Japan (Sarkar, 1992) and Normandy Bridge, France (ONERA, 1989). Finally, in the third part of Tab. 6.1 two footbridges are taken into account: Ruffolo footbridge near Siena (Bartoli and Procino, 2004) and the footbridge of the Olympic Arch in the Olympic Village in Turin (Flamand, 2003b).

Looking at the last four columns of Tab. 6.1, it seems reasonable to consider as opposite limit cases the Tsurumi Fairway Bridge and the Guamà Bridge, whose mass properties will be assumed as reference in the following analyses. In particular, Guamà Bridge is characterized by a concrete deck and consequently by a remarkable mass as compared to the chord B. Tsurumi Fairway Bridge, instead, presents a quite light steel deck with a large chord length.

The non-dimensional mass and radius of inertia of the proposed Messina Strait Bridge are close to those of the Tsurumi Bridge. Flexible footbridges seem to be characterized by values of μ and r_α rather similar to those of Guamà Bridge, since they present usually light but very narrow decks.

Table 6.1: Main geometric and dynamic properties of the considered suspended-span, cable-stayed bridges and footbridges ($\rho = 1.25$ kg/m^3)

	L [m]	B [m]	f_h [Hz]	f_α [Hz]	m [kg/m]	I [kgm^2/m]	γ_ω [-]	μ [-]	r_α [-]	$r_\alpha^2\mu$ [-]	$r_\alpha^2\mu^2$ [-]
Suspended-span bridges											
Tacoma	854	12.0	0.130	0.200	4250	177730	1.54	47.2	0.539	13.7	647.6
Bosporus	1074	28.0	0.162	0.371	13550	1351645	2.29	27.7	0.357	3.5	97.3
Akashi	1991	35.5	0.064	0.150	43790	9826000	2.34	55.6	0.422	9.9	550.3
Messina	3300	60.4	0.0605	0.0796	55000	28000000	1.32	24.1	0.374	3.4	81.2
Cable-stayed bridges											
Indiano	189	22.4	0.573	1.179	17401	545274	2.06	55.5	0.250	3.5	192.3
Guamà	320	14.2	0.331	0.649	22513	566838	1.96	178.6	0.353	22.3	3984.8
Tsurumi	510	38.0	0.204	0.486	32220	2880100	2.38	35.7	0.249	2.2	78.9
Normandy	856	23.8	0.220	0.500	13700	633488	2.27	38.7	0.286	3.2	122.2
Footbridges											
Siena	59.4	3.255	1.735	4.839	1420	810	2.79	214.4	0.232	11.5	2475.8
Turin	156	6.91	0.510	0.590	3347	13502	1.16	112.2	0.291	9.5	1062.7

6.3.2 Simplified equation for critical frequency

In order to draw as general as possible conclusions, it is important to consider a large number of dynamic and aerodynamic data. Since it is assumed that flutter derivatives depend on reduced wind speed and cross-section geometry only, it is possible to combine the aerodynamics of a bridge with the dynamics of a completely different one and perform calculations on this "hybrid" structure. Obviously the results have nothing to do with a real bridge, referring to a non-existent but possible structure. This observation is important because it allows to employ for calculations all the reliable aerodynamic and dynamic data available to the writer and in particular to consider the two limit sets of mass parameters highlighted in the previous section and from now on identified by means of their μ and r_α values. From the aerodynamic point of view let us take into account the behavior of two cross sections quite different from each other: the theoretical flat plate [Theodorsen (1934); Fung (1993); section 2.4.1] and a rectangular cylinder with a chord-to-thickness ratio of 12.5 (Matsumoto, 1996). In particular, it is worth noting that R12.5 is the bluffer rectangular cylinder studied by Matsumoto (1996) among those which do not show negative values of the flutter derivative A_2^*, that meaning tendency to single-degree-of-freedom torsional flutter. For several values of the reduced wind speed U_R the different terms appearing in Eq. (6.10) are compared in Tabs. 6.2-6.3 for the flat

plate case and in Tabs. 6.4-6.5 for the rectangular cylinder case, setting:

$$S_1 = -r_\alpha^2\mu^2 - \mu A_3^* + \frac{\mu A_2^*}{g_h + g_\alpha} + \frac{r_\alpha^2 \mu H_1^*}{g_h + g_\alpha} \tag{6.11}$$

$$S_2 = -r_\alpha^2 \mu H_4^* \tag{6.12}$$

$$S_3 = -H_4^* A_3^* + H_1^* A_2^* + H_3^* A_4^* - H_2^* A_1^* \tag{6.13}$$

$$S_4 = \frac{H_4^* A_2^* + H_1^* A_3^* - H_3^* A_1^* - H_2^* A_4^*}{g_h + g_\alpha} \tag{6.14}$$

Since it can be claimed that g_h and g_α hardly take values larger than 0.02, damping coefficients of 0.001 and 0.03 are taken into account in order to have as general as possible results.

It is evident that the terms S_2, S_3 and S_4 in Eq. (6.10) can be neglected with respect to the term S_1:

$$\begin{aligned}&[\frac{r_\alpha^2\mu^2}{\gamma_\omega^2}(\frac{\gamma_\omega^2 g_h + g_\alpha}{g_h + g_\alpha}) + \frac{\mu}{\gamma_\omega^2}(\frac{g_\alpha A_3^*}{g_h + g_\alpha} - \frac{A_2^*}{g_h + g_\alpha}) - \frac{r_\alpha^2 \mu H_1^*}{g_h + g_\alpha}]X - r_\alpha^2\mu^2 - \mu A_3^* + \\ &\frac{\mu A_2^*}{g_h + g_\alpha} + \frac{r_\alpha^2 \mu H_1^*}{g_h + g_\alpha} = 0\end{aligned} \tag{6.15}$$

It is also important to highlight that:

$$H_1^* A_3^* - H_3^* A_1^* \cong 0 \tag{6.16}$$

This fact is in agreement with two of the relationships between flutter derivatives discussed by Matsumoto *et al.* (1995) and by Matsumoto (1996) for rectangular cylinders and for three bridge deck sections by Scanlan *et al.* (1997) and that seem not to be contradicted by the flutter derivatives of a wide range of cross-sectional geometries:

$$H_1^* \cong K H_3^* \tag{6.17}$$

$$A_1^* \cong K A_3^* \tag{6.18}$$

Table 6.2: Comparison of the actual weight of the terms appearing in the real flutter equation (dynamics: $\mu = 35.7$, $r_\alpha = 0.249$; aerodynamics: thin flat plate)

	$g_h = g_\alpha = 0.001$				$g_h = g_\alpha = 0.03$					
U_R	S_1	S_2	S_3	S_4	S_1	S_2	S_3	S_4	$H_1^* A_3^*$	$-H_3^* A_1^*$
0	-80.7	-3.5	-0.1	0.0	-80.7	-3.5	-0.1	0.0	0.00	0.00
2.5	-3236.3	-3.0	0.1	-73.8	-190.8	-3.0	0.1	-2.5	-0.26	0.19
5.0	-8036.8	-2.0	0.8	-70.0	-367.0	-2.0	0.8	-2.3	-1.90	1.76
7.5	-14931.2	-0.8	2.0	31.0	-626.1	-0.8	2.0	1.0	-7.01	6.79
10.0	-23864.9	0.4	3.9	225.1	-967.7	0.4	3.9	7.5	-18.29	17.97
15.0	-47026.5	2.8	9.9	853.5	-1874.1	2.8	9.9	28.5	-72.11	71.58
20.0	-75881.5	4.8	18.9	1734.5	-3036.0	4.8	18.9	57.8	-190.93	190.18
25.0	-109134.7	6.6	30.9	2811.1	-4411.8	6.6	30.9	93.7	-404.12	403.13

Table 6.3: Comparison of the actual weight of the terms appearing in the real flutter equation (dynamics: $\mu = 178.6$, $r_\alpha = 0.353$; aerodynamics: thin flat plate)

	$g_h = g_\alpha = 0.001$				$g_h = g_\alpha = 0.03$					
U_R	S_1	S_2	S_3	S_4	S_1	S_2	S_3	S_4	$H_1^*A_3^*$	$-H_3^*A_1^*$
0	-3993.7	-35.0	-0.1	0.0	-3993.7	-35.0	-0.1	0.0	0.00	0.00
2.5	-27206.2	-30.3	0.1	-73.8	-4792.4	-30.3	0.1	-2.5	-0.26	0.19
5.0	-59957.5	-20.0	0.8	-70.0	-5965.1	-20.0	0.8	-2.3	-1.90	1.76
7.5	-104416.9	-7.9	2.0	31.0	-7593.5	-7.9	2.0	1.0	-7.01	6.79
10.0	-160026.2	4.5	3.9	225.1	-9666.2	4.5	3.9	7.5	-18.29	17.97
15.0	-299667.3	28.0	9.9	853.5	-14993.5	28.0	9.9	28.5	-72.11	71.58
20.0	-469410.4	48.5	18.9	1734.5	-21652.3	48.5	18.9	57.8	-190.93	190.18
25.0	-662104.0	66.3	30.9	2811.1	-29413.3	66.3	30.9	93.7	-404.12	403.13

Table 6.4: Comparison of the actual weight of the terms appearing in the real flutter equation (dynamics: $\mu = 35.7$, $r_\alpha = 0.249$; aerodynamics: rectangular cylinder R12.5)

	$g_h = g_\alpha = 0.001$				$g_h = g_\alpha = 0.03$					
U_R	S_1	S_2	S_3	S_4	S_1	S_2	S_3	S_4	$H_1^*A_3^*$	$-H_3^*A_1^*$
0	-78.9	0.0	0.0	0.0	-78.9	0.0	0.0	0.0	0.00	0.00
7.4	-11587.2	-1.2	0.6	-459.6	-513.8	-1.2	0.6	-15.3	-7.33	6.53
11.1	-18811.5	1.1	0.0	-170.6	-819.3	1.1	0.0	-5.7	-30.49	29.59
14.8	-25319.4	1.9	-2.5	1137.9	-1118.6	1.9	-2.5	37.9	-74.96	75.32
18.5	-29898.6	4.7	-6.8	5110.3	-1378.3	4.7	-6.8	170.3	-156.95	163.73
22.2	-41134.0	6.1	-11.4	6563.7	-1892.0	6.1	-11.4	218.8	-286.76	296.46

Table 6.5: Comparison of the actual weight of the terms appearing in the real flutter equation (dynamics: $\mu = 178.6$, $r_\alpha = 0.353$; aerodynamics: rectangular cylinder R12.5)

	$g_h = g_\alpha = 0.001$				$g_h = g_\alpha = 0.03$					
U_R	S_1	S_2	S_3	S_4	S_1	S_2	S_3	S_4	$H_1^*A_3^*$	$-H_3^*A_1^*$
0	-3984.9	0.0	0.0	0.0	-3984.9	0.0	0.0	0.0	0.00	0.00
7.4	-89326.4	-12.2	0.6	-459.6	-7086.3	-12.2	0.6	-15.3	-7.33	6.53
11.1	-148732.1	11.0	0.0	-170.6	-9390.2	11.0	0.0	-5.7	-30.49	29.59
14.8	-203653.2	19.6	-2.5	1137.9	-11632.8	19.6	-2.5	37.9	-74.96	75.32
18.5	-252944.4	47.0	-6.8	5110.3	-13811.8	47.0	-6.8	170.3	-156.95	163.73
22.2	-334614.4	61.3	-11.4	6563.7	-17230.5	61.3	-11.4	218.8	-286.76	296.46

Finally, an expression for the non-dimensional frequency X is obtained and it is worth noting that it depends only on the three flutter derivatives H_1^*, A_2^* and A_3^*:

$$X = \gamma_\omega^2 \frac{r_\alpha^2 \mu(g_h + g_\alpha) + A_3^*(g_h + g_\alpha) - A_2^* - r_\alpha^2 H_1^*}{r_\alpha^2 \mu(\gamma_\omega^2 g_h + g_\alpha) + g_\alpha A_3^* - A_2^* - \gamma_\omega^2 r_\alpha^2 H_1^*} \tag{6.19}$$

If damping is neglected, the formula simplifies in the following way:

$$X = \gamma_\omega^2 \frac{A_2^* + r_\alpha^2 H_1^*}{A_2^* + \gamma_\omega^2 r_\alpha^2 H_1^*} \tag{6.20}$$

For coupled flutter prone cross sections it generally results that $H_1^* < 0$, $A_2^* < 0$ and $A_3^* > 0$. As $\gamma_\omega > 1$, being the damping coefficient g_h small enough, it is easy to show that, as expected:

$$1 \leq X = \frac{\omega_\alpha^2}{\omega^2} \leq \gamma_\omega^2 \tag{6.21}$$

The good degree of approximation of this formula can be appreciated by supposing to know the critical reduced wind speed, at which the flutter derivatives are evaluated, and comparing the results given by the eigenvalue analysis and by Eq. (6.19). Zero damping and high damping ratios ($\zeta_h = \zeta_\alpha = 1$ %) are assumed for both bending and torsional modes, in order to better stress the role of this parameter. The results for the four cases previously analyzed are reported in Tab. 6.6 but the capability of the given formula to estimate the flutter critical frequency seems to be highly general.

The result of Eq. (6.19) for the flutter critical frequency is based on the assumption that $g_h + g_\alpha \neq 0$ used to obtain Eq. (6.9). Nevertheless, if $g_h = g_\alpha = 0$ the imaginary flutter equation [Eq. (6.8)] largely simplifies and the result of Eq. (6.20) can be derived directly. That means that it is the imaginary flutter equation which contains mainly the information about the critical frequency, even though it is not possible to obtain directly a closed-form solution for X, unless damping is neglected.

Table 6.6: Comparison between the critical frequency given by the eigenvalue analysis and by Eq. (6.19), supposing to know the critical reduced wind speed

Aerodyn.	Dynamics		$\zeta_h = \zeta_\alpha = 0$				$\zeta_h = \zeta_\alpha = 0.01$			
	μ	r_α	U_{Rc}	f_c (eig.)	f_c (approx.)	Δf_c	U_{Rc}	f_c (eig.)	f_c (approx.)	Δf_c
	[-]	[-]	[-]	[Hz]	[Hz]	[%]	[-]	[Hz]	[Hz]	[%]
Flat plate	35.7	0.249	10.56	0.3178	0.3161	-0.53	10.93	0.3123	0.3102	-0.67
Flat plate	178.6	0.353	25.32	0.4649	0.4639	-0.21	26.51	0.4551	0.4541	-0.22
R12.5	35.7	0.249	7.80	0.3667	0.3752	+2.32	8.25	0.3589	0.3646	+1.59
R12.5	178.6	0.353	14.04	0.5841	0.5824	-0.29	17.32	0.5580	0.5555	-0.45

6.3.3 Simplified equation for critical reduced wind speed

Since we observed that the result of the previous section mainly comes from the imaginary flutter equation, let us come back now to the real flutter equation [Eq. (6.7)], retaining the only trivial simplification $g_h g_\alpha \ll 1$ and rearranging it in the following way:

$$\begin{aligned}&[\mu A_3^* - r_\alpha^2 \mu^2 (X-1)] \cdot (1 - \frac{X}{\gamma_\omega^2}) - r_\alpha^2 \mu H_4^* (X-1) + (g_h \mu A_2^* + g_\alpha \gamma_\omega^2 r_\alpha^2 \mu H_1^*) \frac{X}{\gamma_\omega^2} + \\ &H_4^* A_3^* - H_1^* A_2^* - H_3^* A_4^* + H_2^* A_1^* = 0\end{aligned} \tag{6.22}$$

by defining:

$$T_1 = [\mu A_3^* - r_\alpha^2 \mu^2 (X-1)] \cdot (1 - \frac{X}{\gamma_\omega^2}) \tag{6.23}$$

$$T_2 = -r_\alpha^2 \mu H_4^* (X-1) \tag{6.24}$$

$$T_3 = (g_h \mu A_2^* + g_\alpha \gamma_\omega^2 r_\alpha^2 \mu H_1^*) \frac{X}{\gamma_\omega^2} \tag{6.25}$$

$$T_4 = H_4^* A_3^* - H_1^* A_2^* - H_3^* A_4^* + H_2^* A_1^* \tag{6.26}$$

Eq. (6.22) can be written in the following form:

$$T_1 + T_2 + T_3 + T_4 = 0 \tag{6.27}$$

The term T_3 vanishes if zero damping is assumed. It is interesting to understand which is the actual weight of the four terms in the equation. Therefore each term and their sum are plotted against U_R in Fig. 6.1, for different values of X in the interval $1 \leq X \leq \gamma_\omega^2$ for the chosen case studies. Unrealistically high damping coefficients are assumed ($g_h = g_\alpha = 0.05$) in order to stress the role of the term T_3. The results are shown in the aforementioned graphs. It is possible to observe that the weight of the terms T_2, T_3 and T_4 is definitely negligible with respect to T_1.

$$0 = T_1 + T_2 + T_3 + T_4 \cong T_1 \tag{6.28}$$

In addition, it is also expected that $X \neq \gamma_\omega$, that is $\omega \neq \omega_h$, so that the critical condition becomes:

$$A_3^* - r_\alpha^2 \mu (X-1) = 0 \tag{6.29}$$

Finally, the expression for X given by Eq. (6.19) is substituted in this equation, leading to an approximate formula for the flutter critical reduced wind speed:

$$g_\alpha(A_3^*)^2 + g_\alpha r_\alpha^2 \mu A_3^*(2-\gamma_\omega^2) - A_2^* A_3^* - \gamma_\omega^2 r_\alpha^2 H_1^* A_3^* + r_\alpha^2 \mu A_2^*(\gamma_\omega^2 - 1) - r_\alpha^4 \mu^2 g_\alpha(\gamma_\omega^2 - 1) = 0 \quad (6.30)$$

If damping is neglected, the solution simplifies to:

$$A_2^* A_3^* + \gamma_\omega^2 r_\alpha^2 H_1^* A_3^* - r_\alpha^2 \mu A_2^*(\gamma_\omega^2 - 1) = 0 \quad (6.31)$$

Eq. (6.30) along with Eq. (6.19) constitute an approximate solution of the flutter problem which depends only on modal parameters (r_α, μ, γ_ω, g_h and g_α) and three aeroelastic functions (H_1^*, A_2^*, A_3^*), thus representing a remarkable simplification. In addition, the form of the approximate solution allows to calculate easily, practically by hand, the reduced critical wind speed [from Eq. (6.30)] and the flutter frequency [from Eq. (6.19)].

6.4 Further simplification

For a theoretical flat plate the three flutter derivatives involved in the simplified formulas can be expressed by means of the Theodorsen's Circulatory Function $C(k) = F(k) + iG(k)$ as follows (section 2.4.1):

$$H_1^*(K) = -\pi \frac{F(k)}{k} \quad (6.32)$$

$$A_2^*(K) = -\frac{\pi}{16k}[1 - F(k) - \frac{2G(k)}{k}] \quad (6.33)$$

$$A_3^*(K) = \frac{\pi}{8k^2}[\frac{k^2}{8} + F(k) - \frac{kG(k)}{2}] \quad (6.34)$$

where, as usual, $K = \omega B/U$ and $k = K/2$. Since there are three functions expressed by two independent ones, a relationship between them can be found:

$$A_3^*(K) = -\frac{\pi}{64} - \frac{kA_2^*(K)}{2} - \frac{4+k^2}{32k} H_1^*(K) \quad (6.35)$$

This relationship is exact for a theoretical flat plate but seems to apply more or less reasonably also for a wide range of real bridge deck sections. As a matter of fact, in order to check its validity the flutter derivatives of the rectangular cylinders characterized by a chord-to-thickness ratio of 12.5 and 20 (Matsumoto, 1996), Tsurumi Fairway Bridge (Singh *et al.*, 1995) and Akashi Kaikyo Bridge [Katsuchi *et al.* (1999): modified cross section] are taken into account, as shown in Fig. 6.2. It is evident that the relationship between A_3^*, A_2^* and H_1^* found for the theoretical flat plate is valid for rectangular cross-sections with large chord-to-thickness ratio (R20 for instance) and for streamlined box-girder sections (Tsurumi Fairway Bridge), whose aerodynamic behavior is supposed to be not very different from that of an airfoil. The

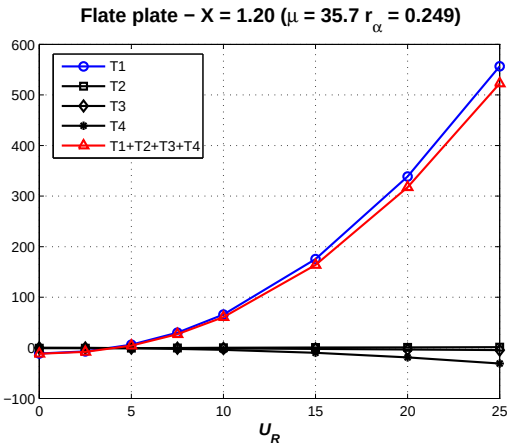
Flate plate − X = 1.20 (μ = 35.7 r α = 0.249)
T1
T2
T3
T4
T1+T2+T3+T4
U R

(a)

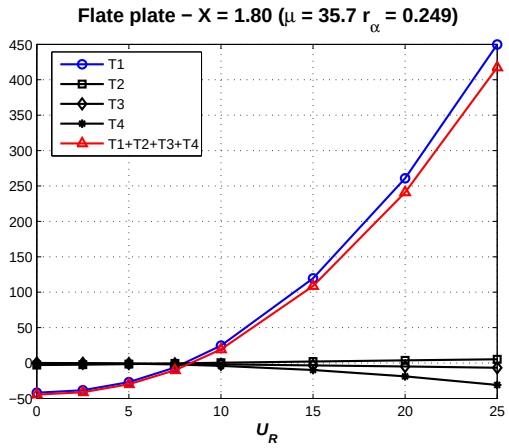
Flate plate − X = 1.80 (μ = 35.7 r α = 0.249)
T1
T2
T3
T4
T1+T2+T3+T4
U R

(b)

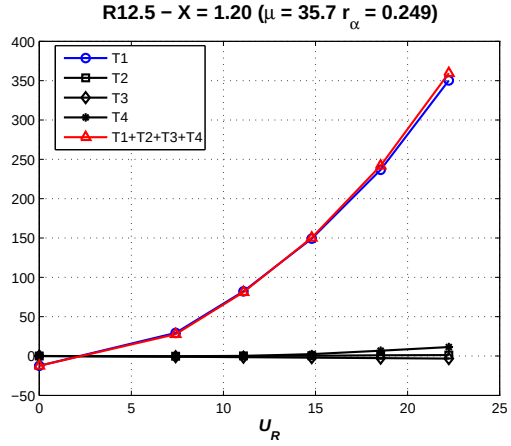
R12.5 − X = 1.20 (μ = 35.7 r α = 0.249)
T1
T2
T3
T4
T1+T2+T3+T4
U R

(c)

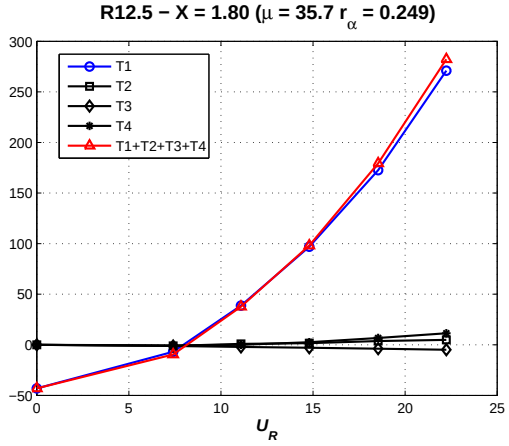
R12.5 − X = 1.80 (μ = 35.7 r α = 0.249)
T1
T2
T3
T4
T1+T2+T3+T4
U R

(d)

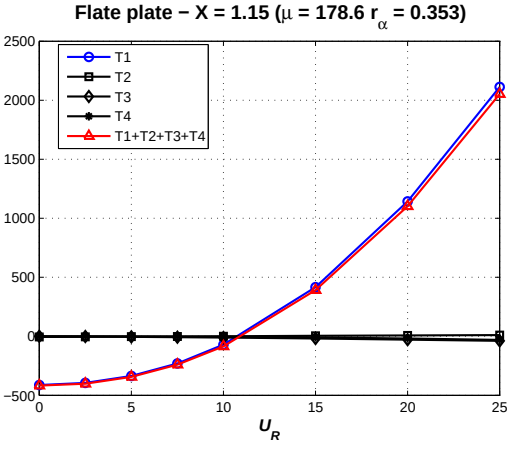
Flate plate − X = 1.15 (μ = 178.6 r α = 0.353)
T1
T2
T3
T4
T1+T2+T3+T4
U R

(e)

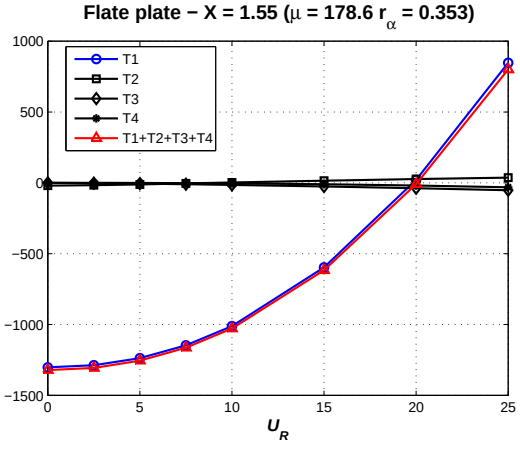
Flate plate − X = 1.55 (μ = 178.6 r α = 0.353)
T1
T2
T3
T4
T1+T2+T3+T4
U R

(f)

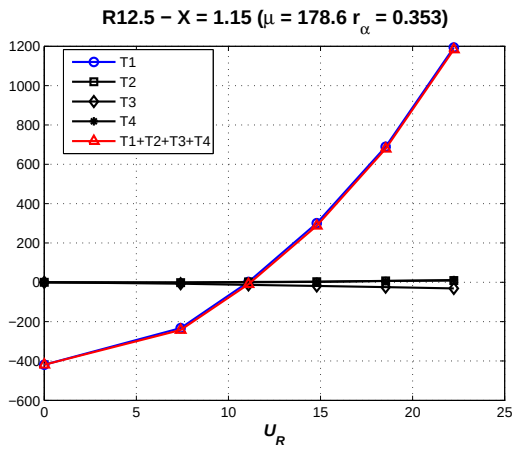

(g)

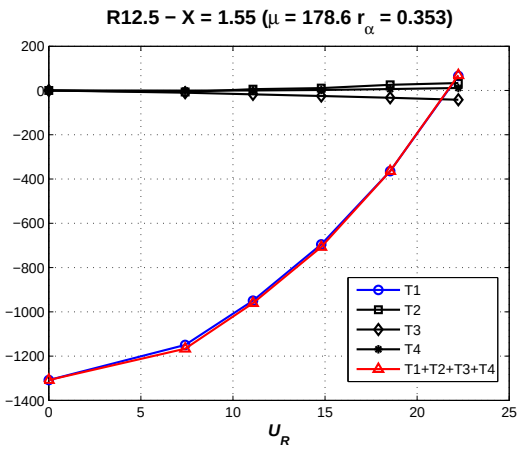

(h)

Figure 6.1: Comparison between the four terms composing the real flutter equation [Eq. (6.22)]

equation is less accurate for bluffer rectangular cross sections (R12.5) and for truss-stiffened girders (Akashi Kaikyo Bridge) but the approximation seems to be still acceptable for some applications. Eq. (6.35) with Eqs. (6.19) and (6.30) constitute a further simplified model to calculate the flutter critical frequency and reduced wind speed, retaining only the flutter derivatives H_1^* and A_2^*.

6.5 Degree of approximation

In order to understand the limits of the proposed approach, for the previous four case studies the computation of the critical reduced wind speed is repeated for different damping levels and frequency ratios γ_ω. The results of this analysis are reported in Fig. 6.3. Some first conclusions can be drawn after the analysis of these graphs. The approximate formulas give results which are close to the one obtainable from the rigorous solution of the eigenvalue-problem of stability for a wide range of frequency ratios both in case of zero and high structural damping.

The greatest limit of the proposed approach is its inability to give reasonable results when the frequency ratio γ_ω tends to unity. It is known that when the still-air torsional frequency is very close to the vertical bending one, the critical reduced wind speed tends to become very high (Dyrbye and Hansen, 1997). The approximate approach is not able to follow this behavior, as it could have been expected from the analysis of T_1 expression [Eq. (6.23)]: when $\gamma_\omega \to 1$, $X \to 1$ as well, so that T_1 tends to vanish instead of being the dominant term in the real flutter equation. Nevertheless, it seems that a frequency ratio of about 1.3, or even less, can usually be sufficient to obtain an acceptable degree of approximation. Frequency ratios very close to unity are fairly uncommon and usually characterize super-long-span bridges (like the proposed Messina Strait Bridge) or non-conventional structures, which obviously are not expected to be analyzed with simplified methods, requiring deep and careful experimental campaigns. In addition, in case of realistic deck geometries the eigenvalue approach gives

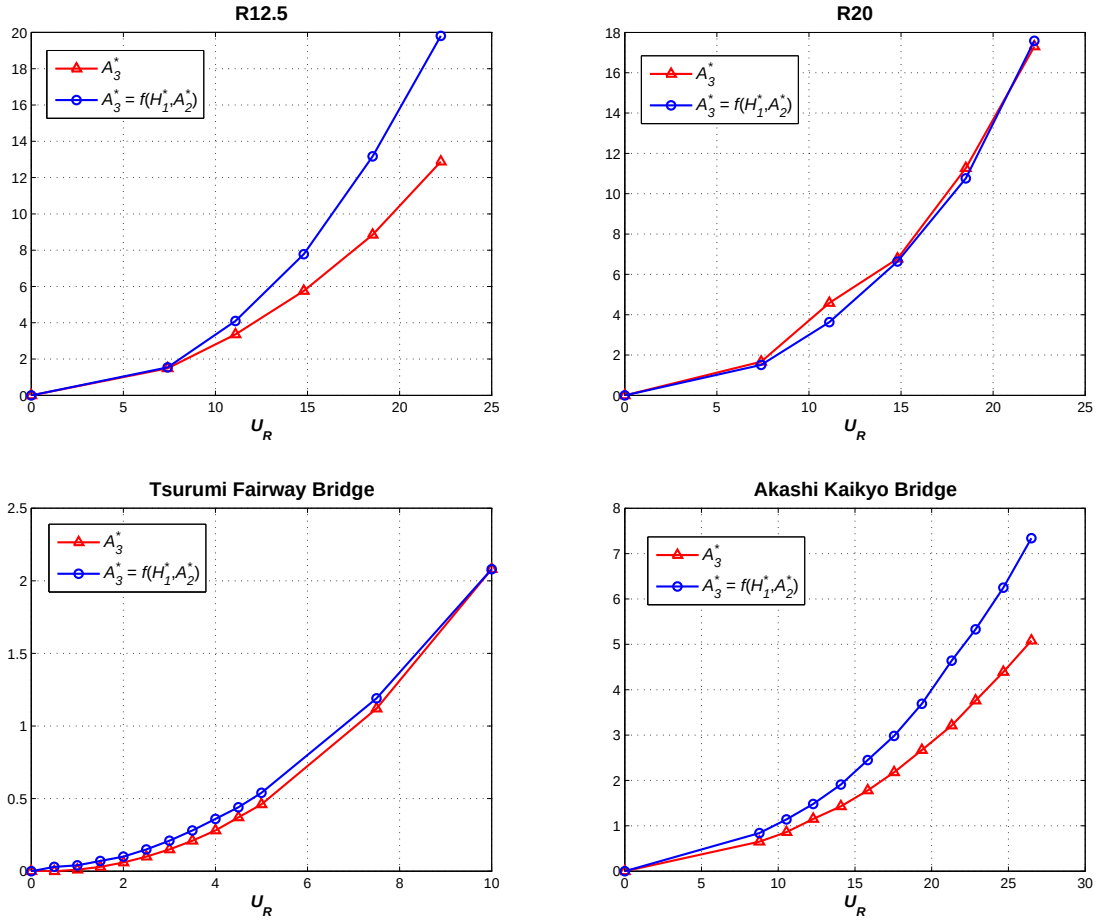

Figure 6.2: Degree of approximation of Eq. (6.35) in the case of four cross-sectional geometries

often doubtful results: the problem sometimes shows many solutions close to each other, also for very low reduced wind speed, or in other cases no solution at all is found.

It is worth noting that the use of the approximate expression for A_3^* given by Eq. (6.35) (approx. sol. II) instead of experimental values (approx. sol. I) does not imply significant differences in the results for the rectangular cylinder R12.5 when the mass parameters $\mu = 35.7$ and $r_\alpha = 0.249$ are assumed. Conversely, assuming $\mu = 178.6$ and $r_\alpha = 0.353$, reductions up to 10 % of the non-dimensional wind speed are observed. Obviously, no distinction between the two formulas can be made when the aerodynamics of the theoretical flat plate is considered.

Finally, concerning the role played by structural damping in the flutter instability onset, it is difficult to outline clear conclusions but it seems that for streamlined cross sections [see Figs. 6.3(a), 6.3(b) and 6.6(a)] its role is definitely marginal, especially for frequency ratios far from unity, whereas for bluffer cross sections [see Figs. 6.3(c), 6.3(d), 6.12(a) and 6.12(b)] it can be relevant depending on the mass parameters. In these cases, not to neglect damping in the simplified formulas given by Eqs. (6.19) and (6.30) is definitely important.

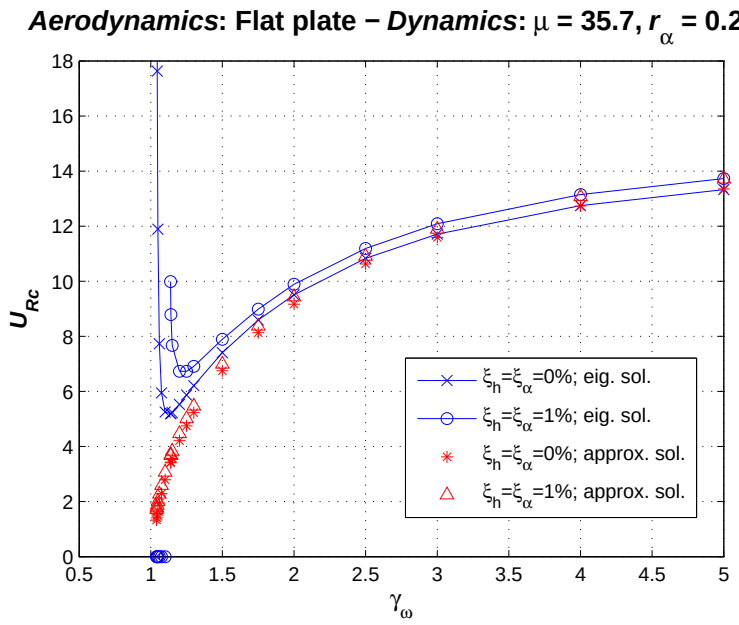
Aerodynamics: Flat plate − Dynamics: μ = 35.7, r_α = 0.249
U_Rc
γ_ω
ξ_h=ξ_α=0%; eig. sol.
ξ_h=ξ_α=1%; eig. sol.
ξ_h=ξ_α=0%; approx. sol.
ξ_h=ξ_α=1%; approx. sol.

(a)

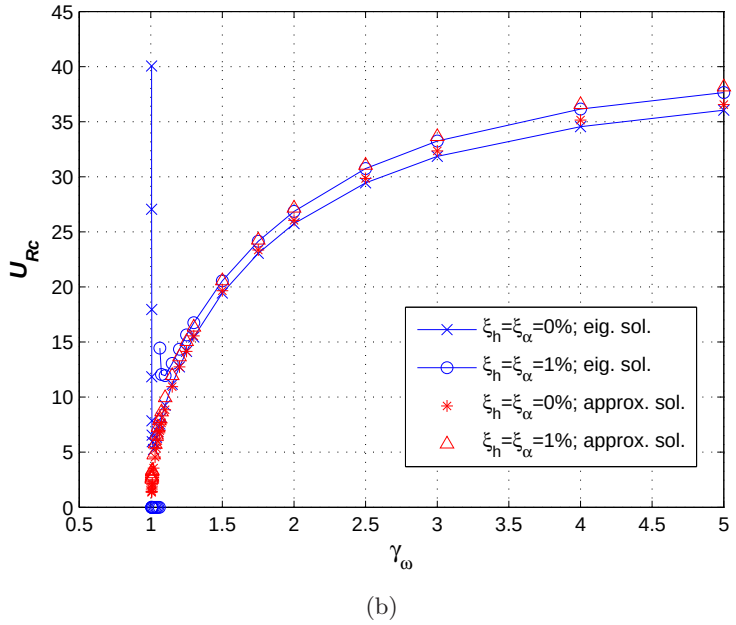
Aerodynamics: Flat plate − Dynamics: μ = 178.6, r_α = 0.353
U_Rc
γ_ω
ξ_h=ξ_α=0%; eig. sol.
ξ_h=ξ_α=1%; eig. sol.
ξ_h=ξ_α=0%; approx. sol.
ξ_h=ξ_α=1%; approx. sol.

(b)

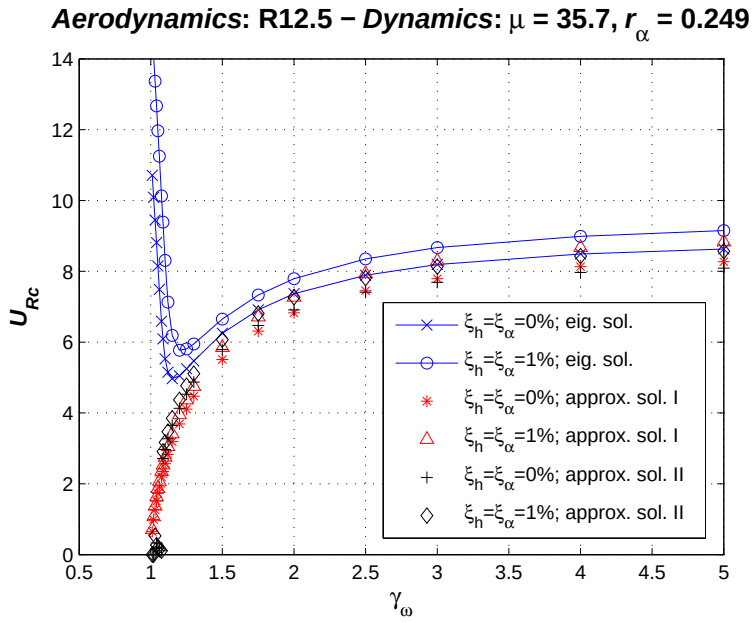

(c)

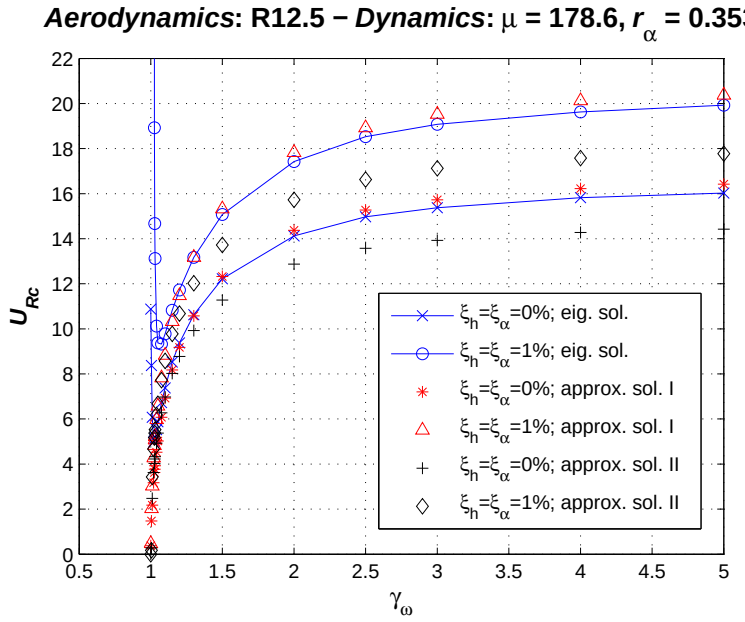

(d)

Figure 6.3: Comparisons between the solutions of the eigenvalue problem of flutter stability (eig. sol.) and those of the approximate Eqs. (6.19) and (6.30) (approx. sol. I) or Eqs. (6.19), (6.30) and (6.35) (approx. sol. II) for different values of the frequency ratio γ_ω and two structural damping ratios (0 % and 1 %). If the theoretical flat plate is assumed as reference for the aerodynamics, there is obviously no difference between the two approximate formulas

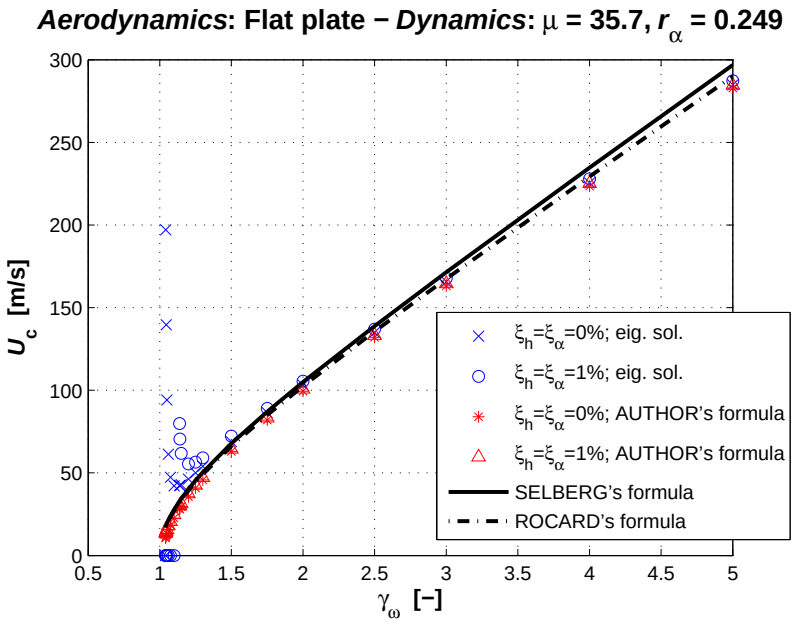

(a)

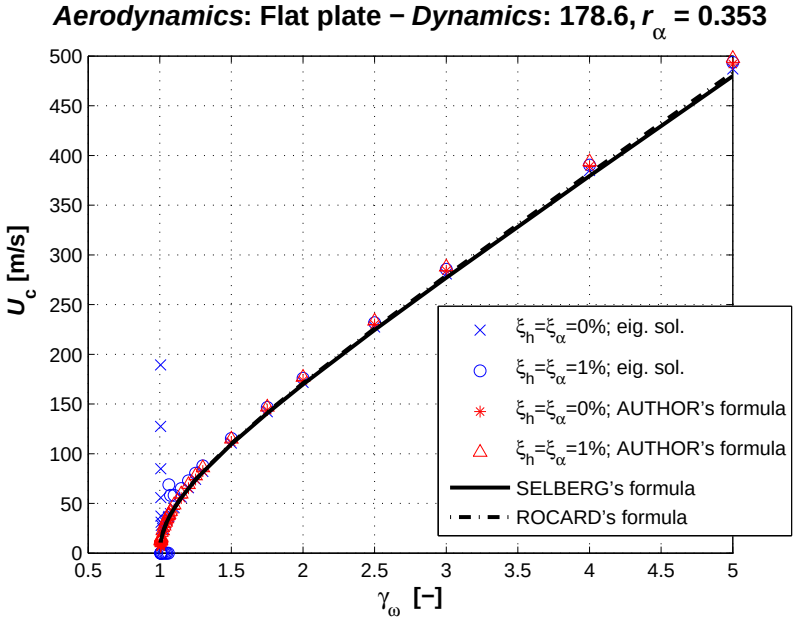

(b)

Figure 6.4: Comparison between the results given by author's formula and Selberg and Rocard's formulas in the case of a thin flat plate

For a thin flat plate the results given by the proposed formulas are very similar to those predicted by Selberg (1961) and Rocard's (Frandsen, 1966) approximate formulas, which are written here according to the notation adopted in the present dissertation:

$$U_c = 2.623 f_\alpha B \sqrt{(1 - \frac{1}{\gamma_\omega^2}) r_\alpha \mu} \qquad \texttt{[Selberg]} \tag{6.36}$$

$$U_c = 6.282 f_\alpha B \sqrt{(1 - \frac{1}{\gamma_\omega^2}) \frac{r_\alpha^2 \mu}{1 + 8 r_\alpha^2}} \qquad \texttt{[Rocard]} \tag{6.37}$$

As it can be seen in Fig. 6.4, all these approaches are not able to reproduce the sudden increase in the critical wind speed appearing when the frequency ratio tends to unity, whereas for larger values of γ_ω they all give excellent results, although author's formulas also account for the contribution of structural damping. Therefore, the proposed simplified method seems to play the same role for realistic bridge deck cross sections as Selberg and Rocard's formulas for the thin flat plate. As a matter of fact, the use of Selberg and Rocard's formulas can be extended to bridge decks only if the critical flutter wind speed is multiplied by an empirical coefficient of "aeroelastic performance" [e.g. Frandsen (1966); Gimsing (1997); Dyrbye and Hansen (1997); Righi (2003); Bartoli and Righi (2004b, 2006)], as already discussed in the first section of this chapter.

6.6 Case studies

In order to further check the validity of the proposed simplified approach, other case studies are taken into account. Some of them refer to real structures, such as Case 5 for the Akashi Kaikyo Bridge [Miyata and Yamaguchi (1993); Katsuchi *et al.* (1999): modified cross section] and Case 6 (Tab. 6.7) for the Tsurumi Fairway Bridge (Sarkar, 1992; Singh *et al.*, 1995); the others, as already explained, are combinations of the modal parameters of some bridges (see Tab. 6.1) and the flutter derivatives measured for a few cross sections prone to coupled flutter: thin flat plate [Fung (1993); section 2.4.1], R12.5 and R20 rectangular cylinders (Matsumoto, 1996), rectangular cylinder with semi-circular fairings and chord-to-thickness ratio of 14.3, called R14.3F (Chowdhury and Sarkar, 2004) and Tsurumi Fairway Bridge (Singh *et al.*, 1995). All case studies are listed in Tab. 6.7 along with the modal properties assumed in the calculations. In Tab. 6.8 the reduced flutter wind speeds and the coupling frequencies calculated through the solution of the eigenvalue-problem of stability and the proposed simplified formulas [approx. sol. I: Eqs. (6.19) and (6.30); approx. sol. II: Eqs. (6.19), (6.30) and (6.35)] are compared. In Fig. 6.5(b) the graphical solution of Eq. (6.30) is presented for the flat plate of Case 1 and for Akashi Kaikyo Bridge (Case 5).

From Tab. 6.8 it can be concluded that the proposed formulas give accurate results in most cases, especially if experimental values for A_3^* are considered (approx. sol. I). In some instances, the results are practically the same as those given by the solution of the eigenvalue problem of stability. The formula for the coupling frequency is particularly accurate. Nevertheless, when the frequency ratio is small (e.g. Case 2), as expected, the accuracy of

the approximation is poorer. The approximate formulas retaining only two flutter derivatives (H_1^* and A_2^*) are less performing than the ones adopting three experimental functions but the degree of approximation seems to be still acceptable.

Table 6.7: Case studies (coupled flutter)

Case	Aerodynamics	μ [-]	r_α [-]	γ_ω [-]	ζ_h [%]	ζ_α [%]
1	Flat plate	35.7	0.249	2.38	0.5	0.5
2	Flat plate	24.1	0.374	1.32	0.6	0.7
3	R12.5	178.6	0.353	1.96	0.8	0.8
4	R12.5	27.7	0.357	2.29	0.5	0.5
5	Akashi Kaikyo	55.6	0.422	2.34	0.5	0.3
6	Tsurumi	35.7	0.249	2.38	0.5	0.5
7	Tsurumi	55.5	0.250	2.06	0.2	0.2
8	R14.3F	47.2	0.539	1.54	0.5	0.5
9	R14.3F	27.7	0.357	2.29	0.5	0.5
10	R20	38.7	0.286	2.27	0.2	0.5

Table 6.8: Results for the case studies presented in Tab. 6.7 (f_c is the coupling frequency, U_{Rc} is the flutter reduced wind speed)

Case	eig. sol.		approx. sol. I				approx. sol. II			
	f_c [Hz]	U_{Rc} [-]	f_c [Hz]	Δf_c [%]	U_{Rc} [-]	ΔU_{Rc} [%]	f_c [Hz]	Δf_c [%]	U_{Rc} [-]	ΔU_{Rc} [%]
1	0.315	10.75	0.314	-0.2	10.48	-2.5	-	-	-	-
2	0.071	6.72	0.072	+0.8	5.46	-18.8	-	-	-	-
3	0.562	16.80	0.560	-0.4	17.17	+2.2	0.553	-1.6	15.20	-9.5
4	0.308	7.64	0.313	+1.4	7.09	-7.2	0.313	+1.5	7.11	-6.9
5	0.138	16.14	0.137	-0.6	16.26	+0.7	0.137	-0.9	14.11	-12.6
6	0.377	8.34	0.349	-7.6	10.07	+20.7	0.351	-6.9	9.82	+17.7
7	0.880	11.04	0.834	-5.2	12.77	+15.7	0.832	-5.5	12.97	+17.5
8	0.180	11.41	0.179	-0.2	10.60	-7.1	0.179	-0.3	9.97	-12.6
9	0.284	10.16	0.282	-0.8	9.40	-7.5	0.282	-1.0	8.86	-12.9
10	0.338	11.21	0.339	+0.4	10.86	-3.1	0.338	-0.0	11.49	+2.5

Much more difficult to explain is the larger errors affecting Case 6 and Case 7, where the aerodynamics of the Tsurumi Fairway Bridge is considered, as it is also evident from Fig. 6.6(b). In Fig. 6.6(a) it is possible to observe that increasing the frequency ratio the degree of approximation does not improve, on the contrary it becomes slightly worse. It must also be remarked that in this case to perform the computation with zero damping is troublesome since several solutions for the eigenvalue problem of stability are found at low wind speeds: that is why damping levels of 0.5 % and 1 % are taken into account in Fig. 6.6(a). This bridge deck

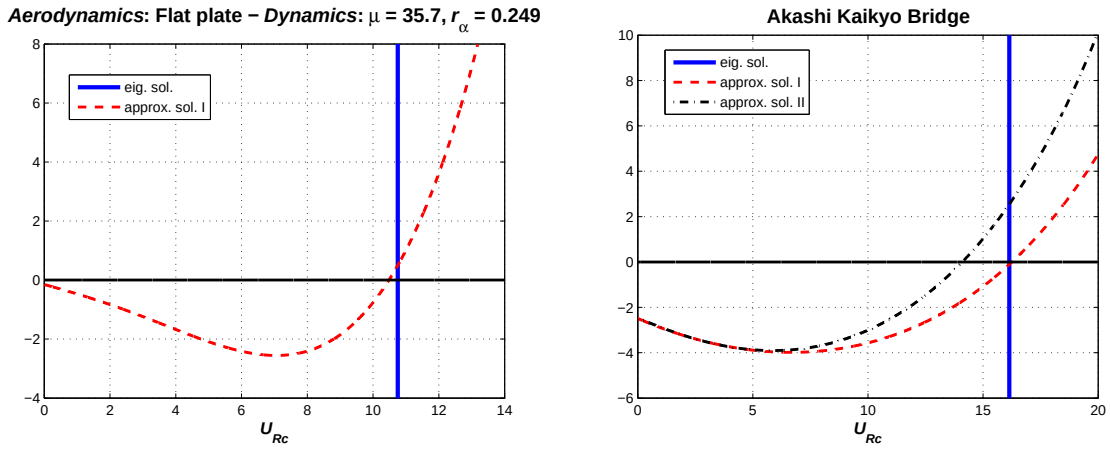

(a) (b)

Figure 6.5: Graphical solution of the approximate formula for flutter reduced wind speed for Case 1 and Case 5 (Akashi Kaikyo Bridge) of Tabs. 6.7-6.8, considering measured A_3^* (approx. sol. I) and approximate values given by Eq. (6.35) (approx. sol. II)

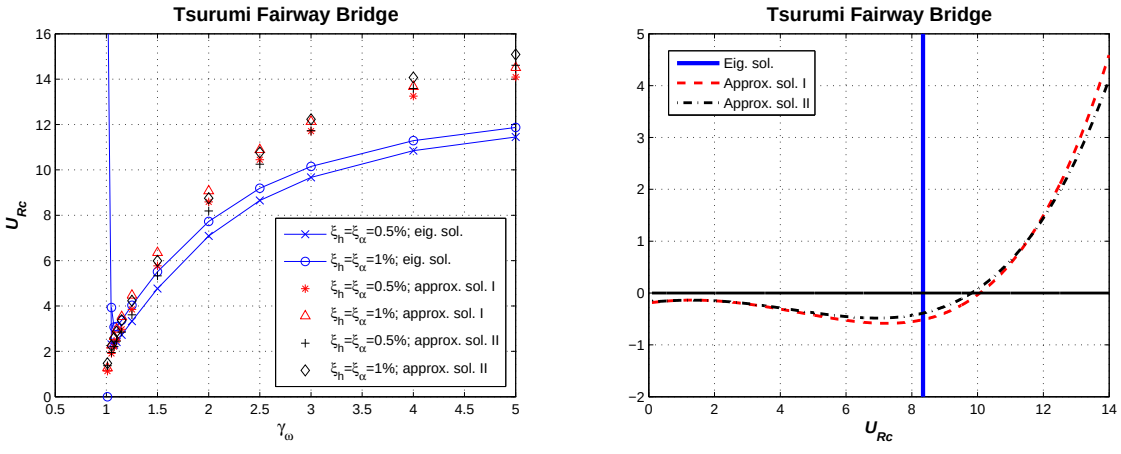

(a) (b)

Figure 6.6: Tsurumi Fairway Bridge: (a) solutions for different frequency ratios and damping ratios; (b) graphical solution of the approximate formula (Case 6 in Tabs. 6.7-6.8)

is characterized by a fairly streamlined cross section and the flutter derivatives seem to agree well with all the simplifications listed in the previous sections. In particular, Eqs. (6.16), (6.19) and (6.28) are very accurate. Conversely, the combination of all these simplifications, resulting in Eq. (6.30), gives poorer results. This particular behavior related to the aerodynamics of the Tsurumi cross section needs further investigation. It is partially reassuring the fact that the errors which affect the reduced wind speed and the coupling frequency are of opposite sign (Tab. 6.8) so that, considering the dimensional flutter wind speed, that is the variable of practical engineering interest, the error is sensibly smaller (around 11 % for Case 1).

The last case study is taken into account is the trapezoidal single-box girder deck with lateral cantilevers, here called "CRIACIV section", whose aeroelastic behavior is presented and discussed in Chapter 3. The approximate formulas are applied to the three test cases reported in Tabs. 3.13 and 3.14. Results are outlined in Tabs. 6.9 and 6.10. The approximate results seem to confirm the considerations drawn for the other case studies. Nevertheless two additional remarks can be pointed out. For "test case 0" and "test case 1" the errors on the critical frequency and reduced wind speed have opposite sign and tend to compensate each other, so that the final error on the dimensional flutter wind speed is much smaller (especially for "test case 0"). This fact could be seen as a pure coincidence but it has already been observed in many case studies (e.g. Case 6 and Case 7 in Tab. 6.8, where the aerodynamics of the Tsurumi Fairway Bridge is considered). The second point concerns "test case 2" for which the approximate formulas give values much closer to the measured flutter boundaries than the rigorous eigenvalue analysis. Again this could be seen as an accidental outcome and probably its surprising accuracy is, but it could also suggest that, as discussed in section 3.5.2, some of the cross-derivatives measured via free-vibration tests far from coupling are functions which do not coincide with the corresponding actual "flutter derivatives". If this is true, more accurate results are expected using three flutter derivatives (measured via free-vibration tests) instead of eight, some functions introducing erroneous information in the computation. Considering the approximate formulas requiring H_1^* and A_2^* only, the reason why they give acceptable results but less accurate than the formulas with three flutter derivatives is evident from the analysis of Fig. 6.7, where it is possible to see that there is a non-negligible discrepancy between the measured values of A_3^* and those calculated with Eq. (6.35).

The flutter derivatives measured for the CRIACIV section are also combined with the two reference sets of mass parameters (section 6.3.2) and the reduced critical wind speed is calculated for several values of the frequency ratio and damping coefficient (Fig. 6.8). In one case [Fig. 6.8(b)] the approximate formulas give accurate results, while in the other case [Fig. 6.8(a)] larger errors occur. Nevertheless, these inaccuracies tend to become smaller when the formula for the reduced wind speed and the one for the coupling frequency are combined in order to obtain the dimensional critical wind speed. This also happens for the wind-tunnel test cases, for which in Fig. 6.9 the critical wind speed is plotted against the frequency ratio.

Finally, it is worth reminding that a significant scatter usually affects flutter derivative values, especially in the case of the neglected aeroelastic functions [Righi (2003); Bartoli and Mannini (2005); Chapter 3 of the present dissertation]. Moreover, non-negligible differences in the results are just due to the chosen analytical interpolation of the experimental data. These effects are in many cases of the same order of magnitude as the errors highlighted in Tab. 6.8, thus confirming the validity of the proposed approach.

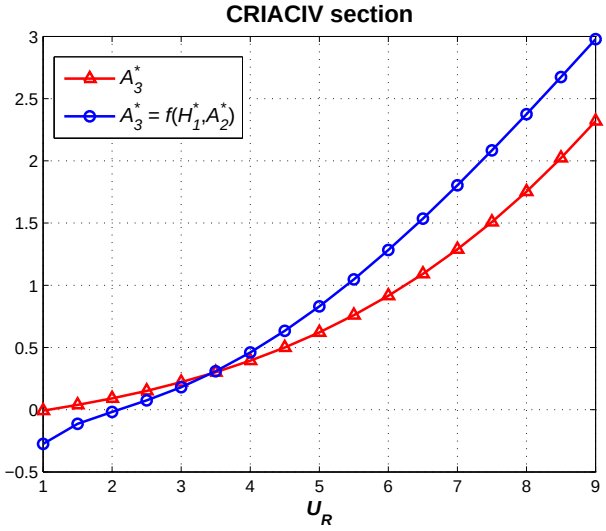

Figure 6.7: Degree of approximation of Eq. (6.35) in the case of the CRIACIV section

Table 6.9: Comparison between the results of the approximate formulas with three flutter derivatives (approx. sol. I), the eigenvalue solution and the measured values of the flutter reduced wind speed and frequency for the section-model test cases presented in section 3.5.2 (the differences are evaluated with respect to the measured values)

Test case	Measured			eig. sol.			approx. sol. I					
	f_c [Hz]	U_{Rc} [-]	U_c [m/s]	f_c [Hz]	U_{Rc} [-]	U_c [m/s]	f_c [Hz]	Δf_c [%]	U_{Rc} [-]	ΔU_{Rc} [%]	U_c [m/s]	ΔU_c [%]
0	4.74	9.30	19.86	4.69	9.42	19.89	5.28	+11.4	8.33	-10.4	19.81	-0.3
1	3.70	9.13	15.20	3.69	9.19	15.27	3.95	+6.7	7.64	-16.3	13.57	-10.7
2	3.56	7.24	11.60	3.44	9.10	14.08	3.59	+4.4	7.25	+0.1	11.71	+0.9

Table 6.10: Comparison between the results of the approximate formulas with two flutter derivatives (approx. sol. II), the eigenvalue solution and the measured values of the flutter reduced wind speed and frequency for the section-model test cases presented in section 3.5.2 (the differences are evaluated with respect to the measured values)

Test case	Measured			eig. sol.			approx. sol. II					
	f_c [Hz]	U_{Rc} [-]	U_c [m/s]	f_c [Hz]	U_{Rc} [-]	U_c [m/s]	f_c [Hz]	Δf_c [%]	U_{Rc} [-]	ΔU_{Rc} [%]	U_c [m/s]	ΔU_c [%]
0	4.74	9.30	19.86	4.69	9.42	19.89	5.28	+11.4	7.46	-19.8	17.73	-10.7
1	3.70	9.13	15.20	3.69	9.19	15.27	3.95	+6.8	6.62	-27.5	11.77	-22.5
2	3.56	7.24	11.60	3.44	9.10	14.08	3.59	+0.9	6.28	-13.3	10.14	-12.6

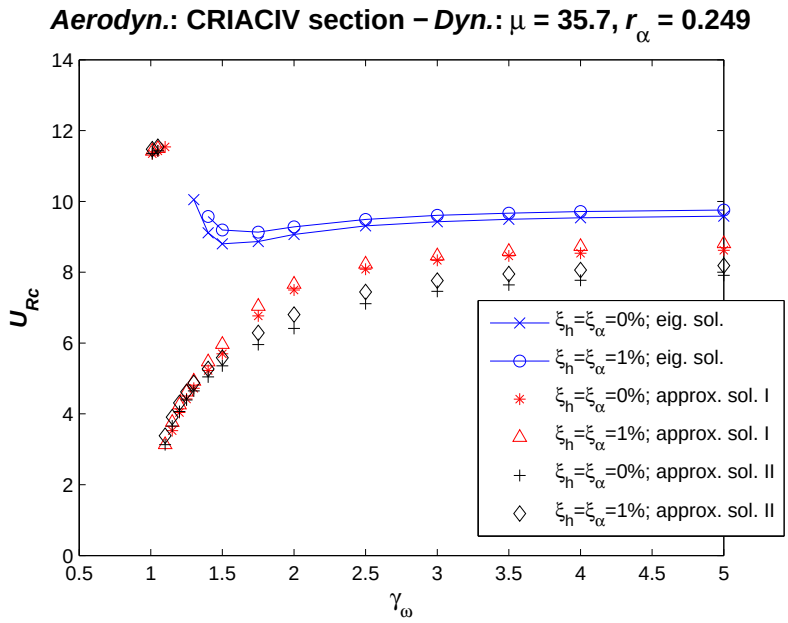

(a)

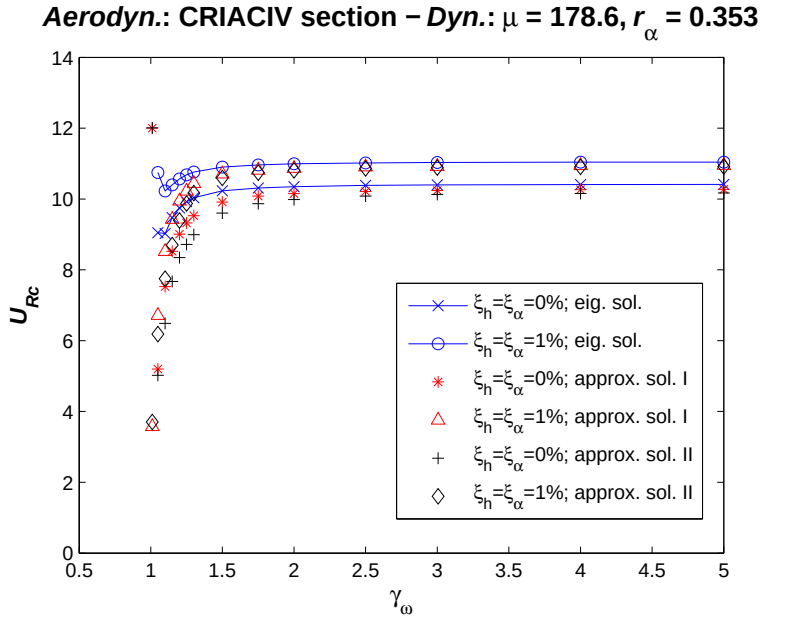

(b)

Figure 6.8: "CRIACIV section": eigenvalue and approximate solutions for different frequency ratios and damping ratios and two reference sets of mass parameters

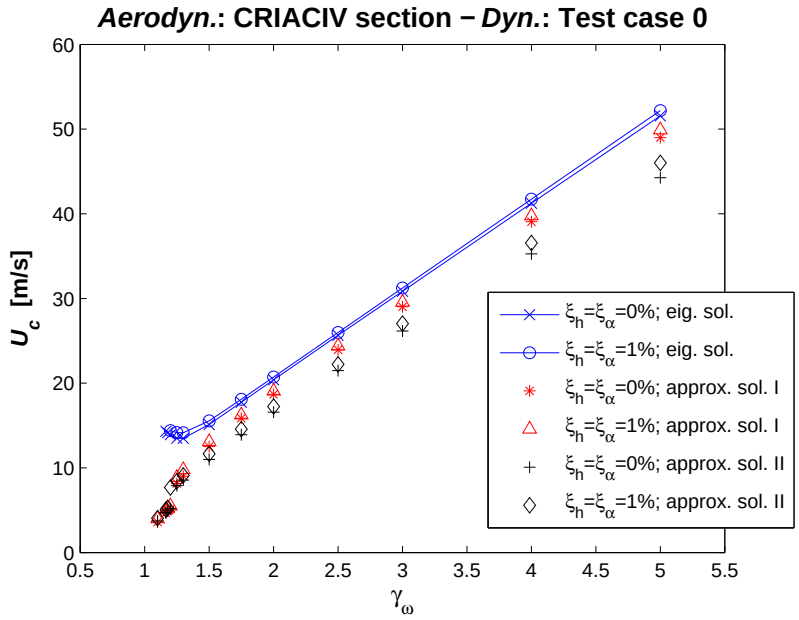

(a)

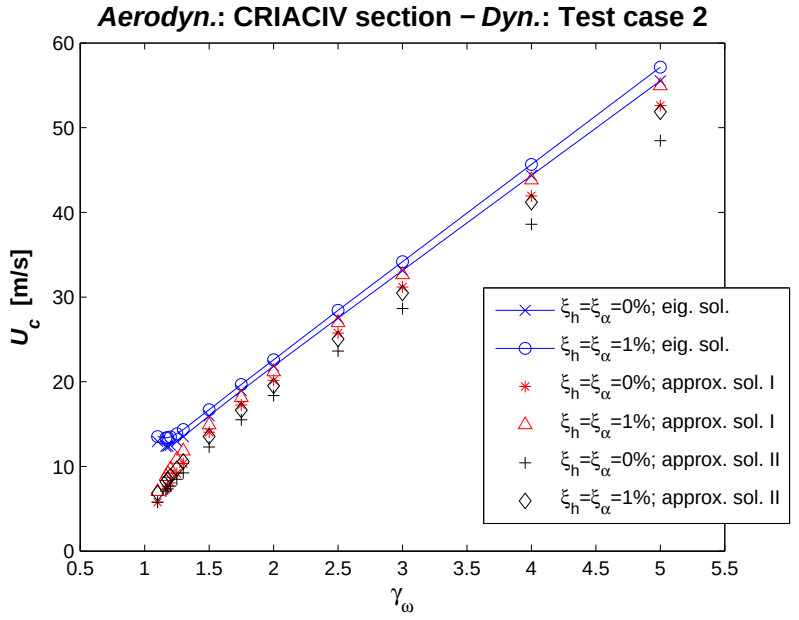

(b)

Figure 6.9: "CRIACIV section": eigenvalue and approximate solutions for different frequency ratios and damping ratios and the mass parameters of two wind-tunnel test cases

6.7 Torsional flutter

The deck cross sections taken into account insofar are all prone to coupled flutter, as confirmed by the monotonic negative trend of H_1^* and A_2^* shown in the given references. Nevertheless, it is well known that a wide range of real bridges, whose deck cross sections are not streamlined, are prone to single-degree-of-freedom torsional flutter. For these bridge decks the function A_2^* tends to reverse its sign from negative to positive at relatively low reduced wind speed introducing negative aerodynamic damping in the torsional modes. In this case, an alternative way to deal with the flutter phenomenon is to consider just the frequency shift due to A_3^* and the damping reduction produced by A_2^*:

$$f_c = f_\alpha[1 + \frac{\rho B^4}{2I} A_3^*(K_c)]^{-\frac{1}{2}} \tag{6.38}$$

$$A_2^*(K_c) = 4\zeta_\alpha \frac{I}{\rho B^4} \cdot \frac{f_\alpha}{f_c(K_c)} \tag{6.39}$$

where $K_c = \frac{U_c}{B 2\pi f_c}$ is the critical reduced frequency, U_c is the critical wind speed, f_c the critical (torsional) frequency. Eqs. (6.38)-(6.39) constitute a nonlinear system (1-DoF problem) which has to be iteratively solved. The 2-DoF and 1-DoF approaches usually give close results, unless the frequency ratio is near to unity.

All the steps which, starting from Eqs. (6.7)-(6.8), led to the simplified formulas discussed in the previous sections, can be checked now in the particular case of cross sections prone to torsional flutter. As reference examples two prototypes characterized again by the mass properties of Tsurumi Fairway Bridge ($\mu = 35.7$, $r_\alpha = 0.249$) and Guamà Bridge ($\mu = 178.6$, $r_\alpha = 0.353$) and by the aerodynamics of a rectangular cylinder with a chord-to-thickness ratio of 5.0 (Matsumoto, 1996), are considered. The simplifications which led to the approximate formula for critical frequency [Eq. (6.19)], discussed in Tabs. 6.2-6.5 for cross sections prone to coupled flutter, are still valid if the analysis is limited to reduced wind speeds in the neighborhood of the zero-crossing point of A_2^*, since it is in that range that the critical flutter speed must be sought. In Fig. 6.10 the weight of the terms constituting the real flutter equation [Eq. (6.22)] are compared for values of X not far from unity, since the single degree-of-freedom torsional flutter always arises with frequency close to the still-air torsional one. It can be understood from the presented graphs that no solution is found beyond a certain value of X. In Fig. 6.11 the relation between the flutter derivatives H_1^*, A_2^* and A_3^* [Eq. (6.35)] is checked for the aforementioned rectangular cylinder R5 and for the First Tacoma Narrows Bridge (Scanlan and Tomko, 1971). The relation assumed between the three aeroelastic functions is based upon the theoretical expression of the flutter derivatives for a thin flat plate and therefore is less effective in the case of a bluff cross section. Nevertheless, it can be observed in Fig. 6.11 that this approximation does not seem completely wrong in the range of interesting reduced wind speeds, that is around A_2^* zero-crossing point.

In Fig. 6.12 the critical reduced wind speed is plotted against the frequency ratio for the two reference sets of mass parameters. It is possible to remark that the critical reduced wind speed is independent of the frequency separation, unless the ratio γ_ω is quite close to unity. In this region the curves lose the flat trend and the 2-DoF eigenvalue approach gives

results that diverge from those obtained through the 1-DoF approach [Eqs. (6.38)-(6.39)]. Conversely, the 1-DoF and the 2-DoF approaches give usually very close solutions for frequency ratios far enough from unity. For a structure characterized by $\mu = 178.6$ and $r_\alpha = 0.353$ [Fig. 6.12(b)], the agreement between the 2-DoF and 1-DoF solutions is practically perfect provided that γ_ω is greater than approximately 1.5. It can be also remarked the strong dependence on structural damping, as already shown in Fig. 6.3(d). On the other hand, for a structure characterized by $\mu = 35.7$ and $r_\alpha = 0.249$ [Fig. 6.12(a)], a much lower influence of damping and a larger discrepancy between 1-DoF and 2-DoF solutions can be observed. A first reason for the difference between the two solutions might be the role played in the instability mechanism by heaving motion. Another possible explanation could be that, when the frequency ratio is small a coupled instability arises before torsional flutter. Nevertheless this fact, experimentally observed by Nakamura (Nakamura and Yoshimura, 1976), is not able to explain the discrepancy between 1-DoF and 2-DoF solutions in Fig. 6.12(a), which, although decreasing, is still significant for large frequency separation. Moreover, if it was the case, it is not clear the reason why the flutter critical wind speed does not tend to increase when $\gamma_\omega \longrightarrow 1$. It is also worth noting in Fig. 6.12 and Table 6.12 that the 2-DoF solution seems to be conservative with respect to the 1-DoF result (lower U_{Rc}, almost the same f_c). The results of the simplified formulas closely follow the 2-DoF eigenvalue solution and the degree of approximation seems generally very good.

Finally, in Table 6.12 the approximate approach is further validated considering the case studies presented in Table 6.11, where the aerodynamic behavior of the rectangular cylinder R10, characterized by a chord-to-thickness ratio of 10 (Matsumoto, 1996), is considered along with the First Tacoma Narrows Bridge (Scanlan and Tomko, 1971) and the previously mentioned rectangular cylinder R5 (Matsumoto, 1996). As reference, the solutions of both 2-DoF [Eqs. (6.7)-(6.8)] and 1-DoF approach [Eqs. (6.38)-(6.39)] are reported.

It seems possible to conclude that the proposed method, although less useful, applies well also in the case of cross sections prone to torsional flutter. The approximate formulas adopting just two flutter derivatives (approx. sol. II) are less accurate for these bluffer cross sections but only in one case (Case 5 in Tables 6.11-6.12) the error is very large (although the difference between 1-DoF and 2-DoF approach is even larger).

Particularly interesting is the case of R10, the most streamlined Matsumoto's rectangular cylinder showing positive values of the flutter derivative A_2^* reversing its sign from negative to positive (Matsumoto, 1996). As compared to R5, the A_2^* zero-crossing takes place at higher reduced wind speed and, above all, with much smaller slope. The proposed approximation is accurate, while the discrepancy between the 1-DoF and the 2-DoF solutions is larger in that case, probably due to the fact that the coupled instability arises before torsional flutter.

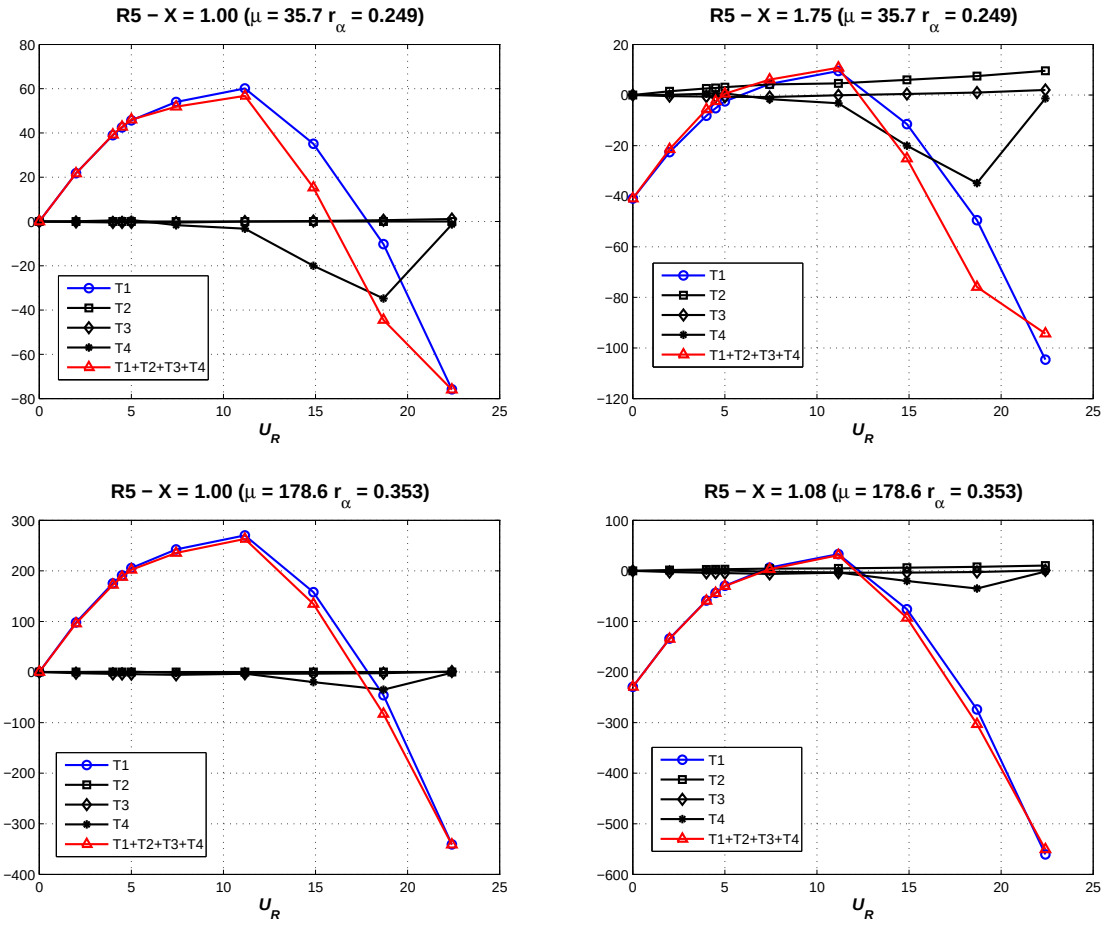

Figure 6.10: Comparison between the four terms composing the real flutter equation [Eq. (6.22)] for the rectangular cylinder R5

Table 6.11: Case studies (single-degree-of-freedom torsional flutter)

Case	Aerodynamics	μ [-]	r_α [-]	γ_ω [-]	ζ_h [%]	ζ_α [%]
1	Tacoma	47.2	0.539	1.54	0.5	0.5
2	R5	47.2	0.539	1.54	0.5	0.5
3	R5	35.7	0.249	2.38	0.5	0.5
4	R5	178.6	0.353	1.96	0.8	0.8
5	R5	24.1	0.374	1.32	0.6	0.7
6	R10	47.2	0.539	1.54	0.5	0.5

Table 6.12: Results for the case studies listed in Tab. 6.11 (f_c is the critical frequency, U_{Rc} is the reduced critical wind speed; the differences are calculated with respect to the 2-DoF eigenvalue solution)

Case	1-DoF sol.		2-DoF eig. sol.		approx. sol. I				approx. sol. II			
	f_c [Hz]	U_{Rc} [-]	f_c [Hz]	U_{Rc} [-]	f_c [Hz]	Δf_c [%]	U_{Rc} [-]	ΔU_{Rc} [%]	f_c [Hz]	Δf_c [%]	U_{Rc} [-]	ΔU_{Rc} [%]
1	0.200	4.81	0.200	4.81	0.200	0.0	4.81	0.0	0.196	-2.0	3.94	-18.1
2	0.189	5.05	0.190	4.41	0.190	+0.4	4.35	-1.2	0.195	+2.5	4.70	+6.5
3	0.376	4.64	0.377	4.08	0.384	+1.9	3.97	-2.5	0.430	+14.0	4.33	+6.2
4	0.626	5.73	0.626	5.56	0.626	+0.0	5.57	+0.1	0.635	+1.5	5.62	+1.1
5	0.066	4.74	0.067	2.76	0.070	+3.6	2.85	+3.4	0.074	+9.8	3.89	+41.2
6	0.182	9.89	0.188	7.65	0.189	+0.1	7.47	-2.3	0.189	+0.4	7.58	-0.9

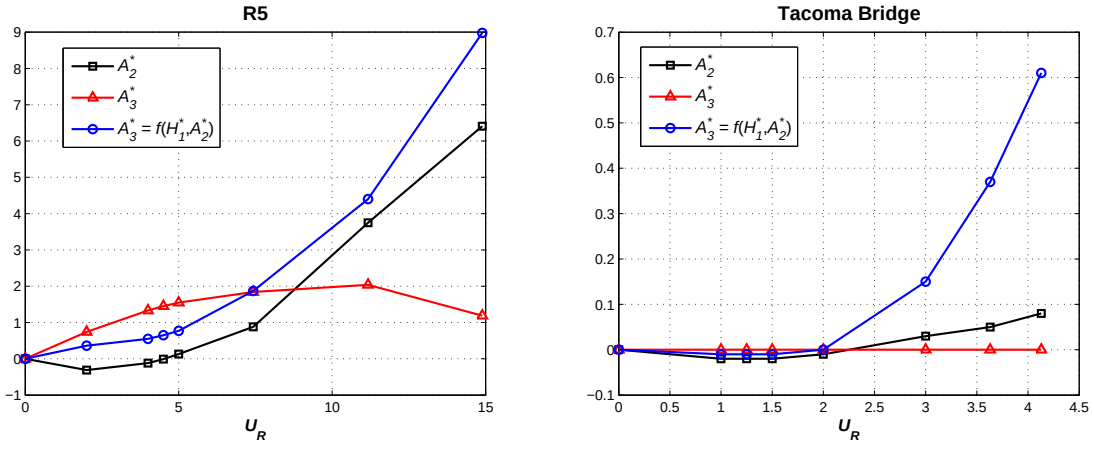

Figure 6.11: Degree of approximation of Eq. (6.35) in the case of the rectangular cylinder R5 and the First Tacoma Narrows Bridge. For the latter A_3^* is declared as "negligible" (Scanlan and Tomko, 1971)

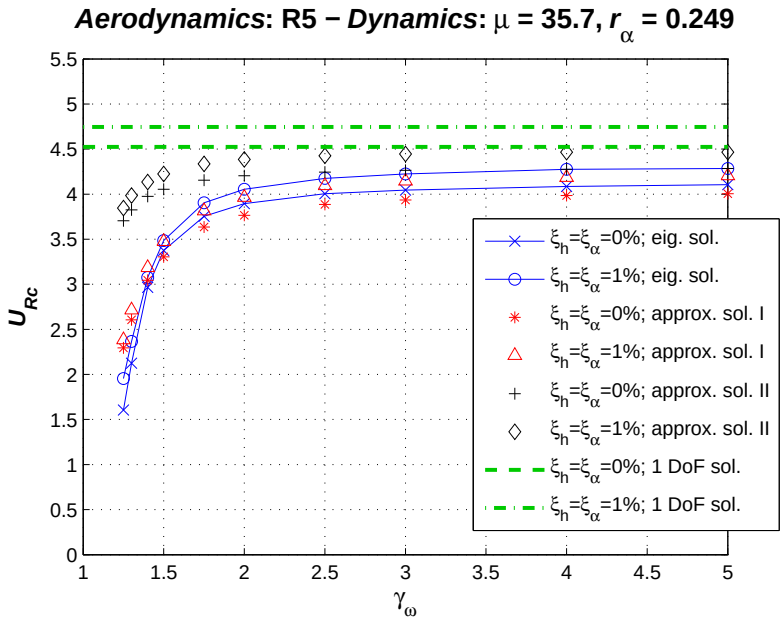

(a)

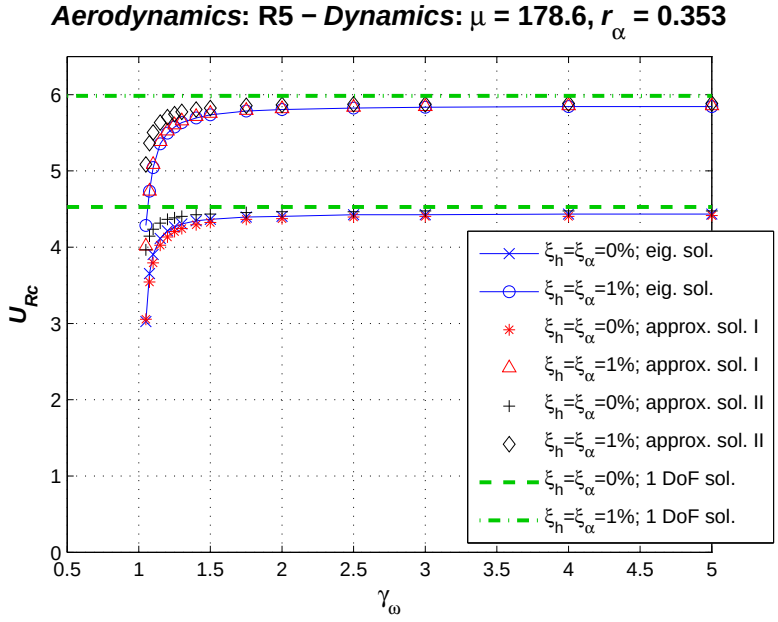

(b)

Figure 6.12: Comparison between the solutions of the 2-DoF eigenvalue flutter problem and those of the approximate formulas. "1-DoF sol." refers to Eqs. (6.38)-(6.39)

6.8 Nakamura's formula

Nakamura (1978) proposed a series of approximate equations for bridge deck flutter which can be easily transformed into the simplified formula proposed herein for the critical reduced wind speed neglecting structural damping [Eq. (6.31)]. For critical frequency a simplified formula analogous to Eq. (6.29) is given.

Nakamura's results are based on the following assumptions about the unsteady aeroelastic behavior of bridge decks:

1. $|H_2^*| \ll |H_3^*|$;

2. $H_1^* = KH_3^*$, $A_1^* = KA_3^*$, $H_4^* = -KH_2^*$, $A_4^* = -KA_2^*$;

3. the stability of the pitching branch is considered, whereas the heaving branch is assumed to be stable. The equivalent center of rotation should not be far from the midchord;

4. the phase angle between heaving and pitching motions is assumed to be small.

These conditions seem quite limiting and perhaps too theoretical, but the author himself claims that they are not seriously restrictive, being the formulas expected to be applicable to a variety of structures ranging from a flat plate to much bluffer bridge deck sections (Nakamura, 1978). Nakamura's experimental work, the investigation reported herein in Chapter 3, as well as the data analyzed in this chapter, seem to confirm the validity of the aforementioned assumptions. In particular, Nakamura shows that the small phase angle between heaving and pitching motions as well as the absolute peculiarity of bridge deck flutter with respect to aircraft wing flutter may be attributed to the absence of inertial coupling.

After comparison with the research outlined in Nakamura (1978), some interesting points of the present work can be summarized:

- the same result as Nakamura's is reached in a completely independent way and without setting any theoretical assumption, by means of a much more "empirical" approach, manipulating and simplifying the flutter equations on the basis of a large number of data.

- Here the formula proposed for the frequency of oscillation at flutter depends on H_1^* and A_2^* [Eq. (6.20)]. Conversely, in Nakamura (1978) Eq. (6.29) is obtained for the same purpose, containing only the flutter derivative A_3^*.

- In the proposed formulas damping is not neglected [Eqs. (6.19) and (6.30)] and its influence on flutter onset is investigated, showing sometimes a significant effect [see Figs. 6.3(d) and 6.12(b)].

- The possibility to take into account two flutter derivatives (H_1^* and A_2^*) instead of three (H_1^*, A_2^* and A_3^*) is also considered and discussed.

6.9 Conclusions

In this chapter an approximate method to calculate the flutter critical wind speed and frequency is presented. The formulas are derived from the manipulation of the flutter equations and seem to give results close to the rigorous solution of the eigenvalue problem of stability. The significant feature of this method is the fact that only three flutter derivatives (H_1^*, A_2^* and A_3^*) or even two (H_1^* and A_2^*) are necessary to perform the calculation. In particular, these functions seem to be the most reliable and the easiest to be identified through wind-tunnel tests. Interestingly, although the formulas are particularly thought for binary coupled flutter, they seem to apply well also in case of cross sections prone to single-degree-of-freedom torsional flutter.

This work, underlying the key role played by the flutter derivatives H_1^* and A_2^*, confirm the results found by Matsumoto for a wide range of rectangular cylinders. Nevertheless, it also suggests the necessity to consider in many instances a third aeroelastic function (A_3^*) in order to obtain accurate estimations of flutter boundaries. Moreover, it is worth noting that the proposed formulas are not directly obtainable either by setting to zero five out of eight flutter derivatives or only applying the inter-dependence relationships suggested by other authors.

The approximate approach proposed herein represents the basis to set up a simplified method of flutter assessment suitable to be implemented in codes and recommendations. In order to do that the generalization of the retained flutter derivatives for classes of deck geometry is still necessary and this step will be discussed in the next chapter. Nevertheless, it is worth noting that by means of these formulas the calculation of the coupled flutter critical wind speed is possible also without identifying cross-flutter derivatives (H_2^*, H_3^*, A_1^*, A_4^*), for instance when a simpler 1-DoF test set-up is adopted.

Another interesting aspect of this work is the theoretical insight it gives in the flutter equations and in the instability mechanism. It mainly highlights the dominant role of the flutter derivatives H_1^* and A_2^* and it supports the idea that Scanlan's model for self-excited forces, with eight empirical aeroelastic functions is somehow redundant [e.g. Bucher and Lyn (1988a,b); Matsumoto (1996, 2005); Borri *et al.* (2005)].

Finally, the role played in the flutter instability mechanism by several structural parameters is investigated. In particular, it is shown that, despite what is usually believed, the contribution of structural damping to flutter onset is not always negligible, depending both on the dynamic and aerodynamic properties of the bridge. Consequently, in some particular cases the flutter critical wind speed can be significantly over- or under-predicted if structural damping is not correctly accounted for.

Chapter 7

A first step towards generalization of flutter derivatives

7.1 Introduction

In Chapter 5 it is pointed out that a bimodal approach is usually adequate to predict the flutter critical wind speed and frequency. Then, in Chapter 6 an approximate method to assess them is proposed and discussed. This method is satisfactorily validated with a wide range of test cases, from the thin flat plate and quasi-streamlined decks to bluff cross sections prone to torsional flutter. The main feature of the proposed formulas, apart from their simple form, is the dependency on at most three flutter derivatives only. These functions, H_1^*, A_2^* and A_3^*, are direct flutter derivatives and can be measured also with relatively easy set-ups through one-degree-of-freedom free-vibration tests. Consequently, a larger number of data are available in the literature and in the experimental laboratories. In addition, they are generally recognized as more reliable than cross-derivatives: for instance it can be observed how the agreement between the flutter derivatives measured for two rectangular cylinders via free-vibration (Righi, 2003) and forced-vibration tests (Matsumoto, 1996) is much better for these three functions than for the other ones.

On these bases an attempt of generalization of flutter derivatives for conventional classes of deck geometries, limiting to the aforementioned three functions, becomes possible. That means to define "universal" curves or envelops which can be adopted as flutter derivatives in flutter calculations, implying small errors in the resulting critical wind speed. This step, corresponding to the upper box of the flow chart presented in Fig. 1.4, would allow to predict the flutter wind speed without performing wind-tunnel tests. As it has been repeated several times in this dissertation, this simplified approach cannot substitute wind-tunnel tests, especially for long-span bridges or non-conventional structures, but it could represent an useful normative tool to understand whether or not flutter is a problem for a bridge structure: if the estimated flutter wind speed is too low, the structural design should be changed from the beginning; conversely, if it is sufficiently high, wind-tunnel tests can be avoided or postponed to the final design validation; in the less obvious cases further experimental investigations are needed. This method, if available in the design codes, even as "recommendations", could be

very useful for bridge engineers, especially in case of medium-span conventional bridges and at pre-design stages. Nevertheless, in order to attempt this generalization of flutter derivatives, a large number of reliable aeroelastic data, measured by different staffs in different laboratories on several similar geometries are necessary. Probably benchmark and parametric studies on particular geometries should be also available. In addition, since the dependence on the mean angle of attack cannot be forgotten [e.g. ONERA (1989); Flamand (2000); Flamand (2001); Diana *et al.* (2004); Fig. 3.41 in the present dissertation], the flutter derivative generalization should take care of this aspect, clearly warning about the wind incidence range of validity of the proposed curves and excluding the cross-sectional geometries very sensitive to small variations of the angle of attack, as well as to the presence of small non-structural details. Another point that should be clarified is the actual dependence of aeroelastic coefficients on Reynolds number, as briefly discussed in sections 3.5.2 and 3.6, in Diana *et al.* (1999) and in Schewe (2006): needless to say that the geometries which are very sensitive to Reynolds number cannot be considered for any sort of generalization.

In the present research work the collection of data has been one of the most difficult tasks. It is also not obvious to find data for which all test conditions, as well as the identification procedure, are known. A wide range of data are kindly made available by the Centre Scientifique et Technique du Bâtiment (CSTB) of Nantes, France, during writer's visiting period in February 2005. In most cases only the flutter derivatives H_1^*, A_2^* and A_3^* are measured via free-vibration technique on 1-DoF set-ups. The aeroelastic coefficients are identified following the simple procedure outlined in Scanlan and Tomko (1971). In most cases only one measurement is performed for each reduced wind speed, nevertheless many close points are available, so that the pattern of the functions is fairly clear and well defined.

In the following, three relevant classes of conventional deck sections for cable-stayed and suspension bridges are taken into account: trapezoidal single-box girder with lateral cantilevers, trapezoidal single-box girder (without lateral cantilevers) and bi-girder. For each group the geometries of the concerned bridge decks are compared and then the corresponding flutter derivative patterns are discussed. Truss-stiffened girder decks are not taken into account here due to the lack of data and also for the difficulty in defining similar geometries from the aeroelastic point of view. Nevertheless, it seems natural to distinguish between "old generation" cross sections, such as Golden Gate Bridge (Simiu and Scanlan, 1996) and Tancarville Bridge (Flamand, 1996), which are prone to single-degree-of-freedom torsional flutter, and "new generation" cross sections, among which Akashi Kaikyo Bridge (Miyata and Yamaguchi, 1993; Katsuchi *et al.*, 1999) is the most important example, which are prone to coupled flutter, showing a relatively good aeroelastic behavior.

Here only a preliminary step towards an actual attempt of generalization is performed but, as far as the writer is aware, it is the first time after the pioneering work of Scanlan and Tomko (1971) that such a relatively large number of aeroelastic data are collected and compared on the basis of geometric similarities.

7.2 Flutter derivatives for classes of deck geometry

7.2.1 Trapezoidal single-box girder decks with lateral cantilevers

The first class of geometry we are taking into account includes the bridge section experimentally studied by the writer. It is worth reminding that this type of cross section has been chosen for wind-tunnel tests mainly because it is fairly common for medium-span cable-stayed and suspension bridge decks, although not many aeroelastic data are available in the literature. This geometry, extensively studied in Chapters 3-4 and displayed in Fig. 7.2(a), is called in the following "CRIACIV section". As it has already been said, it is very similar to the Sunshine Skyway Bridge cross section in the bare-deck configuration (Fig. 3.17) and flutter derivatives are measured via free-vibration techniques and 2-DoF set-up. The other sets of flutter derivatives are measured by the CSTB-Nantes via free-vibration technique and 1-DoF set-up. These refer to Chevanon [Barré *et al.* (1996b); Fig. 7.2(b)], Aswan [Barré *et al.* (1996a); Fig. 7.2(c)] and Trois Bassins [Flamand (2003a); Fig. 7.2(d)] bridges. For the latter only the flutter derivative H_1^* is measured for several positive angles of attack. Conversely, for the other two bridge sections, sets of three flutter derivatives are available both for construction and service configurations.

It is worth noting that in the case of Chevanon and Trois Bassins decks the lateral cantilevers are supported by tubular secondary beams ("bracons" in French), but, not being continuous, these are supposed not to influence much the aerodynamics of the section. The Trois Bassins bridge deck presents definitely the most bluff geometry, even with opposite slope of the box lateral walls. Aswan Bridge seems to be characterized by the most "streamlined" cross section, which is also the one closest to the CRIACIV section, although the chord-to-thickness ratio B/D is significantly higher (7.36 instead of 6.43).

In Fig. 7.2 the flutter derivatives of these bridge sections are plotted together for comparison. As usual, all aeroelastic functions are expressed in the Scanlan's convention, that is according to Eqs. (2.38)-(2.39) and Fig. 2.13.

It is clearly shown that all sets of flutter derivatives are similar and very good agreement is found between the experiments performed in the CSTB-Nantes and CRIACIV wind tunnels. In particular, concerning H_1^*, all sets of functions belong to a relatively narrow spindle of curves, including the much bluffer Trois Bassins Bridge section. The wideness of the envelop of curves increases with the wind speed, according to the physiological dispersion affecting the data, extensively discussed in Chapters 3-4. It is also worth noting that the flutter derivative given by Thodorsen's theory for a thin flat plate almost represents the mean line of the envelop.

The comment of the graph for A_2^* is even more interesting. The first remark concerns Aswan bridge deck in the construction configuration, whose curve is quite different from all the other ones, showing values always close to zero, that means a limited aerodynamic damping in pitching. This result is quite surprising because Aswan deck seems to be characterized by the the most "streamlined" section among those we considered. The reasons for this discrepancy have not been understood yet. All the remaining curves (including the one for Aswan Bridge in the service configuration) present similar patterns. In particular, for $U_R < 7.5$ these all closely follow Theodorsen's theory. Then, for higher reduced wind speeds the aerodynamic damping in pitching suddenly starts to decrease. It is worth reminding that Fig. 3.41 showed that the

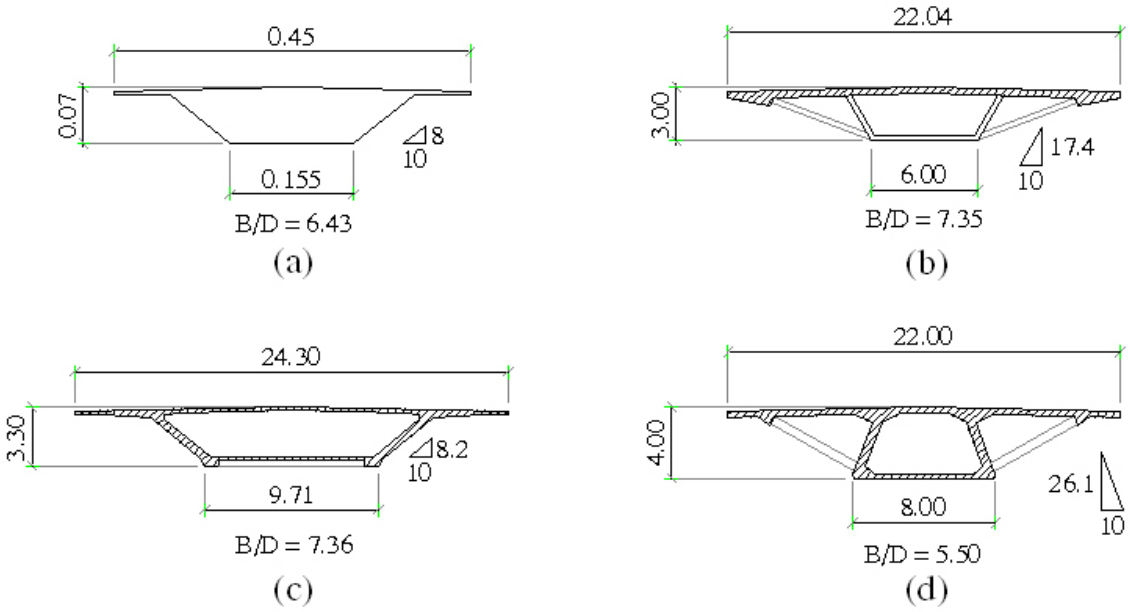

Figure 7.1: Cross-section geometry of the considered trapezoidal single-box girder decks with lateral cantilevers: (a) CRIACIV section; (b) Chevanon; (c) Aswan; (d) Trois Bassins

value of U_R at which the minimum of A_2^* occurs significantly depends on the actual angle of attack, that is in free-vibration set-ups on the pitching stiffness of the system. Nevertheless, despite the fact that different stiffness is adopted for these bridge deck section models, the last portions of the A_2^*-curves are reasonably similar.

Finally, the A_3^*-curves are all very close and CRIACIV section's one, which is obtained by averaging ten measures, is almost identical to the corresponding function given by Theodorsen's theory.

It is now interesting to understand which is the effect on the flutter critical wind speed of the differences in the the flutter derivative patterns. Two reference dynamics, denoted as "dyn1" and "dyn2", are taken into account, as shown in Tab. 7.1. "dyn1" refers to the modal properties of Tsurumi Fairway Bridge (Sarkar, 1992) with damping $\zeta_h = \zeta_\alpha = 0.005$. Conversely, "dyn2" presents the same modal parameters as Guamà Bridge (Rocha *et al.*, 2003) but a frequency ratio of 1.25 and zero damping are assumed in order to obtain flutter solutions without performing any extrapolation of the experimental aeroelastic functions. It is worth noting that the non-negligible stabilizing role of damping for this kind of dynamics, as already underlined in Chapter 6, is confirmed here. In Tab. 7.2 the results of the flutter calculation are shown for three bridge deck geometries: CRIACIV section, Aswan and Chevanon Bridge, the last two in the service configuration. It can be remarked that the differences in the results are non-negligible but definitely moderate, except for the combination of Chevanon aerodynamics and dyn2-dynamics. Nevertheless, it is only the critical frequency to be in this case very different with respect to the other test cases, while the graphical solution of Eq. (6.30) shows many wiggles, in agreement with the non-smooth pattern of the flutter derivatives. This is due

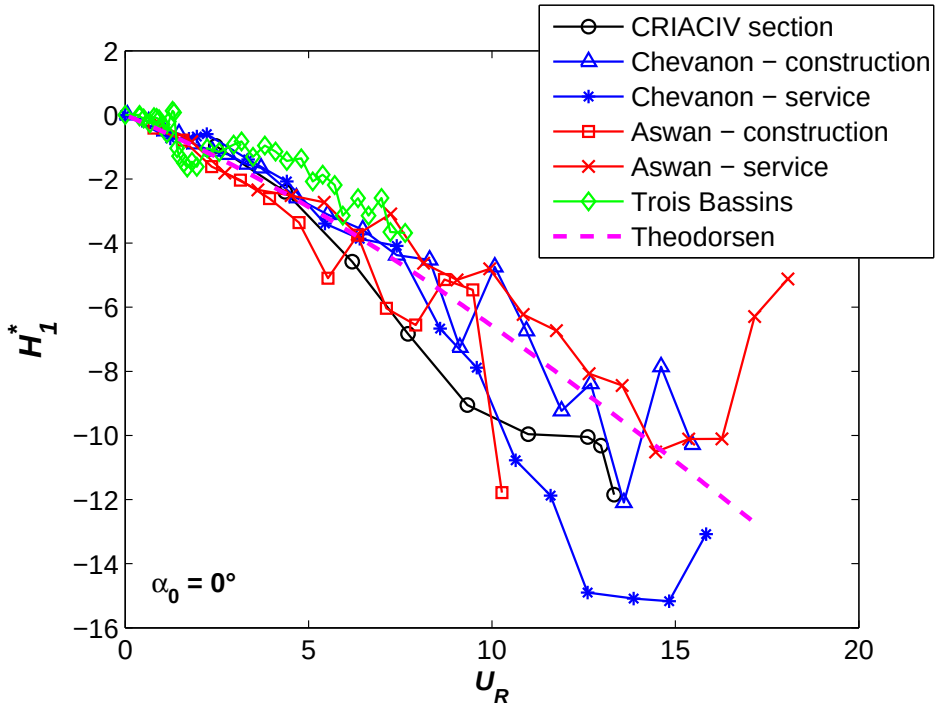
CRIACIV section
Chevanon − construction
Chevanon − service
Aswan − construction
Aswan − service
Trois Bassins
Theodorsen
H_1^*
U_R
α_0 = 0°

(a)

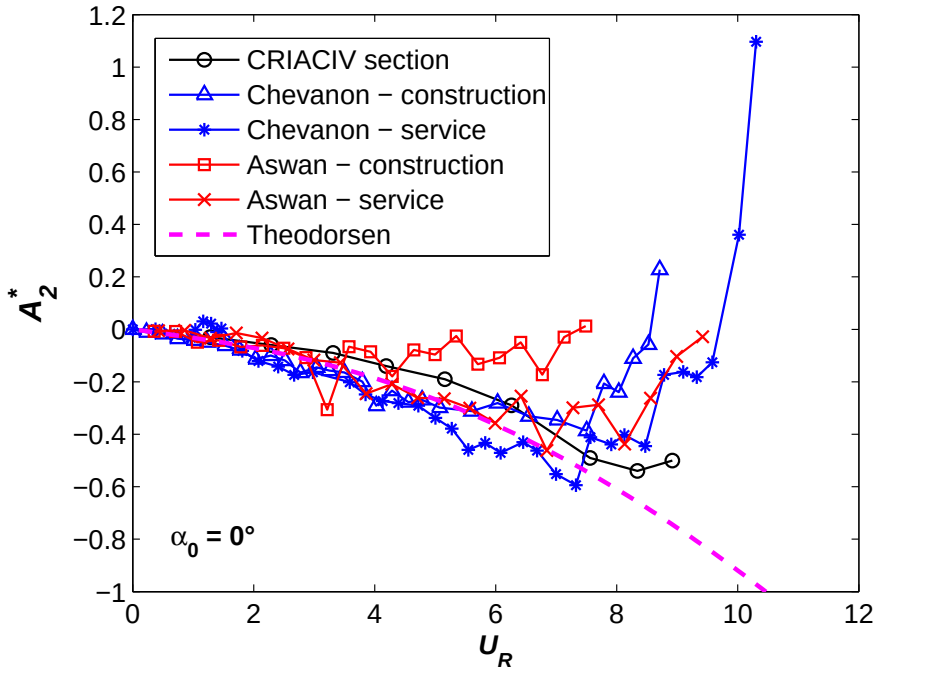
CRIACIV section
Chevanon − construction
Chevanon − service
Aswan − construction
Aswan − service
Theodorsen
A_2^*
U_R
α_0 = 0°

(b)

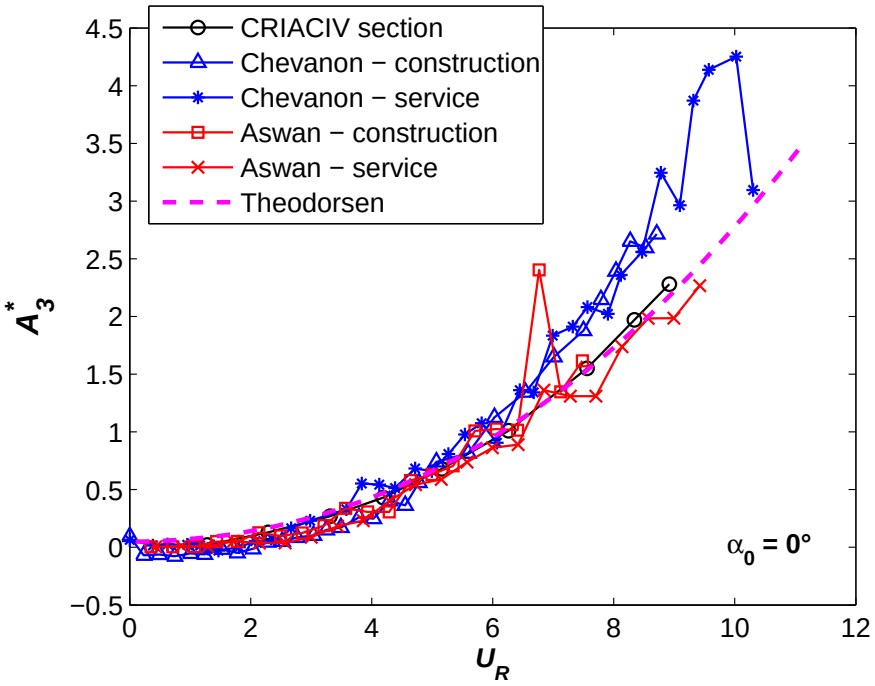

(c)

Figure 7.2: Flutter derivatives for some trapezoidal single-box girder decks with lateral cantilevers. The still-air angle of attack is always $\alpha_0 = 0°$

to the fact that only one measurement is performed for each reduced wind speed. It is believed that the outlying critical frequency is simply due to a wiggle, not reflecting any physical feature of the fluid-structure interaction. This fact is confirmed by the results shown in Tab. 7.3, where Chevanon flutter derivatives are fitted by polynomial curves of second or third order. The reduced critical wind speed does not change significantly while the coupling frequency takes now a value in agreement with the results for the other bridge sections. Conversely, it is worth noting in Tab. 7.3 that the results are significantly different for Aswan Bridge in the construction configuration, due to the previously discussed peculiar pattern of the flutter derivative A_2^*. In particular, in the dyn1-case a flutter solution is not found in the range of reduced wind speed for which flutter derivatives are measured. Furthermore, it can be observed that the Theodorsen's theory for an equivalent thin flat plate predicts a critical wind speed in good agreement with the measured flutter derivatives in the dyn1-case, although due to the product of significantly different critical reduced wind speed and frequency. Conversely, in the dyn2-case the flutter result overestimates very much the critical wind speed calculated with the experimental functions.

The few results proposed here are quite encouraging, showing relatively small differences in the calculated flutter wind speed but, at same time, the case of Aswan Bridge under construction warns about the attention that must be paid in any attempt of generalization. Finally,

this analysis shows the relevance of the formulas presented in Chapter 6, which allow to perform flutter calculations with data not measured for this purpose (except for the CRIACIV section, only three aeroelastic coefficients are available for the other bridge decks). In addition, the results are easier to be understood and discussed, given the limited number of parameters involved in the calculations.

Table 7.1: Sets of modal parameters considered in the flutter calculations

	ρ [kg/m^3]	B [m]	f_h [Hz]	f_α [Hz]	m [kg/m]	I [kgm^2/m]	γ_ω [-]	ζ_h [%]	ζ_α [%]
dyn1	1.25	38.0	0.204	0.486	32220	2880100	2.38	0.5	0.5
dyn2	1.25	14.2	0.331	$1.25f_h$	22513	566838	1.25	0.0	0.0

Table 7.2: Flutter critical reduced wind speed (U_{Rc}), frequency (f_c) and dimensional wind speed (U_c) calculated with the simplified formulas of Eqs. (6.19) and (6.30)

	CRIACIV-section			Aswan serv.			Chevanon serv.		
	U_{Rc} [-]	f_c [Hz]	U_c [m/s]	U_{Rc} [-]	f_c [Hz]	U_c [m/s]	U_{Rc} [-]	f_c [Hz]	U_c [m/s]
dyn1	8.12	0.382	117.9	8.38	0.429	136.6	7.98	0.400	121.2
dyn2	9.30	0.393	51.9	8.75	0.410	51.0	8.58	0.768	93.5

Table 7.3: Further flutter calculations

	Aswan constr.			Chevanon serv. (polynomial)			Theodorsen's theory		
	U_{Rc} [-]	f_c [Hz]	U_c [m/s]	U_{Rc} [-]	f_c [Hz]	U_c [m/s]	U_{Rc} [-]	f_c [Hz]	U_c [m/s]
dyn1	> 8			7.64	0.453	131.6	10.75	0.315	128.7
dyn2	6.28	0.342	30.5	8.42	0.475	56.7	14.18	0.368	74.2

7.2.2 Trapezoidal single-box girder decks

The second bridge deck typology we are taking into account is the trapezoidal single-box girder (without lateral cantilevers), which is common for large-span suspension bridges, as well as truss-stiffened and multi-box girder solutions. These decks are quasi-streamlined and their aeroelastic behavior is usually fairly performing. In particular, data are available for the Viaduct of Millau in the 1998-metal and concrete versions, in the construction and service configurations (Flamand and Grillaud, 1998), Grande Ravine Bridge, with and without porous barriers (Flamand, 2003a), Normandy Bridge (ONERA, 1989), Tsurumi Fairway Bridge (Singh *et al.*, 1995) and Great Belt East Bridge (Reinhold *et al.*, 1992; Larsen, 1995) and for another

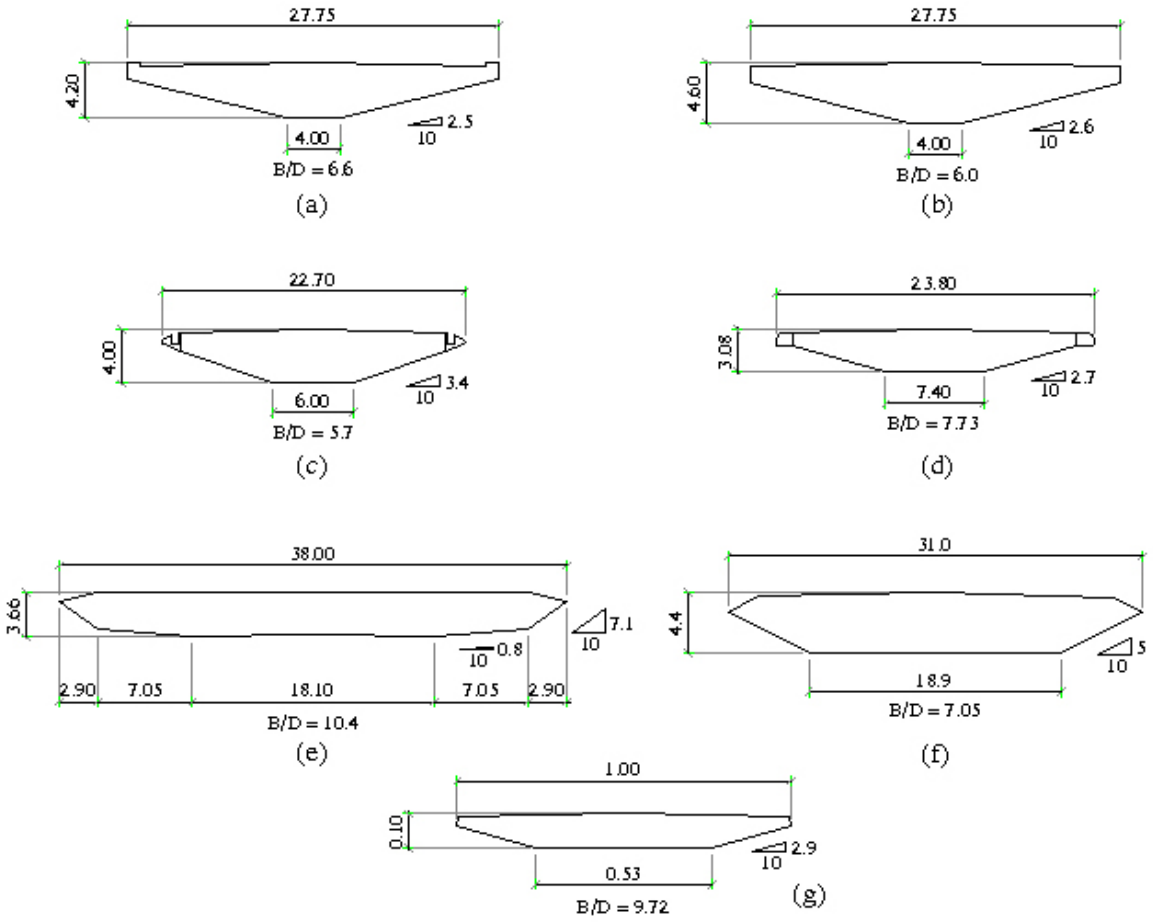

Figure 7.3: Cross-section geometry of the considered trapezoidal single-box girder decks: (a) Millau (metal version 1998); (b) Millau (concrete version 1998); (c) Grande Ravine; (d) Normandy; (e) Tsurumi; (f) Great Belt East Bridge; (g) Deck A

trapezoidal section here called "Deck A". Fig. 7.3 shows the main geometric features of these bridge sections. The flutter derivatives of Normandy Bridge and Deck A are measured via forced-vibration technique. The aeroelastic behavior of Tsurumi Fairway Bridge and Great Belt East Bridge is studied respectively by means of a 3-DoF and 2-DoF free-vibration set-up. In all other cases the aeroelastic coefficients are measured at the CSTB-Nantes via free-vibration technique and 1-DoF set-up.

It can be immediately remarked that there is no big difference between the metal and concrete version of the Viaduct of Millau: substantially in the concrete design the section is only slightly thicker. The deck of Tsurumi Fairway Bridge, strictly speaking, should not be called "trapezoidal"; in any case it seems to present the most performing shape from the aerodynamic point of view, also for the very high chord-to-thickness ratio ($B/D = 10.4$). Great Belt and Deck A are also characterized by fairly "streamlined" cross sections.

Fig. 7.4 compares the flutter derivatives H_1^*, A_2^* and A_3^* for the aforementioned bridge

sections. It can be immediately remarked that the four different configurations of the cross section of the Viaduct of Millau do not imply significant discrepancies concerning the aeroelastic behavior, except for small differences in the A_2^*-curves between the construction and service configurations. In the case of Grande Ravine section, the presence of the porous barriers has a non-negligible effect on the flutter derivatives H_1^* and A_2^* but without dramatic changes in the general trend.

Concerning H_1^*, all the experimental curves follow patterns close to each other and to the theoretical thin flat plate one, although affected by a significant dispersion. A_3^*-curves are even more similar and well defined. Once again the most important differences concern the flutter derivative A_2^*. In this case, two main trends can be highlighted: on the one hand, the Viaduct of Millau (both metal and concrete versions) in the construction configuration and Grande Ravine Bridge without barriers closely follow the corresponding Theodorsen's pattern; on the other hand, the Viaduct of Millau in the service configuration and Grande Ravine Bridge with porous barriers present smaller aerodynamic damping in pitching, close to the behavior of Great Belt and Tsurumi Bridge. Normandy Bridge follow the first mentioned trend but only as far as $U_R \simeq 6$. Deck A presents the same aerodynamic damping as the thin flat plate as far as $U_R \simeq 3$. Afterwards, surprisingly, A_2^* remains practically constant for a wide range of reduced wind speed. The discriminant geometric features between the two patterns have not been understood yet. Finally, it can be remarked that the Grande Ravine deck is affected by vortex-shedding lock-in, both in heaving and pitching, around $U_R \simeq 1$.

On the whole the considered flutter derivative curves show significant common features, which encourage an attempt of generalization once a larger number of data is available.

7.2.3 Bi-girder decks

The geometries of four bi-girder decks are reported in Fig. 7.5. This deck typology is again quite common for medium-span cable-stayed bridges. It is possible to note that Siekierkowski (Flamand, 2001) and Rion Antirion Bridge (Grillaud and Flamand, 1998; Flamand and Grillaud, 1999) are characterized by very similar geometries, although the first presents a larger chord-to-thickness ratio B/D. Both decks are composed by a reinforced concrete slab connected to two I-steel beams, which at regular intervals are stiffened by transversal plates. The geometry of Sucharski Bridge cross section (Flamand, 2000) is similar too, although the slab is supported by two small steel boxes, placed very close to the lateral edges of the deck. Conversely, the geometry of the footbridge of the Olympic Arch in the olympic village in Turin (Flamand, 2003b) is completely different from the others, showing a very narrow steel deck with lateral beams on the upper side of the slab, covered by triangular fairings, which aerodynamically compensate the small B/D ratio.

For the Rion Antirion Bridge deck the data of 1998- and 1999-versions are available. These two cross sections mainly differ for the I-steel beams. Also for Turin footbridge a slightly modified geometry is tested (Flamand, 2003b). In the case of Sucharski deck, both construction and service configurations are studied modelling the Vistula River under the bridge, but for the service configuration the results of a test without the river are available too. It is worth noting that all data are measured by the CSTB-Nantes via free-vibration technique and 1-DoF set-up. The flutter derivatives reported in Fig. 7.6 refer to a still-air initial angle of attack

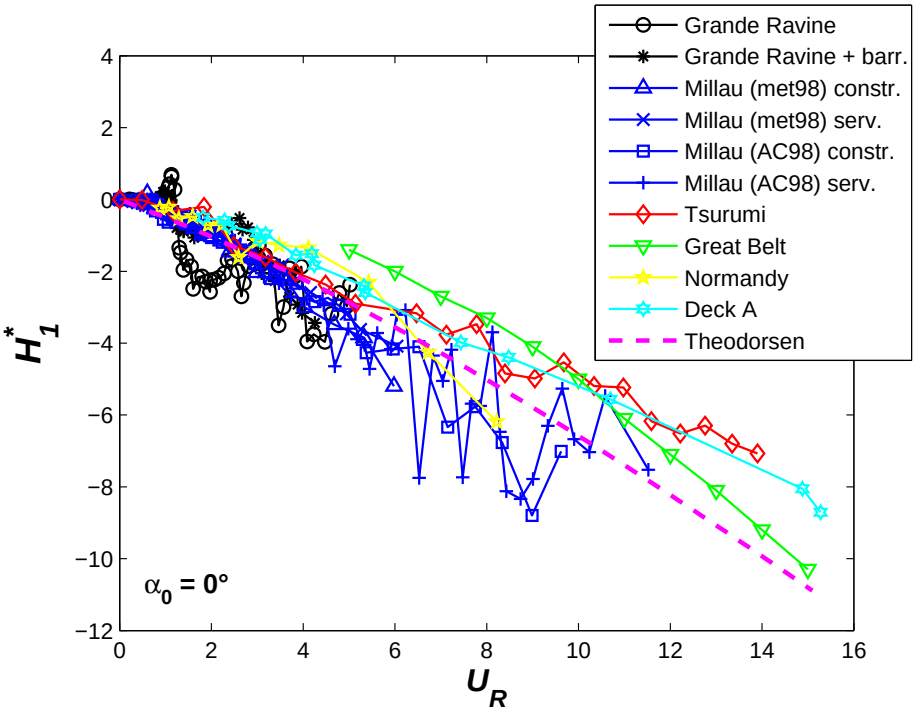
Grande Ravine
Grande Ravine + barr.
Millau (met98) constr.
Millau (met98) serv.
Millau (AC98) constr.
Millau (AC98) serv.
Tsurumi
Great Belt
Normandy
Deck A
Theodorsen
H_1^*
U_R
α_0 = 0°

(a)

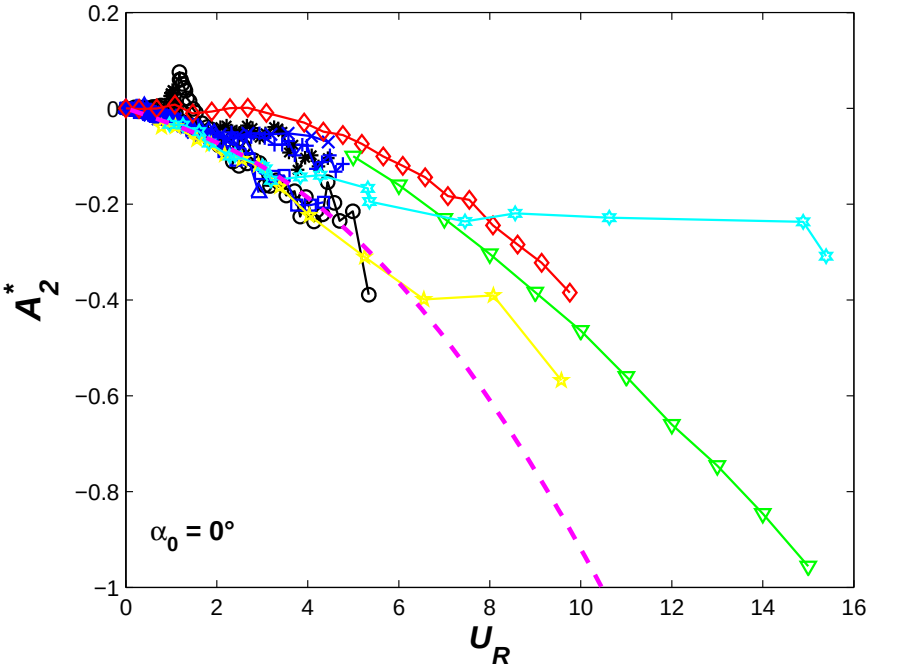
A_2^*
U_R
α_0 = 0°

(b)

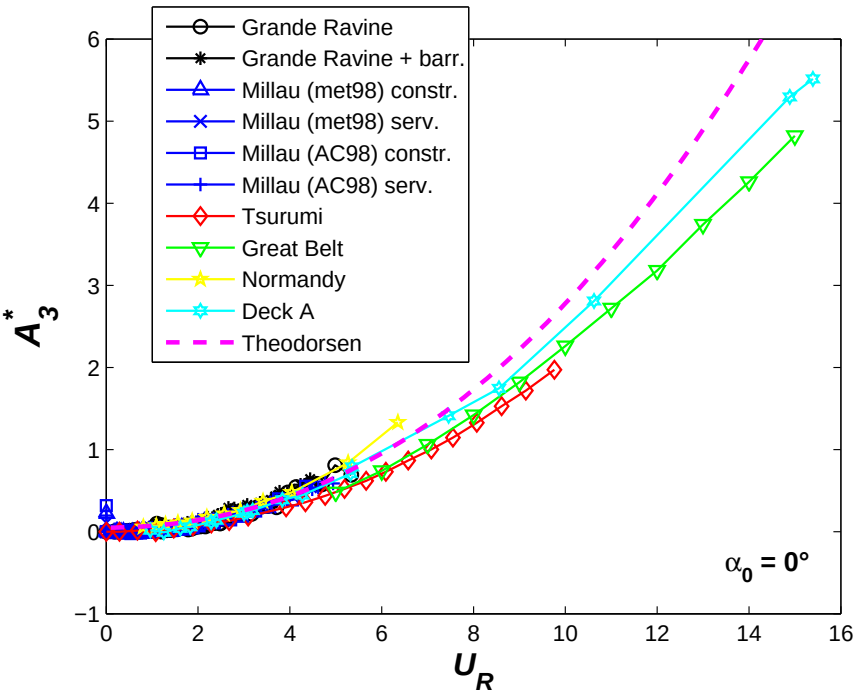

(c)

Figure 7.4: Flutter derivatives for some trapezoidal single-box girder decks. The angle of attack (or still-air angle of attack in case of free-vibration set-ups) is always $\alpha_0 = 0°$

$\alpha_0 = 0°$, except in the case of Siekierkowski cross section, for which the functions corresponding to three angles of attack are plotted in order to show the influence of this parameter on this type of deck section.

Concerning H_1^*, the sets of data form an envelop, whose width increases with the reduced wind speed, coherently with the dispersion of the measures for free-vibrating section models [e.g. Righi (2003); Bartoli and Mannini (2005); section 3.5.2 of the present dissertation]. Apart from the irregular behavior in the range $0 < U_R < 2$, due to vortex-shedding lock-in in the heaving mode, it seems that all sets of curves for Sucharski, Rion Antirion and Turin sections roughly follow the same pattern. Conversely, for Siekierkowski deck section the aerodynamic damping in the heaving mode is slightly higher. The pattern of H_1^* derived from the Theodorsen's theory well agrees with these experimental curves and is particularly close to the one measured for Turin footbridge.

For A_2^* the analysis is more complicate because the curves are very irregular, going up and down, due to the strong sensitivity to vortex-shedding lock-in. In addition, for some cross sections the measures are available only for low reduced wind speeds ($U_R < 2$ for Siekierkowski, $U_R < 5$ for Sucharski and $U_R < 6$ for Rion Antirion). Nevertheless, Rion Antirion and Turin deck sections seem to show the same tendency. Conversely, it is not clear whether A_2^* for Sucharski becomes positive or joins the trend of the other two cross sections for $U_R > 5$.

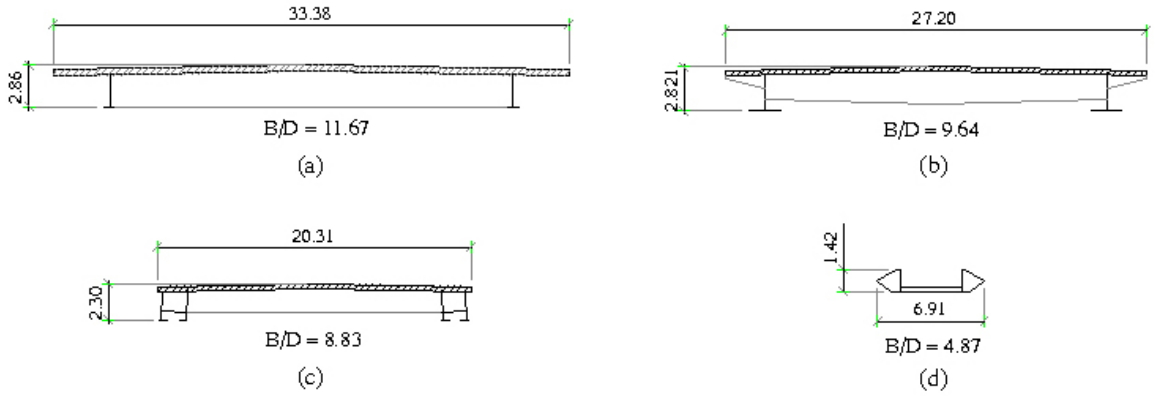

Figure 7.5: Cross-section geometry of the considered bi-girder decks: (a) Siekierkowski; (b) Sucharski; (c) Rion Antirion; (d) Turin footbridge

For A_3^* the agreement between the different curves, including the theoretical one for a thin flat plate, is definitely surprising with the astonishing exception of Siekierkowski deck section which presents a completely different trend. This peculiar behavior is not confirmed for the same cross section with a positive or negative angle of attack $\alpha = \pm 3°$, whose pattern well agrees with all the other curves (it is also worth noting that for both $\alpha = +3°$ and $\alpha = 0°$, A_3^* shows a peak due to vortex-shedding lock-in in the neighborhood of $U_R \simeq 1$). This result could be due to a local instability, somehow similar to the one discussed in Figs. 3.14, 3.15 and 3.32 for the CRIACIV section, but more investigations are necessary to explain this discrepancy and in particular the fact that the angle of attack dramatically affects A_3^* but only slightly H_1^* and A_2^*.

We can conclude that this cross-section typology is very difficult to be treated, also due to the pronounced sensitivity to vortex-shedding lock-in both in heaving and pitching modes, which is known to be strongly affected by non-structural details [e.g. Flamand and Grillaud (1993); Flamand and Grillaud (1996); Grillaud and Flamand (1998)].

7.3 Conclusions

In this last chapter a relatively large number of flutter derivative data (most of them made available by the CSTB-Nantes) are compared and analyzed as a first step towards a possible generalization of flutter derivatives. Three classes of deck cross-sectional geometries, typical for cable-stayed and suspension bridges, are taken into account: trapezoidal single-box girder with lateral cantilevers, trapezoidal single-box girder and bi-girder.

At this stage, it is difficult to say if a generalization is really possible, since more data should be available, better if including reliable statistical descriptions of the measures. Nevertheless, some common features in the graphs shown throughout the chapter and the flutter calculations we performed encourage to continue with this work. The most promising case seems to be the trapezoidal single-box girder deck with lateral cantilevers, whereas especially for the bi-girder

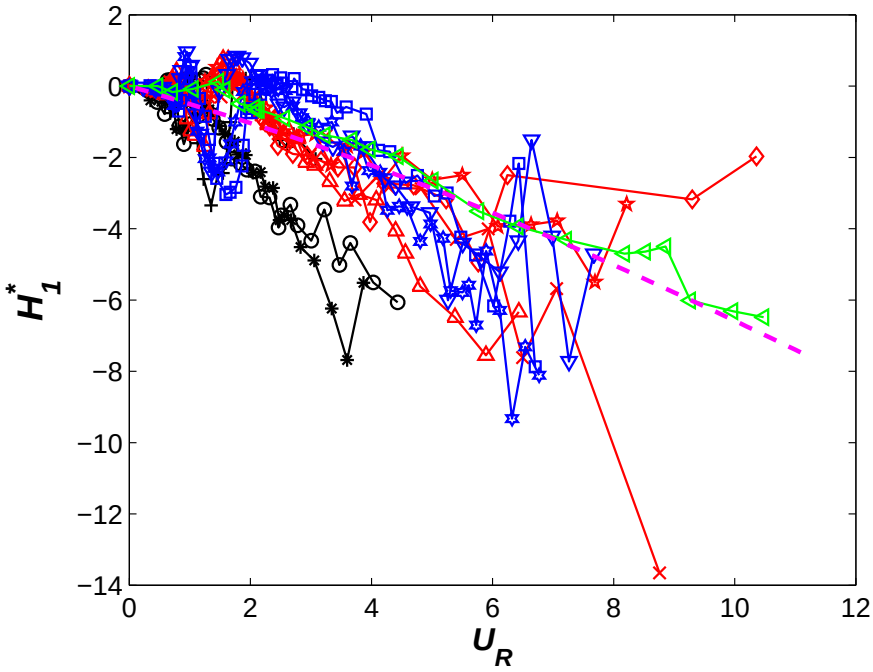
2
0
−2
−4
−6
−8
−10
−12
−14
0
2
4
6
8
10
12
H_1^*
U_R

(a)

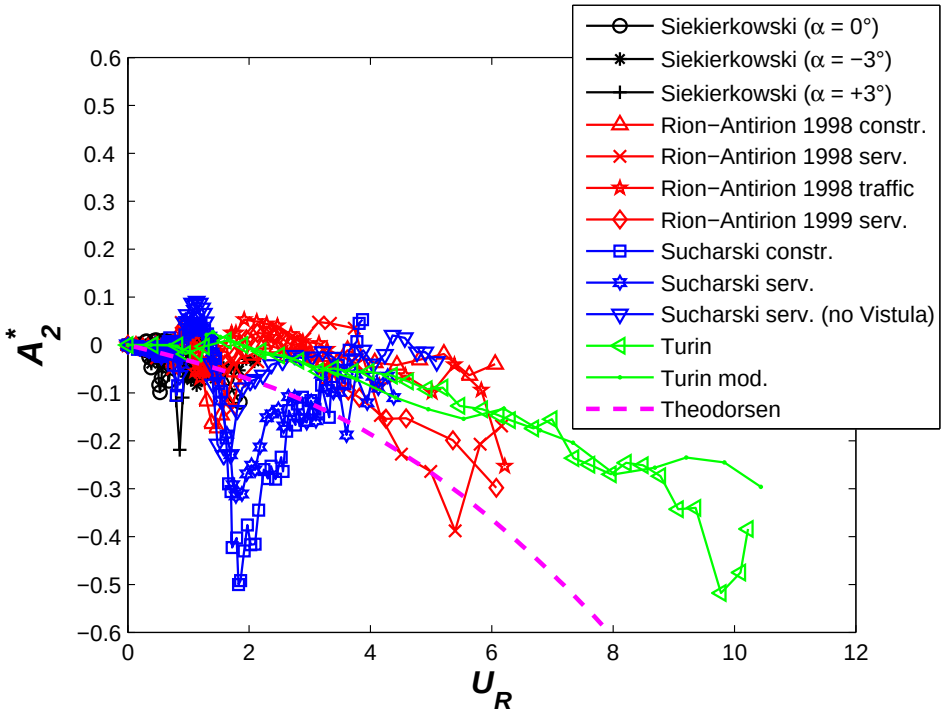
0.6
0.5
0.4
0.3
0.2
0.1
0
−0.1
−0.2
−0.3
−0.4
−0.5
−0.6
0
2
4
6
8
10
12
A_2^*
U_R
Siekierkowski (α = 0°)
Siekierkowski (α = −3°)
Siekierkowski (α = +3°)
Rion−Antirion 1998 constr.
Rion−Antirion 1998 serv.
Rion−Antirion 1998 traffic
Rion−Antirion 1999 serv.
Sucharski constr.
Sucharski serv.
Sucharski serv. (no Vistula)
Turin
Turin mod.
Theodorsen

(b)

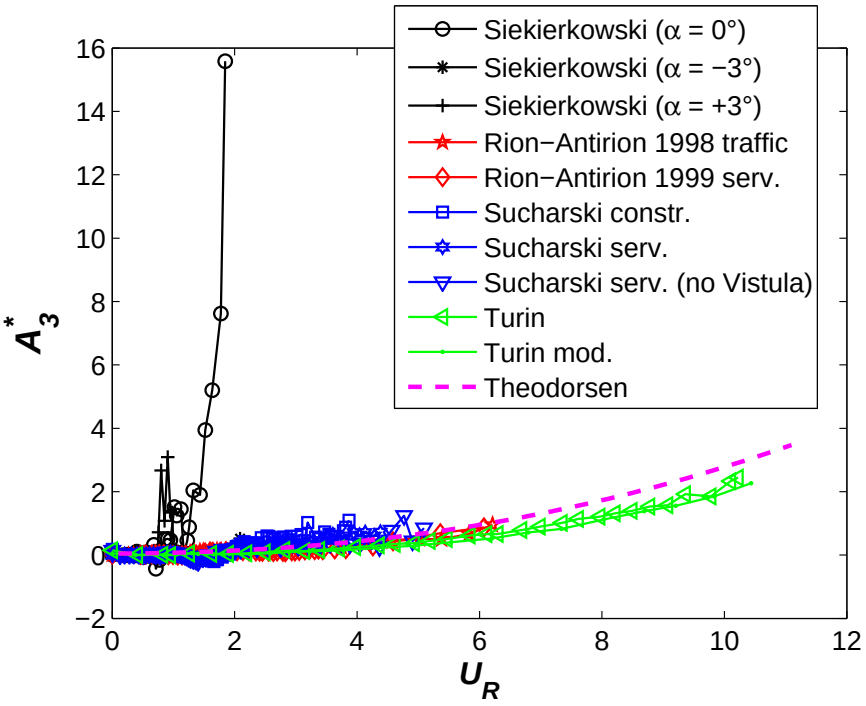

(c)

Figure 7.6: Flutter derivatives for some bi-girder decks. Except for Siekierkowski Bridge, in all other cases the angle of attack is $\alpha = 0°$

typology less clear results are achieved.

Generally speaking, the most relevant differences between the sets of flutter derivatives concern the A_2^*-functions, while for the considered cross sections H_1^*- and especially A_3^*-curves do not present large discrepancies between them and even with respect to the Theodorsen's theory.

As a future development, it might be necessary to refine the definition of the classes of deck cross-sectional geometry, identifying specific sub-classes with homogeneous aeroelastic behavior on the basis of a few geometrical parameters (chord-to-thickness ratio B/D, slope of the lateral walls of the box, etc.). It will be also important to better study the effect of non-structural details in the service configuration as well as of Reynolds number. Obviously all that will be possible only if a much wider range of data is available. Moreover, it could be interesting to perform additional flutter calculations with the approximate formulas presented in the previous chapter. This could help to better understand what is the actual effect of the more-or-less small discrepancies between the analyzed flutter derivative curves on the critical wind speed, which is the parameter of engineering interest for bridge flutter. Despite the fact that a big effort has still to be done, we believe that the work described herein represents an important base for further research in this direction.

General conclusions and outlook

In this doctoral work the vulnerability ring in the chain of risk analysis of flexible bridges with respect to flutter is dealt with. The first contribution is the application of Performance-Based Design philosophy to collapse limit state due to flutter, in agreement with the Pacific Earthquake Engineering Research Center (PEER) formulation. For the first time, flutter derivatives are considered as random variables and the flutter problem is approached in a probabilistic way via Monte-Carlo simulations. A single-box deck girder is experimentally studied in the CRIACIV wind tunnel in order to get data to be used for this particular analysis. Results are obtained with this approach both for this section model and for two rectangular cylinders. In the future it could be interesting to apply this method to other case studies in order to better understand its potentialities. In addition, the outlined vulnerability analysis could be included in the larger frame of a complete risk analysis for a real bridge structure.

The second contribution of this work is a sort of "pre-normative" study concerning flutter assessment, which could be useful to enhance the codes, as a measure of risk mitigation. As final goal a simplified method to estimate flutter critical wind speed without performing wind-tunnel tests should be set up. Such a tool could be of great interest for bridge engineers, especially concerning medium-span flexible bridges and/or pre-design stages. First, the passage from multimodal to bimodal approach to flutter is analyzed and discussed and then a simplified formula retaining only three (or even two) aeroelastic functions is derived. This strong simplification is validated on the basis of a wide range of dynamic and aerodynamic data, showing its extensive applicability. Finally, a relatively large number of aeroelastic data, collected during the three years of the doctoral course, are compared and analyzed according to the definition of a few classes of deck cross-sectional geometry. The previously mentioned simplified formulas allow to take into account three flutter derivatives only, thus making possible an attempt of generalization. Although this is only a first step towards this ambitious goal, it shows all the difficulties which have to be overcome but it also highlights some interesting and encouraging results. As future development, the database should be definitely enlarged, considering data measured in different laboratories and reorganizing them according to more refined and detailed classes of deck cross-sectional geometry. In addition, both the passage from multimodal to bimodal approach and the simplified formulas for flutter should be further investigated, identifying the cases for which the multimodal analysis is definitely necessary and clarifying few points in the simplified procedure which have not been fully understood yet.

Bibliography

AFGC (2002). *Comportement au vent des ponts*. Presses de l'Ecole Nationale des Ponts et Chaussées, Paris, first edition. (Association Française de Génie Civil).

Alexander, D. (2003). Lecture in: Pre-warning and monitoring of natural man-induced disasters as prevention/reduction measures. Socrates Intensive Program (Borri, C. and Peil, U. Editors), Villa Vigoni, Como.

Augusti, G., Chiarugi, A., and Vignoli, A. (1980). Experimental analysis of a cable-stayed bridge. *Inserto Costruzioni Metalliche*, **3**, 2–16.

Augusti, G., Spinelli, P., Borri, C., Bartoli, G., Giachi, M., and Giordano, S. (1995). The C.R.I.A.C.I.V. Atmospheric Boundary Layer Wind Tunnel. In *Proc.* 9^{th} *International Conference on Wind Engineering*, New Delhi. Wiley Eastern Ltd.

Augusti, G., Borri, C., and Niemann, H.-J. (2001). Is Aeolian risk as significant as other environmental risks? *Reliability Engineering and System Safety*, **74**, 227–237.

Baker, J. and Cornell, C. (2003). Uncertainty specification and propagation for loss estimation using FOSM method. PEER Report 2003/07, Pacific Earthquake Engineering Research Center.

Barré, C., Flamand, O., and Grillaud, G. (1996a). Aerodynamic stability of Aswan cable stayed bridge over the Nile. EN-ECA 96.5 C, CSTB, Nantes.

Barré, C., Flamand, O., and Grillaud, G. (1996b). Propriétés aérodynamiques des viaducs de l'Autoroute A89. EN-ECA 96.14 C, CSTB, Nantes.

Bartoli, G. and Mannini, C. (2005). Reliability of bridge deck flutter derivative measurements in wind tunnel tests. In G. Augusti and M. Ciampoli, editors, *Proc.* 9^{th} *International Conference On Structural Safety And Reliability*, pages 1193–1200, Rome. Millpress, Rotterdam.

Bartoli, G. and Procino, L. (2004). Prove in galleria del vento su modello sezione di una passerella pedonale in loc. Ruffolo (Siena). Internal Report, CRIACIV.

Bartoli, G. and Righi, M. (2004a). Analisi del flutter per sezioni rettangolari in flusso laminare e turbolento. In *Proc.* 8^{th} *Italian National Conference on Wind Engineering IN-VENTO*, pages 53–62, Reggio Calabria.

Bartoli, G. and Righi, M. (2004b). Flutter optimization of bridge decks: experimental and analytical procedures. In F. Bontempi, editor, *Proc. 2^{nd} International Conference on Structural and Construction Engineering*, volume 3, pages 2375–2381, Rome. Balkema.

Bartoli, G. and Righi, M. (2006). Flutter mechanism for rectangular prisms in smooth and turbulent flow. *J. Wind Eng. Ind. Aerodyn.*, **94**, 275–291.

Bartoli, G., Borri, C., and Gusella, V. (1995). Aeroelastic behaviour of bridge decks: a sensitivity analysis of the turbulent nonlinear response. In *Proc. 9^{th} International Conference on Wind Engineering*, pages 851–862, New Delhi. Wiley Eastern Ltd.

Bisplinghoff, R., Ashley, H., and Halfman, R. (1996). *Aeroelasticity*. Dover Publications, Inc., New York, first edition.

Blevins, R. (1990). *Flow-induced vibration*. Van Nostrand Reinhold, New York, second edition.

Borri, C. and Biagini, P. (2005). Wind response of large roofs of stadions and arena. In J. Náprstek and C. Fischer, editors, *Proc. 4^{th} European and African Conference on Wind Engineering*, Prague.

Borri, C. and Costa, C. (2004). Numerical simulation of buffeting forces in bridge deck aerodynamics via indicial functions. In *Proc. 8^{th} Italian National Conference on Wind Engineering IN-VENTO*, pages 121–130, Reggio Calabria.

Borri, C. and Höffer, R. (2000). Aeroelastic wind forces on flexible girders. *Meccanica*, **35**(10), 1–15.

Borri, C., Costa, C., and Salvatori, L. (2005). Reliability of indicial functions in bridge deck aeroelasticity. In G. Augusti and M. Ciampoli, editors, *Proc. 9^{th} International Conference On Structural Safety And Reliability*, pages 1217–1224, Rome. Millpress, Rotterdam.

Brancaleoni, F. and Diana, G. (1993). The aerodynamic design of the Messina Straits Bridge. *J. Wind Eng. Ind. Aerodyn.*, **48**(2-3), 395–409.

Brownjohn, J. and Jakobsen, J. (2001). Strategies for aeroelastic parameter identification from bridge deck free vibration data. *J. Wind Eng. Ind. Aerodyn.*, **89**, 1113–1136.

Bruno, L. and Khris, S. (2003). The validity of 2D numerical simulations of vortical structures around a bridge deck. *Mathematical and Computer Modelling*, **37**, 795–828.

Bucher, C. and Lyn, Y. (1988a). Effect of spanwise correlation of turbulence field on the motion stability of long-span bridges. *J. Fluids and Structures*, **2**, 437–451.

Bucher, C. and Lyn, Y. (1988b). Stochastic stability of bridges considering coupled modes I. *J. Eng. Mech. ASCE*, **114**(12), 2055–2071.

Bucher, C. and Lyn, Y. (1989). Stochastic stability of bridges considering coupled modes II. *J. Eng. Mech. ASCE*, **115**(2), 384–400.

Buresti, G. (1998). Vortex-shedding from bluff bodies. In Riera and Davenport, editors, *Wind effects on buildings and structures*. Balkema, Rotterdam.

Caracoglia, L. (2000). *Wind-structure oscillations on long-span suspension bridges*. Ph.D. thesis, University of Trieste.

Caracoglia, L. and Jones, N. (2003a). A methodology for the experimental extraction of indicial functions for streamlined and bluff deck sections. *J. Wind Eng. Ind. Aerodyn.*, **91**(5), 609–636.

Caracoglia, L. and Jones, N. (2003b). Time domain vs. frequency domain characterization of aeroelastic forces for bridge deck sections. *J. Wind Eng. Ind. Aerodyn.*, **91**(3), 371–402.

Chen, X. and Kareem, A. (2000). Nonlinear response analysis of long-span bridges under turbulent winds. In *Proc.* 4^{th} *International Colloquium on Bluff Body Aerodynamics and Applications*, Bochum.

Chen, Y. (1972). Fluctuating lift forces on the Kármán vortex streets on single circular cylinders and in tube bundles; part 1: the vortex street geometry of the single circular cylinder; part 2: lift forces of single cylinders. *Journal of Engineering for Industry*, **94**(2), 603–612 & 613–622. Transactions of the ASME series B.

Chowdhury, A. and Sarkar, P. (2003). A new technique for identification of eighteen flutter derivatives using a three-degree-of-freedom section model. *Engineering Structures*, **25**, 1763–1772.

Chowdhury, A. and Sarkar, P. (2004). Identification of eighteen flutter derivatives of an airfoil and a bridge deck. *Wind and Structures*, **7**(3), 187–202.

Contri, S. (2003). *Il flutter negli impalcati da ponte: identificazione delle derivate aeroelastiche in galleria del vento*. Master's thesis, University of Florence.

Cornell, C. and Luco, N. (2001). Ground motion intensity measures for structural performance assessment at near-fault sites. In *Proc. U.S.-Japan Joint Workshop and Third Grantees Meeting, U.S.-Japan Cooperative Research on Urban Earthquake Disaster Mitigation*, pages 30–38, University of Washington,Seattle.

Costa, C. (2004). *Time-domain models in bridge deck aeroelasticity*. Ph.D. thesis, University of Florence.

Costa, C. (2006). Aerodynamic admittance functions and buffeting forces for bridges via indicial functions. *J. Fluids and Structures*, (in press).

Costa, C. and Borri, C. (2006). Application of indicial functions in bridge deck aeroelasticity. *J. Wind Eng. Ind. Aerodyn.*, **94**(11), 859–881.

CSI (1999). *SAP 2000 Analisi statica, dinamica, lineare e non lineare agli elementi finiti*. Computer and Structures, Inc., Barkely, California, USA. Italian translation in September 2000 by Brunetta and Perin Engineering Srl.

D'Asdia, P. and Sepe, V. (1998). Aeroelastic instability of long-span suspended bridges: a multi-mode approach. *J. Wind Eng. Ind. Aerodyn.*, **74-76**, 849–857.

Davenport, A. (1962). Buffeting of a suspension bridge by storm winds. *J. Struct. Eng.*, **88**(ST3), 233–268.

Davenport, A. and King, J. (1982). A study of the wind effect for the Sunshine Skyway Bridge, Tampa, Florida, concrete alternate. BLWT-SS24-1982, The Boundary Layer Wind Tunnel Laboratory, The University of Western Ontario, London, Canada.

de Grenet, E. and Ricciardelli, F. (2005). The span-wise correlation of aerodynamic forces on a rectangular cylinder for different vibration regimes. In C. Soize and G. Schuëller, editors, *Proc.* 6^{th} *European Conference on Structural Dynamics*, pages 373–378, Paris. Millpress.

Diana, G., Falco, M., Bruni, S., Cigada, A., Larose, G., Damsgaard, A., and Collina, A. (1995). Comparisons between wind tunnel tests on a full aeroelastic model of the proposed bridge over Stretto di Messina and numerical results. *J. Wind Eng. Ind. Aerodyn.*, **54-55**, 101–113.

Diana, G., Cheli, F., Zasso, A., and Bocciolone, M. (1999). Suspension bridge response to turbulent wind: Comparison of a new numerical simulation method results with full scale data. In Larsen, Larose, and Livesey, editors, *Wind Engineering into the* 21^{st} *Century, Proc.* 10^{th} *International Conference on Wind Engineering*, Copenhagen. Balkema, Rotterdam.

Diana, G., Resta, F., Zasso, A., Belloli, M., and Rocchi, D. (2004). Forced motion and free motion aeroelastic tests on a new concept dynamometric section model of the Messina suspension bridge. *J. Wind Eng. Ind. Aerodyn.*, **92**(6), 441–462.

Diana, G., Bruni, S., and Rocchi, D. (2005a). A numerical and experimental investigation on aerodynamic nonlinearities in bridge response to turbulent wind. In J. Náprstek and C. Fischer, editors, *Proc.* 4^{th} *European and African Conference on Wind Engineering*, Prague.

Diana, G., Bruni, S., Rocchi, D., Resta, F., and Belloli, M. (2005b). A numerical and experimental investigation on aerodynamic nonlinearities in bridge response to turbulent wind. In C. Soize and G. Schuëller, editors, *Proc.* 6^{th} *European Conference on Structural Dynamics*, pages 397–402, Paris. Millpress.

Dyrbye, C. and Hansen, S. (1997). *Wind Loads on Structures*. John Wiley & Sons, first edition.

ECCS (1987). Recommandations pour le calcul des effets du vent sur les constructions, deuxième édition. European Convention for Constructional Steelwork (ECCS) - Comité Technique 12 "Vent".

Eikenberg, C. (1998). *Journalistenhandbuch zum Katastrophenmanagement*. German IDNDR Committee, Bonn, fifth edition.

EN1990 (2002). Eurocode 1: Basis of design.

ENV1991-2-4 (1995). Eurocode 1: Basis of design and actions on structures. Part 2-4: Wind actions.

Farquharson, F. (1949). Aerodynamic stability of suspension bridges with special reference to the Tacoma Narrows Bridge. Bulletin of the University of Washington, Seattle, Washington.

Fathi, S. (2003). Méthodes d'identification des coefficients aéroélastiques des tabliers de ponts: application à la technique CBHM. EN-CAPE 04.015 R, CSTB, Nantes.

Feng, C. (1968). *The measurement of vortex induced effects in flow past stationary and oscillating circular and D-section cylinders*. Ph.D. thesis, University of British Columbia, Canada.

Flamand, O. (1994). Rain-wind induced vibration of cables. In *Proc. International Conference on cable-stayed and suspension bridges (AFPC)*, Deauville.

Flamand, O. (1996). Etude du comportement aérodynamique du Pont de Tancarville. EN-ECA 96.6 C, CSTB, Nantes.

Flamand, O. (2000). Stabilité aérodynamique du tablier du Pont Sucharski à Gdansk. EN-AEC 00.38 C, CSTB, Nantes.

Flamand, O. (2001). Stabilité aérodynamique du tablier du Pont Siekierkowski à Varsovie. EN-AEC 01.55 C, CSTB, Nantes.

Flamand, O. (2003a). Stabilité aérodynamique des ponts de Grande Ravine et de Trois Bassins sur la route des Tamarins à la Réunion. EN-CAPE 03.075 C - V0, CSTB, Nantes.

Flamand, O. (2003b). Validation de la stabilité aérodynamique d'une passerelle à Turin. EN-CAPE 03.210 C - V0, CSTB, Nantes.

Flamand, O. and Grillaud, G. (1993). Stabilité aérodynamique des ponts de Barranca et Quetzalapa: étude complementaire. EN-ECA 93.3 C, CSTB, Nantes.

Flamand, O. and Grillaud, G. (1996). Etude aérodynamique du pont de Beaucaire-Tarascon à géométrie modifiée. EN-ECA 96.4 C, CSTB, Nantes.

Flamand, O. and Grillaud, G. (1998). Stabilité aérodynamique du tablier du Pont de Millau. EN-AEC 98.80 C, CSTB, Nantes.

Flamand, O. and Grillaud, G. (1999). Aerodynamic stability of the Rion Antirion bridge deck. Complementary cross-sectional test results. ARD 00015 A, CSTB, Nantes.

Frandsen, A. (1966). Wind stability of suspension bridges. Application of the theory of "thin airfoils". In *Proc. International Symposium on Suspension Bridges*, pages 609–627, Lisbon.

Fung, Y. (1993). *An introduction to the theory of aeroelasticity*. Dover Publications, Inc., New York.

Gerhold, T., Galle, M., Friedrich, O., and Evans, J. (1997). Calculation of complex three-dimensional configurations employing the DLR-Tau code. In *Proc.* 35^{th} *AIAA Aerospace Sciences Meeting and Exhibit, AIAA Paper 97-0167*, Reno, Nevada, USA.

Gimsing, N. (1997). *Cable Supported Bridges - Concepts and Design*. John Wiley & Sons, Inc., New York, second edition.

Graham, J. (1970). Lifting-surface theory for the problem of an arbitrary yawed sinusoidal gust incident on a thin aerofoil in incompressible flow. *Aeronautical Quaterly*, **21**, 182–198.

Grillaud, G. and Flamand, O. (1998). Aerodynamic stability of the Rion Antirion bridge deck. EN-AEC 98.48 C, CSTB, Nantes.

Gu, M., Zhang, R., and Xiang, H. (2000). Identification of flutter derivatives of bridge decks. *J. Wind Eng. Ind. Aerodyn.*, **84**, 151–162.

Hatanaka, A. and Tanaka, H. (2002). New estimation method of aerodynamic admittance function. *J. Wind Eng. Ind. Aerodyn.*, **84**(2), 151–162.

Hikami, Y. and Shiraishi, N. (1988). Rain-wind induced vibrations of cables stayed bridges. *J. Wind Eng. Ind. Aerodyn.*, **29**, 409–418.

Ibrahim, S. and Mikulcik, E. (1977). A method for the direct identification of vibration parameters from the free response. *The Shock and Vibration Bull.*, **47**(Part 4).

Jain, A., Jones, N., and Scanlan, R. (1996). Coupled flutter and buffeting analysis of long-span bridges. *J. Struct. Eng., ASCE*, **122**(7), 716–725.

Jakobsen, J. (1995). *Fluctuating wind load and response of a line-like engineering structure with emphasis on motion-induced wind forces*. Ph.D. thesis, The Norwegian Institute of Technology, Trondheim.

Jakobsen, J., Savage, M., and Larose, G. (2003). Aerodynamic derivatives from buffeting response of a flat plate model with stabilizing winglets. In *Proc.* 11^{th} *International Conference on Wind Engineering*, pages 673–680, Lubbock, Texas.

Jensen, A. and Höffer, R. (1998). Flat plate flutter derivatives: an alternative formulation. *J. Wind Eng. Ind. Aerodyn.*, **74-76**, 859–869.

Katsuchi, H., Jones, N., and Scanlan, R. (1999). Multimode coupled flutter and buffeting analysis of the Akashi Kaikyo Bridge. *J. Struct. Eng., ASCE*, **125**(1), 60–70.

Kravchenko, A. and Moin, P. (2000). Numerical studies of flow over a circular cylinder at Re_D=3900. *Physics of Fluids*, **12**(2).

Küssner, H. (1936). Zusammenfassender Bericht über den instationären Auftrieb von Flügeln. *Luftfahrtforsch.*, **Bd. 13**(11).

Larose, G. (2005). Aerodynamic admittance of bridge decks: a proposal. In C. Soize and G. Schuëller, editors, *Proc. 6th European Conference on Structural Dynamics*, pages 391–395, Paris. Millpress.

Larsen, A. (1993). Aerodynamic aspects of the final design of the 1624 m suspension bridge across the Great Belt. *J. Wind Eng. Ind. Aerodyn.*, **48**, 261–285.

Larsen, A. (1995). Prediction of aeroelastic stability of suspension bridges during erection. In *Proc. 9th International Conference on Wind Engineering*, New Delhi.

Larsen, A. (1998). Advances in aeroelastic analyses of suspension and cable-stayed bridges. *J. Wind Eng. Ind. Aerodyn.*, **74-76**, 73–90.

Larsen, A. and Astiz, M. (1998). Aeroelastic considerations for the Gibraltar Bridge feasibility study. In Larsen and Esdahl, editors, *Proc. Bridge Aerodynamics*, pages 165–173. Balkema, Rotterdam.

Li, Q. (1995). Measuring flutter derivatives for bridge sectional models in water channel. *J. Eng. Mech., ASCE*, **121**(1), 90–101.

Lin, Y. (1996). Stochastic stability of wind-excited long-span bridges. *Probab. Eng. Mech.*, **11**, 257–261.

Lourenco, L. and Shih, C. (1993). Characteristics of the plane wake of a circular cylinder. A particle image velocimetry. From Kravchenko & Moin Report TF-73, 1998, Stanford University, California.

Lyn, D., Einav, S., Rodi, W., and Park, J.-H. (1995). A laser-Doppler velocimetry study of ensemble-averaged characteristics of the turbulent near wake of a square cylinder. *J. Fluid Mech.*, **304**, 285–319.

Mannini, C., Soda, A., and Voss, R. (2006a). Computational investigation of flow around bridge sections. In J. Radić, editor, *Proc. International Conference on Bridges*, pages 343–350, Dubrovnik, Croatia.

Mannini, C., Soda, A., Voss, R., and Schewe, G. (2006b). URANS and DES simulation of the flow around bridge sections. In *Proc. 9th Italian National Conference on Wind Engineering IN-VENTO*, Pescara.

Martini, S. (2004). *Entwurf der Gründung einer Hängebrücke unter Berücksichtigung von Erdbebenbeanspruchungen gemäß EC8-Teil2*. Master's thesis, Bergische Universität, Wuppertal.

Matsumoto, M. (1996). Aerodynamic damping of prisms. *J. Wind Eng. Ind. Aerodyn.*, **59**, 159–175.

Matsumoto, M. (2004). Personal communication.

Matsumoto, M. (2005). Flutter instability of structures. In J. Náprstek and C. Fischer, editors, *Proc. 4^{th} European and African Conference on Wind Engineering*, Prague.

Matsumoto, M., Shiraishi, N., and Shirato, H. (1992). Rain-wind induced vibration of cables in cable-stayed bridges. *J. Wind Eng. Ind. Aerodyn.*, **43**, 2011–2022.

Matsumoto, M., Kobayashi, K., Niihara, Y., Shiarto, H., and Hamasaki, H. (1995). Flutter mechanism and its stabilisation of bluff bodies. In *Proc. 9^{th} International Conference on Wind Engineering*, pages 827–838, New Delhi. Wiley Eastern Ltd.

Matsumoto, M., Daito, Y., Yoshizumi, F., Ichikawa, Y., and Yabutani, T. (1997). Torsional flutter of bluff bodies. *J. Wind Eng. Ind. Aerodyn.*, **69-71**, 871–882.

Matsumoto, M., Daito, Y., Kanamura, T., Shigemura, Y., Sakuma, S., and Ishizaki, H. (1998). Rain-wind induced vibration of cables in cable-stayed bridges. *J. Wind Eng. Ind. Aerodyn.*, **74-76**, 1015–1027.

Matsumoto, M., Yoshizumi, F., Yabutami, T., Abe, K., and Nakajima, N. (1999). Flutter stabilization and heaving-branch flutter. *J. Wind Eng. Ind. Aerodyn.*, **83**, 289–299.

Matsumoto, M., Nakajima, N., Taniwaki, Y., and Shijo, R. (2001). Grating effect on flutter instability. *J. Wind Eng. Ind. Aerodyn.*, **89**, 1487–1497.

Matsumoto, M., Taniwaki, Y., and Shijo, R. (2002). Frequency characteristics in various flutter instabilities of bridge girders. *J. Wind Eng. Ind. Aerodyn.*, **90**, 1973–1980.

Minh, N., Miyata, T., Yamada, H., and Sanada, Y. (1999). Numerical simulation of wind turbulence and buffeting analysis of long-span bridges. *J. Wind Eng. Ind. Aerodyn.*, **83**(1-3), 301–315.

Miyata, T. (1995). Full model testing of large cable-supported bridges. In *State of the Art in Wind Engineering; 9^{th} International Conference on Wind Engineering*, pages 249–280, New Delhi. Wiley Eastern Ltd.

Miyata, T. and Yamaguchi, K. (1993). Aerodynamics of wind effects on the Akashi Kaikyo Bridge. *J. Wind Eng. Ind. Aerodyn.*, **48**, 287–315.

Miyata, T., Yamada, H., Boonyapinyo, V., and Santos, J. (1995). Analytical investigation on the response of a very long suspension bridge under gusty wind. In *Proc. 9^{th} International Conference on Wind Engineering*, pages 1006–1017, New Delhi.

Moe, G. and Henriksen, M. (1999). Flow induced vibrations of line-like structures. In *Proc. 3^{rd} International Cable Dynamics Conference*, Trondheim.

Nakamura, Y. (1978). An analysis of binary flutter of bridge deck sections. *J. Sound and Vibration*, **57**(4), 471–482.

Nakamura, Y. (1979). On the aerodynamic mechanism of torsional flutter of bluff structures. *J. Sound and Vibration*, **67**(2), 163–177.

Nakamura, Y. and Matsukawa, T. (1987). Vortex excitation of rectangular cylinders with a long side normal to the flow. *J. Fluid Mech.*, **180**, 171–191.

Nakamura, Y. and Mizota, T. (1975). Torsional flutter of rectangular prisms. *J. Eng. Mech. Div.*, **101**(EM2), 125–142.

Nakamura, Y. and Ohya, Y. (1984). The effects of turbulence on the mean flow past two-dimensional rectangular cylinders. *J. Fluid Mech.*, **149**, 255–273.

Nakamura, Y. and Yoshimura, T. (1976). Binary flutter of suspension bridge deck sections. *J. Eng. Mech. Div.*, **102**(EM4), 685–700.

Noè, S., Fathi, S., and D'Asdia, P. (2004). Modello analitico per la stima della ampiezza di oscillazione per distacco di vortici. In *Proc.* 8^{th} *Italian National Conference on Wind Engineering IN-VENTO*, pages 397–404, Reggio Calabria.

Novak, M. and Tanaka, H. (1972). Pressure correlations on vertical cylinder. In *Proc.* 4^{th} *International Conference on Wind Effects on Structures*, pages 227–232, Heathrow, U.K. Cambridge University Press.

Obasaju, E. (1983). An investigation of the effects of incidence on the flow around a square section cylinder. *Aeronautical Quarterly*, **34**, 243–259.

Okajima, A. (1982). Strouhal numbers of rectangular cylinders. *J. Fluid Mech.*, **123**, 379–398.

ONERA (1989). Etude du comportement dans le vent du tablier définitif du pont de Normandie. Rapport Technique n°15/3588 RY 091R-391G.

Ong, L. and Wallace, J. (1996). The velocity field of the turbulent very near wake of a circular cylinder. *Exp. Fluids*, **20**.

Parkinson, G. and Smith, J. (1964). The square cylinder as an aeroelastic non-linear oscillator. *J. Mech. Appl. Math.*, **17**, 225–239.

Parkinson, G. and Wawzonek, M. (1981). Some considerations of combined effects of galloping and vortex resonance. *J. Wind Eng. Ind. Aerodyn.*, **8**(1-2), 135–143.

Pastò, S. (2005). *Fatigue-risk assessment of slender structures with circular cross-section at lock-in*. Ph.D. thesis, University of Florence - TU Braunschweig.

Paulotto, C., Ciampoli, M., and Augusti, G. (2004). Some proposals for a first step towards a Performance Based Wind Engineering. In *Proc.* 1^{st} *International Forum in Engineering Decision Making (IFED)*, Stoos.

Peil, U. and Clobes, M. (2005). Time domain model for buffeting wind loads verified in full scale measurements. In C. Soize and G. Schuëller, editors, *Proc.* 6^{th} *European Conference on Structural Dynamics*, Paris. Millpress.

Peil, U. and Clobes, M. (2006). Modelle zur instationären übertragung der Windturbulenz im Zeitbereich. In *Proc. VDI-Baudynamik Conference*, Kassel.

Peil, U. and Nahrath, N. (2003). Modeling of rain-wind induced vibrations. *Wind and Structures*, **6**(1), 41–52.

Peil, U., Behrens, M., and Nahrath, N. (2002). Dynamic response of slender structures under wind load. In *Proc.* 5^{th} *European Conference on Structural Dynamics*, Munich.

Peil, U., Nahrath, N., and Dreyer, O. (2003). Modeling of rain-wind induced vibrations. In *Proc.* 11^{th} *International Conference on Wind Engineering*, Lubbock, Texas.

Plate, E. (1997). Dams and safety management at downstream valleys. In *Betamio de Almeida A. and Viseu T., Dams and safety management at downstream valleys*, pages 27–43. Balkema, Lisbon.

Plate, E. (1998). Stochastic hydraulic modelling - a way to cope with uncertainty. In *Proc.* 3^{rd} *International Conference on Hydro- Science and Engineering*, Cottbus.

Plate, E. (2000). Flood risk and flood management. In A. Bronstert, C. Bismuth, and L. Menzel, editors, *Proc. European Conference on Advances in Flood Research*, Potsdam.

Plate, E. (2003a). Lecture in: Pre-warning and monitoring of natural man-induced disasters as prevention/reduction measures. Socrates Intensive Program (Borri, C. and Peil, U. Editors), Villa Vigoni, Como.

Plate, E. (2003b). Towards development of a Human Security Index. In *Proc. Osiris Workshop*, Berlin.

Rackwitz, R. (2003). Lecture in: Pre-warning and monitoring of natural man-induced disasters as prevention/reduction measures. Socrates Intensive Program (Borri, C. and Peil, U. Editors), Villa Vigoni, Como.

Reinhold, T., Brinch, M., and Damsgaard, A. (1992). Wind tunnel tests for the Great Belt link. In A. Larsen, editor, *Proc.* 1^{st} *International Symposium on Aerodynamics of Large Bridges*, Copenhagen. Balkema, Rotterdam.

Ricciardelli, F. and de Grenet, E. (2002). Evaluation of bridge flutter derivatives from wind excited vibration of section models. In *Proc.* 5^{th} *European Conference on Structural Dynamics*, pages 587–592, Munich.

Ricciardelli, F. and Hangan, H. (2001). Pressure distribution and aerodynamic forces on stationary box bridge sections. *Wind and Structures*, **4**(5), 399–412.

Righi, M. (2003). *Aeroelastic stability of long span suspended bridges: flutter mechanism on rectangular cylinders in smooth and turbulent flow*. Ph.D. thesis, University of Florence.

Rocha, M., Loredo-Souza, A., Paluch, M., and Núñez, G. (2003). Aspectos aerodinâmicos a serem considerados no projeto de pontes estaiadas - Estudo de caso: ponte sobre o Rio Guamà. In *Proc.* 5^{th} *Simpósio EPUSP sobre Estruturas de Concreto*, São Paulo.

Roshko, A. (1954). On the development of turbulent wakes from vortex streets. Report 1191, NACA.

Roshko, A. (1961). Experiments on the flow past a circular cylinder at very high Reynolds number. *J. Fluid Mech.*, **10**(3), 345–356.

Rung, T., Lübcke, H., Xue, L., Thiele, F., and Fu, S. (1999). Assessment of Explicit Algebraic Stress Models in transonic flows. In W. Rodi and D. Laurence, editors, *Proc.* 4^{th} *International Symposium on Engineering Turbulence Modelling and Experiments*, pages 659–668, Ajaccio, France. Elsevier, Amsterdam.

Sallet, D. (1973). The lift and drag due to von Kármán vortex wake. *Journal of Hydronautics*, **7**(4), 161–165.

Salvatori, L. and Spinelli, P. (2006a). A discrete 3D model for bridge aerodynamics and aeroelasticity: nonlinearities and linearizations. *Meccanica*, (in press).

Salvatori, L. and Spinelli, P. (2006b). Effects of structural nonlinearity and along-span wind coherence on suspension bridge aerodynamics: some numerical simulation results. *J. Wind Eng. Ind. Aerodyn.*, **94**, 415–430.

Sarkar, P. (1992). *New identification methods applied to the response of flexible bridges to wind*. Ph.D. thesis, John Hopkins University, Baltimore.

Sarkar, P., Jones, N., and Scanlan, R. (1994). Identification of aeroelastic parameters of flexible bridges. *J. Eng. Mech., ASCE*, **120**(8), 1718–1742.

Scanlan, R. (1984). Role of indicial functions in buffeting analysis of bridges. *J. Struct. Eng.*, **110**(7), 1433–1446.

Scanlan, R. (1998). Bridge flutter derivatives at vortex lock-in. *J. Struct. Eng.*, **124**(4), 450–458.

Scanlan, R. and Jones, N. (1999). A form of aerodynamic admittance for use in bridge aeroelastic analysis. *J. Fluids Struct.*, **13**, 1017–1027.

Scanlan, R. and Lin, W.-H. (1978). Effects of turbulence on bridge flutter derivatives. *J. Eng. Mech. Div.*, **104**(EM4), 719–733.

Scanlan, R. and Tomko, J. (1971). Airfoil and bridge deck flutter derivatives. *J. Eng. Mech. Div. Proc. ASCE*, **97**, 1717–1737.

Scanlan, R., Béliveau, J.-G., and Budlong, K. (1974). Indicial aerodynamic functions for bridge decks. *J. Eng. Mech. Div.*, **100**(EM4), 657–672.

Scanlan, R., Jones, N., and Singh, L. (1997). Inter-relations among flutter derivatives. *J. Wind Eng. Ind. Aerodyn.*, **69-71**, 829–837.

Schewe, G. (1983). On the force fluctuations acting on a circular cylinder in cross flow from subcritical up to transcritical Reynolds numbers. *J. Fluid Mech.*, **133**.

Schewe, G. (1984). Untersuchung der aerodynamischen Kräfte, die auf stumpfe Profile-bei großen Reynolds-Zahalen wirken. DFVLR-Mitt.84-19, DLR, Institut für Aeroelastik, Göttingen.

Schewe, G. (1986). Sensitivity of transition phenomena to small perturbations in flow round a circular cylinder. *J. Fluid Mech.*, **172**, 33–46.

Schewe, G. (1989). Nonlinear flow-induced resonances of an H-shaped section. *J. Fluids and Structures*, **3**, 327–348.

Schewe, G. (1990). Analyse der Aerodynamischen Kraftschwankungen, die auf Quadratprofil bei Anstellwinkelvariation wirken. In *Proc. DGLR-Symp. "Strömung mit Ablösung"*, Achen.

Schewe, G. (2001). Reynolds-number effects in flow around more-or-less bluff bodies. *J. Wind Eng. Ind. Aerodyn.*, **89**, 1267–1289.

Schewe, G. (2005). Reynolds-number effects and their influence on flow induced vibrations. In *Proc.* 6^{th} *European Conference on Structural Dynamics*, pages 337–342, Paris. Millpress, Rotterdam.

Schewe, G. (2006). Influence of the reynolds-number on flow-induced vibrations of generic bridge sections. In J. Radić, editor, *Proc. International Conference on Bridges*, pages 351–358, Dubrovnik, Croatia.

Schewe, G. and Larsen, A. (1998). Reynolds number effects in the flow around a bluff bridge deck cross section. *J. Wind Eng. Ind. Aerodyn.*, **74-76**, 829–838.

Sears, W. (1941). Some aspects of non-stationary airfoil theory and its practical application. *J. Aeronaut. Sci.*, **8**, 104–108.

Seidel, C. and Dinkler, D. (2006). Rain-wind induced vibrations: phenomenology, mechanical modelling and numerical analysis. *Computer and Structures*, **84**(24-25), 1584–1595.

Selberg, A. (1961). Oscillation and aerodynamic stability of suspension bridges. In *Acta Polytechnica Scandinavica, Civ. Eng. and Build. Constr. Series n°13*, Oslo.

Shortreed, J., Hicks, J., and Craig, L. (2003). Basic frameworks for risk management. Final report, Prepared for The Ontario Ministry of the Environment, NERAM.

Simiu, E. and Scanlan, R. (1996). *Wind effects on structures*. John Wiley & Sons, Inc., New York, third edition.

Singh, L., Jones, N., Scanlan, R., and Lorendeaux, O. (1995). Simultaneous identification of 3-dof aeroelastic parameters. In *Proc.* 9^{th} *International Conference on Wind Engineering*, pages 972–981, New Delhi. Wiley Eastern Ltd.

Spalart, P. and Allmaras, S. (1992). A one-equation turbulence model for aerodynamic flows. In *Proc.* 30^{th} *AIAA Aerospace Sciences Meeting and Exhibit, AIAA Paper 92-0439*, Reno, Nevada, USA.

Strouhal, V. (1878). Über eine besondere Art der Tonerregung. *Annalen der Physik und Chemie*, pages 216–251.

Theodorsen, T. (1934). General theory of aerodynamic instability and the mechanism of flutter. NACA Technical Report 496, Aeronautics, Twentieth Annual Report of the National Advisory Committee for Aeronautics, NACA.

Thompson, J. and Stewart, H. (2002). *Nonlinear dynamics and chaos*. John Wiley & Sons, New York, second edition.

van Nunen, J. (1974). Pressure and forces on a circular cylinder in a cross flow at high reynolds number. In E. Naudascher, editor, *Flow Induced Structural Vibrations*. Springer-Verlag, Berlin.

von Kármán, T. and Rubach, H. (1912). Über den Mechanismus des Flüssigkeits- und Luftwiderstandes. *Physikalische Zeitschrift*, **15**(2), 49–59.

Wagner, H. (1925). Über die Entstehung des dynamischen Auftriebes von Tagflügeln. *Z. Angew. Math. Mech.*, **Bd. 5-Helft 1**.

Wooton, L. (1969). The oscillations of large circular stacks in wind. *Proc. Inst. Civ. Eng.*, **43**, 573–598.

Wooton, L. and Scruton, C. (1970). Aerodynamic stability. In *Seminar on Modern Design of Wind-Sensitive Structures*, pages 65–81. Construction Industry Research and Information Association (CIRIA), London.

Yamaguchi, H. (1990). Analytical study on growth mechanism of rain vibration of cables. *J. Wind Eng. Ind. Aerodyn.*, **31**, 73–80.

Zasso, A. (1996). Flutter derivatives: Advantages of a new representation convention. *J. Wind Eng. Ind. Aerodyn.*, **60**, 35–47.

Zasso, A., Cigada, A., and Negri, S. (1996). Flutter derivatives identification through full bridge aeroelastic model transfer function analysis. *J. Wind Eng. Ind. Aerodyn.*, **60**, 17–33.

Zdravkovich, M. (1997). *Flow around circular cylinders*. Oxford University Press, Oxford.

Zhang, Y. and Brownjohn, J. (2004). Effect of relative amplitude on bridge deck flutter. *J. Wind Eng. Ind. Aerodyn.*, **92**(6), 493–508.

Zhang, Y., Brownjohn, J., and Omenzetter, P. (2003). Time domain formulation of self-excited forces on bridge deck for wind tunnel experiment. *J. Wind Eng. Ind. Aerodyn.*, **91**(6), 723–736.

Appendix A

Other wind-tunnel test results

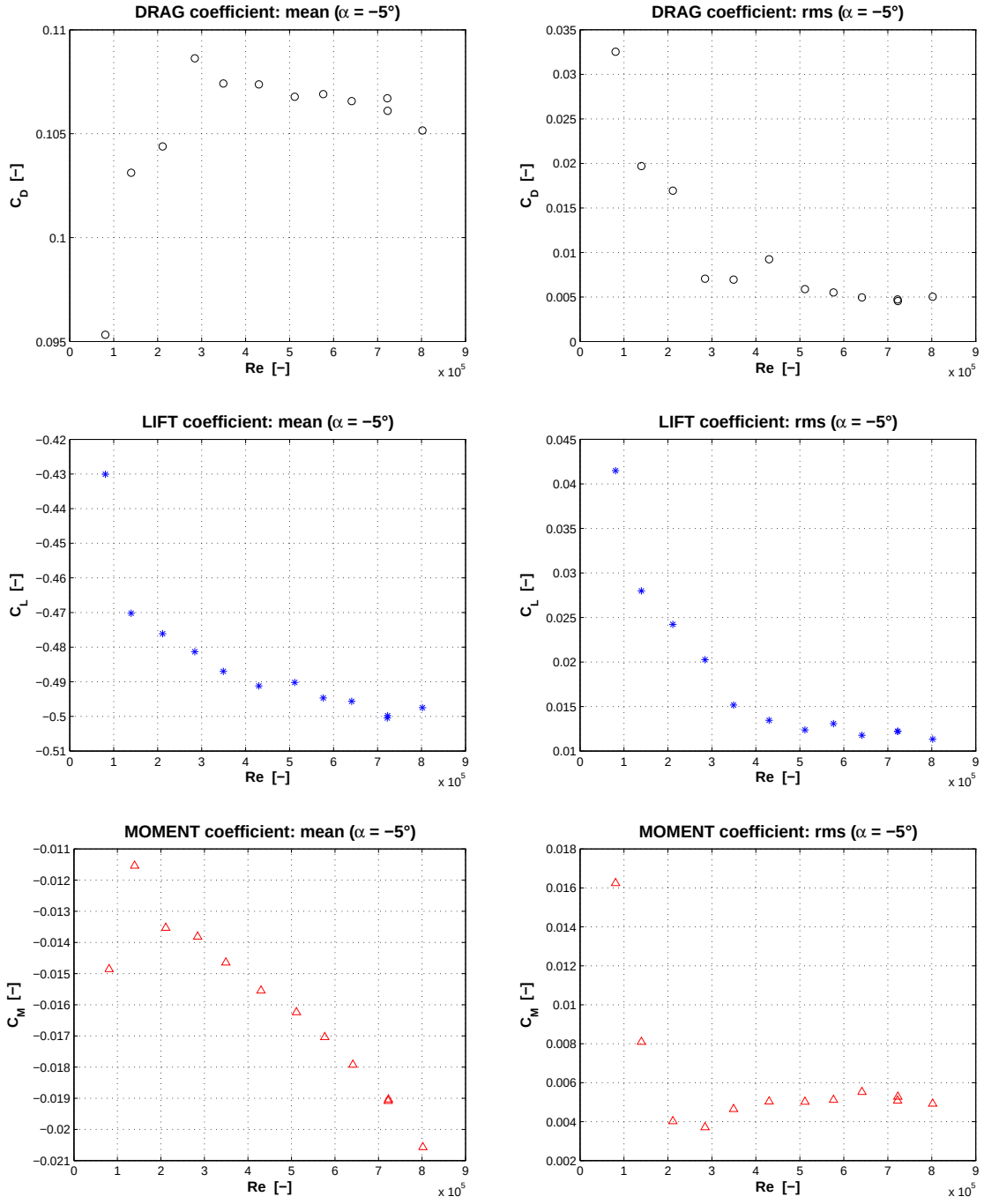

Figure A.1: Mean and rms-values of the aerodynamic force coefficients depending on Reynolds number at -5° angle of attack (frequency of acquisition: 2000 Hz; length of the signals: 120 s)

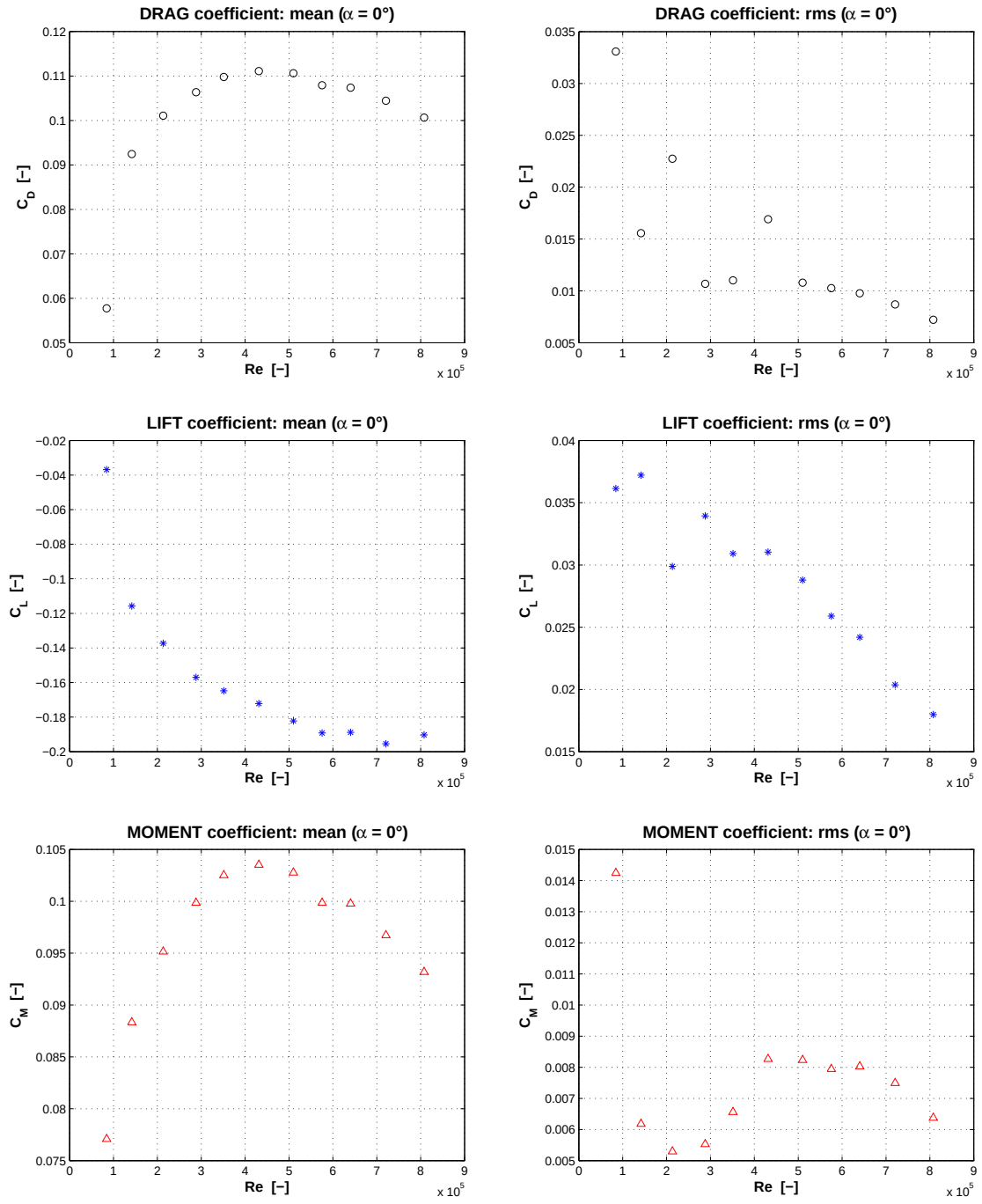

Figure A.2: Mean and rms-values of the aerodynamic force coefficients depending on Reynolds number at 0° angle of attack (frequency of acquisition: 2000 Hz; length of the signals: 120 s)

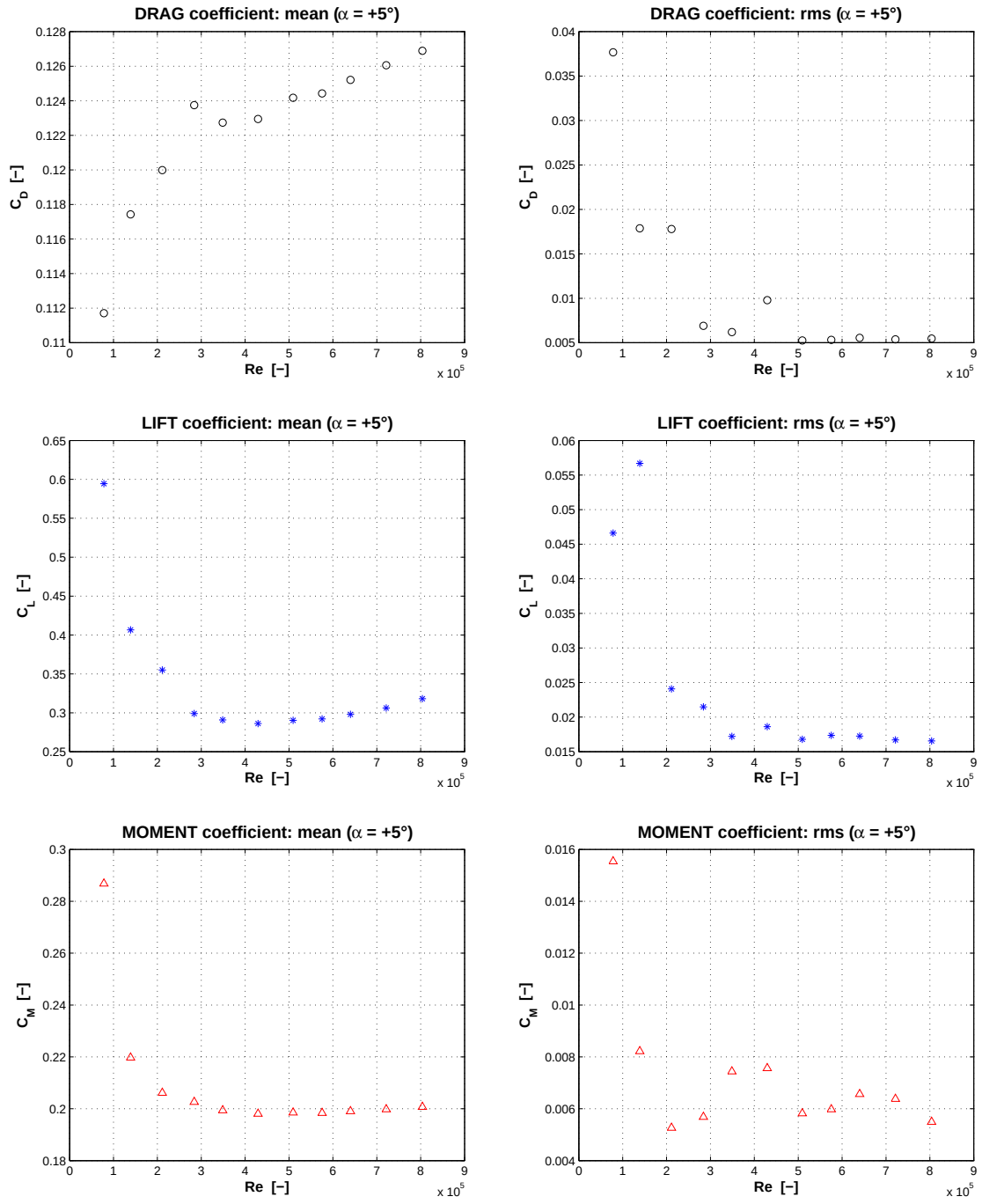

Figure A.3: Mean and rms-values of the aerodynamic force coefficients depending on Reynolds number at +5° angle of attack (frequency of acquisition: 2000 Hz; length of the signals: 120 s)

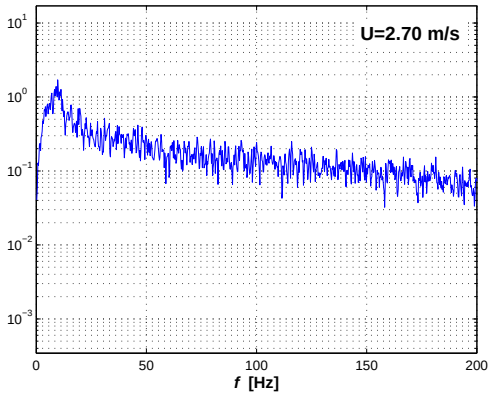
U=2.70 m/s
f [Hz]

(a)

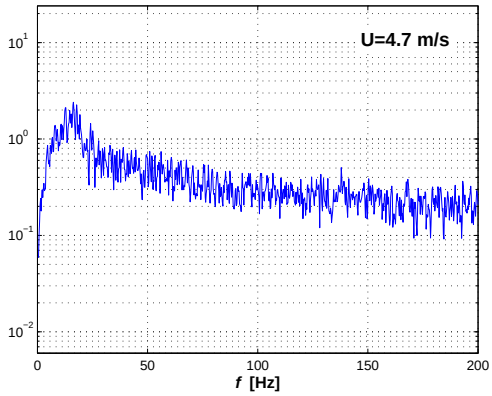
U=4.7 m/s
f [Hz]

(b)

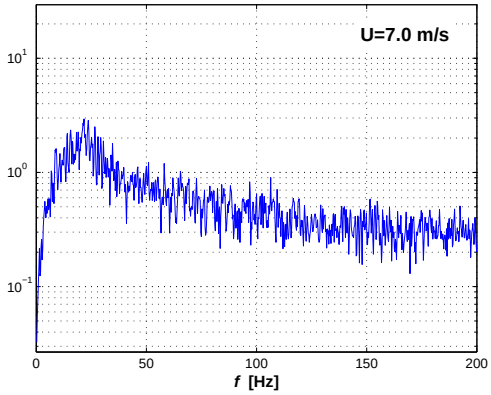
U=7.0 m/s
f [Hz]

(c)

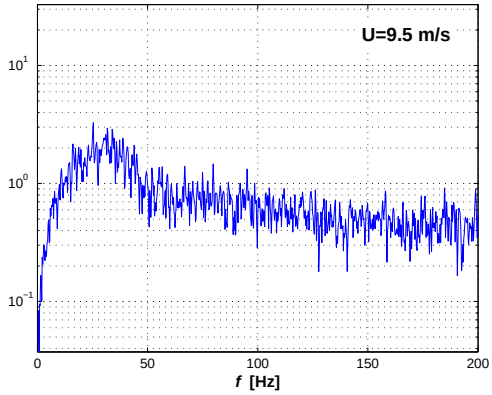
U=9.5 m/s
f [Hz]

(d)

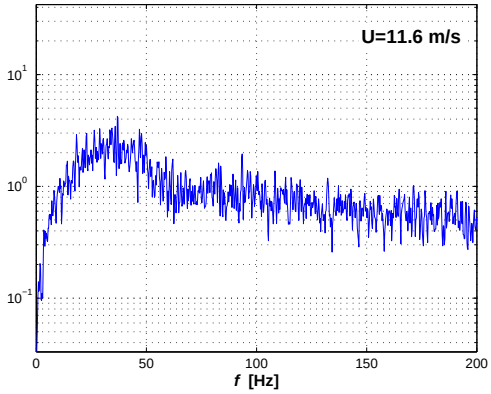
U=11.6 m/s
f [Hz]

(e)

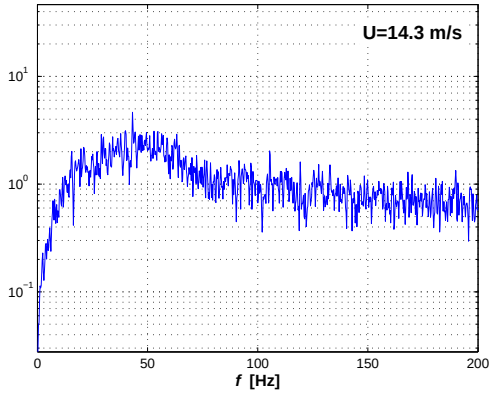
U=14.3 m/s
f [Hz]

(f)

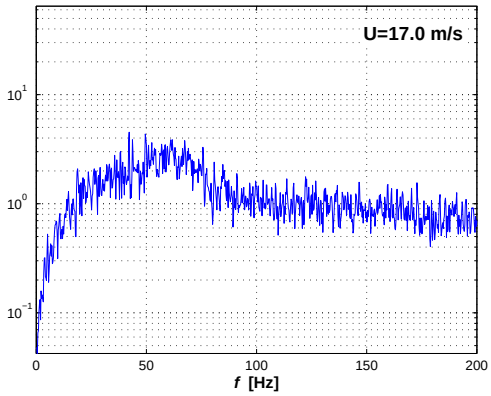

(g)

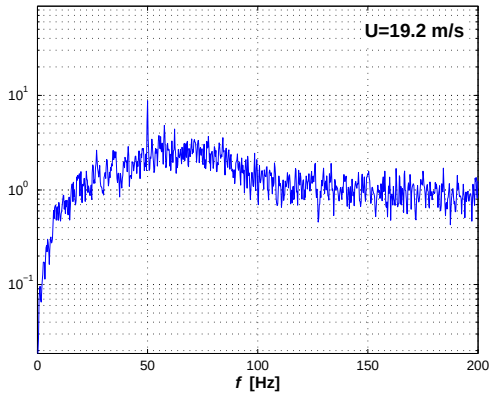

(h)

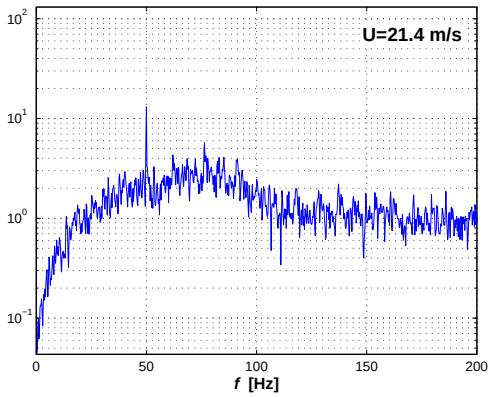

(i)

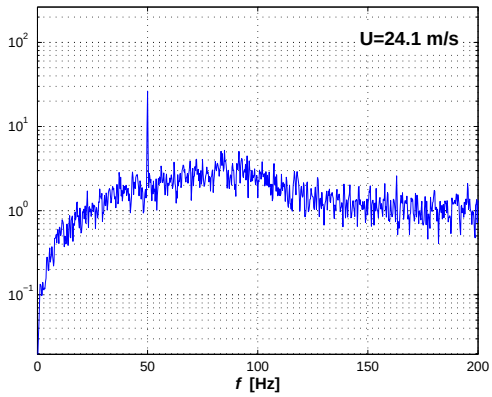

(j)

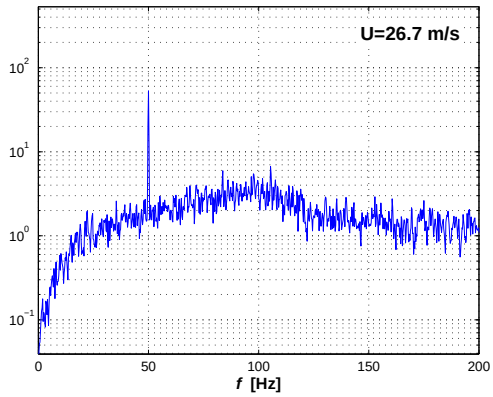

(k)

Figure A.4: Power spectral density of the wind speed fluctuation signals registered by the hot-wire anemometer placed in the wake of model at -5° angle of attack (frequency of acquisition: 2000 Hz; length of the signals: 120 s)

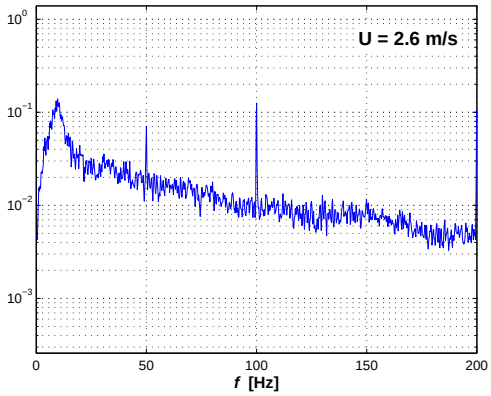
U = 2.6 m/s
f [Hz]

(a)

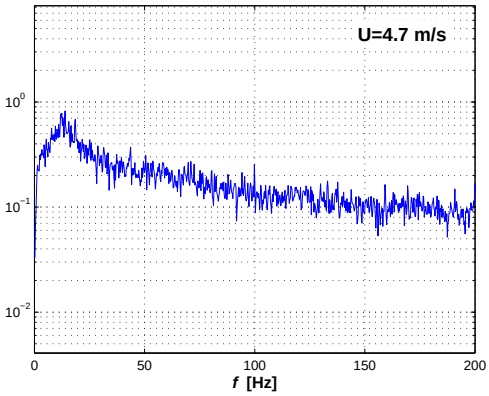
U=4.7 m/s
f [Hz]

(b)

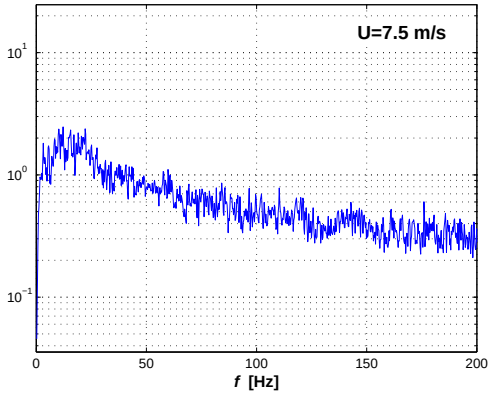
U=7.5 m/s
f [Hz]

(c)

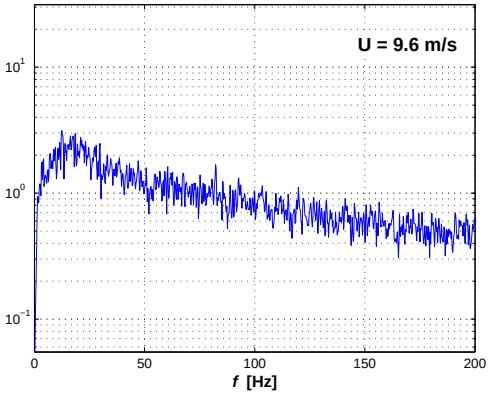
U = 9.6 m/s
f [Hz]

(d)

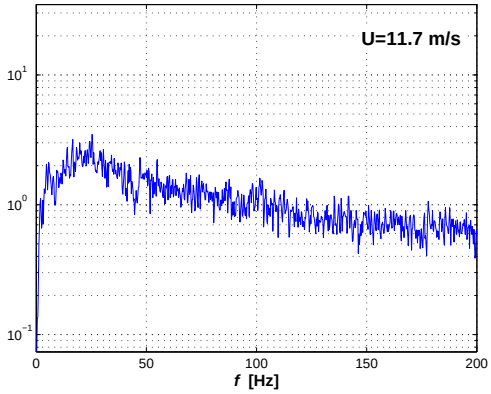
U=11.7 m/s
f [Hz]

(e)

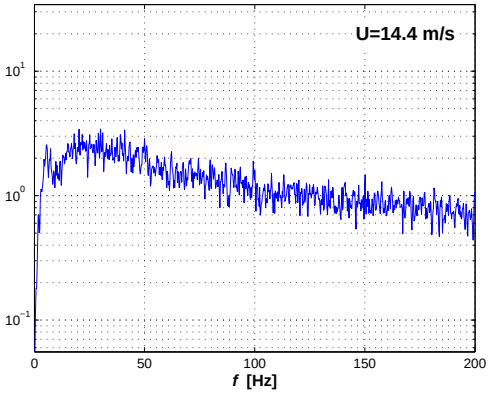
U=14.4 m/s
f [Hz]

(f)

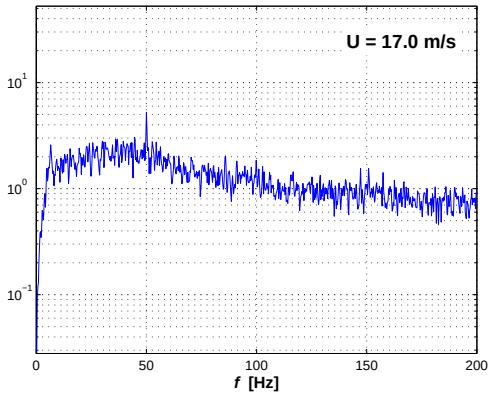

(g)

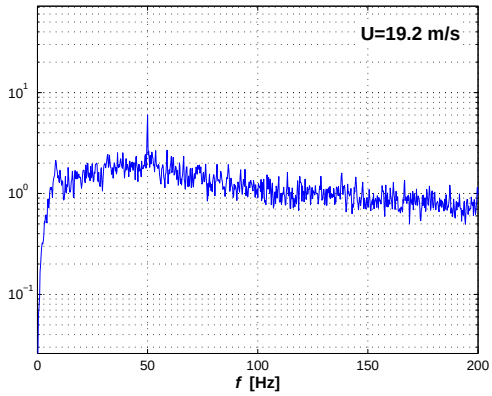

(h)

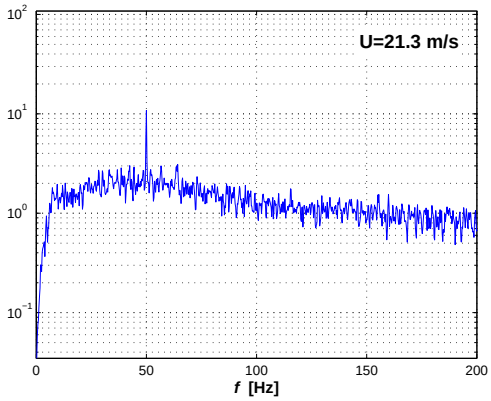

(i)

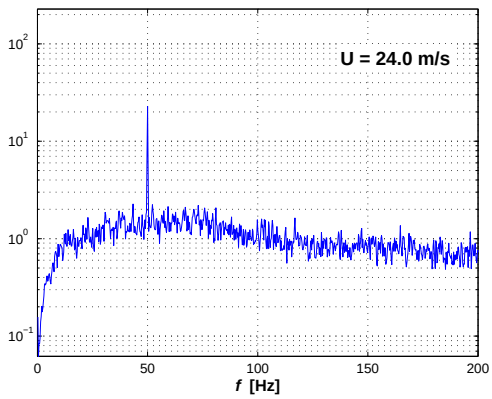

(j)

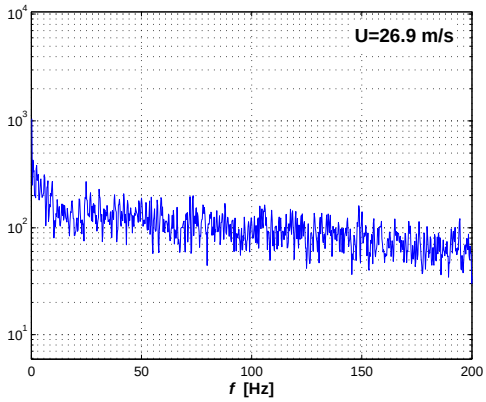

(k)

Figure A.5: Power spectral density of the wind speed fluctuation signals registered by the hot-wire anemometer placed in the wake of model at 0° angle of attack (frequency of acquisition: 2000 Hz; length of the signals: 120 s)

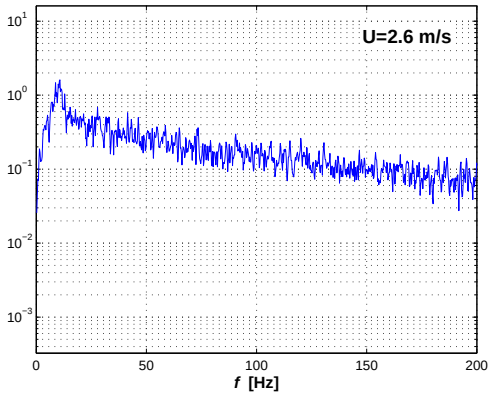
U=2.6 m/s
f [Hz]

(a)

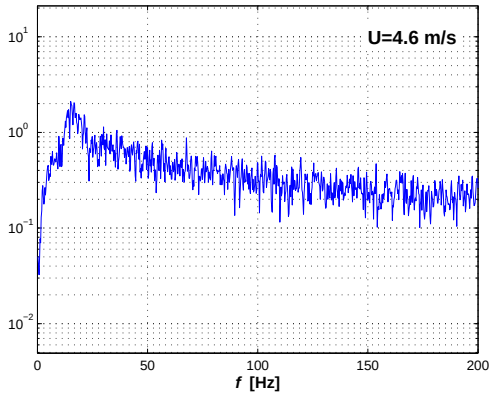
U=4.6 m/s
f [Hz]

(b)

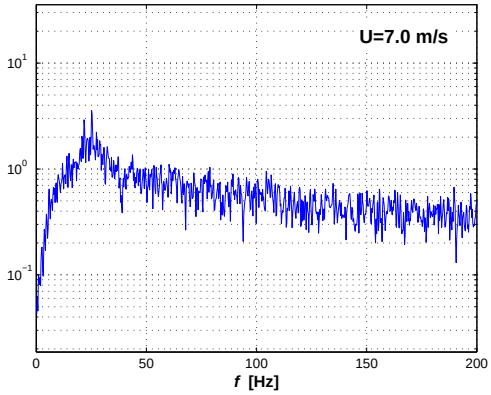
U=7.0 m/s
f [Hz]

(c)

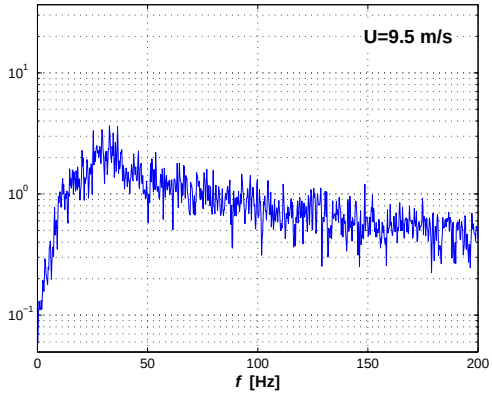
U=9.5 m/s
f [Hz]

(d)

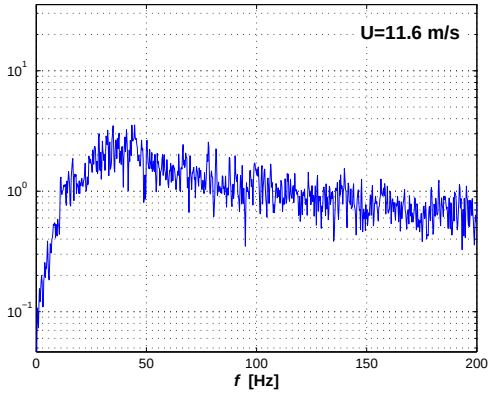
U=11.6 m/s
f [Hz]

(e)

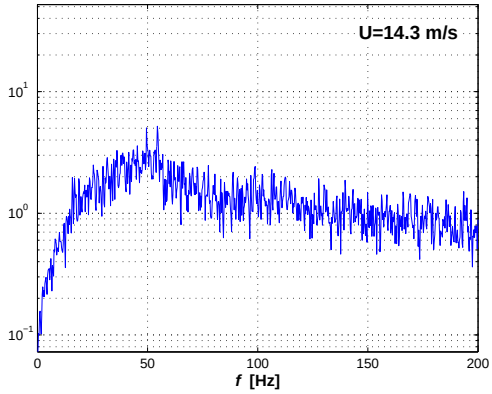
U=14.3 m/s
f [Hz]

(f)

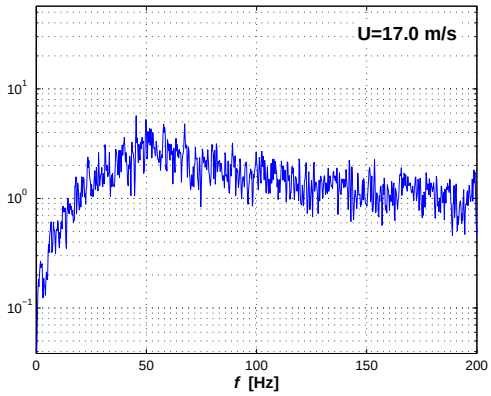

(g)

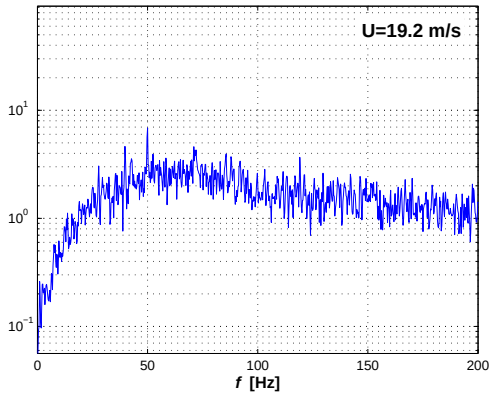

(h)

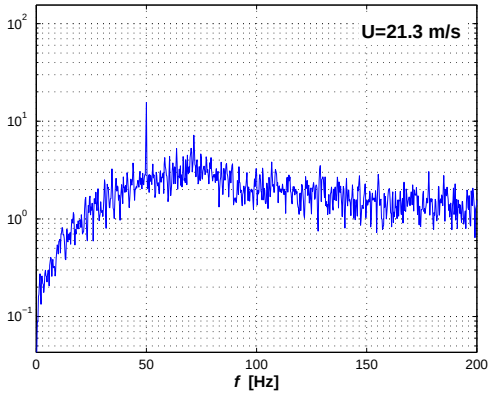

(i)

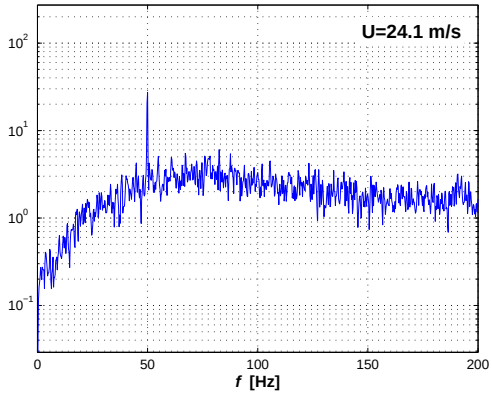

(j)

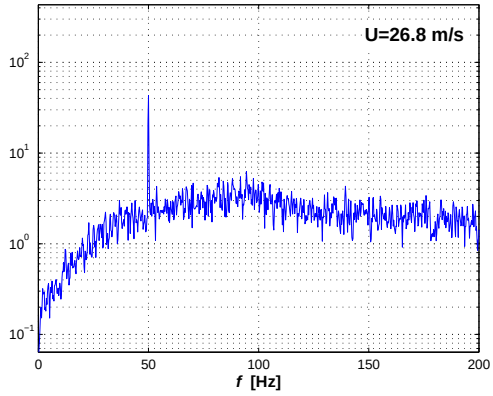

(k)

Figure A.6: Power spectral density of the wind speed fluctuation signals registered by the hot-wire anemometer placed in the wake of model at +5° angle of attack (frequency of acquisition: 2000 Hz; length of the signals: 120 s)

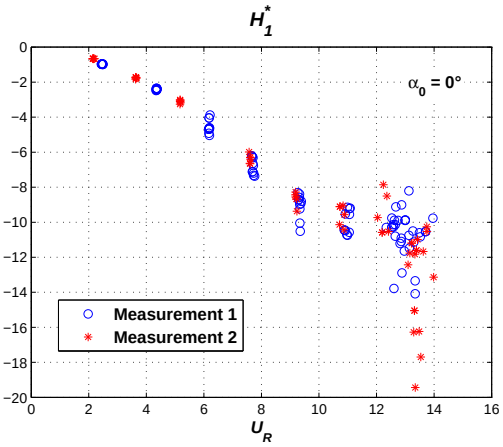
H_1^*
α_0 = 0°
Measurement 1
Measurement 2
U_R

(a)

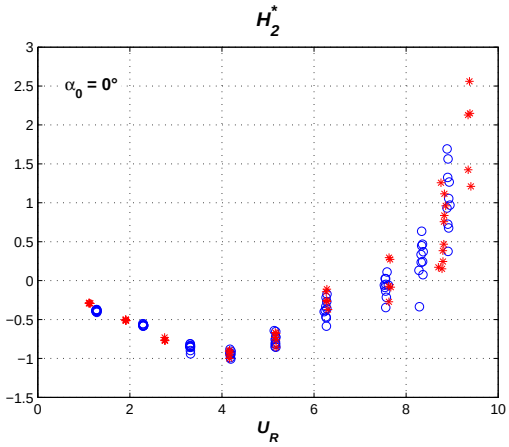
H_2^*
α_0 = 0°
U_R

(b)

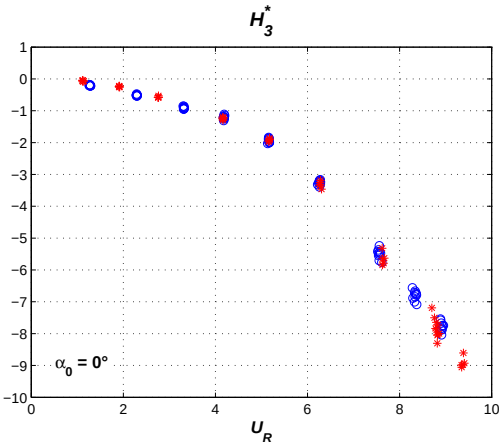
H_3^*
α_0 = 0°
U_R

(c)

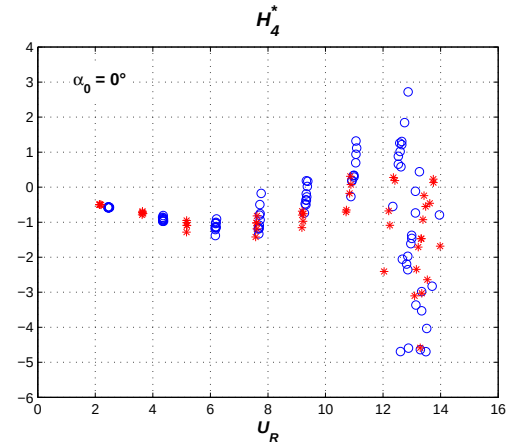
H_4^*
α_0 = 0°
U_R

(d)

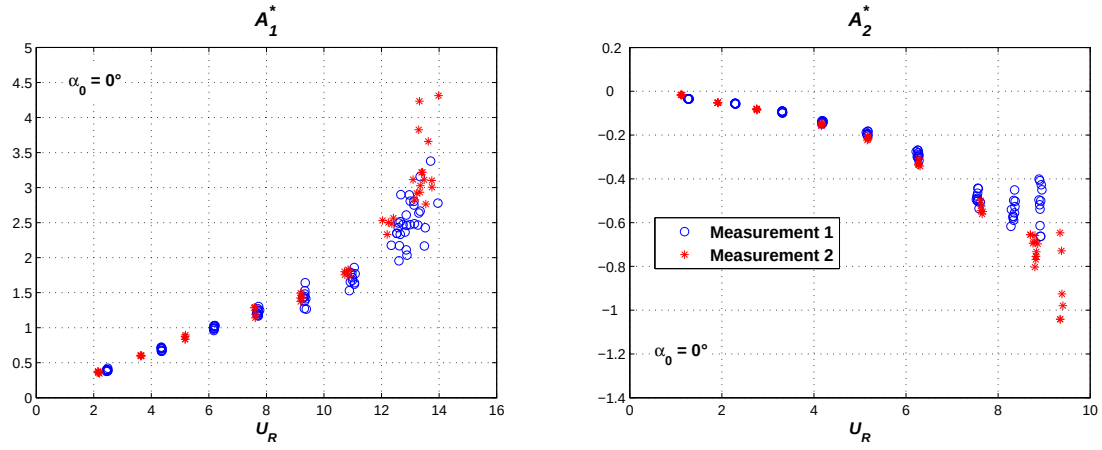

(e) (f)

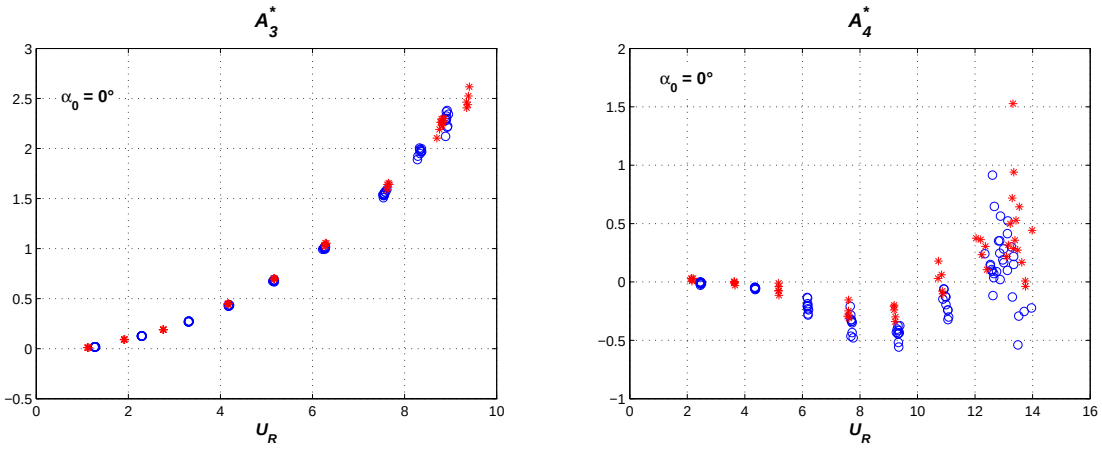

(g) (h)

Figure A.7: Repeatability of the flutter derivative measurements

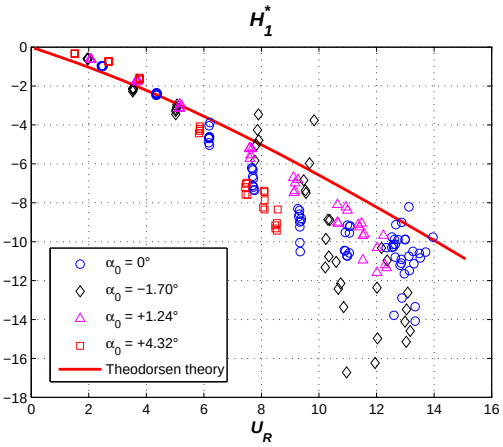
H_1^*
U_R
α_0 = 0°
α_0 = −1.70°
α_0 = +1.24°
α_0 = +4.32°
Theodorsen theory

(a)

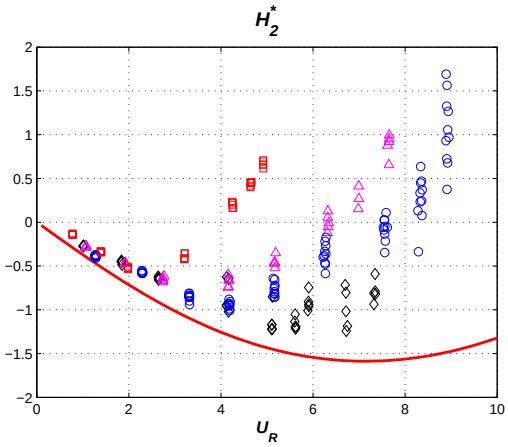
H_2^*
U_R

(b)

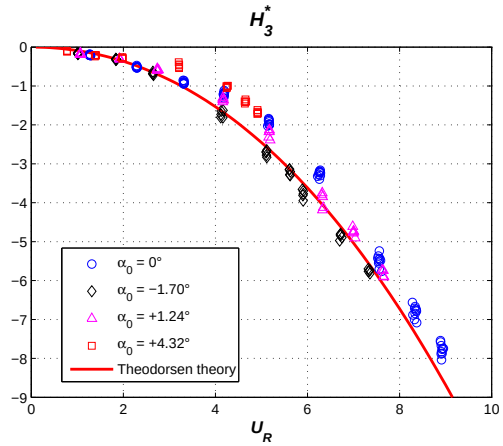
H_3^*
U_R
α_0 = 0°
α_0 = −1.70°
α_0 = +1.24°
α_0 = +4.32°
Theodorsen theory

(c)

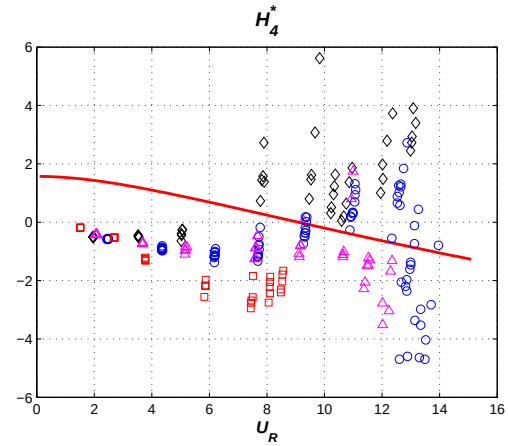
H_4^*
U_R

(d)

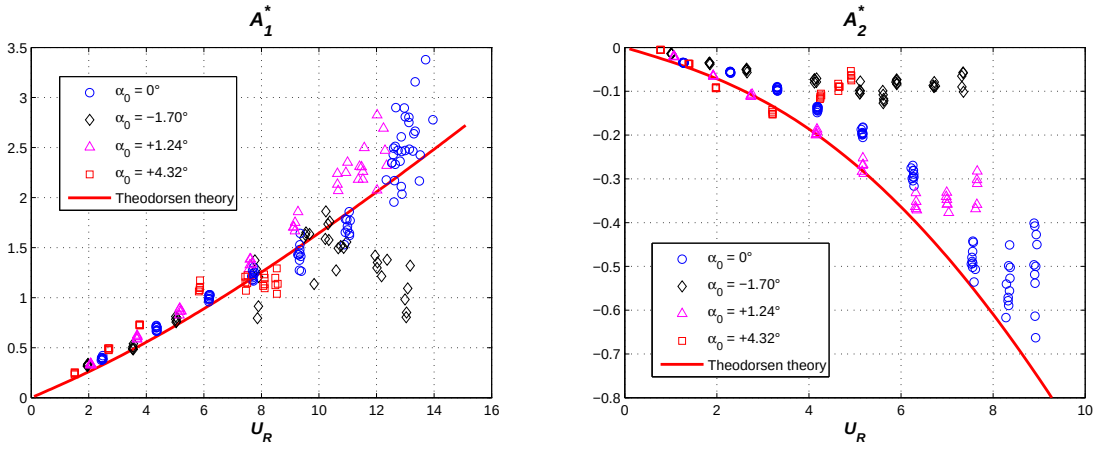

(e) (f)

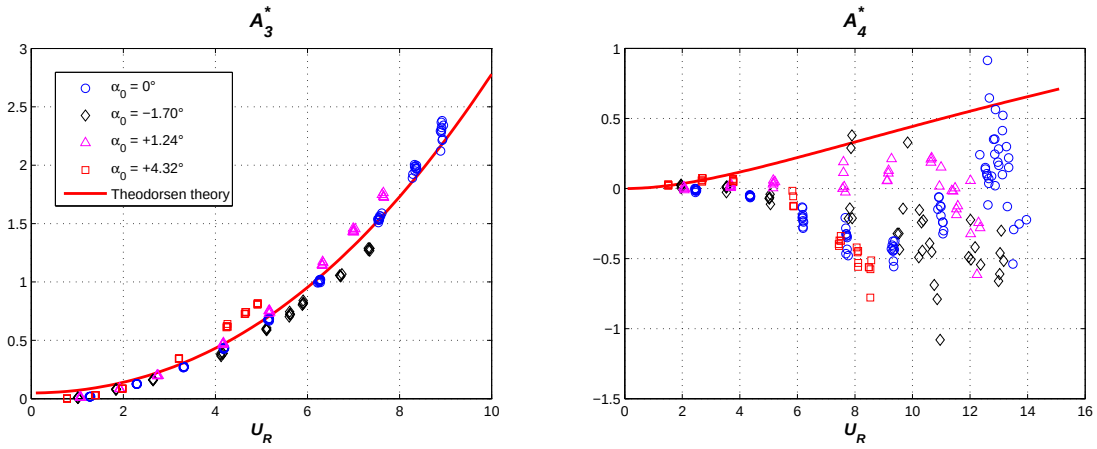

(g) (h)

Figure A.8: Flutter derivatives for four different still-air angles of attack α_0

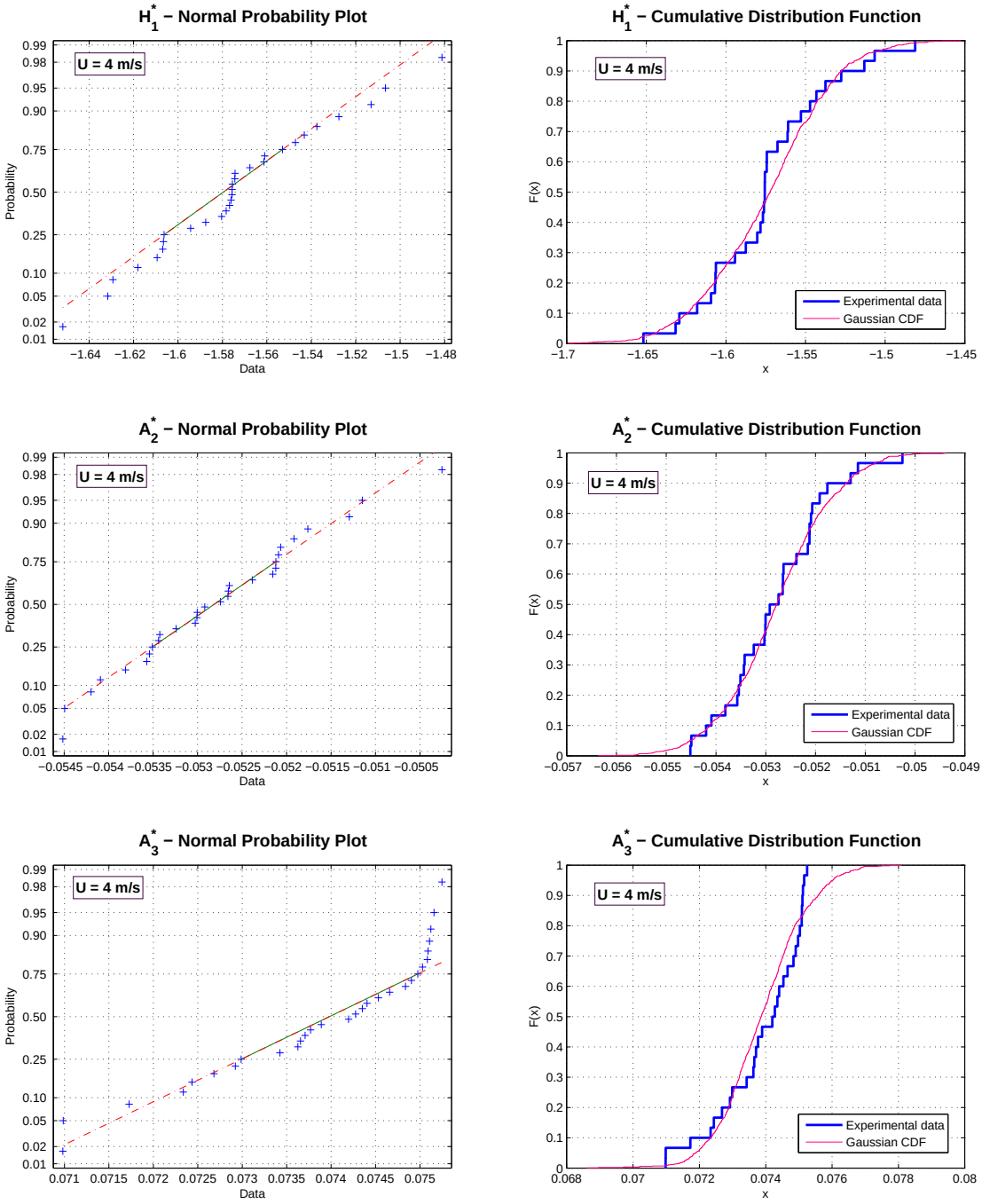

Figure A.9: Probability plot and cumulative distribution function for the flutter derivatives H_1^*, A_2^*, A_3^* measured at a wind speed of 4 m/s (sample size $N = 30$)

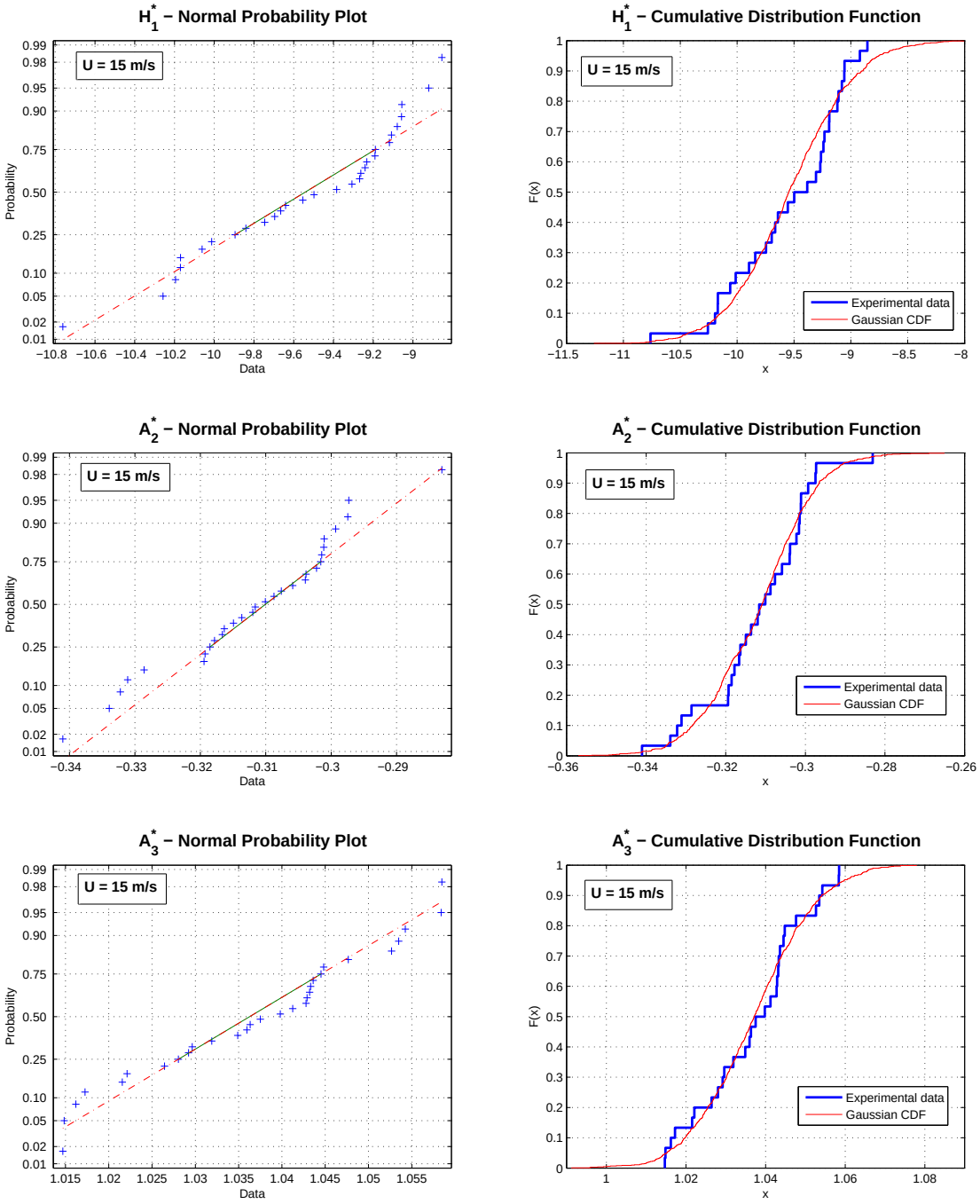

Figure A.10: Probability plot and cumulative distribution function for the flutter derivatives H_1^*, A_2^*, A_3^* measured at a wind speed of 15 m/s (sample size $N = 30$)

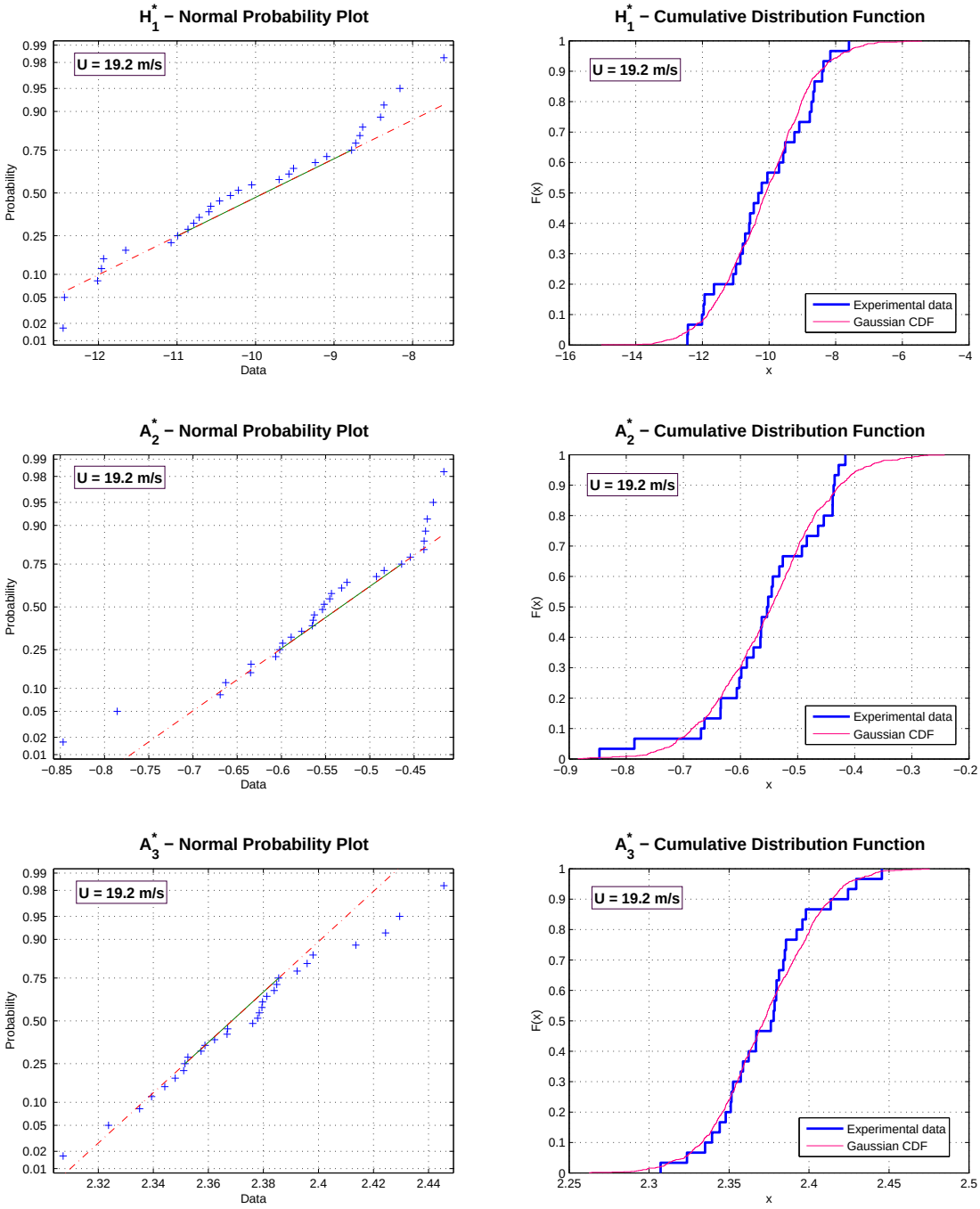

Figure A.11: Probability plot and cumulative distribution function for the flutter derivatives H_1^*, A_2^*, A_3^* measured at a wind speed of 19.2 m/s (sample size $N = 30$)